Diagnostic and Therapeutic Devices and Applications of Endoscopic Optical Coherence Tomography

by

Osman Oguz Ahsen

B.S., Electrical and Electronics Engineering
Bilkent University, 2010

S.M., Electrical Engineering and Computer Science
Massachusetts Institute of Technology, 2013

Submitted to the
DEPARTMENT OF ELECTRICAL ENGINEERING AND COMPUTER SCIENCE
in partial fulfillment of the requirements for the degree of
DOCTOR OF PHILOSOPHY

at the

MASSACHUSETTS INSTITUTE OF TECHNOLOGY
June 2018

Signature of Author _____
Department of Electrical Engineering and Computer Science
May 18, 2018

Certified by _____
James G. Fujimoto
Elihu Thomson Professor of Electrical Engineering and Computer Science
Thesis Supervisor

Accepted by _____
Leslie A. Kolodziejski
Professor of Electrical Engineering and Computer Science
Chair, Department Committee on Graduate Students

Diagnostic and Therapeutic Devices and Applications of Endoscopic Optical Coherence Tomography

by

Osman Oguz Ahsen

Submitted to the Department of Electrical Engineering and Computer Science on May 18, 2018 in Partial Fulfillment of the Requirements for the Degree of Doctor of Philosophy in Electrical Engineering and Computer Science

Abstract

There is an increased demand for developing transformative technologies to satisfy unmet needs in the clinical management of a number of gastrointestinal (GI) tract diseases. With the maturation of swept-source lasers, OCT technology has undergone major advancements over the last few years. Swept-source laser sources based on Fourier domain mode locking (FDML), akinetic and vertical cavity surface emitting laser (VCSEL) technologies have shown to reach and exceed MHz OCT imaging speeds. Our group has harnessed these advances by developing an ultrahigh-speed endoscopic OCT system that operated at and above 600 kHz A-scan rates, > 10 times faster than commercial endoscopic OCT systems. Equipped with distal rotating micromotor catheters, this system allowed visualization of microstructures and functional processes that were not possible to observe with the older generation OCT systems.

The overarching aim of this thesis was to showcase novel clinical and research applications that were enabled by this next generation ultrahigh-speed endoscopic OCT system. Towards this aim, this thesis focused on two main projects, 1) Demonstrating clinical applications of volumetric *en face* and cross-sectional OCT, and OCT angiography (OCTA) and 2) Developing integrated OCT imaging and esophageal electrical muscle stimulation methods. For the first project, two gastrointestinal (GI) tact diseases were investigated: Barrett's esophagus (BE) and associated dysplasia, and chronic radiation proctopathy (CRP). For the second project, esophageal electrical muscle stimulation methods were assessed to achieve circumferential esophageal tissue coverage for catheter imaging and therapeutic applications, with experiments performed in living swine. Furthermore, methods for improving scanning stability and robustness of the ultrahigh-speed endoscopic OCT system, as well as for optimizing data acquisition and visualization were discussed.

This thesis illustrated that ultrahigh-speed endoscopic OCT technology powered by the next generation swept-source light sources and precision scanning micromotor catheters opened new research directions ranging from diagnosis of early cancers to studying the pathophysiology of GI tract diseases and assessing efficacy of and response to therapeutic interventions. As the field of OCT continues to evolve, endoscopic OCT is one step closer to find its niche in solving prolonged clinical problems.

Thesis Supervisor: James G. Fujimoto
Title: Elihu Thomson Professor of Electrical Engineering

Acknowledgements

I appreciate my thesis advisor Prof. James Fujimoto for giving me the opportunity to work in his research group and providing the facilities and guidance that enabled me to complete this thesis.

I would like to thank many of the graduate students and postdoctoral associates that were immensely helpful during my graduate studies. Kenny Tao was instrumental in teaching me fundamental concepts of optics and OCT technology. Similarly, Chao Zhou, Ireneusz Grulkowski, Mike Giacomelli and Jonathan Liu were always reachable and did not hesitate to share their experience and wisdom. I am very glad to be working closely with the endoscopy team in our group including Tsung-Han Tsai, Hsiang-Chieh Lee, Kaicheng Liang and Zhao Wang. I got the opportunity to work with Tan Nguyen, Jason Zhang, Siyu Chen and Oscar Carrasco-Zevallos towards the ends of my studies and found them to be highly skillful and pleasant to interact with, and wish them the best for their upcoming tenures at MIT. Members of the ophthalmic and microscopy groups including Chen Lu, Tadayuki Yoshitake, Lennart Husvogt, Lucas Cahill, Eric Moult, Patrick Yiu and Ben Lee were always available to complement our knowledge and cheer us up during stressful times. Ben Potsaid was very helpful especially in setting up and operating the VCSEL light sources, as well as bridging our collaboration with Thorlabs. I am very grateful for the comments and insights of Aaron Aguirre on various projects and his sincere advice on matters of graduate life. I am very thankful to Julia Schottenhamml, for not only helping me with her programming experience on different projects but also for accompanying me in various extracurricular adventures. I can not thank Dorothy Fleischer enough for not only her excellent job as our group's administrative assistant but also for her wonderful personality and caring spirit.

I also would like to acknowledge the clinical support of Veterans Affairs Boston Healthcare personnel. Dr. Hiroshi Mashimo was a great clinical collaborator, mentor and friend. Dr. Qin Huang was always available for interpreting the pathological data with his unique positive attitude. Marisa Figueiredo, Frances Achee, Lisa Jepeal, Rayhme Collins and Greg Daniels were instrumental in patient scheduling and other logistical arrangements, and maintaining our research credentials and protocols. The VA nursing staff including Annalee Murphy and Joanne Hill were immensely helpful in facilitating our studies at the VA hospital.

I also would like to acknowledge the help of MIT E25 animal facility veterinary personnel and staff, including Dr. Alison Hayward, in facilitating our swine studies. I thank Prof. Giovanni Traverso for giving access to swine under his research protocols for OCT imaging and EMS experiments.

Last but not least I would like to thank my family and friends for all their unconditional support over the years as I navigated through the rough paths of graduate life. My friends from the Turkish gang including Sukru Cinar, Burak Dura, Halil Tekin, Erman Timurdogan, Onur Ornek, Melih Okan, Mustafa Yalcinoz and Ahmet Demir were always right by my side whenever I needed their support. My friends from MIT Outing club including Katherine Rosenfeld, Shireen Warnock, Colie Pilling, Maike Sonnewald, Hariharan Rahul and Ben Thompson were always up for an adventure and showed me that it is possible to have fun while doing things that are physically extremely challenging.

I look forward to continuing my endeavors in tackling clinical issues related to debilitating diseases and do my very best in the never-ending struggle to improve the human condition.

"So many people live within unhappy circumstances and yet will not take the initiative to change their situation because they are conditioned to a life of security, conformity, and conservatism, all of which may appear to give one peace of mind, but in reality nothing is more dangerous to the adventurous spirit within a man than a secure future. The very basic core of a man's living spirit is his passion for adventure. The joy of life comes from our encounters with new experiences, and hence there is no greater joy than to have an endlessly changing horizon, for each day to have a new and different sun."

Jon Krakauer

This thesis is dedicated to the kind ones, to the compassionate ones, to the fair ones and to the ones who want to do good for this world.

Contents

Abstract 2

Acknowledgements 3

Chapter I. Introduction 7

1.1. Overview of Barrett's esophagus and chronic radiation proctopathy 7
1.2. Recent advances in endoscopic OCT technology 9
1.3. Scope of the thesis 13

Chapter II. Improvements to the Ultrahigh-speed Endoscopic OCT System 16

2.1. Motivation 16
2.2. Optimization of pullback uniformity 24
2.3. Optimization of rotational scanning uniformity 27
2.4. Optimization of data acquisition and visualization 35
2.4.1. Data acquisition 35
2.4.2. Data visualization 37

Chapter III. Endoscopic OCT in Barrett's Esophagus 41

3.1. Motivation 41
3.2. Clinical overview of Barrett's esophagus and dysplasia 43
3.2.1. Incidence and treatment 43
3.2.2. Detection and diagnosis methods of dysplasia 45
3.3. Structural *en face* and cross-sectional OCT for identifying dysplasia 47
3.3.1. Methods 47
3.3.2. Results 54
3.3.3. Discussion 58
3.4. Ultrahigh-speed endoscopic OCT for Endoscopic Mucosal Resection 69
3.4.1. Case Presentation and Methods 69
3.4.2. Results 69
3.4.3. Discussion and Conclusion 71

Chapter IV. Non-endoscopic OCT Assessment of Chronic Radiation Proctopathy 76

4.1. Motivation 76
4.2. Clinical overview of CRP 78
4.2.1. Pathophysiology 78
4.2.2. Prevalence and Diagnosis 81
4.2.3. Clinical Management and Treatment 82
4.3. Non-endoscopic OCT assessment of CRP 88

4.3.1. Materials and methods 88
4.3.2. Results 90
4.3.3. Discussion 97
Chapter V. Integrated OCT Imaging and Electrical Muscle Stimulation (EMS) 104
5.1. Motivation 104
5.2. Mechanism and safety considerations of EMS 105
5.3. Electrical muscle stimulation experiments 107
5.3.1. Construction of the flexible, semi-transparent EMS circuits 107
5.3.2. Integrated EMS/OCT balloon catheter and *in vivo* swine experiments 110
Chapter VI. Conclusion and Biography 117
6.1. Summary of thesis work 117
6.2. Future work and conclusion 120
6.3. Publications produced during thesis 124
Appendix – training materials 134
Bibliography 154

Chapter I

Introduction

1.1. Overview of Barrett's esophagus and chronic radiation proctopathy

Over the last decades there was an increased demand for developing transformative methods and technologies to satisfy unmet needs in the clinical management of a number of gastrointestinal (GI) tract diseases. The following sections will briefly overview the current clinical status and unmet needs for two of these diseases that were the subjects of this thesis. More detailed information about these diseases will be given in the subsequent chapters.

Barrett's esophagus, dysplasia and esophageal adenocarcinoma

Despite significant advances in oncology that decreased the incidence and mortality of a number of cancers such as breast and prostate cancer, GI tract cancers remain one of the most common and lethal malignancies. In 2017, it is estimated that the esophagus, stomach, colon, rectum and anal cancers will have a total incidence of 188,570, and 78,280 people will die from complications related to them. Esophageal cancer is a particularly high malignant cancer with an estimated incidence of 16,940 in 2017 and a five-year survival rate of only 18% [1]. Current programs for screening and surveillance of esophageal cancer are not optimal as evidenced by the fact that most of these cancers are detected at late stages, and an estimated number of 15,960 will die from this disease in 2017 [1].

Barrett's esophagus (BE) is a precursor to the most common form of esophageal cancer in the US, esophageal adenocarcinoma (EAC), and undergoes a number of cytological and tissue architectural alterations to progress to low-grade dysplasia (LGD) and then to high-grade dysplasia (HGD) over a patient's lifetime [2]. HGD is associated with 30-35% risk of developing EAC within 5 years [3]. Several endoscopic therapies have been developed over the last few

decades and an endoscopic eradication therapy (EET) that uses a combination of radiofrequency ablation (RFA) and endoscopic mucosal resection (EMR) was shown to eradicate BE and dysplasia in >90% of the patients [4, 5]. Therefore, detecting dysplasia in BE patients is of paramount importance in order to prevent progression to EAC.

The current standard of care for detecting dysplasia for a patient diagnosed with BE is the "Seattle protocol", which necessitate the acquisition of random biopsies every 1 – 2 cm throughout the BE segment, and taking additional target biopsies from lesions suspicious under white light endoscopy (WLE) examination [6]. However, owing to the multi-focal and patchy nature of dysplasia [7], Seattle protocol is prone to sampling errors. To motivate efforts for developing advanced imaging technologies to detect dysplasia, the American Society of Gastrointestinal Endoscopy (ASGE) has published a PIVI (Preservation and Incorporation of Valuable Endoscopic Innovations) statement that established a baseline for the required diagnostic performance of an advanced imaging technology. A sensitivity of 90%, negative predictive value of 98% and specificity of 80% is established as necessary to replace the approach of random and WLE-targeted biopsies [8]. Several studies with various advanced endoscopic imaging technologies have been conducted to determine if the PIVI criteria could be met.

Chronic radiation proctopathy

It has been estimated that in 2016 more than 400,000 patients will be diagnosed with pelvic cancer (prostate, urinary bladder, uterus, rectum, cervix or anal cancer) in the US [9]. Furthermore, in 30-60% of these cases, radiation therapy will be used as part of the treatment approach [10, 11]. In up to 20 – 30% of these patients chronic radiation proctopathy (CRP) will develop, which is a debilitating condition associated with the formation of abnormal vascular lesions that may lead to persistent rectal bleeding [12].

Up to 75% of patients receive pelvic radiation therapy have acute radiation proctopathy (RP) symptoms such as diarrhea, cramping, increased bowel frequency and rectal discomfort, while rectal bleeding is not typically reported [13]. In the majority of the cases, the acute symptoms cease within 6 months after cessation of the radiation therapy [14, 15]. CRP, on the

other hand, has the hallmark of hematochezia (rectal bleeding) that does not heal without intervention, and significantly affects patient quality of life.

Diagnosis of CRP requires rectal examination with a colonoscope to assess the rectal mucosa for the presence of ulceration, friability and telangiectasias [16]. Biopsies can be taken to rule out other conditions that may present similar symptoms such as inflammatory bowel disease but are generally not recommended due to the potential of complications such as fistulae formation [17]. In conjunction with a CRP diagnosis, the severity of the disease should be rated using a grading system in order to assess progression and efficacy of subsequent interventions.

There are three tiers of treatment approaches for clinical management of CRP, where the invasiveness of the treatment gradually escalates based on patients' response to interventions: 1) observation or medical therapy, 2) endoscopic therapy, 3) surgical therapy [18]. There have been several medical therapy approaches, such as sucralfate, formalin, hyperbaric oxygen, salicylic acid, short chain fatty acid, probiotics and antioxidants, and several endoscopic therapies, such as cauterization and heater probe, argon plasma coagulation (APC), Nd:YAG and KTP laser ablation, RFA and cryoablation were developed to treat the mucosal friability and rectal bleeding associated CRP. RFA has recently emerged a promising endoscopic intervention for CRP, and studies by our group showed its effectiveness in controlling rectal bleeding in the majority of the patients without any major complications [19, 20]. However, all these treatment options have different complication profiles, and comparative studies are lacking to establish the optimal treatment paradigm [18, 21-24].

1.2. Recent advances in endoscopic OCT technology

With the maturation of swept-source lasers, OCT technology has undergone major advancements over the last few years. Swept-source laser sources based on Fourier domain mode locking (FDML) [25], akinetic [26, 27] and vertical cavity surface emitting laser (VCSEL) [28-30] technology have shown to reach and exceed MHz OCT imaging speeds. Our group has harnessed these advances by developing an ultrahigh-speed endoscopic OCT system that operated at 600 kHz A-scan rate [31]. The fast OCT imaging speeds also necessitated high-speed

rotational scanning that was not achievable by traditional OCT catheters that used proximal rotary scanning to rotate the entire > 2 m catheter. Our group had previously demonstrated the possibility of using micromotors to achieve distal rotational scanning using micromotors at the distal end of the catheter albeit at low rotational scanning rates (2 Hz) [32]. Our group improved on this design to demonstrate a micromotor based OCT catheter (micromotor catheter) that could perform rotational scanning at 400 Hz [33]. The author of this thesis worked with a collaborative team to subsequently translate this VCSEL-based ultrahigh-speed endoscopic OCT technology with micromotor catheters to the endoscopy imaging suite of the VA Boston Healthcare System (VABHS) at the Jamaica Plain campus [31].

The ultrahigh-speed endoscopic OCT system with the distal scanning micromotor catheters allowed visualization of tissue structures and functional processes that were not possible to visualize by the earlier and current commercial slower-speed endoscopic OCT systems. One of the major improvement was the ability to visualize mucosal patterns, which are associated with early cancerous progression. Another advantage of this system was the ability to generate OCT angiography (OCTA), which is a technique to visualize tissue microvasculature by detecting the signal intensity variations between consecutive overlapping cross-sectional OCT images caused by erythrocyte motion [31]. A recent study by our group reported 94% sensitivity and 69% specificity for identifying dysplasia in BE using blinded assessment of OCTA images with 32 patients [34].

One of the limitations of our clinical endoscopic OCT system was the small diameter of the micromotor imaging catheter. The 3.4 mm diameter of the micromotor catheter was able to be introduced through the 3.7 mm accessory channel of the endoscope to allow simultanous OCT imaging and biopsy/EMR tissue sampling, while covering only a fraction of the esophageal circumference. Therefore, comprehensive imaging required repositioning the catheter to different esophageal quadrants. To overcome this limitation we have demonstrated circumferential imaging with a balloon [35] and capsule catheter in living swine [36]. We have subsequently translated a version of the capsule catheter to perform clinical imaging at the VABHS [37]. Capsule based imaging may be attractive in the long term because it can be

performed without sedation [38]. If sufficient sensitivity and specificity for identifying dysplasia can be achieved, capsules may enable low-cost BE screening and surveillance. We have also recently demonstrated a cycloid-scanning capsule that allowed precise two-dimensional distal scanning of 1 mm x 38 mm strips using a combination of micromotor and PZT scanner [39]. Structural OCT and OCTA images with minimal scanning distortion were demonstrated in the human rectum *in vivo.*

During the same time period, a commercial endoscopic OCT company has been formed and named as Ninepoint Medical™ (launched in 2013). The first commercial product of this company was Volumetric Laser Endoscopy (VLE) imaging system (NvisionVLE®) [40, 41]. The VLE system used OCT catheters of ~ 2.4 mm diameters which could be introduced to the biopsy accessory port of standard endoscopes. These catheters had a balloon at their most-distal ~6 cm portion that could be inflated to sizes of 14, 17 and 20 mm after being deployed to the target imaging site. The VLE system had a 50,000 kHz A-scan rate, more than an order of magnitude slower than the ultrahigh-speed endoscopic OCT system developed by our group [42]. Furthermore, the large circumferential coverage and slow imaging speeds necessitated the use of large spot sizes (~ 40 µm FWHM) and slow rotational speeds (~ 10 Hz). All these factors limited image quality, made the system more susceptible to motion and prevented visualization of certain tissue microarchitectural and microvascular features, such as mucosal and vascular patterns, in comparison to the ultrahigh-speed endoscopic OCT system.

Despite the aforementioned limitations, the VLE system was able to image circumferential and large areas of the esophagus (~ 6 cm x 6 cm area coverage within single 90 seconds acquisition using the 20 mm balloon). Cross-sectional images over the imaging area were acquired. Due to difficulties of obtaining histological correlation, initial studies assessed *ex vivo* EMR samples in order to establish features that were correlated with dysplasia in BE [42-44]. At the same time, *in vivo* VLE studies have suggested that some of the *ex vivo* features of dysplasia might appear different *in vivo* [45].

Furthermore, a 1000-patient registry study was conducted by the participation of 18 major medical centers across the US assessing the feasibility of VLE in the BE surveillance and

determining further research and development directions [46]. A major development for the VLE system was the laser marking feature which was launched in 2016 [47]. Laser making allowed areas of suspicious OCT appearance to marked using a high power laser that was visible at the subsequent endoscopic examination. This feature allowed precise histological correlation with the VLE images *in vivo,* paving the way to prospective, *in vivo* clinical studies assessing the diagnostic utility of the VLE system in BE surveillance.

In addition to the clinical developments, there were other technological developments in the endoscopic OCT technology, yet to be comprehensively assessed in clinical settings. Amongst these developments, optical coherence elastography (OCE) can quantify tissue mechanical properties by applying a mechanical stimulus to produce tissue displacement and measure the resulting strain [48]. It has been hypothesized that neoplastic progression might alter the elasticity of the tissues by an extracellular matrix remodeling accompanied by cellular alterations [49]. Needle-based OCE probes have been demonstrated, but these are yet to be translated into an *in vivo* imaging setting [50, 51].

Polarization-sensitive OCT (PS-OCT) can measure tissue birefringence properties by probing the tissue with alternating polarization states [52, 53]. Achieving PS-OCT in a probe-based imaging setting was traditionally challenging as the proximal rotational scanning employed in the endoscopic OCT catheters also altered the polarization state of the incident light in a non-controlled way. Nevertheless, several solutions have been proposed to modulate the incident light such that different polarization states can be encoded in a way that will be preserved during the rotation of the catheter [54-56]. Endoscopic PS-OCT was demonstrated in pulmonary and cardiovascular OCT imaging applications [57, 58], and recently in esophageal imaging application in a living swine [59]. PS-OCT may allow better delineation of tissue layers in the esophagus such as muscularis mucosa and muscularis propria that may have an important role during the progression of BE to dysplasia and EAC.

Another busy domain of endoscopic OCT research was multi-modal imaging applications where OCT is combined with an adjunct imaging modality to gather additional molecular and/or functional information. In this front, integration of ultrasound (US) with OCT imaging may allow

probing into deeper tissue depths, allowing applications such as cancer staging [60]. Integrated probe-based OCT/ultrasound imaging was demonstrated in cardiovascular imaging applications [61, 62]. Integrated photoacoustic/OCT imaging catheter [63, 64] allowed deeper tissue penetration similar to ultrasound, as well as assessment of hemodynamic functions such as oxygen saturation [65]. Finally, integration of OCT imaging with fluorescence imaging was demonstrated in pulmonary [66], cardiovascular [67, 68] and endoscopic applications [69]. Fluorescence imaging can open a window to directly probe molecular information either by intrinsic auto-fluorescence or by using extrinsic contrast agents that could be tailored for the clinical application.

1.3. Scope of the thesis

The broader aim of this thesis is to showcase novel clinical and research applications that were enabled by the next generation ultrahigh-speed endoscopic OCT system described in the previous section. Towards this aim, this thesis focuses on two main projects, 1) Demonstrating clinical applications of volumetric *en face* and cross-sectional OCT and OCTA and 2) Developing integrated OCT imaging and esophageal electrical muscle stimulation methods. For the first project, two gastrointestinal (GI) tact diseases were investigated using the ultrahigh-speed endoscopic OCT system: Barrett's esophagus (BE) and associated dysplasia, and chronic radiation proctopathy (CRP). For the second project, esophageal electrical muscle stimulation methods were assessed to achieve circumferential tissue coverage for catheter imaging and therapeutic applications.

Chapter I outlined the current clinical and endoscopic OCT landscape. It demonstrated unmet clinical needs in BE surveillance to identify dysplastic lesions, as well as the requirement for new tools for elucidating the pathophysiology and therapeutic assessment of CRP. It also highlighted recent technological advanced in the field of endoscopic OCT. The commercialization of the endoscopic OCT technology under the brand of volumetric laser endomicroscopy (VLE) and recent VLE studies were discussed.

Chapter II discussed engineering efforts that were undertaken to improve the scanning stability and robustness of the ultrahigh-speed endoscopic OCT system, as well as hardware improvements and processing steps applied to improve and optimize data acquisition and visualization. The effects of selecting low-friction materials for improving catheter pullback uniformity and development of a post-processing algorithm for improving rotational uniformity and for visualization of *en face* structures and achieving OCTA were discussed. The effects of various image processing steps such as dynamic range compression, high-dynamic-range filtering and depth projection on *en face* OCT images were demonstrated.

Chapter III demonstrated two clinical studies with the ultrahigh-speed endoscopic OCT system related to Barrett's esophagus and dysplasia. In the first study, we investigated a novel approach of interpreting OCT data by assessing a combination of depth-resolved *en face* and cross-sectional OCT features. We have reported the associations between *en face* and cross-sectional OCT features with histology and treatment history based on blinded readings of three independent OCT readers. This study has suggested associations that can be relevant to understanding the pathogenesis of BE dysplasia and could be important for identifying future diagnostic markers. In the second study, we have demonstrated the clinical utility of the ultrahigh-speed endoscopic OCT and OCTA for assessing a dysplastic lesion at the gastroesophageal junction (GEJ), its lateral margins before and immediately after EMR, and at 2-months follow-up. This study suggested that probe-based OCT/OCTA may improve diagnostic capabilities and enhance clinical utility by identifying dysplastic areas, assessing lesion margins, and evaluating regions immediately post-treatment and on follow-up.

Chapter IV discussed an application of OCT in the non-endoscopic assessment of chronic radiation proctopathy (CRP). A detailed overview of CRP pathophysiology was provided, including the histological structure of normal rectum and CRP-associated microstructural and microvascular changes. Strengths and shortcomings of current clinical management strategies including observation, medical therapy and endoscopic interventions were discussed. This was followed by reporting an OCT study in which the rectum and anal canal of 8 CRP patients undergoing RFA treatment and 2 normal patients were assessed non-endoscopically with the

ultrahigh-speed endoscopic OCT system using the micromotor catheter. We have demonstrated changes that occur due to CRP progression, as assessed by *en face* OCT and OCTA, as well as effects of RFA in normalizing the tissue microvascular architecture. We have also demonstrated the correlation of OCTA assessment with the clinical assessment made by endoscopic examination. OCT and OCTA had the advantage to assess submucosal tissue architecture and microvasculature, allowing insights into studying CRP pathophysiology and progression that are not achievable by endoscopic examination.

Chapter V discussed the development of esophageal muscle stimulation (EMS) techniques and their integration with a balloon-based micromotor catheter. We have developed methods to fabricate flexible, semi-transparent circuits that can be integrated with OCT catheters. We demonstrated an integrated EMS/OCT imaging catheter that had electrodes on its outer surface to apply electrical stimulation to the esophageal muscles in order to contract them around the catheter. *In vivo* swine studies have demonstrated the feasibility of esophageal muscle stimulation to achieve circumferential tissue coverage. We have concluded that this approach can be used in a broad range of therapeutic and endoscopic OCT imaging applications as any type of catheter-based therapy or imaging suffers from sub-optimal and unpredictable tissue contact.

Chapter VI summarized the thesis work and discussed future research directions. The thesis is ended with a list of author's publications during the thesis period followed by the bibliography.

Chapter II

Improvements to the Ultrahigh-speed Endoscopic OCT System

2.1. Motivation

The ultrahigh-speed endoscopic OCT system described in the previous chapter enabled very high axial OCT scan rates, which directly translates into acquisition of datasets with higher sampling density for a given data acquisition time. This is a crucial advantage for endoscopic imaging applications because physiological motion artifacts such as breathing and respiration have detrimental effects on image quality. The ability to acquire datasets in shorter time greatly reduces the effects of such artifacts on the images.

One critical advance that was enabled by the ultrahigh-speed endoscopic OCT system was the ability to visualize structures in the *en face* plane, in addition to traditional cross-sectional OCT imaging (**Figure 2.1**). Although cross-sectional imaging is the primary niche of the OCT technology, it also represents a challenge to existing endoscopic imaging and diagnostic paradigms as the endoscopists are not used to or trained to interpret cross-sectional images. Endoscopic ultrasound provides cross-sectional images similar to OCT, but its use in the US has declined over the past years and is mainly reserved for patients with more advanced esophageal cancer. Therefore, endoscopists working in a community setting performing screening and surveillance endoscopies are generally not trained with that imaging technology. Furthermore, contrast mechanisms, resolutions and imaging depths of ultrasound are significantly different from OCT imaging, hence a familiarity in one domain might not be directly transferable to the other domain.

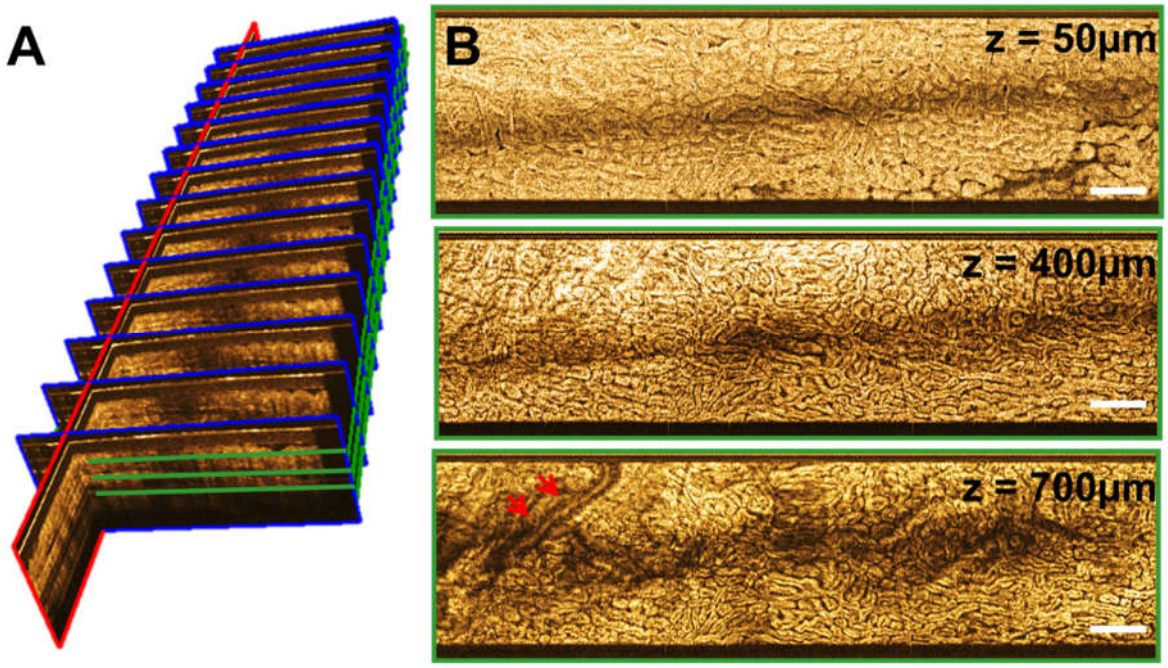

Figure 2.1 Volumetric OCT dataset visualization. **A**, representation of volumetric OCT dataset showing cross-sectional (blue frame), longitudinal (red frame) and *en face* views (green frame) which are intrinsically co-registered. The series of cross-sectional OCT images at sequential longitudinal positions could be scrolled for rapid viewing, or specific cross-sections from en face regions of interest (ROIs) viewed selectively. **B**, depth-resolved en face OCT images at various depths. The *en face* OCT image near the surface shows the superficial mucosal architecture, whereas deeper images delineate the mucosal patterns in greater detail and contrast. At depths near the muscularis mucosa/submucosa (~ 700 µm) boundary, vascular features can be observed. Arrows point to a large vessel observed by its shadowing within the muscularis mucosa/submucosa, as scattering from blood in the vessel produces attenuation of OCT signals from deeper levels. *En face* OCT images at a given depth are viewed by summing over +/-50 µm depth (100 µm projection range) to improve contrast and reduce noise. *En face* OCT images in this figure are cropped from a larger dataset to exclude regions which are out of contact with the OCT catheter. Scale bars are 1 mm.

On the contrary, endoscopists are familiar with the endoscopic appearance which shows tissue structures in an *en face* plane. As early as the 1990s it was recognized that intestinal tissues have specific patterns visible on the *en face* views (**Figure 2.2** and **Figure 2.3**) [70, 71]. These patterns were named as mucosal surface patterns, or pit patterns in the lower GI setting, and changes occurring to them in association with cancerous progression were extensively studied [72-76].

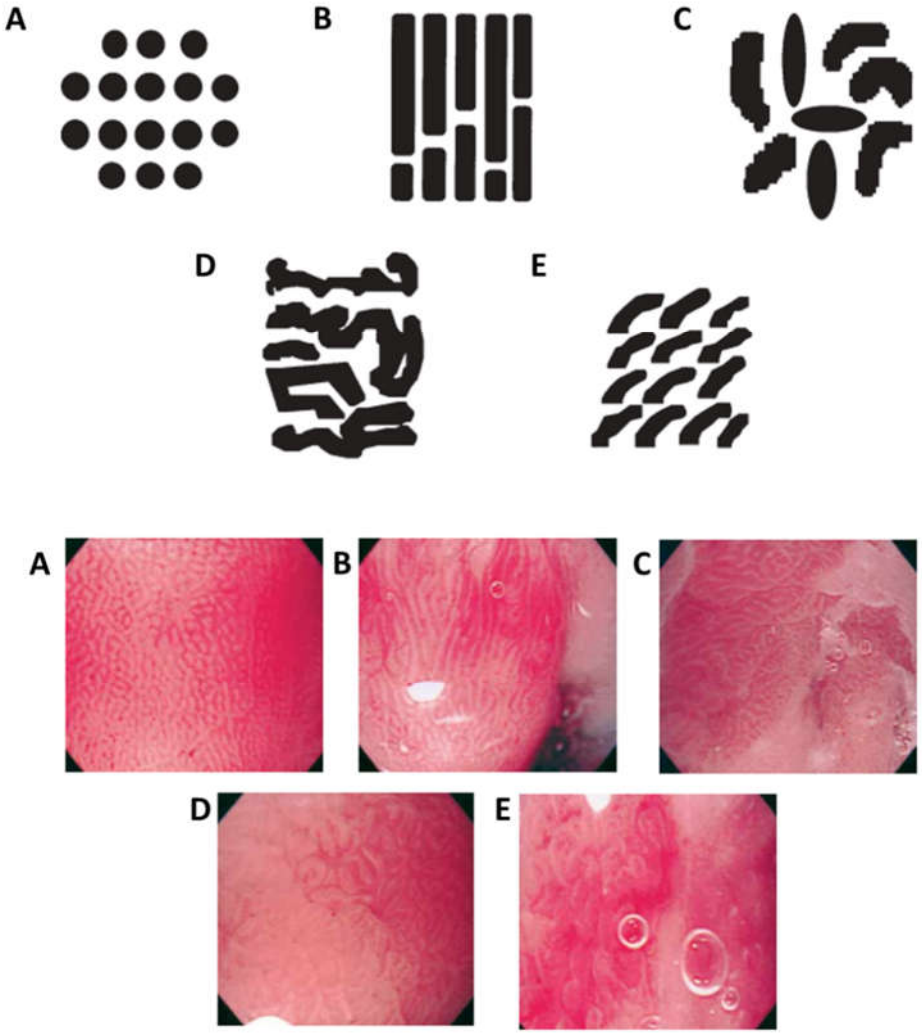

Figure 2.2. Mucosal surface patterns in the upper gastrointestinal tract. The set of images on the upper part are cartoon drawings of the patterns while the set of images on the lower part are magnifying white light endoscopy images corresponding to those drawings. **A,** pit-1, small round, **B,** pit-2, straight, **C,** pit-3, long oval, **D,** pit-4, tubular, **E,** pit-5, villous. Pit-3, pit-4 and pit-5 are strongly associated with intestinal metaplasia. Images are modified from [70].

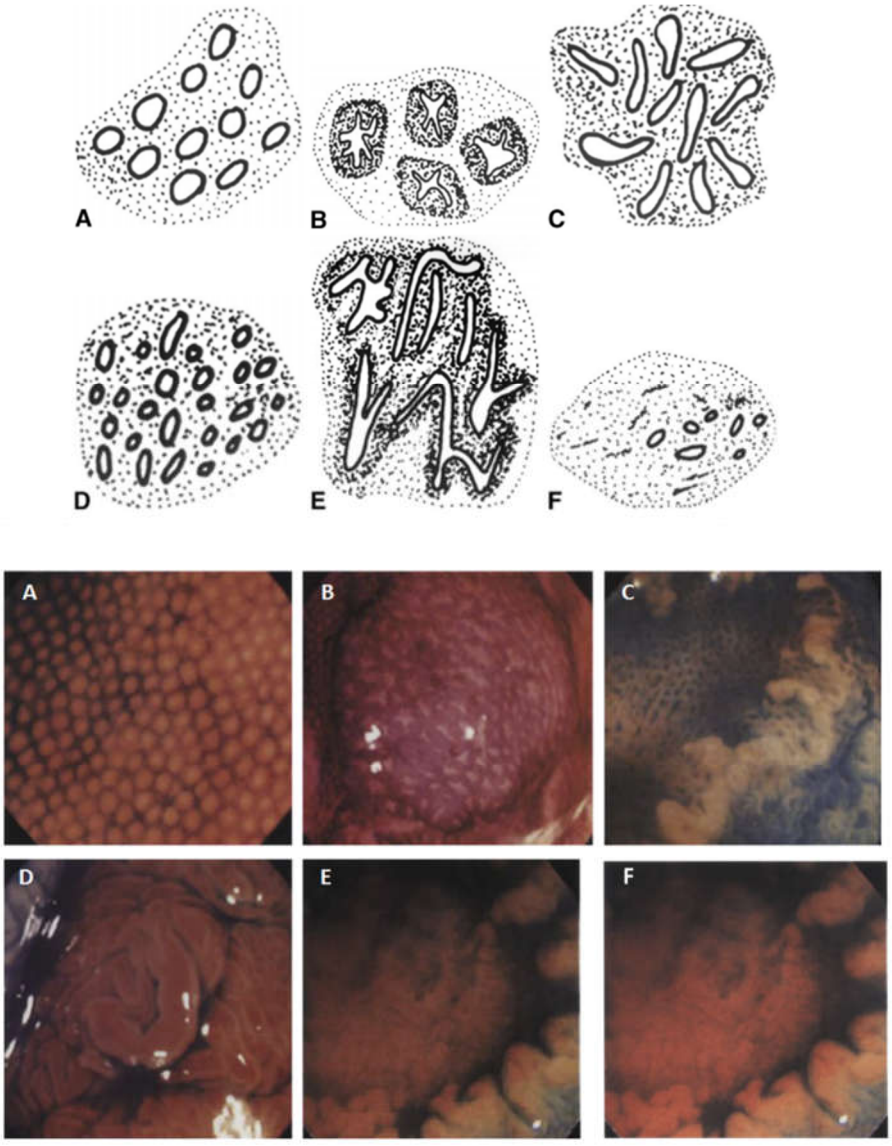

Figure 2.3. Mucosal surface patterns in the lower gastrointestinal tract. The set of images on the upper part are cartoon drawings of the patterns while the set of images on the lower part are magnifying chromoendoscopy images obtained with indigo carmine spraying corresponding to those drawings. **A,** Type I, round pits, **B,** Type II, stellar or papillary pits, **C,** Type III-L, large tubular or roundish pits, **D,** Type III-S, small tubular or roundish pits, **E,** Type IV, branch-like or gyrus-like pits. **F,** Type V, non-structural pits. Type I – Type III patterns are associated with hyperplasia and adenoma while Type – IV and Type – V patterns are associated with invasive cancer. Type – V pattern has a strong association with submucosal layer involvement. Images are modified from [71].

While *en face* OCT images were shown with the earlier generation FDML based endoscopic OCT imaging systems, imaging speeds were low (<50 kHz A-line rate), which prevented visualization of the mucosal patterns in *in vivo* settings. Slow imaging speeds made it challenging to acquire datasets with high sampling density and made the datasets susceptible to physiological

motion artifacts due to breathing, respiration etc. Example *en face* OCT images in **Figure 2.4** show the difference between visualization of the mucosal patterns with the early generation FDML based endoscopic OCT systems and the VCSEL-based ultrahigh-speed endoscopic OCT system developed during this thesis work. In both lower and upper GI tissues, the specific regular circular mucosal patterns of Barrett's esophagus and colonic mucosa cannot be clearly discerned from the images acquired by the early generation OCT systems, while they can be clearly visualized with the ultrahigh-speed endoscopic OCT system.

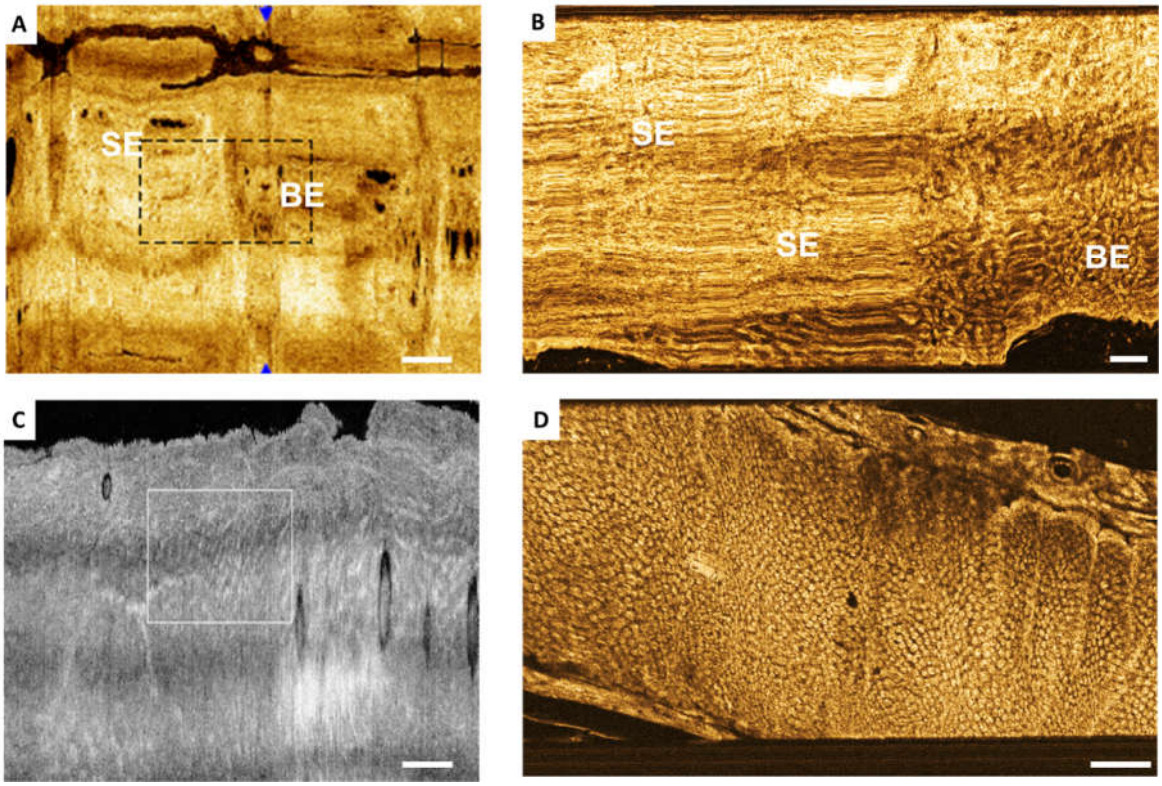

Figure 2.4. Comparison of *en face* images obtained by the older generation FDML-based endoscopic OCT systems and the VCSEL-based ultrahigh-speed endoscopic OCT system developed during this thesis work. **A, B,** *En face* OCT images around the squamocolumnar junction in the upper gastrointestinal tract of a patient with Barrett's esophagus (BE) obtained with the FDML and VCSEL systems, respectively. The regular circular mucosal patterns characteristic of BE can be visualized in **B** while they can not be discerned in **A. C, D,** *En face* OCT images in the lower gastrointestinal tract of a patient obtained with the FDML and VCSEL system, respectively. The regular circular mucosal patterns characteristic of the normal rectum and large intestine can be visualized in **D** while they can not be discerned in **C.** SE: Squamous esophagus, BE: Barrett's esophagus. Scale bars are 1 mm. Images in **A** and **C** are modified from [77] and [78], respectively.

The high OCT imaging speeds made it possible to acquire datasets with higher sampling density, however, a number of artifacts due to non-uniform scanning and motion was still present. One particular artifact commonly observed in the *en face* OCT images was the cardiac motion. As exemplified in **Figure 2.5**, there is a motion artifact that imparts a periodic stretching/compression on the *en face* structures can be observed at the tissue depths (**Figure 2.5B**) while it is not observed at the catheter depths (**Figure 2.5A**). This implies that this imaging artifact was generated by the tissue motion rather than non-uniform pullback of the catheter. The periodicity and rate of this artifact (60 stretches-per second) suggested that the primary motion observed in this image is due to the cardiac cycle. It should be noted that we observed that the effect of this cardiac motion on the images was highly depended on the patient as well as the imaging location. In some patients motion artifacts had a significant impact on the *en face* image quality (in the form of the stretching and/or compression of the tissue structures as shown in **Figure 2.5**) while in other patients these artifacts were negligible. Imaging locations closer to heart, such as mid-esophagus, exhibited more pronounced artifacts while imaging locations further away from the heart, such as gastro-esophageal junction, exhibited less severe artifacts related to this physiological motion. Needless to say, imaging in lower GI tract did not exhibit these artifacts given its distance from the heart, and *en face* image quality in the lower GI tract was in general significantly better compared to image quality in the upper GI tract.

Another source of imaging artifacts was the non-uniform scanning of the micromotor catheter. Endoscopic OCT images are acquired by a helical scanning pattern, where the micromotor at the distal end of the catheter performs a fast rotary scanning to generate the cross-sectional OCT images, while the entire optical assembly is pulled back internally within the catheter sheath to acquire cross-sectional OCT images at different longitudinal positions. Non-uniformities of these two scanning mechanisms generated imaging artifacts. The next two sections discussed various method we have applied to optimize pullback and rotational scanning uniformity.

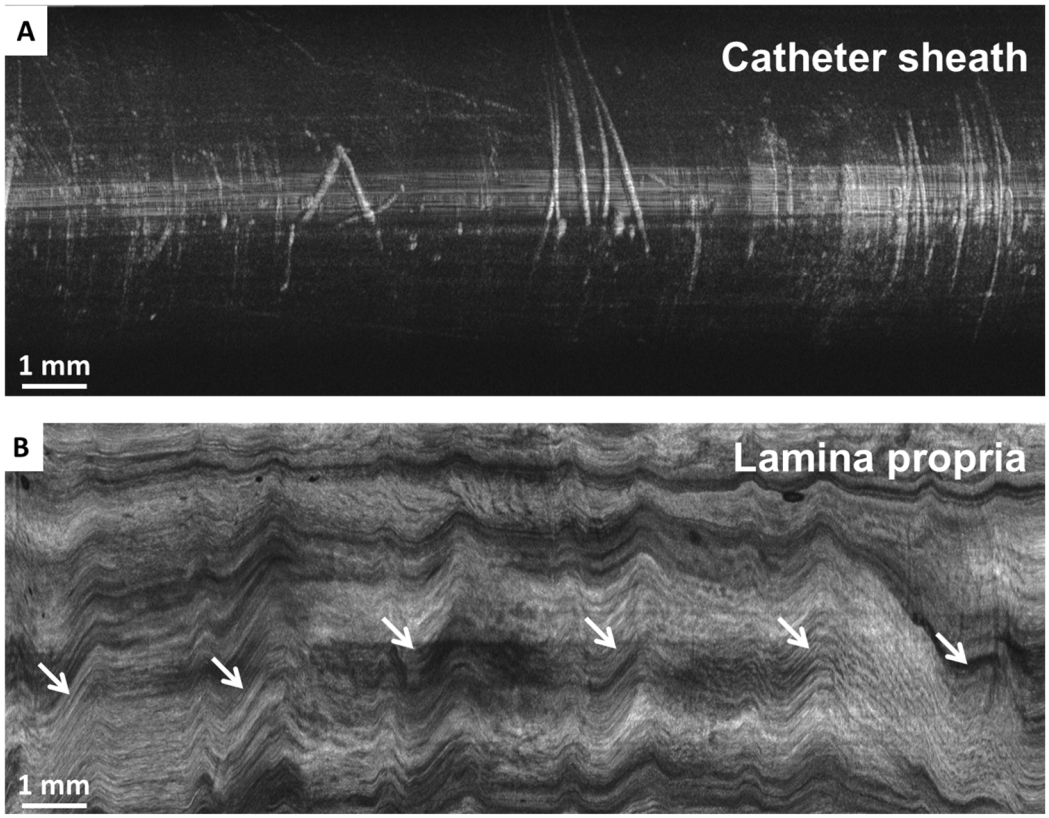

Figure 2.5. Effect of cardiac motion on the *en face* OCT images. **A,** shows an *en face* OCT image at the depth of the catheter sheath surface, showing scratches and other defects on the sheath. **B,** shows an *en face* OCT image from the normal squamous esophagus of a patient at a depth of ~ 300 μm below the tissue surface, around deep epithelium/lamina propria layer. Both images are from the same dataset that spans a 20 mm pullback region acquired over 10 seconds. Periodic artifacts with a rate of 60 per second can be observed in **B** while they are not observed in **A,** suggesting that the artifact is from the cardiac cycle rather than the pullback scanning.

The prototype ultrahigh-speed endoscopic OCT system used in this work was developed by a team led by former graduate student Tsung-Han Tsai with the assistance of Benjamin Potsaid, Yuankai Tao and the author of this thesis. The micromotor catheter was originally designed by Tsung-Han Tsai, but then revised and improved by Hsiang-Chieh Lee and the author of this thesis as discussed later in this chapter. All micromotor catheters used throughout this thesis was constructed by Hsiang-Chieh Lee and the author of this thesis. The data acquisition software was originally designed by a team led by former visiting scientist Martin Kraus with the assistance of Jonathan Liu, Chen Lu and the author of this thesis. This software was modified and optimized for the endoscopic OCT system by the author of this thesis, as described in the next

sections. The author of this thesis designed and built the patient interface unit (PIU) which enclosed the linear translation stage used for the pullback and had the electrical and optical connections between the micromotor catheter and the OCT system (**Figure 2.6**). Pullback optimization experiments were conducted by the thesis author and Hsiang-Chieh Lee with assistance from Kaicheng Liang. The non-uniform rotational distortion (NURD) correction algorithm was developed by the thesis author. Application of high-dynamic range (HDR) filtering on *en face* images was inspired by the work of former graduate student Jonathan Liu. Other image processing steps, including depth projection and application of colormaps, were based on work of former graduate students Desmond Adler and Aaron Aguirre, as well as general GI OCT and optical coherence microscopy (OCM) literature. All human imaging experiments were conducted at the VA hospital by the endoscopy team including Tsung-Han Tsai, Hsiang-Chieh Lee, Kaicheng Liang, Zhao Wang, Michael Giacomelli and the author of this thesis with the help of our clinical collaborator (Hiroshi Mashimo) and VA nursing and administrative staff. Hsiang-Chieh Lee and Kaicheng Liang were involved in the majority of the discussions that led to the experiments described this chapter.

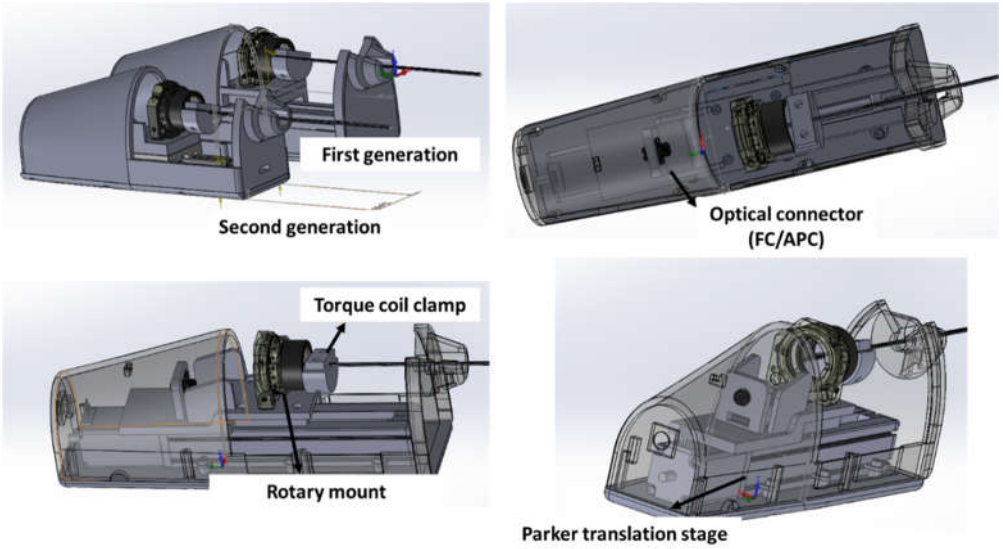

Figure 2.6. Three-dimensional rendering of the patient interface unit (PIU). The second generation PIU currently used in the clinic has a size of 236 mm (l) x 66 mm (w) x 95 mm (h). The torque coil is clamped onto the PIU which is attached to a rotary mount to allow small angular adjustments of the imaging window. A Parker™ translation stage (LP28_T0075D01) was used to allow a maximum of 75 mm pullback at a maximum speed of 10 mm/sec.

2.2. Optimization of pullback uniformity

As discussed in the previous section, physiological motion such as cardiac motion affects the *en face* visualization by imparting a stretching and/or compression artifacts to the structures. This essentially changes effective pullback speed of the catheter. Another source that can affect the effective pullback speed is the internal pullback mechanism. As depicted in **Figure 2.7**, the basic components relevant to the pullback of the OCT catheters are the torque coil and the encompassing sheath. The torque coil carries the optical fiber as well as the electrical cables while having the optical components for focusing the imaging beam at its distal end. At its proximal end, the torque coil is connected to a patient interface unit (PIU) that houses a linear translation stage to perform the pullback. The torque coil is contained within a fully water-sealed clear plastic sheath which prevents liquids and other substances to contaminate the optical elements. As a result, the torque coil is pulled back within the sheath and the frictional forces between the torque coil and sheath determine the smoothness of the pullback.

We have constructed a setup to measure the pullback speed with different torque coil/sheath combinations. As depicted in **Figure 2.7**, dummy OCT catheters were built and a textured element was added to their distal end. The catheters consisted of a 2.2 mm OD stainless-steel torque coil (ACTONE^{TM}, Asahi Intecc, CA) pulled back within an AWG9 (3 mm inner diameter, 200 µm wall thickness) FEP or PTFE sheath (Zeus Industrial Products, SC), as indicated in the figure. In order to simulate PTFE coating, an AWG11 PTFE sheath (2.4 mm inner diameter, 200 µm wall thickness, Zeus Industrial Products, SC) was used. These catheters had the same length of a regular micromotor catheter (~ 216 cm) and were positioned in a way that would simulate the major bends encountered during upper GI imaging. A camera was used to capture the motion of the textured distal end of the catheter from which the effective pullback speed of the distal end could be measured. For all experiments, a 2 mm/sec pullback speed was used consistent with the pullback speed used with the ultrahigh-speed endoscopic OCT system for the human imaging studies.

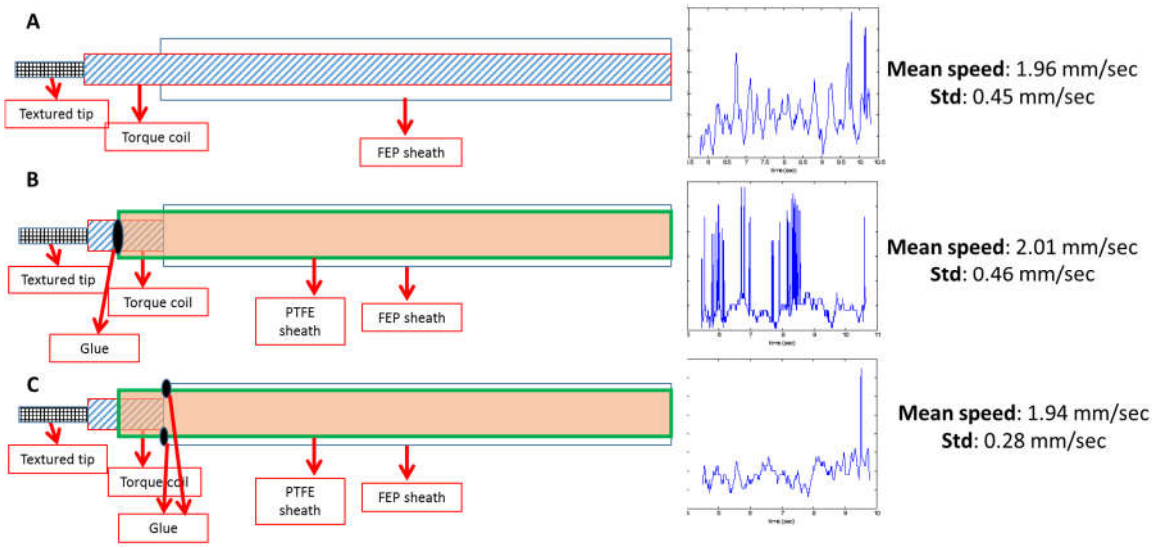

Figure 2.7. Pullback speed test for three different torque coil/sheath configurations. **A,** is the standard combination where a 2.2mm OD torque coil moves within a 3 mm ID FEP sheath. **B,** torque coil is glued to a 2.4 mm ID, 200 µm wall thickness PTFE sheath, such that PTFE sheath moves together with the torque coil within the FEP sheath same as in **A**. **C,** PTFE sheath same as in **B** is glued to FEP sheath same as in **B,** such that the torque coil moves within the PTFE sheath. This simulates the movement of the torque coil within a PTFE sheath. The mean pullback speeds in all three configurations are about 2 mm/sec, which is the speed of the proximal translation stage. The standard deviation is significantly smaller for the configuration in **C.**

We have tested two different torque coil designs. The standard torque coil was constructed from stainless steel (2.2 mm OD, ACTONE^{TM}, Asahi Intecc, CA), while we also had custom-made version where a PTFE coating was applied onto the steel coil (2.2 mm OD, Asahi Intecc, CA). Furthermore, in addition to the standard FEP-based sheath commonly used in the OCT catheters, we have tested a PTFE-based sheath (AWG9, 3 mm inner diameter, Zeus Industrial Products, SC). For both the torque coil and sheath, the PTFE material was hypothesized to have a better pullback performance resulting from a lower frictional constant.

The mean and standard deviation of pullback speeds for these different configurations were given in **Figure 2.8**. The mean distal pullback speed was about 2 mm/sec, consistent with the speed of the proximal translation stage, however, the standard deviation varied significantly between different torque coil/sheath configurations. Of particular note, PTFE coated torque coil had significantly worse pullback performance in both within the FEP and PTFE sheaths and exhibited speed spikes during the pullback. This suggested that the friction between two plastic

materials, such as FEP vs PTFE or PTFE vs PTFE, results in an undesired pullback performance. The best pullback performance was observed when the standard uncoated torque coil was pulled back within the PTFE sheath. This configuration was used in the subsequent micromotor catheter assemblies since early 2014.

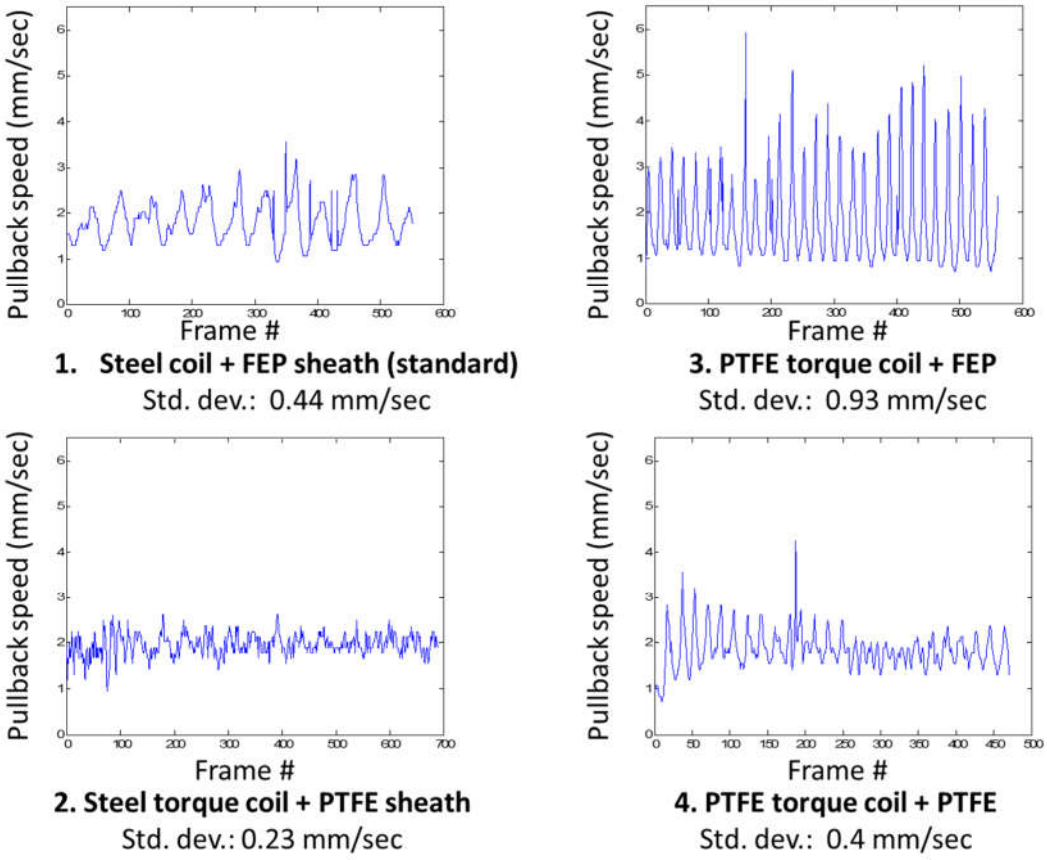

Figure 2.8. Pullback speed test for four different torque coil/sheath configurations. The standard configuration was to use a stainless steel torque coil (2.2 mm outer diameter) within an AWG9 FEP sheath (AWG9: 3 mm inner diameter, 200 µm wall thickness). A PTFE-coated version of the same torque coil was used in configurations 3. and 4. PTFE sheath was used instead of the FEP sheath in configurations 2. and 4. Proximal pullback speed was set to 2 mm/sec in all configurations. Configuration 2. shows the best pullback performance in terms of standard deviation of pullback speed variations.

2.3. Optimization of rotational scanning uniformity

Nonuniform rotational distortion (NURD) is a common problem in catheter-based imaging systems such as intravascular and endoscopic Optical Coherence Tomography (OCT) and ultrasound [79, 80]. Conventional catheter-based imaging systems employ proximal actuation to rotate the optical assembly and generate a circumferential scan. In these systems, NURD is observed for both *in vivo* human and *ex vivo* phantom studies, suggesting that it is inherently present due to mechanical friction between the catheter torque coil and sheath [79, 80]. Physiological motion, as well as bends encountered in endoscopic and cardiovascular imaging applications, can exacerbate the severity of the rotational nonuniformity.

Micromotor catheters perform distal rotational scanning and eliminate some of the aforementioned problems associated with proximal rotation [81, 82]. Rotation speed as high as 3.2kHz was reported with a micromotor catheter, which cannot be attained by proximal actuation [83]. Unfortunately, NURD is still observed in micromotor imaging catheters due to motor mechanical instability, although it is significantly less than in proximally actuated catheters [84]. A motor with an encoder or other closed-loop feedback would improve the uniformity of the rotation, but the increased size might not be suitable for clinical applications.

Several methods have been demonstrated to correct NURD in catheter-based imaging systems, such as registering neighboring A-lines or frames by maximizing cross-correlation signal intensity [80, 85-87], or using structural landmarks (e.g. stent struts) to aid registration of subsequently acquired datasets [88]. The reflections from the sheath or optical components of the catheters are also used for correcting rotational fluctuations caused by NURD [89]. However, methods using cross-correlation or phase information typically require highly correlated images. Some methods require disabling the longitudinal scan (pullback) entirely [85, 89], or provide only moderate improvement in rotational uniformity when tested *in-vivo* [80, 85]. For catheter-based applications with significant patient or operator motion, methods that do not rely on dynamic image features for correction may be desirable.

With recent advances in OCT speed, rapid volumetric imaging became possible. Following these developments, *en face* OCT is emerging as a powerful tool, especially for assessing ocular pathology [90]. Furthermore, OCT angiography was developed as a functional extension of OCT, enabling three-dimensional visualization of vasculature without requiring exogenous contrast agents [91, 92]. OCT angiography using OCT signal intensity has several advantages over phase sensitive techniques such as Doppler OCT or phase variance OCT, including relaxed system phase stability requirements and good sensitivity to slow blood flow occurring in capillaries [93, 94]. Our group recently demonstrated the combination of high-speed imaging and distal rotation to achieve highly stable scanning required for assessment of *en face* mucosal patterns and for endoscopic OCT angiography [31]. However, visualizing fine details with *en face* OCT or performing endoscopic OCT angiography further increases scanning uniformity requirements.

In this section of the thesis, we present a computationally efficient method for correcting the NURD encountered in catheter-based OCT. The method uses fiducial markers located on the catheter and resamples the cross-sectional images in accordance with the detected marker positions. We characterize the magnitude and frequency spectra of the rotational nonuniformity and quantify NURD correction algorithm accuracy. We also present exemplary *en face* OCT and OCT angiograms acquired with an ultrahigh-speed endoscopic OCT system *in vivo* to show the image quality improvement.

Methods

This study was conducted using an ultrahigh-speed endoscopic swept source OCT system with a VCSEL and micromotor catheter as described in reference [31]. Briefly, the VCSEL operated at 300 kHz bi-directional sweep rate and 110 nm tuning range, enabling 600 kHz A-line rate and 8 µm axial resolution in tissue, respectively. The output power of the system was ~ 80 mW, while the power on tissue was ~ 20 mW including the transmission through the micromotor catheter. This resulted in a measured sensitivity of ~ 101 dB, about 6 dB less than the theoretical shot-noise limit at this operation setting. Sources of sensitivity loss was optical elements in the catheter, patient interface unit and losses in the fiber-optic components (e.g. circulator, coupler, mating sleeve). The A/D card (ATS9360, AlazarTech) was optically clocked at 1.1 GHz maximum

clock frequency, resulting in a 3.3 mm imaging range in air. We used a micromotor catheter with a 3.4 mm outer diameter (OD), which passed through the 3.7mm endoscope accessory port. The distal part of the catheter consisted of a ~ 2.6 mm OD, 16 mm length, in-house fabricated brass housing to hold the distal optical components (focuser and microprism) and the micromotor (**Figure 2.9C**). A custom-made focuser consisting of a SMF-pigtailed GRIN lens (Go!Foton Corp., NJ) was used to focus the beam to a spot size if ~ 15 µm (FWHM) in tissue. An aluminum coated 1 mm microprism (Tower Optical, FL) was mounted onto the micromotor shaft to deflect the optical beam towards to the tissue. The optical beam exited focuser with a slight tilt (~ 8 degrees from the probe axis) to avoid specular reflection from the probe sheath. A 2 mm OD brushless DC micromotor (DBL02, Namiki Precision, CA) was used for rotary scanning. The micromotor rotated at 400 Hz and the catheter was proximally pulled back at 2 mm/sec. Each dataset consisted of 3200 frames with 1500 A-lines per frame. This resulted in a sampling pitch of 6.7 µm in rotation and 5 µm in pullback. Catheter was pulled back via a ~ 2 m long stainless-steel torque coil (2.2 mm OD, ACTONE^{TM} , Asahi Intecc, CA).

NURD correction was performed on sequential cross-sectional rotary OCT images in linear intensity scale prior to generating *en face* OCT images and OCT angiograms. *En face* OCT image stacks were then generated from the NURD-corrected 3D-OCT datasets with square root compression and projected over 140 µm depth at various depth levels. Endoscopic OCT angiography was performed by calculating the intensity decorrelation between sequential frames, similar to reference [95]. This requires spatially overlapping cross-sectional images in the pullback; hence images are intentionally oversampled in this direction. Following decorrelation calculation, three consecutive decorrelation images are averaged to reduce noise, and intensity thresholded to remove noise from low signal regions. Finally, *en face* OCT angiograms were generated from the cross-sectional OCT angiography stacks and projected over a 140 µm range at various depth levels.

Imaging was performed on patients at the Boston VA Healthcare System (VABHS) under IRB approved protocols and written informed consent was obtained prior to the study.

NURD correction algorithm

Figure 2.9 shows an example OCT image and a drawing of the catheter imaging probe. **Figure 2.9A** is an *in vivo* image of the human esophagus which corresponds to a single rotary scan of the catheter micromotor. The OCT image shows four fiducial positions which are created by the micromotor mount in **Figure 2.9B**. The fiducials could also be placed on the catheter sheath.

The NURD correction algorithm operates by detecting the fiducial positions on sequential OCT images, corresponding to sequential rotary scans. The fiducials correspond to fixed angular positions or fixed circumferential positions in the scan, but NURD causes the fiducial to appear at varying times or A-line positions. It is important to note that NURD causes not only a timing jitter (translation) in the positions of sequential OCT images, but also stretching or compression of images in the transverse direction because the rotational period and the number of A-lines per rotation is varying.

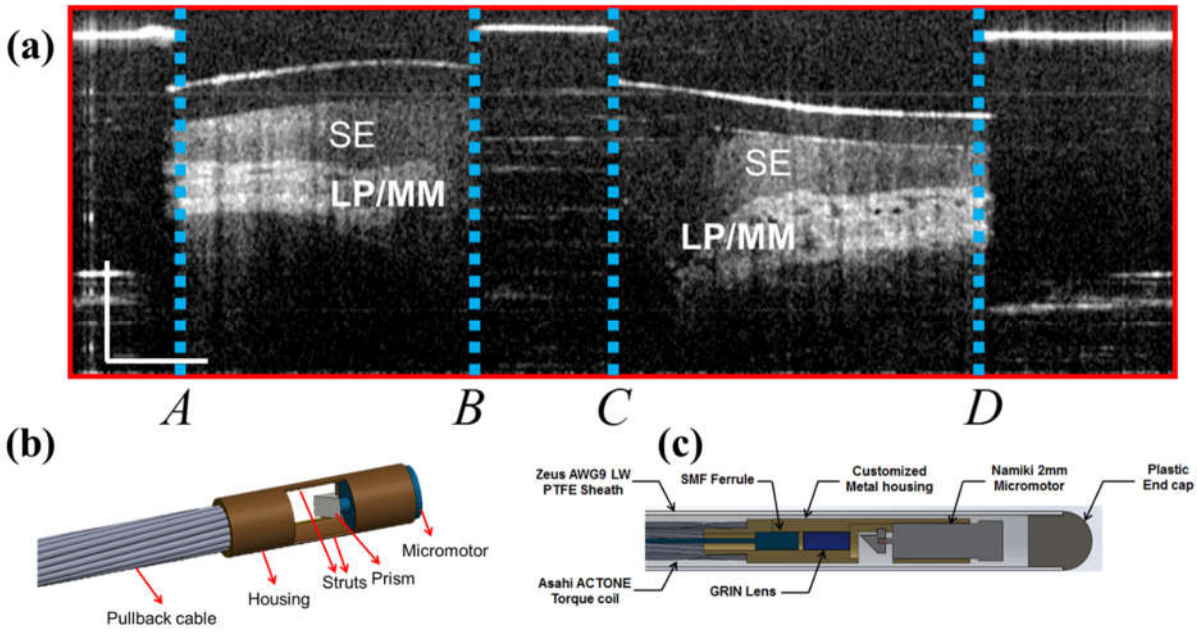

Figure 2.9. Description of the fiducial marker NURD correction algorithm for a micromotor catheter. **A,** Example OCT image showing fiducial positions. **B,** Drawing of a micromotor catheter with two struts and two imaging windows generating four fiducial positions. **C,** Detailed drawing of the distal assembly of the micromotor catheter showing the internal components. SE: Squamous epithelium, LP/MM: Lamina propria/muscularis mucosa. Scale bars are 1 mm.

The volumetric OCT dataset is composed of sequential cross-sectional OCT images from rotary scans sampled at constant A-scan rate. The OCT data is generated with a constant transverse pixel sampling rate, but varying angular / circumferential velocity. The objective of the NURD correction algorithm is to resample the volumetric OCT data such that the transverse pixels correspond to registered and equally space angular / circumferential positions, correcting for both timing jitter (translation) and stretching / compression of the OCT images in successive rotary scans. This resampling process is somewhat analogous to resampling the OCT spectrum from lambda to constant frequency or k interval which occurs in spectral domain OCT. The positions of the fiducials are used to generate a cubic spline resampling which is continuous in position as well as first and second derivative of the position in time, corresponding to the assumption that the rotation has continuous velocity and acceleration.

Using more than one fiducial per rotation will increase the number of angular / circumferential reference locations and improve the accuracy of the resampling. This resampling essentially performs a non-rigid registration in the transverse direction. The axial position of the image is assumed to be constant because tissue is in contact with the catheter sheath.

Two fiducials per rotation were used to measure the NURD. As shown in **Figure 2.10A**, without NURD correction, the angular deviation of the fiducial in sequential frames oscillates significantly with a standard deviation of 16.4 mrad (26.2 μm in circumferential position assuming 3.3 mm probe OD). The mean value of the angular deviation for 10 different acquisitions on different patients was 16.8 mrad (min = 10 mrad, max = 26 mrad, coefficient of variation = 0.3. The frequency analysis in **Figure 2.10C** shows this variation has a significant component around 130 Hz. This instability appears to be from the micromotor and was observed in multiple different catheters. Additional measurements by placing multiple photodetectors around the probe (*ex vivo*) were performed to confirm that this was not aliased from higher frequencies. Following the Nyquist criteria, using two fiducials per rotation for NURD correction, i.e. sampling at twice the rotation frequency can correct instabilities up to 400Hz for the parameters in this study.

Results

To quantify the correction algorithm performance, we used two fiducials per rotation for stabilization (e.g. **A** and **C** shown in **Figure 2.9A**), and two other fiducials for measurement (e.g. **B** and **D** shown in **Figure 2.9A**). Measurements show the angular deviation is significantly reduced. Following NURD correction, the angle standard deviation is reduced to 1mrad (1.7 µm in circumference assuming 3.4 mm probe OD), equivalent to a greater than 15-fold improvement in rotational stability (**Figure 2.10B**). **Figure 2.10D** further illustrates the improvement in rotational stability at 130Hz as well as at other frequency components. The mean value of the angular deviation for 10 different acquisitions on different patients was 1.4 mrad (min = 0.9 mrad, max = 1.7 mrad, coefficient of variation = 0.2).

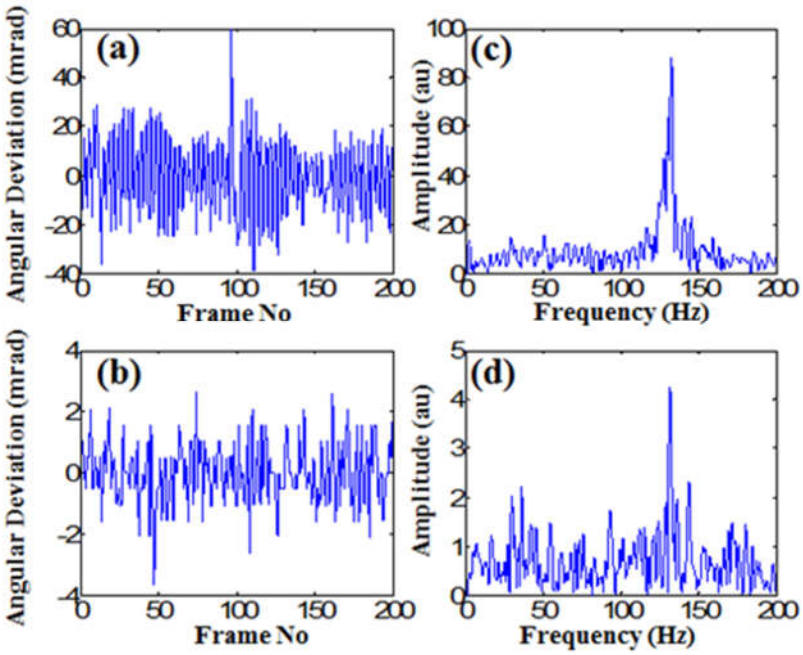

Figure 2.10. Characterization of NURD before and after software correction. **A,** Temporal positions of a fiducial from 200 sequential frames prior to correction (around zero mean). **B,** Temporal position of a fiducial (not used for correction) from 200 sequential frames post-correction (around zero mean). **C, D,** Fourier transforms of the waveforms from **A** and **B** respectively.

Figure 2.11 shows the performance of the correction algorithm for endoscopic OCT images of the human GI tract. **Figure 2.11A** and **Figure 2.11C** show *en face* OCT images acquired from the rectum of a patient before and after NURD correction, where regular crypt architecture

(pit pattern) can be observed, characteristic of normal colon. Without NURD correction, severe distortion can be observed in the *en face* pit patterns, as shown in **Figure 2.11A**. **Figure 2.11C** shows the distortions are significantly reduced with NURD correction. **Figure 2.11B** and **Figure 2.11D** show endoscopic OCT angiograms from the esophagus of a patient. Before correction, OCT angiography images exhibit decorrelation artifacts due to rotational instability between consecutive frames. This results in increased OCT angiography background noise and vertical streaks along the pullback direction (**Figure 2.11B**). As shown in **Figure 2.11D**, the algorithm improves registration of consecutive frames, reducing decorrelation noise and improving angiography quality.

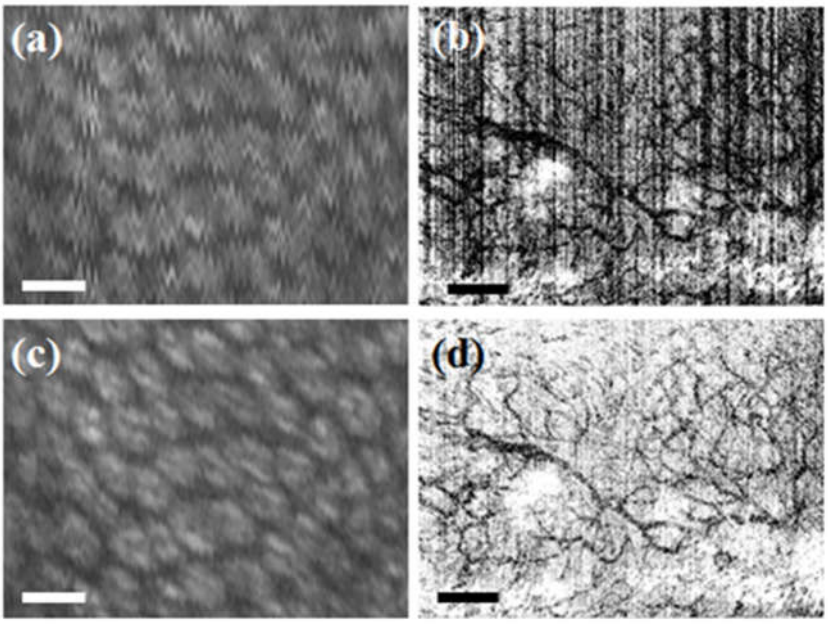

Figure 2.11. Demonstration of the NURD correction algorithm for *en face* OCT and OCT angiography images. **A** and **C** show *en face* OCT images before and after applying the correction algorithm, respectively. **B** and **D** show OCT angiograms before and after applying the correction algorithm, respectively. All figures are generated by projection over 140 µm of depth, and about 150-500 µm beneath the tissue surface. **A** and **C** are taken from the rectum, and **B** and **D** are taken from the esophagus of two patients who were undergoing endoscopic surveillance. Same signal thresholds are applied for **A** and **C**, and for **B** and **D**. Scale bars are 200 µm for **A** and **C**, and 500 µm for **B** and **D**.

Discussion

The scanning parameters in these experiments yielded sampling pitches of 6.7 µm and 5 µm along the rotation and pullback direction, respectively. Given the 15 µm spot size, even very small scanning instabilities will cause significant decorrelation noise between adjacent frames. Furthermore, because a helical pullback scanning is typically used for catheter-based imaging systems, it is not possible to acquire several repeated frames at precisely the same longitudinal location, in contrast to ophthalmic OCT angiography which uses galvanometer scanning. NURD correction addresses rotational instability, but endoscopic OCT angiography is still limited by pullback instability. Pullback instability might be corrected by using fiducials on the catheter sheath.

In addition, other instabilities arise from the relative movement of the tissue with respect to the catheter. This causes large-scale image distortion in the 3D-OCT data and uncertainty in registration relative to the tissue. Using fiducial markers that are located on the catheter will not correct for tissue motion. However, this study was less vulnerable to tissue motion, due to the ultrahigh speed acquisition.

The applicability of the fiducial marker method requires minimal modification of catheter design. For micromotor catheters, the housing struts or shadows from cables can be used as inherent fiducials. Rotational as well as longitudinal fiducial lines can be printed or laser etched on the inner or outer surfaces or even internal to the transparent probe sheath. The number of fiducial markers required to effectively suppress the NURD will depend on the rotation stability and the frequency of the dominant instabilities.

In conclusion, a computationally efficient method is demonstrated that corrects image distortion from rotational nonuniformity. This method can be used to effectively correct instabilities up to a Nyquist frequency determined by the temporal spacing between two serially detected fiducial markers. By increasing the number of fiducials, the correction accuracy can be improved. Our study shows that two fiducial markers per frame are sufficient to effectively suppress the NURD in high-speed micromotor endoscopy and provide a non-distorted *en face* or

angiographic image. However larger diameter imaging probes would require larger numbers of fiducials. This method can be applied to both proximally and distally actuated catheter designs. Due to its accuracy and suitability for high-speed imaging, this correction method could be a valuable tool for next-generation endoscopic and cardiovascular OCT systems which acquire combined structural and functional image information to assess pathological and physiological markers of disease.

2.4. Optimization of data acquisition and visualization

2.4.1. Data acquisition

As discussed in the previous sections, there are various sources of imaging artifacts encountered in endoscopic OCT imaging, hence it was essential to develop methods to optimize data acquisition and visualization in order to minimize the effects of those in the resulting images.

The OCT acquisition platform was a C++ based software originally implemented by the visiting scientist Martin Kraus from the University of Erlangen-Nuremberg with the collaboration of other group members such as Jonathan Liu, Chen Lu and Ben Potsaid. This platform was primarily developed for the use of the VCSEL-based ophthalmological OCT imaging systems, hence it was not optimized for some of the critical functions required for endoscopic OCT imaging. The author of this thesis was primarily responsible for adopting this software for the endoscopic OCT system and use in the VA hospital. One of the changes that were implemented was to the image preview. A screenshot of the image preview tab of the endoscopic OCT software is shown in **Figure 2.12.** In **Figure 2.12A,** the top-left panel displays the preview of the cross-sectional OCT image, a real-time view of the scanned region. Once a dataset is acquired then the bottom-left and the right panels display cross-sectional and *en face* images of the acquired data. The *en face* view is particularly important as it shows if there are any overt image artifacts or if the tissue is making contact with the catheter throughout the acquisition. Furthermore, it allows determining if certain landmarks, such as squamocolumnar junction, is captured within the datasets.

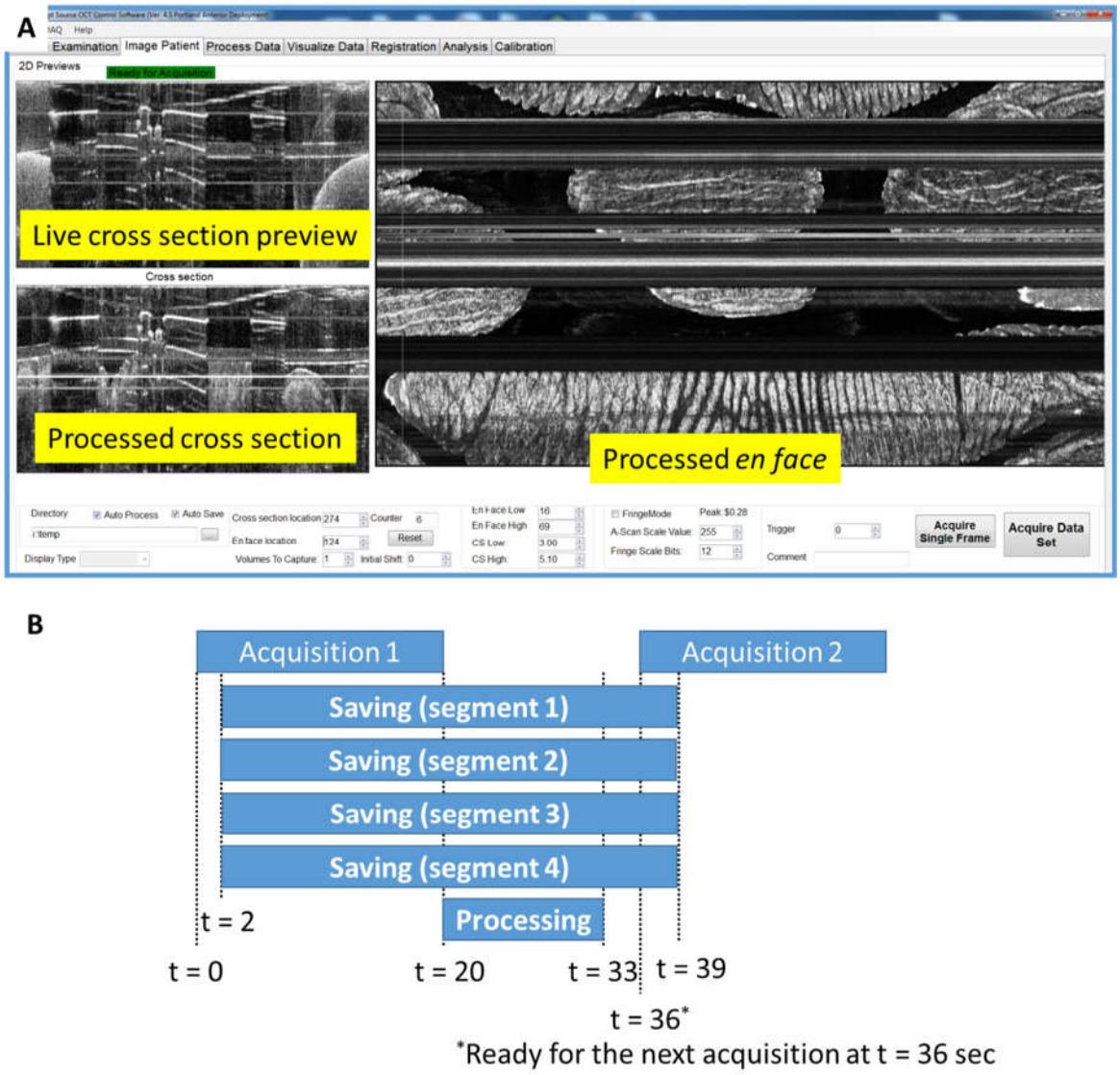

Figure 2.12. Overview of data acquisition software. **A,** shows the preview where cross-sectional and *en face* images of a human finger are displayed. **B,** shows the timing diagram for a 20 seconds (~ 20GB) dataset acquisition. Dataset was divided into four segments and each segment is saved in a different thread. A PCI-e SSD raid array card was used to shorten data saving speed as much as possible. Datasets were processed asynchronously with the acquisition to allow rapid *en face* preview. Acquisition of the next dataset could start a few seconds before the saving was finished. The main limiting factor was data saving speeds, which added about 16 seconds lag time after the data acquisition was finished.

Another concern was the efficiency of data acquisition, processing and saving during the endoscopic imaging procedure. Since the size of the datasets was high (~ 10 GB for the majority of the clinical datasets in this thesis), it was critical to optimize each of these aspects so that OCT imaging was not adding significant time to the endoscopy procedure. A high-speed data

acquisition card (Alazar ATS9370) was used to digitize the OCT spectrums at a maximum sampling rate of ~ 1.2 Gsamples/sec. We have implemented separate threads for the preview, processing, and saving so that they can be done simultaneously and the program has minimal downtime to wait for other processes to finish. **Figure 2.12B** depicts an example data acquisition for a 20 GB OCT dataset. As can be seen there, a feature of the Alazar digitization card called "stream to disk" was implemented, that allowed the data to start saving to hard drive as soon as the acquisition started (with 2 seconds of lead time to accumulate some initial data into the memory). Saving was done by dividing the datasets into several segments and saving them concurrently to an SSD raid array card. This was implemented to ensure that larger datasets did not take a significant amount of time to save due to hard drive fragmentation problems. Data processing was started as soon as the acquisition was finished, and the processing code of the software was modified and optimized to make the data processing as fast as possible (~ 1.5GB/sec processing speed). Processing was sped up to a point such that the main bottleneck became the saving speed such that there was about a 16 seconds delay between the end of acquisition and end of saving before the subsequent acquisition could be started. This speed was limited by various factors such as computer bus speed and the SSD raid array card performance.

2.4.2. Data visualization

Traditionally cross-sectional OCT images are displayed with a logarithmic compression, where the logarithm of the intensity images are taken and scaled to a bit depth of 16 bits after applying a threshold to crop the noise level and high-intensity reflections. Taking the logarithm essentially compresses the dynamic range of the intensity image, which is necessary for cross-sectional OCT images as there is a large variation of the signal intensity across different depths of the image. However, for *en face* OCT images that correspond to specific depths, the signal variation is not as high as it is in the cross-sectional OCT images. Therefore, logarithmic compression can be overshoot for displaying *en face* OCT and may remove some of the fine details of the structures that may have small variations in signal intensity. The uncompressed images, on the other hand, might still have too much intensity variation across the image. Consequently, a square-root compression is considered as an optimal trade-off for the display of the *en face* OCT images,

which balances the intensity variations and the visualization of fine details in the images [96, 97]. Example of *en face* OCT images from a patient with NDBE with these three compression methods applied were given in **Figure 2.13**.

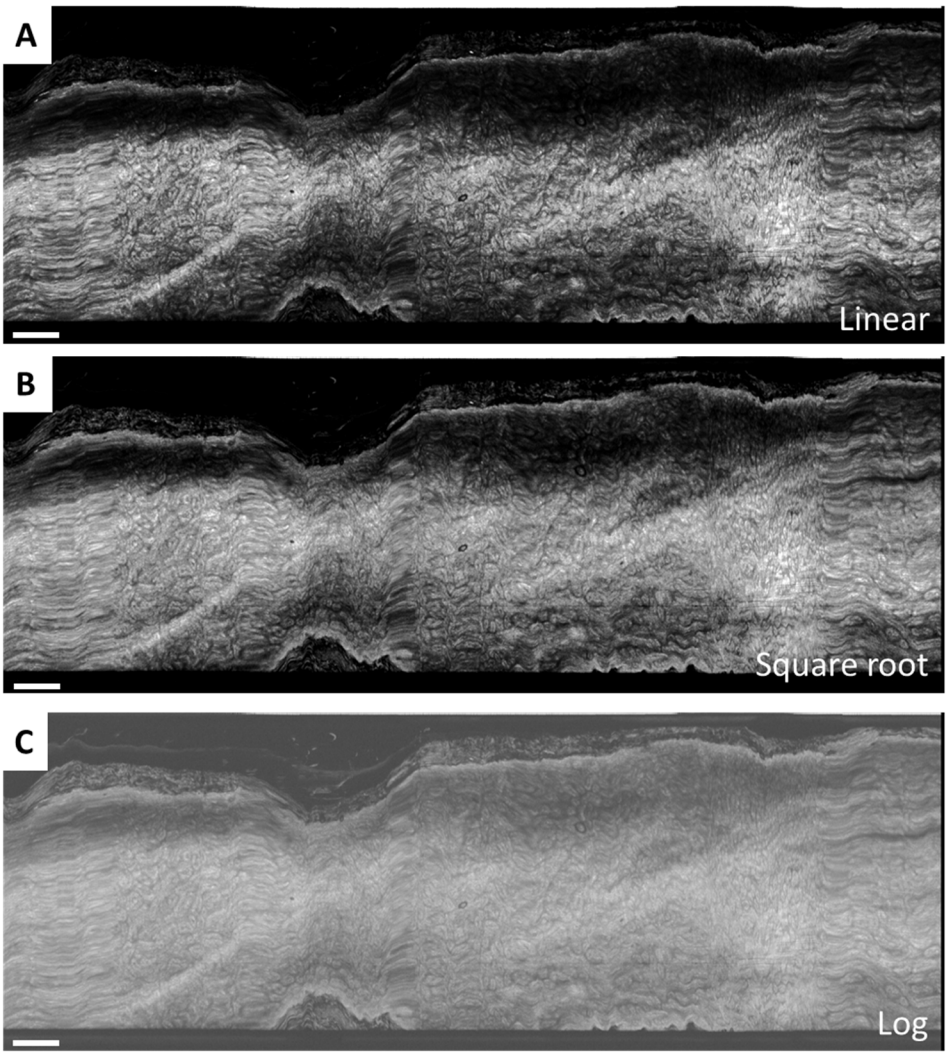

Figure 2.13. Effects of different dynamic scale compressions on visualization of mucosal patterns on the *en face* OCT images. Images are from a patient with non-dysplastic Barrett's esophagus and projected over a 100 µm depth. Scale bars are 1 mm.

It is also possible to use image filters to further enhance the visualization of the mucosal patterns. In this regard, we have tested a high-dynamic-range (HDR) filter to normalize signal intensity variations and enhance the visibility of finer details [98]. Examples of *en face* OCT images from upper and lower GI tissues with and without the HDR filtering were given in **Figure 2.14**. It can be observed that HDR filtering reduced the signal intensity variations across the image while

improving the contrast of the mucosal patterns. However, the application of image filters may introduce imaging artifacts and may make the visualization of other image features such as dilated glands more challenging. Therefore, we have decided not to use image filters such as the HDR filter to display the *en face* OCT images in the clinical studies presented in this thesis.

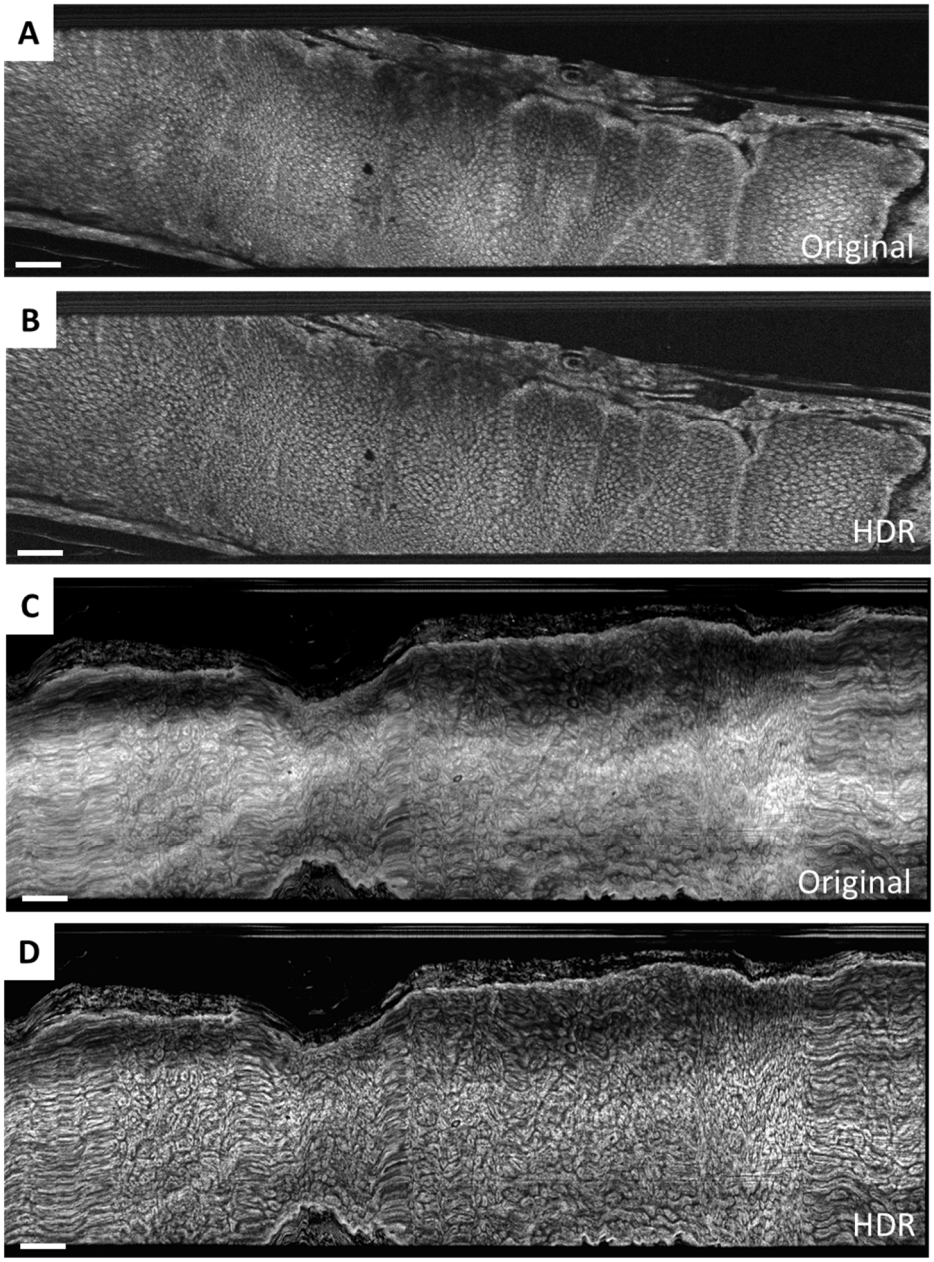

Figure 2.14. Effects of high-dynamic-range (HDR) filtering on visualization of mucosal patterns on the *en face* OCT images. **A, B,** are from the normal rectum of a patient and **C, D,** are from a patient with non-dysplastic Barrett's esophagus. All images are projected over a 100 μm depth. Scale bars are 1 mm.

Another choice for visualization was the use of pseudocolor maps. Especially in the field of ultrasonography the use of false colors as opposed to grayscale display has been shown to increase the sensitivity and specificity of the radiological readings [99, 100]. As shown in **Figure 2.15,** the use of a false colormap such as the sepia may allow better delineation of the mucosal patterns on the *en face* OCT images compared to grayscale. **Figure 2.15** also displays *en face* OCT images with different projection amounts. The contours and fine details of the mucosal patterns are not easily discernible for smaller projection depths such as 20 µm, while the features start to have a blurry appearance for large projection depths such as 200 µm. A projection amount of 100 µm, which is on the order of the size of the individual mucosal ridges and crypts, deemed to be optimal and was used to display the majority of the *en face* OCT images acquired by the ultrahigh-speed endoscopic OCT system reported in this thesis.

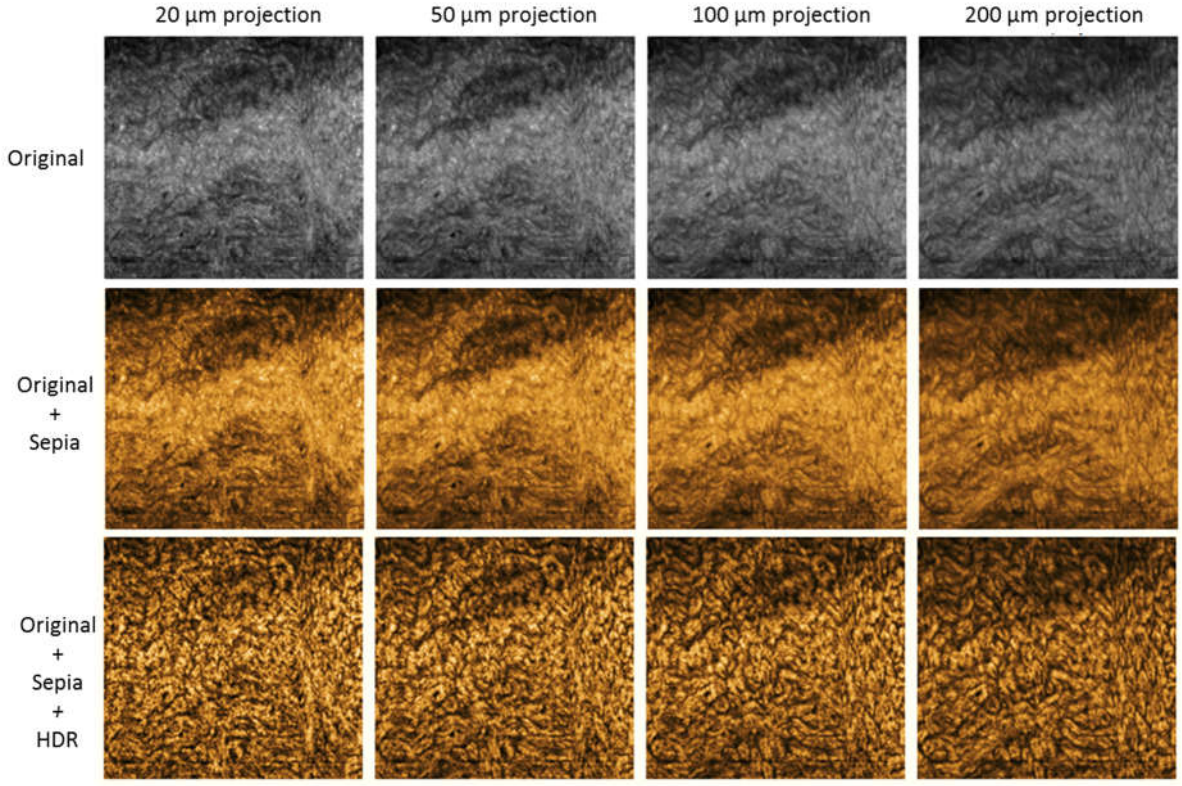

Figure 2.15. Effects of different projection depths and sepia filtering on visualization of mucosal patterns on the *en face* OCT images. Images are from a patient with non-dysplastic Barrett's esophagus.

Chapter III

Endoscopic OCT in Barrett's Esophagus

3.1. Motivation

Esophageal adenocarcinoma (EAC) is among the most lethal cancers, and incidence has increased dramatically over the last few decades [101]. Barrett's esophagus (BE) is a precursor to EAC [102], which is due to a progression of BE from low-grade dysplasia (LGD) to high-grade dysplasia (HGD), accompanied by cytological and tissue architectural alterations [103]. Dysplasia of any grade increases cancer risk by an order of magnitude [104], and HGD is associated with 30-35% risk of developing EAC within 5 years [3]. Endoscopic therapies such as radiofrequency ablation (RFA) and endoscopic mucosal resection (EMR) are highly effective in eradicating dysplasia [105]. Therefore, identifying dysplasia in BE is important to prevent progression to EAC.

Surveillance protocols for BE (Seattle protocol) involve 4-quadrant biopsies during white light endoscopy (WLE) [106], but suffer from sampling errors due to the patchy and multifocal nature of dysplasia [7]. Advanced imaging techniques such as narrowband imaging (NBI) [107] and confocal laser endomicroscopy (CLE) [108, 109] individually or with WLE have been shown to improve sensitivity for identifying dysplasia. However, NBI exhibits interobserver variability, while CLE has limited coverage, extends procedure time, and requires intravenous fluorescein.

Endoscopic optical coherence tomography (OCT) enables high speed, volumetric imaging at microscopic resolution without contrast agents [78, 110]. OCT was commercialized as volumetric laser endomicroscopy (VLE, NinePoint, Bedford, MA) [111], which employs balloon catheters of ~ 20 mm diameter to image 6 cm longitudinal segments of the esophagus. Studies have investigated cross-sectional OCT features of dysplasia [42, 45], and a diagnostic algorithm was developed by Leggett et al. (known as 'VLE-DA') that assessed a combination of features including: mucosal layering, surface vs subsurface signal intensity and number of atypical glands

for identifying dysplasia [43]. However, many VLE studies were performed on *ex vivo* specimens due to challenges in correlating histology with in vivo imaging.

We have developed ultrahigh-speed endoscopic OCT technology with imaging speeds >10 times faster than commercial instruments [31]. Using distal scanning micromotor catheters, volumetric OCT datasets were acquired with higher lateral resolution and sampling density than VLE. In addition to cross-sectional OCT images, depth-resolved *en face* OCT images were extracted from volumetric OCT datasets, enabling visualization of mucosal patterns with high resolution and contrast. This chapter describes two studies conducted with this ultrahigh-speed endoscopic OCT system related to the clinical management of BE and dysplasia.

In one study we investigated volumetric *en face* and cross-sectional OCT for identifying dysplasia. Three readers with differing endoscopy/OCT experience assessed OCT datasets blinded to the histological diagnoses of non-dysplastic BE (NDBE), LGD, HGD and EAC to assess associations of *en face* and cross-sectional OCT features with neoplasia, NDBE and treatment history. Findings suggested features of dysplasia that are relevant to understanding the pathogenesis of dysplasia and could be important for identifying future diagnostic markers.

In another study we have demonstrated the clinical utility of the ultrahigh-speed endoscopic OCT and OCTA for assessing a dysplastic lesion at the gastroesophageal junction (GEJ), its lateral margins before and immediately after EMR, and at 2-months follow-up. OCT/OCTA prior to EMR visualized the dysplastic lesion and its lateral margins. Immediately post EMR OCT/OCTA showed a residual dysplastic margin of the resection site which was confirmed by EMR at 2-months follow-up. This study suggested that probe-based OCT/OCTA may improve diagnostic capabilities and enhance clinical utility by identifying dysplastic areas, assessing lesion margins, and evaluating regions immediately post-treatment and on follow-up. It also concluded that probe-based OCT/OCTA may have advantages over balloon- and capsule-based OCT and confocal endomicroscopy in certain settings.

The prototype ultrahigh-speed endoscopic OCT system and data acquisition system used in this work was developed by the team described in **Chapter II.** All human imaging experiments

were conducted at the VA hospital by the endoscopy team including Hsiang-Chieh Lee, Kaicheng Liang and Zhao Wang with the help of our clinical collaborators and the VA staff. Qin Huang performed histopathology readings for the excised EMR and biopsy specimens, and provided the snapshot images of the correlated histology slides included in this chapter. The structural reading protocol was developed throughout prolonged discussions amongst the endoscopy team involving the thesis author, Hsiang-Chieh Lee, Kaicheng Liang, Zhao Wang, with critical insight and inputs from James Fujimoto and Hiroshi Mashimo. Julia Schottenhamml has modified the open source software (3D Slicer™) used in the readings to allow simultaneously display *en face* and cross-sectional OCT images with interactive brightness and contrast adjustment. Zhao Wang and Kaicheng Liang participated in a number of pilot diagnostic readings conducted by the thesis author and shared their experiences and feedback to improve subsequent readings. Hsiang-Chieh Lee and Kaicheng Liang were involved in the majority of the discussions related to the studies described in this chapter.

3.2. Clinical overview of Barrett's esophagus and dysplasia

3.2.1. Incidence and treatment

Esophageal adenocarcinoma (EAC) is the most common form of esophageal cancer in the US and its incidence has increased by ~ 300-500% over the last 40 years, the fastest of any cancer [101, 112]. EAC is among the most lethal cancers with a five-year survival rate of only 18% [1]. In 2017, 16,940 new esophageal cancer cases and 15,690 deaths are expected in the United States. Barrett's esophagus (BE) is defined by the replacement of squamous epithelium by columnar epithelium and is a precursor to EAC. BE is associated with gastroesophageal reflux disease (GERD), which affects up to one-third of the adult population [102, 113-116], and approximately 5-15% have BE [117].

EAC is thought to arise from the progression of BE from low to high grades of dysplasia [7], as characterized by increasing cytologic and tissue architectural abnormalities [2, 118]. BE with any grade of dysplasia increases cancer risk by an order of magnitude and high-grade dysplasia (HGD) is associated with 10–60% risk of developing EAC within 3-5 years [2, 119, 120]. Patients undergoing endoscopic surveillance for HGD often have cancer detected at earlier stages,

resulting in improvements in 5-year survival rates (62%) compared to non-surveillance groups [121]. Therefore, identifying dysplasia in BE is important to prevent progression to EAC.

Several endoscopic treatment modalities have been developed over the past few decades to treat dysplastic Barrett's esophagus. Earlier treatment options included photodynamic therapy [122], argon plasma coagulation (APC) [123] and laser ablation [124]. Although they were showing improved outcomes compared to alternative surgical methods such as esophagectomy, these treatment modalities had high complication rates such as the formation of strictures, chest pain, and perforation. Radiofrequency ablation (RFA) had been developed as an alternative endoscopic treatment modality to treat superficial esophageal lesions such as high-grade dysplasia [125-129]. The advantage of RFA was the use of tightly spaced bipolar electrodes (with a 250 μm bipolar electrode spacing) that limits the ablation to the superficial mucosal depths. It was hypothesized that the high complication rate of previous ablation techniques stemmed from their inability to localize the ablation to superficial depths.

The pioneering multi-center trial by Shaheen et al. have shown that one year after the initial RFA treatment, complete eradication of dysplasia was achieved in 90.5% of patients with low-grade dysplasia (LGD) and in 81% of patients with HGD [128]. A follow-up study has shown that complete eradication of dysplasia was achieved in 98% of LGD patients and 93% of HGD patients at two-years after the initial RFA treatment [130]. Furthermore, eradication of BE was achieved in 93% of the patients with dysplasia after two years of initial RFA treatment [130], and in 92% of the patients with no dysplasia (NDBE) after five years of initial RFA treatment [129]. Further comparative studies and meta-analysis have shown that RFA is an effective treatment modality with fewer complications compared to alternative treatment options [131].

At the same time, the superficial treatment depth of RFA makes is challenging to target lesions that may have a large depth extent, such as a nodular lesion that can have intramucosal carcinoma or a more advanced stage cancer. Therefore, current treatment strategy endorsed by the GI societies is to initially perform EMR over any suspicious nodular lesion [4]. In addition to eradicating nodular lesions, EMR also has the advantage of excising a large tissue which can be

assessed for pathological grading of the lesion. After all nodular lesions are removed, RFA is commenced to eradicate remaining BE and dysplasia.

In short, there are effective and safe treatment options that can eradicate dysplasia in BE, preventing progression to EAC. However, detecting dysplastic BE is still a major unmet need as BE is a relatively common disease (affecting up to 3% of the adult population in the US) and treating all BE cases (regardless of presence of dysplasia) is not economically viable. Therefore, OCT can be a major synergistic tool in this paradigm of detecting and treating dysplastic BE lesions.

3.2.2. Detection and diagnosis methods of dysplasia

Studies indicate that up to 85% of dysplastic lesions have only subtle changes in their mucosal and vascular patterns compared to NDBE tissue, and only 13% of dysplastic lesions are present in the form of a readily discernible nodular lesion [132, 133]. Furthermore, dysplasia has a multi-focal and patchy nature [7]. Currently, the widely accepted standard of care is called the "Seattle protocol", which requires the endoscopists to perform biopsies in 4 quadrants every 2 cm along the length of BE visible on white-light endoscopy (WLE). Biopsy intervals are decreased to every 1 cm for patients with a known history of dysplasia [6]. However, this approach samples only a fraction of the BE tissue, therefore is prone to sampling errors given the subtle appearance of dysplastic lesions. Furthermore, this approach of random sampling generates significant pathology workload, and is accompanied by an increased complication risk associated with multiple biopsies [134].

The aforementioned factors make it challenging to detect dysplasia via conventional endoscopy and Seattle protocol [133, 135] and motivate the need for developing advanced imaging techniques to adjunct endoscopic assessment for identifying dysplasia. To acknowledge this need for developing advanced imaging techniques and establish guidelines on the required diagnostic performance of the imaging technology, the American Society of Gastrointestinal Endoscopy (ASGE) have published a statement in 2012 named as "The American Society for Gastrointestinal Endoscopy PIVI (Preservation and Incorporation of Valuable Endoscopic Innovations) on imaging in Barrett's Esophagus" [8]. The PIVI criteria state that the imaging

technology should have a per-patient sensitivity of at least 90% and a negative predictive value (NPV) of at least 98% for detecting HGD or EAC compared with the current standard protocol of WLE with Seattle protocol and targeted biopsies. The requirement of high sensitivity is critical in the PIVI criteria as it determines the likelihood of missing a patient with dysplasia. PIVI criteria also include a statement on specificity, specifying that it should be "sufficiently high" to reduce the number of biopsies. An 80% number for the specificity is proposed.

Having the guidelines for the required diagnostic performance set by the PIVI criteria, several endoscopic imaging studies have conducted to determine if the criteria can be met with different advanced imaging techniques. Narrowband imaging (NBI) [136] and confocal laser endomicroscopy (CLE) [108, 109] have been studied individually or with WLE to improve detection sensitivity. Early studies of NBI with magnification endoscopy achieved >95% sensitivity for dysplasia detection [73, 137]. Recent prospective studies reported sensitivity and specificity in the 70-80% range and moderate interobserver agreement for detecting HGD and early carcinoma in BE patients [117, 138]. However, majority of NBI studies were performed at tertiary referral centers with expert endoscopists, while studies with non-expert endoscopists reported only fair interobserver agreement with suboptimal sensitivity and specificity [139]. For CLE, two of the largest prospective, multicenter controlled trials to date with 101 and 192 patients showed 68.3% and 95% sensitivity, and 87.8% and 92% specificity for probe based CLE and endoscope based CLE for dysplasia detection, respectively [140, 141].

In the subsequent section, we summarize the results of a study where a combination of *en face* and cross-sectional OCT information is used for identifying dysplasia. 74 OCT datasets with correlated biopsy/endoscopic mucosal resection histology (49 non-dysplastic BE (NDBE), 25 neoplasia) were obtained from 14 BE patients with dysplasia history and 30 with NDBE. The associations between irregular mucosal patterns on *en face* OCT, and absence of mucosal layering, surface signal > subsurface, and >5 atypical glands on cross-sectional OCT versus histology and treatment history were assessed by 3 blinded readers. The study results suggested an important association of atypical glands and irregular mucosal patterns with dysplasia which

is relevant to understanding the pathogenesis of dysplasia and could be important for identifying future diagnostic markers.

3.3. Structural *en face* and cross-sectional OCT for identifying dysplasia

3.3.1. Methods

Study setting and patient recruitment

Imaging was conducted at the VA Boston Healthcare System (VABHS) under an IRB protocol approved by VABHS, Harvard Medical School and Massachusetts Institute of Technology. Patients with BE (14 with dysplasia history and 30 NDBE) undergoing endoscopic surveillance or therapy were imaged between September 2013 and March 2017. Dual-channel endoscopes were used to view the OCT catheter position and obtain biopsy/EMR from the OCT-imaged region, however biopsy/EMR was not guided in real time (**Figure 3.1**). Ultrahigh-speed endoscopic OCT was used with OCT micromotor catheters to acquire volumes at the 6 o'clock position ranging from the gastroesophageal junction (GEJ) to the squamocolumnar junction (SCJ) and also from regions with nodularity and/or irregular mucosal/vascular patterns on WLE/NBI. OCT datasets were categorized as NDBE if correlated histology indicated NDBE and as neoplasia if histology indicated LGD/HGD/EAC. NDBE datasets from patients with dysplasia history were not used for reading. Histology was assessed by an experienced gastrointestinal pathologist (QH) with confirmation from expert referral centers.

Technical details of the ultrahigh-speed endoscopic OCT instrument

The prototype ultrahigh-speed endoscopic OCT instrument [31] used in this study operated at 600,000 depth (axial) scans / second, >10 times faster than commercial instruments [142]. Distal rotary beam scanning was performed using a 3.4 mm outer diameter (OD) OCT micromotor catheter with an internal 2.0 mm OD micromotor (Namiki, Japan) at 400 Hz (400 cross-sectional OCT images per second). More technical details of the clinical ultrahigh-speed OCT system and micromotor catheter were provided in **Chapter II**. The internal assembly of the OCT catheter was proximally pulled back at 2 mm / second to generate volumetric datasets. Each OCT volume was acquired in 8 seconds and covered an area of ~ 10 mm x 16 mm (circumferential x longitudinal)

with 3,200 cross-sectional OCT images of 1,500 A-scans each. The depth (axial) range was 2.4 mm with an 8 µm (full width half maximum) resolution and lateral image resolution was 20 µm. Cross-sectional OCT images were corrected for non-uniform rotational distortion to improve *en face* visualization [143]. *En face* OCT data at a given depth was viewed by summing over +/-50 µm depth (100 µm projection range) to improve contrast and reduce noise. The stack of cross-sectional OCT images at various longitudinal positions could be scrolled for rapid viewing, or specific cross-sections from *en face* regions of interest (ROIs) viewed selectively. **Table 3.1** compares the prototype OCT instrument with VLE, magnification NBI, and pCLE.

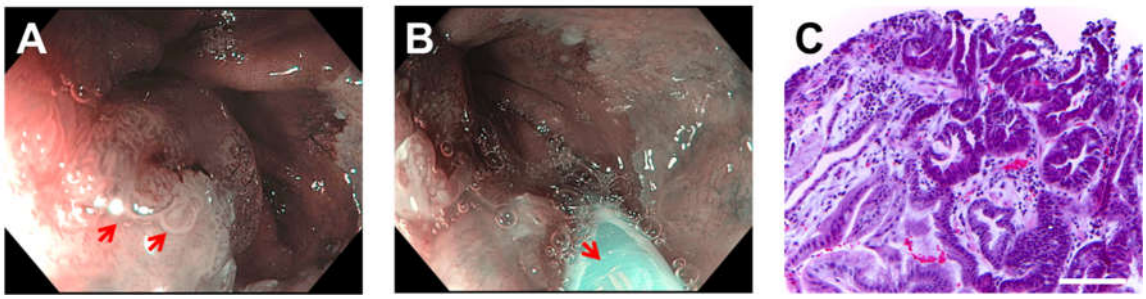

Figure 3.1. Acquisition of OCT datasets with correlated biopsy/EMR histology. **A**, WLE/NBI image showing a dysplastic lesion at the squamocolumnar junction. Arrows point to the nodular lesion. **B**, WLE/NBI image with the OCT catheter introduced through the dual-channel endoscope (GIF-2TH180, Olympus, Japan) to enable biopsy/EMR from the OCT imaged region. Arrow points to the OCT catheter. **C**, H&E histology of the resected specimen indicating high-grade dysplasia. Scale bar is 100 µm.

Reading criteria and methodology

Reading criteria were developed by an investigator (OOA) excluded from the formal reading. The feature of regular vs irregular mucosal patterns was used to assess subsurface *en face* OCT images [144] (**Figure 3.2**). The features: absence of mucosal layering, surface signal > subsurface and >5 atypical glands were used to assess cross-sectional OCT images, similar to the previously published VLE-DA features [43] (**Figure 3.3**). Mucosal layering in cross-sectional OCT was defined as absent (complete effacement) if layering was absent in >50% of the images in the series, otherwise it was defined as present (partial effacement). Surface signal was defined as higher than subsurface signal (surface signal > subsurface) if it was higher in >50% of the images in the series, otherwise it was defined as lower or equal (surface signal ≤ subsurface).

	Ultrahigh-speed OCT with micromotor catheters	VLE [42]	Magnification NBI (GIF Q240Z/260Z series) [145]	pCLE [146]††
Field of view (single acquisition/image)	~ 10 mm x 16 mm†	~ 60 mm x 60 mm	~ 3 mm diameter circle at maximal magnification	240-600 µm diameter circle
Imaging time (single acquisition/image)	8 seconds	90 seconds	~ 30 msec (video rate)	~ 80 msec (12 images per second)
Frame sampling interval	5 µm	~ 50 µm	Not applicable	Not applicable
Depth (axial) scan rate	600,000 A-scans/sec	50,000 A-scans/sec	Not applicable	Not applicable
Lateral resolution	20 µm	40 µm	6-8 µm	1-4 µm
Depth (axial) resolution	8 µm	7 µm	Low, see discussion in the text	5 µm
Depth (axial) range (imaging depth)	2.4 mm	3 mm	Shallow, see discussion in the text	40 - 130 µm
Catheter diameter	3.4 mm	14 mm, 17 mm, 20 mm balloon	10 mm (endoscope)	2.5 mm
Main strengths	• High imaging speed reduces motion artifacts • Depth-resolved *en face* visualization of mucosal patterns	• Large area imaging • Recent systems have laser marking for more precise histological correlation	• NBI integrated with endoscope • Visualizes mucosal and vascular patterns	• Cellular details visible
Main limitations	• Limited circumferential coverage	• Slow imaging speed limits *en face* visualization	• Depth-resolved imaging is not possible	• Small field of view • Requires contrast agents

†: The longitudinal pullback length used in this study was standardized to 16 mm, but can be increased.
††: pCLE: probe based CLE. Endoscope based CLE (eCLE) was not included since it has been discontinued.

Table 3.1 Comparison of ultrahigh-speed endoscopic OCT with VLE, magnification NBI and pCLE.

Atypical glands were defined to be present if there were a total of >5 atypical glands in the image series. Dilated glands were considered atypical glands if they had irregular size, shape, contained internal debris, or had clustered appearance, similar to previous descriptions [42, 43]. These features were combined using VLE-DA to assess cross-sectional OCT [43]: datasets with mucosal layering present and ≤5 atypical glands, or datasets with mucosal layering absent and surface

signal ≤ subsurface were classified as VLE-DA negative for neoplasia; while datasets with mucosal layering present and >5 atypical glands, or datasets with mucosal layering absent and surface signal > subsurface were classified as VLE-DA positive for neoplasia.

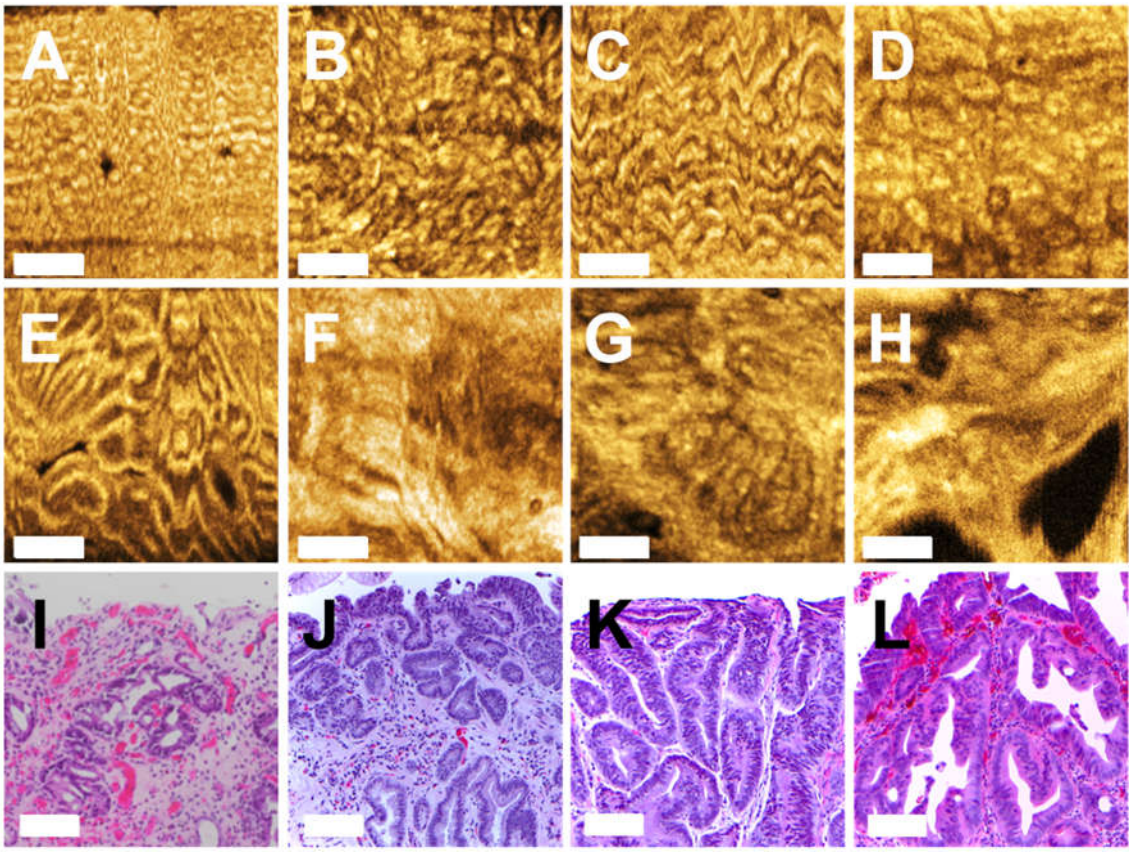

Figure 3.2. Mucosal pattern features assessed in *en face* OCT. **A – D**, representative en face OCT images of regular mucosal patterns from non-dysplastic Barrett's esophagus (NDBE) datasets. Mucosal patterns show variations in size and shape. **E – H**, representative *en face* OCT images of irregular mucosal patterns from neoplasia datasets. Branching, distortion and absence of mucosal patterns can be observed. **I – L**, H&E histology correlated with the datasets in **E – H**, respectively, with histological diagnosis of low-grade dysplasia (**I**), high-grade dysplasia (**J and K**) and esophageal adenocarcinoma (**L**). *En face* OCT images are cropped from larger datasets to highlight regions of interest. Scale bars are 500 µm in **A – H**, 100 µm in **I – L**.

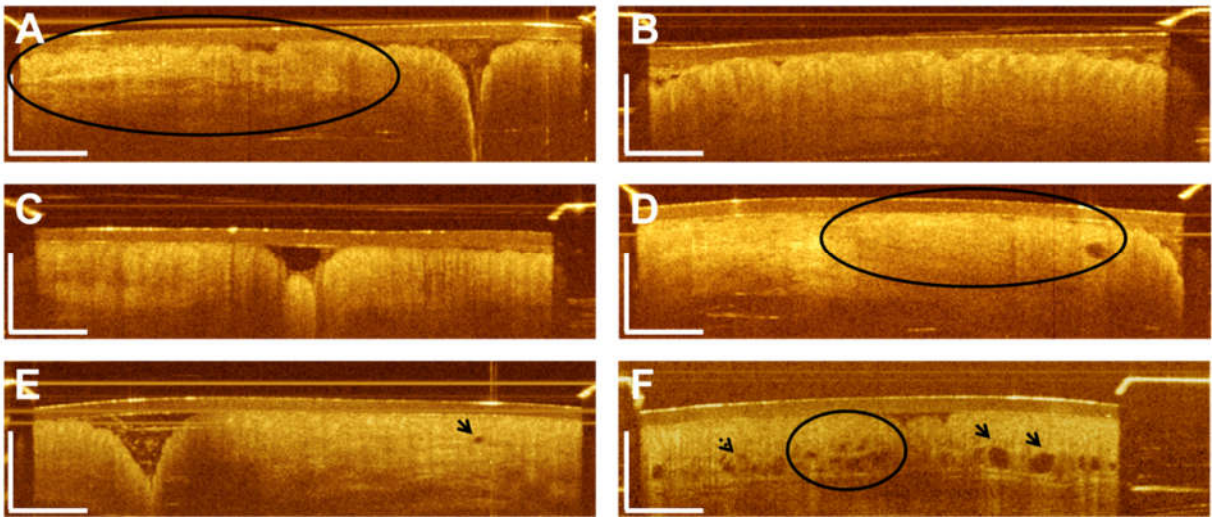

Figure 3.3. Cross-sectional OCT features assessed include mucosal layering, surface signal vs subsurface and atypical glands. **A, B**, representative cross-sectional OCT images showing presence or absence of mucosal layering, respectively. The oval indicates an area with mucosal layering present. **C, D**, representative cross-sectional OCT images showing surface signal ≤ subsurface, and surface signal > subsurface, respectively. The oval indicates an area with surface signal > subsurface. **E**, representative cross-sectional OCT image showing normal-appearing glandular architecture. Solid arrow points to a dilated gland with normal appearance. **F**, representative cross-sectional OCT image showing atypical glandular architecture. Solid arrows point to atypical glands with irregular size and shape. Dashed arrow points to an atypical debris-filled gland. The oval marks an area with clustered atypical glands. Scale bars are 1 mm.

Training and volumetric OCT reading workflow

13 representative OCT datasets were used for training, followed by a pretest of 7 datasets (**Table 3.2**). Blinded readings were performed on the remaining 54 datasets (37 NDBE, 6 LGD, 9 HGD, 2 EAC). Reader 1 was a non-clinician OCT trainee, reader 2 an attending gastroenterologist with OCT experience, and reader 3 a clinical GI trainee with no prior OCT experience. In a pretest following the training, readers identified features independently, but subsequently received feedback from the investigator. Readers were required to assess >75% of the features in accord with the study investigator's assessment to participate in the validation reading.

OCT datasets with correlated biopsy/EMR histology, no.	NDBE	LGD	HGD	EAC	Total
Training session	8	3	2	0	13
Pretest session	4	1	2	0	7
Validation session	37	6	9	2	54

Table 3.2 Histology of the OCT datasets.

Readers assessed depth-resolved *en face* OCT images followed by cross-sectional OCT images (**Figure 3.4**). Readers recorded the positions of features in the *en face* OCT depth series and cross-sectional OCT series. Reader's confidence ("high"/"low") and reading times were also recorded. Readings were performed using open source software (3D Slicer [147]) that allowed simultaneous orthoplane visualization of the *en face* and cross-sectional OCT image series with brightness and contrast adjustment. During training, pretest and validation reading, entire *en face* and cross-sectional OCT image series were used which covered a ~ 10 mm x 16 mm area. The *en face* OCT image series included images from all depths and readers were trained to recognize structural variations of mucosal patterns vs vascular structures at different depths.

The following workflow was used in the readings:

1) First only *en face* viewing was enabled. Readers read the *en face* OCT image series at various depths and assessed *en face* OCT features. If a region with irregular mucosal patterns was identified, it was demarcated on the image. The confidence of the assessment was noted as "high" or "low".

2) Next, cross-sectional and *en face* viewing were enabled. Readers read the cross-sectional OCT image series at different longitudinal positions. The confidence of the each assessment was noted as "high" or "low". If >5 atypical glands are identified, atypical glands were defined to be present and the frame number (longitudinal position) with most atypical glands was recorded.

3) After performing steps 1 and 2 sequentially on each dataset, the readers reviewed the "low" confidence datasets using both *en face* and cross-sectional views. The readers could then change his/her assessments and/or confidence of the assessments.

Important slides that were used during the training were provided in the appendix at the end of the thesis.

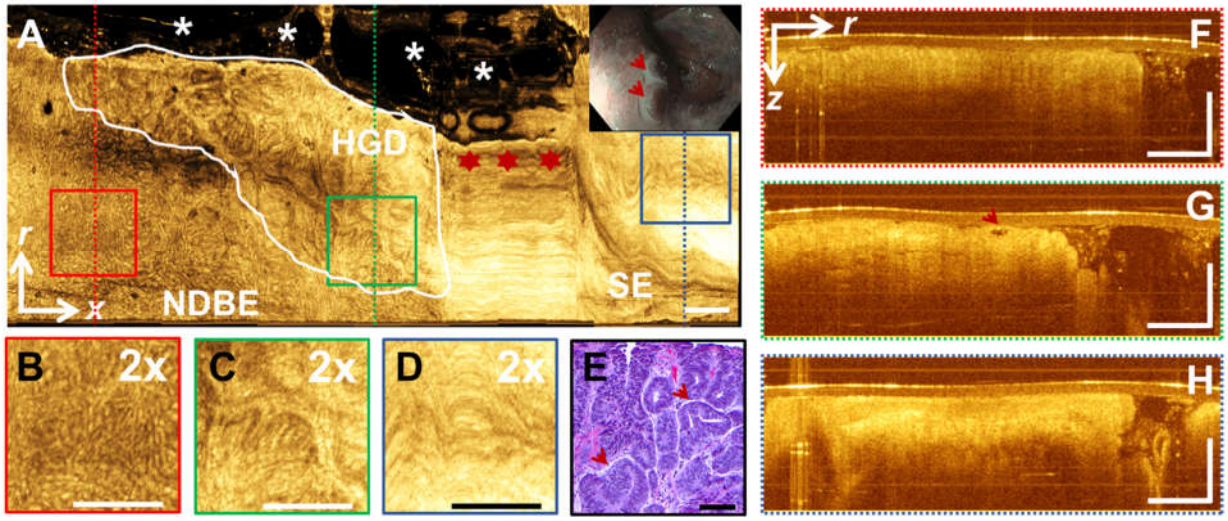

Figure 3.4. Volumetric OCT dataset of high-grade dysplasia (HGD). **A**, En face OCT at ~ 400 µm below the tissue surface showing the entire 10 mm x 16 mm catheter field of view. The HGD region is shown by the white line, with adjacent non-dysplastic Barrett's esophagus (NDBE) and normal squamous esophagus (SE) regions. The NDBE region has regular mucosal patterns, while HGD region has irregular mucosal patterns. The SE region has a relatively smooth appearance and high OCT signal. The stars indicate artifacts caused by non-uniform OCT catheter longitudinal actuation. Asterisks indicate regions where the mucosa is out of contact with catheter. Inset shows the corresponding WLE/NBI image of the dysplastic lesion prior to endoscopic mucosal resection (EMR). Arrows point to the nodular lesion. **B, C, D**, show 2x zoom over the boxed areas in **A**. **E**, H&E histology of the EMR specimen showing atypical glandular architecture and dysplastic glands with irregular size and shape (pointed by the arrows) consistent with HGD. **F, G, H**, cross-sectional OCT images of the areas in dotted lines in **A**. **G** shows atypical glandular architecture, mucosal layering present and surface signal ≤ subsurface in the HGD region. Arrow points to an atypical debris-filled gland. r: circumferential, x: longitudinal, z: depth directions. Scale bars are 100 µm in **E**, 1 mm otherwise.

Statistical analysis

All statistical calculations were performed in MATLAB (Mathworks, MA). Quantitative metrics were represented as mean ± standard deviation. Interobserver agreement was assessed using unweighted kappa statistics, where <0.21 was defined as poor, 0.21 to 0.4 was fair, 0.41 to 0.6 was moderate and 0.61 to 0.8 was substantial agreement [148, 149]. The t-test was used to

compare reading times of *en face* and cross-sectional OCT features. A *p*-value of <0.05 was considered statistically significant.

3.3.2. Results

Patient and dataset characteristics

74 OCT datasets correlated with biopsy/EMR histology were obtained (**Table 3.3**, 49 NDBE, 10 LGD, 13 HGD, 2 EAC). Of the neoplasia datasets, 12/25 (48%) were from treatment-naïve patients (n=10) while the remaining 13/25 (52%) were from previously-treated patients (ablation/EMR, n=8), four of whom were also imaged when treatment-naïve.

Patient demographics (n = 44)	
Age, mean (± SD)	70 (7.6)
Sex, male, no. (%)	43 (98)
Race, white, no. (%)	43 (98)
Baseline histology	
NDBE, subjects, no. (%)	30 (68)
Neoplasia (LGD/HGD/EAC), subjects, no. (%)	8/5/1 (32)
Previously-treated, subjects, no. (%)	4 (9)
Treatment-naïve, subjects, no. (%)	10 (23)
Length of BE (cm)	
Circumferential extent (C), mean (± SD)	2.3 (3.9)
Maximum extent (M), mean (± SD)	3.9 (4.1)
Number of OCT datasets with correlated biopsy/EMR histology per subject, median (range)	1 (1-5)
Characteristics of OCT datasets with correlated biopsy/EMR histology (n = 74)	
NDBE, no. (%)	49 (66)
From previously-treated patients, no. (%)	0 (0)
From treatment-naïve patients, no. (%)	49 (66)
Neoplasia (LGD/HGD/EAC), no. (%)	10/13/2 (34)
From previously-treated patients, no. (%)	13 (18)
From treatment-naïve patients, no. (%)	12 (16)

Table 3.3 Patient demographics and characteristics of OCT datasets with correlated biopsy/EMR histology included in the reading.

Reading results

Reader's pooled assessments are reported. Readers identified irregular mucosal patterns in 100% of neoplasia datasets, and in 35% of NDBE datasets (43% of short and 28% of long-segment NDBE, respectively) (**Table 3.4**). In cross-sectional OCT, mucosal layering was absent and surface signal

> subsurface in 35% and 29% of neoplasia datasets (21% and 21% in the treatment-naïve subgroup), and in 53% and 30% of NDBE datasets, respectively (**Table 3.5**). Atypical glands (>5) were present in 75% of neoplasia datasets (96% in the treatment-naïve subgroup) and in 59% of NDBE datasets (**Table 3.4**). These numbers represent the independent occurrence of features anywhere within the OCT datasets.

	Reader 1	Reader 2	Reader 3	Overall (%)
Fraction of irregular mucosal patterns				
In NDBE	13/37	11/37	15/37	39/111 (35)
Short-segment (≤3 cm) NDBE	8/17	7/17	7/17	22/51 (43)
Long-segment (>3 cm) NDBE	5/20	4/20	8/20	17/60 (28)
Away (>3 cm) from GEJ	4/12	2/12	3/12	9/36 (25)
Near (≤3 cm) the GEJ	1/8	2/8	5/8	8/24 (33)
In neoplasia	17/17	17/17	17/17	51/51 (100)
Treatment-naïve	8/8	8/8	8/8	24/24 (100)
Previously-treated	9/9	9/9	9/9	27/27 (100)
Fraction of atypical glands (> 5)				
In NDBE	23/37	20/37	23/37	66/111 (59)
Short-segment (≤3 cm) NDBE	14/17	14/17	12/17	40/51 (78)
Long-segment (>3 cm) NDBE	9/20	6/20	11/20	26/60 (43)
Away (>3 cm) from GEJ	3/12	2/12	5/12	10/36 (28)
Near (≤3 cm) the GEJ	6/8	4/8	6/8	16/24 (67)
In neoplasia	11/17	13/17	14/17	38/51 (75)
Treatment-naïve	7/8	8/8	8/8	23/24 (96)
Previously-treated	4/9	5/9	6/9	15/27 (56)

Table 3.4 Association of irregular mucosal patterns and atypical glands with correlated histological diagnosis and treatment history.

	Reader 1	Reader 2	Reader 3	Overall (%)
Fraction of absent mucosal layering				
In NDBE	23/37	13/37	23/37	59/111 (53)
In neoplasia	8/17	6/17	4/17	18/51 (35)
Treatment-naïve	3/8	2/8	0/8	5/24 (21)
Previously-treated	5/9	4/9	4/9	13/27 (48)
Fraction of Surface signal > subsurface				
In NDBE	15/37	7/37	11/37	33/111 (30)
In neoplasia	5/17	6/17	4/17	15/51 (29)
Treatment-naïve	1/8	3/8	1/8	5/24 (21)
Previously-treated	4/9	3/9	3/9	10/27 (37)

Table 3.5 Association of absent mucosal layering and surface signal > subsurface with correlated histological diagnosis and treatment history.

The positions of *en face* and cross-sectional features within the OCT datasets were also evaluated to assess their co-location. Atypical glands were present (co-localized) under irregular mucosal patterns in 75% of neoplasia datasets (96% in the treatment-naïve subgroup) and 30% of NDBE datasets (43% and 18% in short and long-segment NDBE, respectively) (**Table 3.6**). Within the long-segment NDBE subgroup, atypical glands under irregular mucosal patterns were present in 25% of datasets ≤ 3 cm the GEJ and 14% >3 cm from the GEJ.

	Reader 1	Reader 2	Reader 3	Overall (%)
Fraction of atypical glands under irregular mucosal patterns	21/54	23/54	27/54	71/162 (44)
In NDBE	10/37	10/37	13/37	33/111 (30)
Short-segment (≤3 cm) NDBE	8/17	7/17	7/17	22/51 (43)
Long-segment (>3 cm) NDBE	2/20	3/20	6/20	11/60 (18)
Away (>3 cm) from GEJ	1/12	1/12	3/12	5/36 (14)
Near (≤3 cm) the GEJ	1/8	2/8	3/8	6/24 (25)
In neoplasia	11/17	13/17	14/17	38/51 (75)
Treatment-naïve	7/8	8/8	8/8	23/24 (96)
Previously-treated	4/9	5/9	6/9	15/27 (56)
Fraction of atypical glands under regular mucosal patterns	13/54	10/54	10/54	33/162 (20)
In NDBE	13/37	10/37	10/37	33/111 (30)
In neoplasia	0/17	0/17	0/17	0/51 (0)

Table 3.6 Association of atypical glands co-localized under mucosal patterns, stratified according to correlated histological diagnosis and treatment history.

	Reader 1	Reader 2	Reader 3	Overall (%)
Fraction of absent mucosal layering				
Under regular mucosal patterns	16/54	11/54	11/54	38/162 (24)
In NDBE	16/37	11/37	11/37	38/111 (34)
In neoplasia	0/17	0/17	0/17	0/51 (0)
Under irregular mucosal patterns	15/54	8/54	12/54	35/162 (22)
In NDBE	7/37	2/37	8/37	17/111 (15)
In neoplasia	8/17	6/17	4/17	18/51 (35)
Fraction of surface signal > subsurface				
Under regular mucosal patterns	11/54	5/54	9/54	25/162 (15)
In NDBE	11/37	5/37	9/37	25/111 (23)
In neoplasia	0/17	0/17	0/17	0/51 (0)
Under irregular mucosal patterns, no./all	9/54	8/54	6/54	23/162 (14)
In NDBE	4/37	2/37	2/37	8/111 (7)
In neoplasia	5/17	6/17	4/17	15/51 (29)

Table 3.7 Association of mucosal patterns with absent mucosal layering and surface signal > subsurface, stratified according to correlated histological diagnosis.

The association of *en face* OCT irregular mucosal patterns and cross-sectional VLE-DA criteria with correlated histological diagnosis and treatment history are shown in **Table 3.8**. *En face* OCT irregular mucosal patterns and VLE-DA criteria for dysplasia were present in 23% of NDBE datasets, in 77% of neoplasia datasets and in 93% of treatment-naïve neoplasia datasets.

	Reader 1	Reader 2	Reader 3	Overall (%)
Fraction of irregular mucosal patterns on *en face* OCT with VLE-DA features of dysplasia on cross-sectional OCT				
In NDBE	8/37	9/37	8/37	25/111 (23)
In neoplasia	13/17	14/17	12/17	39/51 (77)
Treatment-naïve	6/8	8/8	8/8	22/24 (92)
Previously-treated	7/9	6/9	4/9	17/27 (63)

Table 3.8 Association of *en face* OCT and VLE-DA criteria with correlated histological diagnosis and treatment history.

The interobserver agreement was substantial (kappa = 0.73) for irregular mucosal patterns, moderate (kappa = 0.6) for absent mucosal layering, poor (kappa = 0.17) for surface signal > subsurface and substantial (kappa = 0.73) for atypical glands (**Table 3.9**). In 81% of the datasets, readers assessed all OCT features with high confidence (**Table 3.10**). Average reading times for e*n face* and cross-sectional features were 60±51 and 69±42 seconds, respectively (**Table 3.11**).

	Kappa value (95% CI)
Irregular mucosal patterns	0.73 (0.69-0.77)
VLE-DA features of	
Absent mucosal layering	0.6 (0.56-0.64)
Surface signal > subsurface	0.17 (0.13-0.21)
Atypical glands	0.73 (0.69-0.77)

Table 3.9 Interobserver agreement of *en face* and cross-sectional OCT features.

	Reader 1	Reader 2	Reader 3	Overall (%)
Irregular mucosal patterns				
High-confidence	47/54	43/54	50/54	140/162 (87)
NDBE	30/37	30/37	34/37	94/111 (85)
Neoplasia	17/17	13/17	16/17	46/51 (90)
All features				
High-confidence	41/54	41/54	49/54	131/162 (81)
NDBE	28/37	30/37	34/37	92/111 (83)
Neoplasia	13/17	11/17	15/17	39/51 (77)

†: *En face* OCT feature of irregular mucosal patterns and all three cross-sectional OCT features were assessed with high-confidence.

Table 3.10 Confidence of the readers' assessment of *en face* and cross-sectional OCT features.

	Reader 1	Reader 2	Reader 3	Overall
En face assessment				
Mean (SD), secs	53 (48)	80 (66)	47 (22)	60† (51)
Cross-sectional assessment				
Mean (SD), secs	69 (40)	71 (56)	66 (36)	69† (42)
Overall assessment				
Mean (SD), secs	122 (70)	152 (93)	113 (35)	129 (72)

†: *p-value* for the comparison between the average *en face* and cross-sectional assessment is 0.12.

Table 3.11 Average reading times per dataset.

3.3.3. Discussion

Early *in vivo* OCT studies identifying dysplasia using isolated cross-sectional images reported 83% sensitivity and 68% specificity with 55 patients [150], and 75% sensitivity and 82% specificity with 33 patients [151]. VLE uses balloon catheters to image up to a 6 cm length of esophagus, but imaging speed is insufficient to visualize *en face* OCT features. Leggett et al. developed a VLE diagnostic algorithm (VLE-DA) showing 86% sensitivity and 88% specificity with *ex vivo* specimens from 27 patients [43]. Swager et al. used VLE-DA features with a scoring-based criteria and reported 83% sensitivity and 71% specificity with *ex vivo* specimens from 29 patients [42], and developed an automated computer algorithm that achieved 90% sensitivity and 93% specificity with *ex vivo* specimens from 29 patients [44]. These VLE studies demonstrated precise registration of OCT images with histology, but the appearance of features potentially differs from *in vivo* OCT. Laser marking should enable biopsy guided by *in vivo* OCT features [47, 152].

We used depth-resolved *en face* OCT and assessed mucosal patterns as well as cross-sectional features. The size/shape of mucosal patterns varied between patients (**Figure 3.2**), consistent with NBI observations. Therefore, we included a large number of NDBE datasets in the study to adequately represent NDBE. *En face* OCT assessment used in this study was analogous to the recent NBI classification system (BING criteria), which showed 80% sensitivity and 88% specificity for identifying dysplasia by expert readers in a study of 97 patients [144]. Despite similarity to NBI, *en face* OCT has a distinct appearance because OCT has different contrast mechanisms and resolution. NBI uses visible light to illuminate tissue and therefore visualizes predominantly superficial features. The reflected / scattered light is collected without depth information. OCT uses infrared light which has deeper penetration into tissue, and detects depth-resolved differences in light backscattering and transmission from mucosal architecture [37]. OCT can visualize subsurface features, but the appearance of deeper structures are affected by optical attenuation and scattering from superficial structures. Subsurface *en face* OCT can mitigate deleterious effects of surface reflections and debris on image quality and can have improved contrast/resolution compared to NBI. *En face* and cross-sectional views are intrinsically co-registered, such that specific features in *en face* OCT images can viewed simultaneously in a registered cross-sectional image or vice versa. Finally, OCT does not require contrast agents and can be used after biopsy/EMR [153], where visibility with NBI can be reduced by bleeding.

En face OCT irregular mucosal patterns were present in 100% of the neoplasia datasets, however, the majority of these datasets were obtained from regions with nodularity and/or irregular mucosal/vascular patterns on WLE/NBI and are therefore subject to selection bias. Irregular mucosal patterns were also present in 35% of the NDBE datasets. Cross-sectional OCT features of absent mucosal layering and surface signal > subsurface were present in 35% and 29% of neoplasia datasets, but also present in 53% and 30% of NDBE datasets. This unexpectedly high rate in NDBE might be caused by biopsy sampling error (see “Discussion of features in the NDBE datasets”), motion artifacts (**Figure 3.4**), distortion from excessive pressure exerted by the OCT catheter, or the features may have inherent low specificity. OCT was not used to guide biopsy/EMR, and our study was not designed to compare OCT to WLE/NBI. Future OCT studies with laser marking should allow more precise histological correlation with imaging.

The association of atypical glands and irregular mucosal patterns is a key finding of our study. Atypical glands were present (co-localized) under irregular mucosal patterns in 75% of neoplasia datasets and 96% of the treatment naïve subgroup of neoplasia. By contrast, atypical glands under irregular mucosal patterns were present in much fewer, 30% of NDBE datasets. Further stratifying by length of BE showed atypical glands under mucosal patterns in 43% of short-segment NDBE and 18% of long-segment NDBE. Within the long-segment NDBE subgroup, they were present in 25% of datasets within ≤3 cm of the GEJ, but only 14% of datasets >3 cm from the GEJ. Cardiac glands occur near the GEJ and could not be distinguished from atypical glands on OCT, therefore they may have been misinterpreted as atypical glands.

The association of mucosal patterns on *en face* OCT with individual cross-sectional OCT features was also assessed stratified according to correlated histological diagnosis, treatment history and BE length **(Table 3.6, Table 3.7**). Atypical glands were present under irregular mucosal patterns in 44% of datasets (NDBE and neoplasia), but were present under regular mucosal patterns in only 20% of the datasets (NDBE and neoplasia), suggesting a general association of atypical glands with irregular mucosal patterns. Furthermore, atypical glands occurred more frequently overall than irregular mucosal patterns. These results are consistent with previous literature which suggests that atypical glands may be a precursor to irregular mucosal patterns and dysplasia in pathogenesis [154]. Specifically, due to its metaplastic nature, BE mucosa frequently shows baseline/metaplastic atypia in histopathology, however, without dysplastic progression the atypia is limited to the glands at the base of the mucosa and does not extend to the surface epithelium [155]. Inflammation in the setting of chronic acid exposure can induce regenerative cytological alterations and may exacerbate atypia on the glands at the base of the crypts, while these cytological alterations would be still lacking on the surface epithelium [155]. A series of cytological changes occur in the progression from NDBE to neoplasia including enlargement/elongation of nuclei, nuclear stratification, pleomorphism and loss of nuclear polarity [156]. These changes subsequently cause distortions in the crypt architecture, including villiform crypt architecture, branched and cribriform glands, as well as cellular debris within the glands [155]. These distortions in the crypt architecture affecting the surface epithelium may then appear as irregular mucosal patterns observed in the *en face* plane [141].

Atypical glands either under irregular mucosal patterns or independently might be a potential marker for dysplasia, especially in long-segment BE in proximal regions further from the GEJ, where interpretation is not confounded by cardiac glands and where dysplasia most frequently occurs [157]. However, further investigation is needed to determine if OCT can better differentiate atypical vs cardiac glands in order to improve utility. The cross-sectional features of absent mucosal layering and surface signal > subsurface had poor association with neoplasia even in treatment-naïve cases, and were present at high rates in NDBE.

In this study, we also used VLE-DA to assess cross-sectional OCT images because it is one of few validated protocols for an image series, rather than individual images. Although it has not yet tested *in vivo*, its performance was reported to be better than previous OCT dysplasia detection criteria [151]. Readers assessed each cross-sectional OCT feature independently, so that separate cross-sectional OCT features could be tested in addition to VLE-DA which uses cross-sectional features in an algorithm. As indicated in the reading workflow in **Methods**, cross-sectional OCT features were assessed immediately after *en face* OCT reading without a separate reading session or washout period. Our reading protocol was designed to investigate volumetric OCT reading, where the *en face* and cross-sectional (orthoplane) information is used jointly. However, this may result in a bias in the cross-sectional OCT reading.

In this study, LGD datasets were grouped with HGD and EAC datasets, and all were categorized as neoplasia. This contrasts with some previous studies that either excluded LGD or grouped it with NDBE. We have studied the association of *en face* and cross-sectional OCT features with correlated histological diagnosis when the neoplasia datasets are separated into LGD vs HGD/EAC (**Table 3.12**). Irregular mucosal patterns were present in 35% of NDBE datasets, in 100% of LGD datasets and in 100% of HGD/EAC datasets. Atypical glands were present in 59% of NDBE datasets, in 83% of LGD datasets and in 70% of HGD/EAC datasets. Atypical glands under irregular mucosal patterns were present in 30% of NDBE datasets, in 83% of LGD datasets and in 70% of HGD/EAC datasets. Mucosal layering was absent in 50% of NDBE datasets, in 50% of LGD datasets and in 27% of HGD/EAC datasets. Surface signal > subsurface in 30% of NDBE datasets, in 28% of LGD datasets and in 30% of HGD/EAC datasets. This analysis suggested that LGD

exhibited irregular mucosal patterns and atypical glands features that are more similar to HGD/EAC than to NDBE. Our results are consistent with recent reports suggesting that endoscopic treatment is indicated for LGD [158]. The histological diagnosis of all LGD cases was made by a specialized expert gastrointestinal (GI) pathologist with >15 years of experience in GI pathology (QH). A third-party confirmation from expert referral centers, such as The Joint Pathology Center, MD or the Brigham and Women's Hospital, MA was obtained when necessary.

	NDBE* (%)	LGD* (%)	HGD/EAC* (%)
Fraction of irregular mucosal patterns	39/111 (35)	18/18 (100)	33/33 (100)
Fraction of atypical glands (> 5)	66/111 (59)	15/18 (83)	23/33 (70)
Fraction of atypical glands under irregular mucosal patterns	33/111 (30)	15/18 (83)	23/33 (70)
Fraction of absent mucosal layering	55/111 (50)	9/18 (50)	9/33 (27)
Fraction of surface signal > subsurface	33/111 (30)	5/18 (28)	10/33 (30)

*: Overall for three readers.

Table 3.12 Association of *en face* and cross-sectional OCT features with correlated histological diagnosis stratified into NDBE, LGD and HGD/EAC.

Given limited sample size and variability in reader OCT experience, we asked readers to rate their confidence for each feature assessment in order to assess robustness of feature recognition and estimate potential performance improvement with additional training/experience, similar to previous NBI and CLE studies [144, 159]. In 81% of datasets, all features were assessed with high-confidence (**Table 3.10**), suggesting that even readers with limited OCT experience can make assessments after brief training (average training time of 77 minutes).

Limitations of this study include small sample size, particularly for dysplastic/treatment-naïve patients. Most patients with neoplasia had already undergone ablation/EMR treatment. Although inclusion of previously-treated patients is common in OCT/NBI literature [43, 144], some features were associated with treatment history (**Table 3.4, Table 3.6**). Furthermore, the reading was performed retrospectively. Prospective studies on larger cohorts of treatment-naïve and/or BE surveillance patients are needed.

Discussion of features in the NDBE datasets

Features associated with neoplasia were also observed in NDBE datasets at higher than expected rates. *En face* OCT irregular mucosal patterns were observed in 35% of the NDBE datasets, suggesting that if this feature were used to detect neoplasia it would have a moderate specificity. This specificity is lower than recent NBI studies that use analogous criteria to assess mucosal patterns [144]. Possible reasons for these results include:

1) Sampling error: The majority of irregular mucosal patterns in *en face* OCT in NDBE were focal regions within regular mucosal patterns. As discussed in the **Methods**, OCT datasets were categorized as NDBE and included only if they were from patients without dysplasia history and correlated histology was NDBE. Biopsy/EMR under OCT guidance was not performed in our study and was not approved by our IRB. Biopsies from NDBE patients were taken following Seattle protocol and thus there was a possibility of sampling error. OCT datasets covered a >10 times larger area than the area sampled by a standard pinch biopsy forceps and focal dysplastic regions may be missed by biopsy. At the same time, it is unlikely that sampling error could explain a 35% rate of irregular mucosal patterns in NDBE. Future studies with OCT guided biopsies with laser marking techniques can allow more precise histological correlation with OCT images [47].

2) Previous OCT studies noted that the OCT catheter can compress tissues and alter the mucosal architecture in cross-sectional OCT images [160, 161]. In this study we also noticed that excessive catheter pressure on tissue distorted mucosal patterns in *en face* OCT images. **Figure 3.5** illustrates this effect in two NDBE datasets acquired with varying catheter pressure. When the pressure was increased, mucosal layer thickness decreased and regular mucosal patterns appeared distorted. Although it is challenging to control the pressure exerted by the catheter, it is possible to reacquire datasets having possible image artifacts, such as in **Figure 3.5B**. However, this is limited by the time constraints of the endoscopy session. It is likely that similar pressure artifacts occur with VLE imaging balloons.

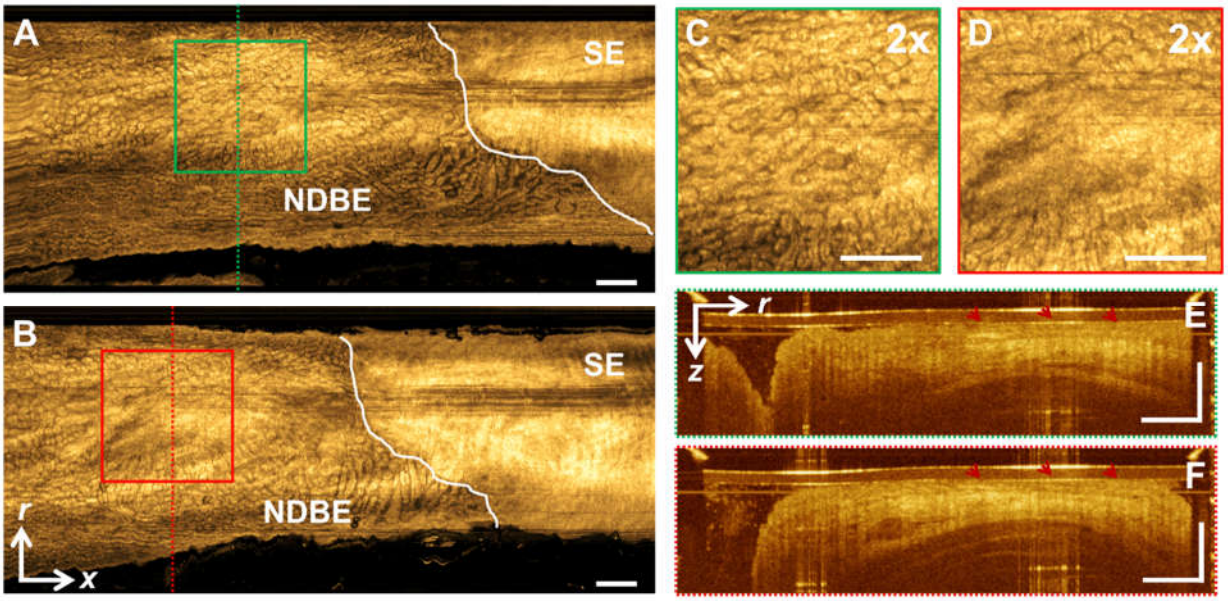

Figure 3.5. Effects of variations in catheter pressure on tissue. Non-dysplastic Barrett's esophagus (NDBE) datasets acquired approximately at the same longitudinal position along the esophagus imaged with different catheter pressure. **A**, *En face* OCT at ~ 400 µm below the tissue surface showing squamocolumnar junction, demarcated by the white line, and regular mucosal patterns in the NDBE region. **B**, *En face* OCT at ~ 400 µm below the tissue surface where a higher catheter pressure is exerted compared to **A**. Artifactual distortion of the regular mucosal patterns is apparent. **C, D**, show 2x zoom over the boxed areas in **A** and **B**, respectively, showing the region where catheter pressure produces the largest distortion of mucosal patterns. **E, F**, cross-sectional OCT images of the areas in dotted lines in **A** and **B**, respectively, showing artifactually decreased mucosal layer thickness (pointed by arrows), and increased submucosal layer signal due to pressure. r: circumferential direction, x: longitudinal direction, z: depth direction. SE: Normal squamous esophagus. Scale bars are 1 mm.

Atypical glands were also present at unexpectedly high rates, in 59% of the NDBE datasets (**Table 3.4**). To investigate this further, we stratified the NDBE data according to BE segment length and longitudinal imaging location with respect to the gastroesophageal junction (GEJ) (**Table 3.4**). Atypical glands were present in 78% of the NDBE datasets from short-segment (≤3 cm) NDBE patients and in 43% of the NDBE datasets from long-segment (>3 cm) NDBE patients. Furthermore, in the long-segment cohort, the majority of atypical glands were found near the GEJ (67% ≤3 cm from the GEJ vs 28% >3 cm from the GEJ). The NDBE OCT datasets were obtained at standardized positions relative to the GEJ and covered a larger area than sampled by standard pinch biopsy forceps, so it is difficult to biopsy the glands. There is a high density of non-neoplastic cardiac glands in the cardia and near the GEJ, so it is likely they are misinterpreted as

atypical glands [162, 163]. Further studies with higher resolution OCT and more precise histological correlation are needed to assess whether OCT can detect differences between cardiac vs atypical glands near the GEJ.

Training materials and general study observations

This section provides some important slides that were used during the training phase of this study. Some important comments and remarks about the training and reading are also provided.

On average, training took about ~ 80 minutes for each of the three readers. As discussed before, reader 3 had not prior OCT experience and reader 2 had limited experience in assessing entire OCT datasets. It was noted that assessing an entire OCT dataset is significantly challenging than assessing pre-selected individual cross-sectional OCT images. Various imaging artifacts that would typically not observed in the pre-selected, representative images existed in the full datasets which had the potential to affect the reading results. Examples of these included mucous debris between the catheter sheath and tissue surface decreasing the penetration depth of the underlying tissue, high catheter reflections at particular rotational angles affecting the brightness of the underlying signal, out of contact regions affecting visualization of layered architectures etc. In addition to artifacts, the mucosal patterns also varied significantly between different regions of the imaging field. Especially for long-segment BE cases we have noted a gradual increase in the size of the individual mucosal ridges and pits as the longitudinal pullback position was moved away from the stomach. We have provided examples of wide field NBI images of NDBE tissues to illustrate that this variation in the mucosal pattern was normal and should not be marked as an irregularity on the mucosal pattern. Overall, given these broad range of imaging artifacts and variations, the training sets had to be selected very carefully so that they span a variety of observed imaging artifacts and variations of tissue structures.

There was also catheter pressure related imaging artifacts as discussed in previous sections. Since OCTA information was not available, datasets with these artifacts were still included in the study and it was not possible to train the reader to assess for the presence of this artifact, which might have resulted in reduced specificity of the reading by the presence of more

regions with irregular mucosal patterns due to this imaging artifact. However, as discussed previously, for a typical dataset the area with catheter pressure artifact was rather small and the readers were instructed in the training to ignore small regions with irregular patterns within regular mucosal patterns. The cartoons that are provided within the training material in the next few pages illustrate examples of how these artifacts looked like and how the readers were trained to ignore those regions.

Effects of catheter pressure on OCTA

Previous OCT studies have found that external tissue also affects vasculature perfusion, impairing vascular flow and affecting OCTA visualization [164]. We have also assessed the effects of catheter pressure variation on the OCTA images. **Figure 3.6** illustrates an example of anal canal imaging where the micromotor catheter was directly introduced to the anal canal so that the applied pressure could be readily manipulated by the operator. When the applied pressure was low, then a rich vascular network could be observed both in the epithelium and deeper lamina propria/muscularis mucosa layers (**Figure 3.6A** and **Figure 3.6B**). When the acquisition is repeated over the same area with a higher applied pressure, then vascular impairment was observed at most of the imaging regions (**Figure 3.6D** and **Figure 3.6E**), at all depths. The effect of increasing pressure could be also clearly visualized by the cross-sectional OCT images in **Figure 3.6C** and **Figure 3.6F.**

It is worth noting that the examples illustrated in **Figure 3.6** are rather extreme cases, where the operator was able to control the amount of pressure since the catheter was directly introduced. However, in an endoscope-based imaging scenario, such as upper GI imaging, it is not straightforward to control the amount of pressure, and usually the datasets show high-pressure artifacts only at localized regions. As an example, **Figure 3.7** shows co-registered *en face* OCT and OCTA images acquired at the SCJ of the NDBE patient. When the exerted pressure was lower, regular circular mucosal and honeycomb-like vascular patterns can be observed over the NDBE region (**Figure 3.7A** and **Figure 3.7B**). When the exerted pressure is increased then the effects of higher pressure are observed in some localized regions, as encircled in the image. The mucosal patterns on this region is distorted and the vascular flow is impaired.

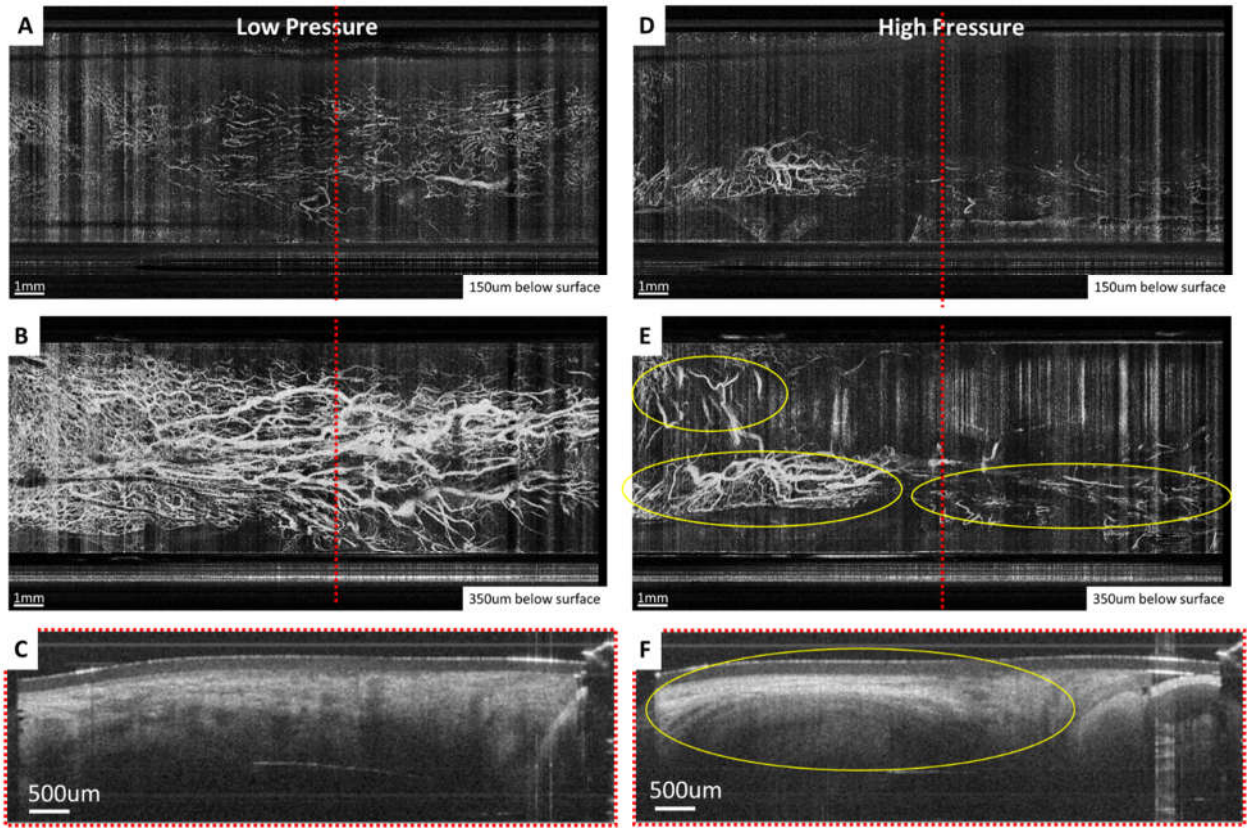

Figure 3.6. Effects of variations in catheter pressure exerted on the tissue on OCTA images acquired from human anal canal. Micromotor catheter was directly introduced to the anal canal and the operator could readily change the applied pressure. **A, B,** *En face* OCTA image at ~ 150 µm and 350 µm below the tissue surface, respectively, with a low catheter pressure exerted to the tissue. A rich vascular network can be observed in both images for most of the imaging field. Larger and more intricate vascular is observed at deeper depths, corresponding to the lamina propria/muscularis mucosa layer. **C,** cross-sectional OCT image of the area in dotted lines in **A** and **B.** A thin squamous epithelium layer can be observed at the surface followed by the lamina propria/muscularis mucosa layers at deeper depths. **D, E,** *En face* OCTA image at ~ 150 µm and 350 µm below the tissue surface, respectively, of the same region but with a higher catheter pressure exerted to the tissue. The vascular flow is impaired in most of the imaging field at all depths except at the encircled regions on the borders of the imaging field. **F,** cross-sectional OCT image of the area in dotted lines in **D** and **E.** Compression of the tissue layers and a significant increase in signal intensity is evident.

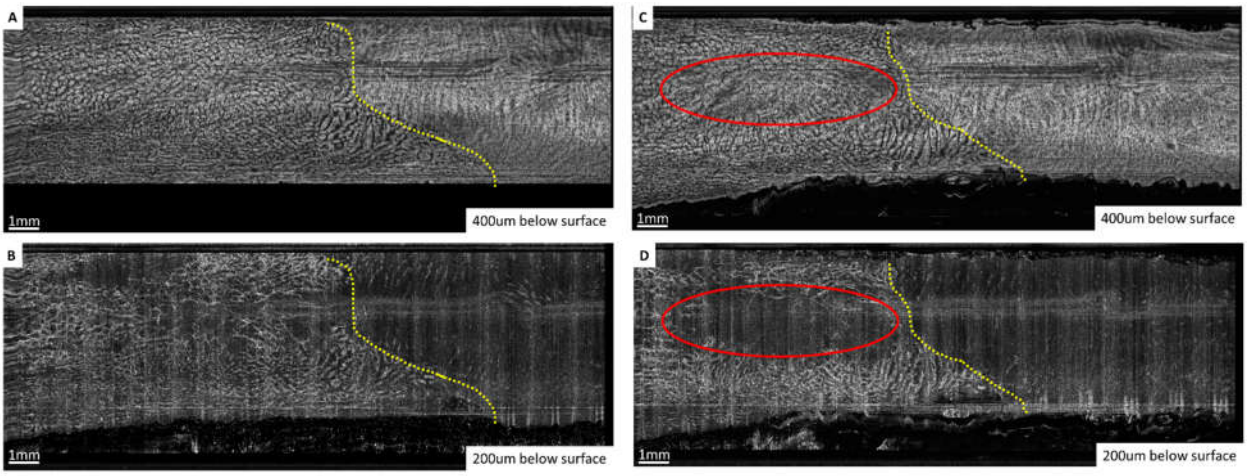

Figure 3.7. Further illustration of the effects of catheter pressure exerted on the tissue on co-registered *en face* OCT and OCTA images. Datasets have histological diagnosis of non-dysplastic Barrett's esophagus (NDBE) and acquired approximately at the same longitudinal position along the esophagus. **A,** *En face* OCT image at ~ 400 µm below the tissue surface showing squamocolumnar junction, demarcated by the yellow line, and regular mucosal patterns on the NDBE region. **B,** *En face* OCTA image at ~ 200 µm below tissue surface showing regular honeycomb-like vascular pattern on the NDBE region. **C,** *En face* OCT image at ~ 400 µm below the tissue surface corresponding to the same dataset as in **A** where a higher pressure is exerted with the micromotor catheter compared to **A** that distorts the appearance of the regular mucosal patterns at the encircled region. **D,** *En face* OCTA image at ~ 200 µm below tissue surface corresponding to the same dataset as in **C** showing impaired vascular flow on the encircled region.

The ability of OCTA visualization can be a good surrogate marker to assess if a region has distorted/irregular mucosal patterns because of higher catheter pressure. Datasets that have this artifact, such as in **Figure 3.6D** and **Figure 3.7C** can be immediately reacquired by instructing the operator to exert less pressure. However, the requirement of obtaining OCTA increases the complexity of the imaging system as overlapping areas need to be imaged and the scanning needs to be performed very uniformly, or image registration algorithms such as discussed previously need to be applied to correct for scanning non-uniformities.

3.4. Ultrahigh-speed endoscopic OCT for Endoscopic Mucosal Resection

3.4.1. Case Presentation and Methods

This study was conducted under protocols at the Veteran Affairs Boston Healthcare System (VABHS) Institutional Review Board (IRB), Harvard Medical School (HMS) Office of Human Research Administration (OHRA) and Massachusetts Institute of Technology (MIT) Committee on the Use of Humans as Experimental Subjects (COUHES). Written informed consent was obtained prior to imaging allowing presentation of this case and data. A 75 y.o. male was scheduled for endoscopic eradication therapy of known BE with confirmed high-grade dysplasia (HGD) at the GEJ. The patient had a C0M5 BE segment [165] and no prior endoscopic treatment. Endoscopic OCT and OCTA images were acquired before and immediately post EMR. The patient was imaged again at 2-months follow-up. The OCT probe was introduced through the accessory channel of a dual-channel endoscope (GIF-2TH180, Olympus, Japan) to allow co-registered imaging during EMR (Duette® Multi-band Mucosectomy, Cook Medical, IN). Each OCT/OCTA dataset covered an area of 10 mm x 16 mm (circumferential x longitudinal), and was acquired in 8 seconds [31]. Multiple acquisitions were performed by varying probe placement around the lesion and resection margins.

3.4.2. Results

WLE/NBI images prior to EMR showed a dysplastic lesion with nodularity and irregular mucosal and vascular patterns located at the GEJ within a sliding hiatal hernia (inset, **Figure 3.8A**). OCT/OCTA images acquired prior to EMR showed the lesion and its lateral margins (**Figure 3.8**). In the en face OCT image at 250 µm depth, the gastric/non-dysplastic BE (NDBE) region was identified by regular circular mucosal patterns (**Figure 3.8A**). The adjacent dysplastic lesion exhibited irregular mucosal patterns. In the en face OCTA image at 250 µm depth, the gastric/NDBE region was identified by regular honeycomb microvascular patterns (**Figure 3.8B**). The adjacent dysplastic lesion exhibited abnormal vessel branching. Cross-sectional OCT of the gastric/NDBE region was identified by regular vertical crypt architecture (**Figure 3.8C**). Cross-sectional OCT of the dysplastic region exhibited atypical glandular architecture, dilated glands, as well as surface signal intensity higher than subsurface (**Figure 3.8D**). Subsequent histology of the

resected EMR specimen confirmed the presence of HGD with focal intramucosal carcinoma (IMC, inset, **Figure 3.8B**).

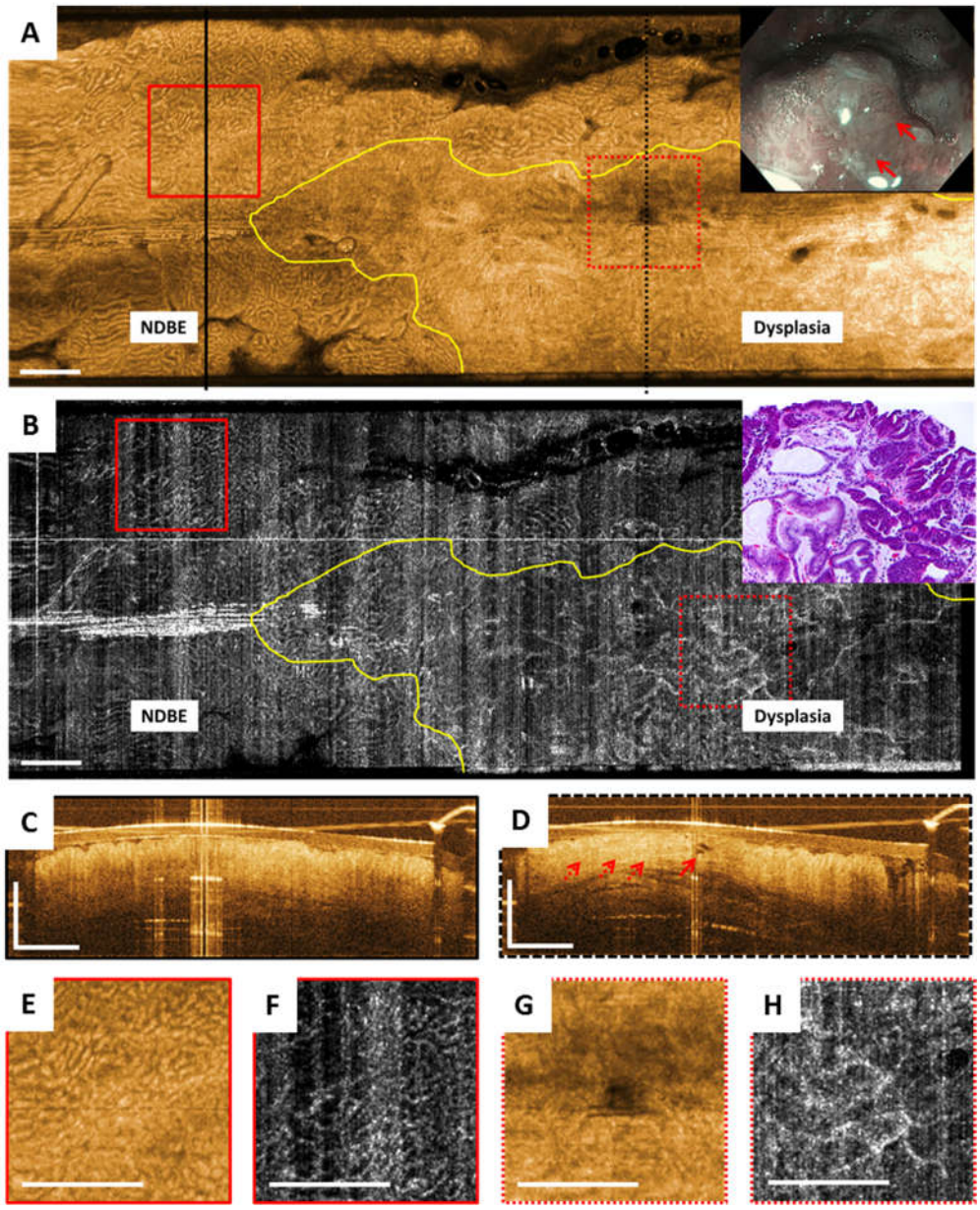

Figure 3.8. OCT,OCTA and endoscopy images acquired prior to EMR. **A,** shows *en face* OCT and **B,** shows *en face* OCTA image at ~ 250 µm below the tissue surface. Yellow lines delineate the distal and one of the transverse margins of the dysplastic lesion. **C, D,** show cross-sectional OCT images of the areas in black lines in **A.** Solid red arrow in **D** points to dilated glands and the dotted red arrows show atypical glandular architecture and surface signal intensity higher than subsurface. **E, F, G, H**, show 2x zoom over the boxed areas in **A** and **B**. Inset in **A** shows corresponding WLE/NBI image prior to EMR. Solid red arrows point to the nodular lesion. Inset in **B** shows H&E histology of the resected specimen. Scale bars are 1 mm.

Immediately post EMR, the resection site exhibited bleeding, debris and cautery marks (inset, **Figure 3.9B**). The resection site was identified in the *en face* OCT image at 250 µm depth by its relatively smooth appearance caused by the cauterized tissue and lamina propria/muscularis mucosa (LP/MM) layers displaced to the surface (**Figure 3.9A**). In the *en face* OCTA image at 250 µm depth, the resection site was identified by its lack of vascular contrast (**Figure 3.9B**). A region with irregular mucosal patterns was observed between the gastric/NDBE region and resection site, suggesting a positive lateral margin and residual dysplasia. Cross-sectional OCT of this region exhibited atypical glandular architecture, dilated glands (solid red arrow, **Figure 3.9C**) and irregular surface (dotted red arrows**, Figure 3.9C)**. Cross-sectional OCT of the resection site showed cauterized tissue and the LP/MM layers on the surface as hyper-reflective layers, as well as deep ductal/lymphatic structures (dotted red arrows, **Figure 3.9D**).

WLE/NBI and OCT/OCTA images from the EMR region on follow-up endoscopy at 2 months showed a residual dysplastic lesion, confirming OCT findings of the resection site immediately post EMR (inset, **Figure 3.10A** and **Figure 3.10,** respectively). In the *en face* OCT image at 250 µm depth, neosquamous mucosa was identified by the relatively smooth appearance and bright OCT signal (**Figure 3.10A**), while in the *en face* OCTA image at 250 µm depth this region showed normal branching vascular appearance, characteristic of the LP layer (**Figure 3.10B**). The adjacent dysplastic lesion exhibited irregular mucosal and microvascular patterns similar to that previously described. This area was resected via EMR and subsequent histology of the resected specimen confirmed presence of HGD (inset, **Figure 3.10B**). The patient subsequently underwent several EMR, cryoablation and radiofrequency ablation procedures until complete remission of intestinal metaplasia (CRIM) was achieved.

3.4.3. Discussion and Conclusion

This case demonstrates probe-based endoscopic OCT for comprehensive evaluation of a dysplastic lesion before and after endoscopic therapy. OCT/OCTA prior to EMR visualized the dysplastic lesion and its lateral margins. This could be particularly helpful for flat lesions where localization of dysplasia by WLE/NBI can be difficult.

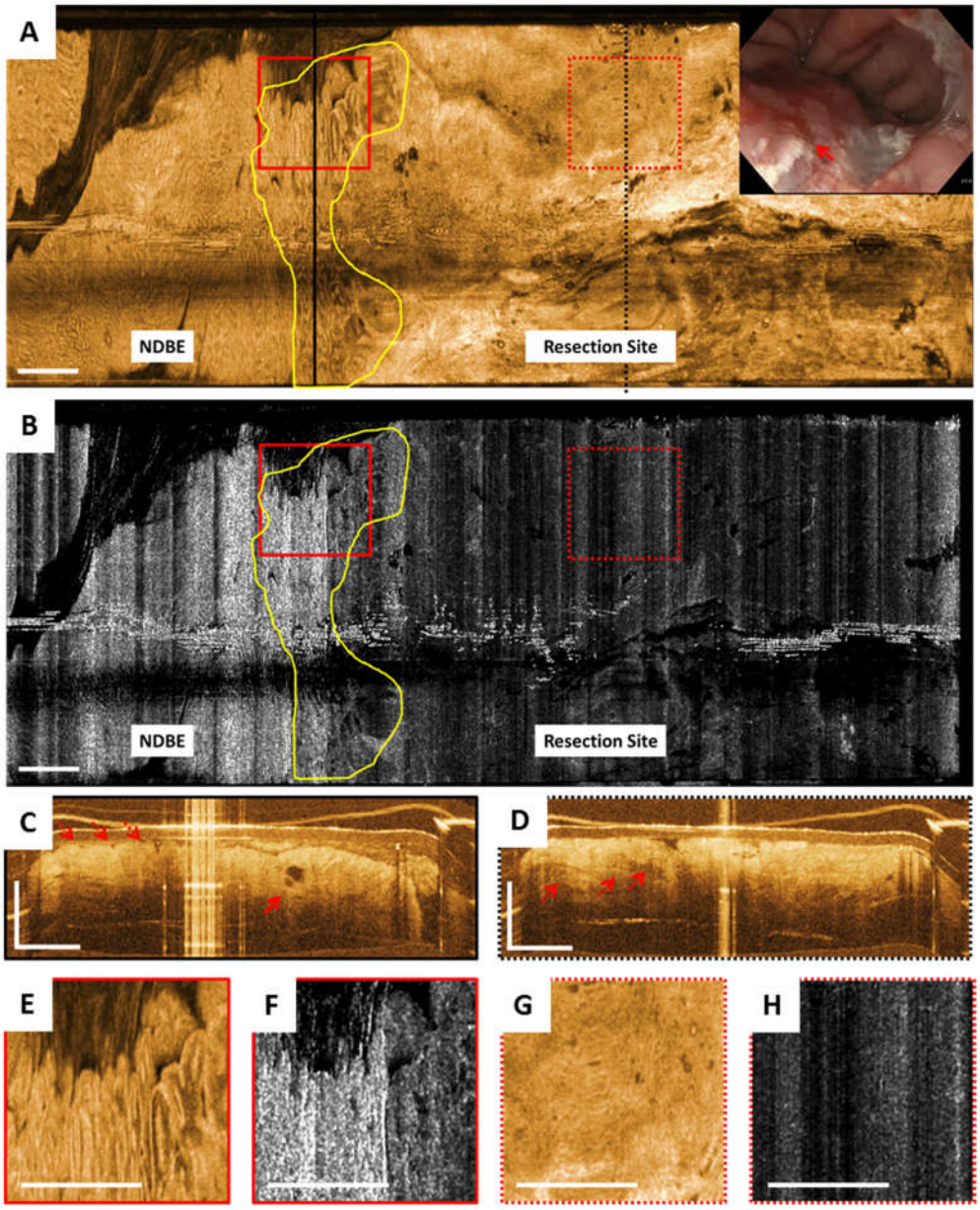

Figure 3.9. OCT, OCTA and endoscopy images acquired immediately post EMR. **A,** shows *en face* OCT and **B**, shows *en face* OCTA image at ~ 250 µm below the tissue surface. Yellow lines mark an area with irregular mucosal patterns between the gastric/NDBE region and the resection site suggesting a positive lateral margin and residual dysplasia. OCTA images of the gastric/NDBE region and lateral EMR margin exhibit high noise due to motion artifacts. **C, D,** show cross-sectional OCT images of the areas in black lines in **A.** Solid red arrow in **C** points to dilated glands and the dotted red arrows show atypical glandular architecture and irregular surface. Dotted red arrows in **D** show deep ductal/lymphatic structures at the resection site. **E, F, G, H**, show 2x zoom over the boxed areas in **A** and **B**. Inset in **A** shows corresponding WLE image immediately post EMR. Solid red arrow points to the resection site, where endoscopic visibility is limited due to bleeding, debris and cautery marks. Scale bars are 1 mm.

Immediately post EMR, when WLE/NBI visualization can be compromised by tissue distortion, electrocautery and blood, the OCT probe allowed direct lavage over the area, and OCT/OCTA showed residual dysplasia at the distal resection margin. Confocal endomicroscopy, which generally requires intravenous contrast, is ineffective immediately post EMR because of dye leakage. Due to software limitations at the time of this study, OCTA images were not available in real time during the endoscopy and resection under OCT/OCTA guidance was not approved under IRB protocols, so additional EMR was not performed at the time of initial treatment. However, these results suggest that OCT/OCTA can potentially play an important role in guiding endoscopic eradication therapies such as EMR, to facilitate complete removal of dysplastic lesions in a single visit.

The probe-based micromotor catheter used in this study [31, 166] has a smaller field of view but finer transverse resolution compared to balloon- and capsule-based imaging (the probe diameter was 3.4 mm, while balloons and capsules can have 12 to 20 mm diameters) [35, 37, 167]. A balloon catheter can be inflated to stabilize the esophagus and image the portions of the esophagus that are in contact with the balloon. However, there can be sampling errors where the esophagus is not in contact and a simultaneous endoscopic view of the OCT imaged region is not possible. Tethered capsules can image large fields of view by proximally pulling back the capsule, but can also have sampling errors due to incomplete esophageal contact or non-uniform pullback [37]. The small diameter of the OCT probe allows direct assessment of the cardia and hiatal hernia under endoscopic guidance. However, its smaller field of view necessitates multiple image acquisitions to cover large regions of interest.

In interpreting the OCT/OCTA images, previously published features were used to outline regions of dysplasia [34, 43, 144]. Specifically, in *en face* OCT/OCTA images, regions with irregular mucosal and microvascular patterns were classified as dysplastic. In cross-sectional OCT images, regions with atypical glandular architecture, dilated and debris-filled glands, surface signal intensity higher than subsurface and irregular surface were classified as dysplastic. Optimal criteria for identifying dysplasia with volumetric OCT is still under investigation.

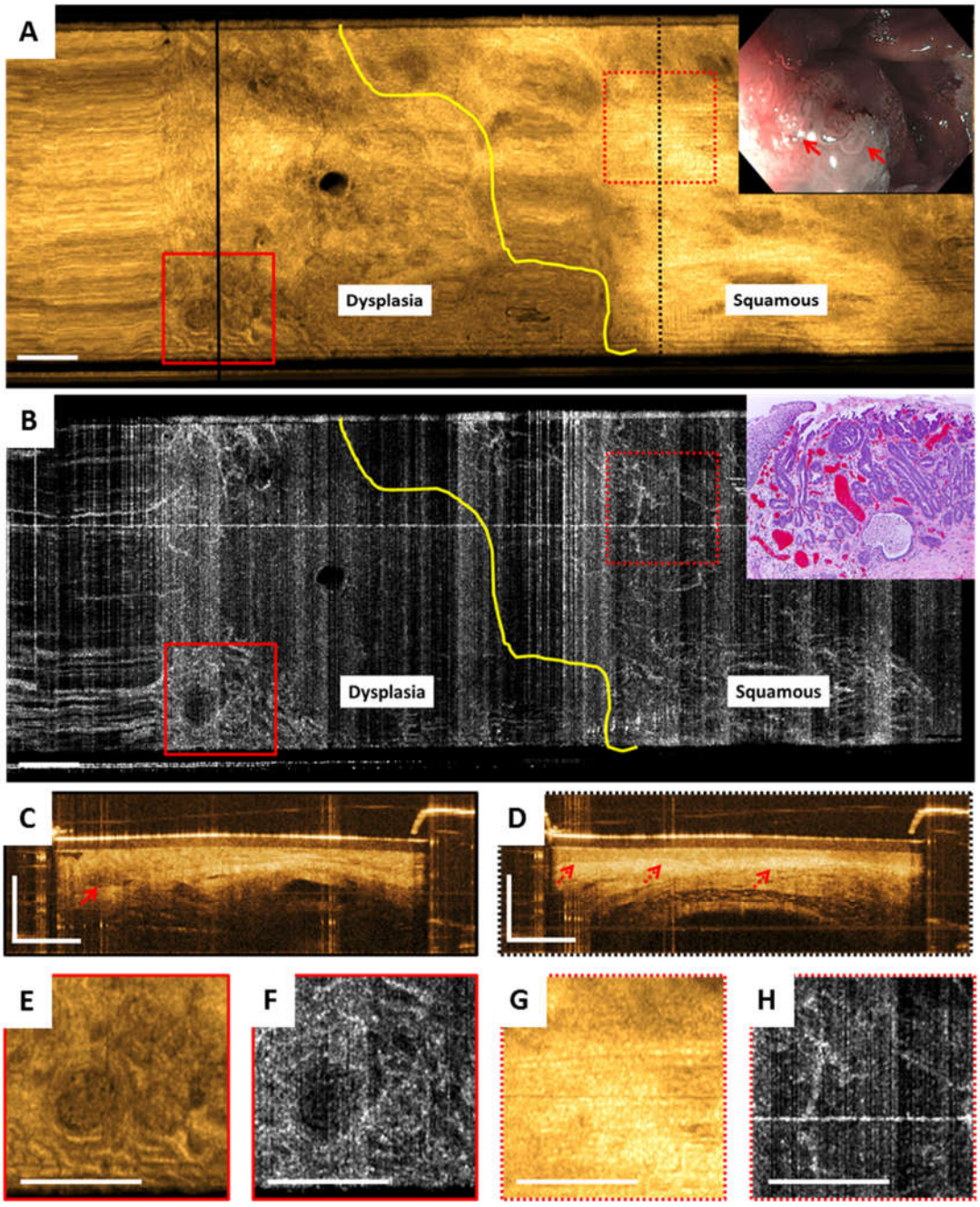

Figure 3.10. OCT, OCTA and endoscopy images acquired over the previous EMR area at 2-months follow-up. **A,** shows *en face* OCT and **B**, shows *en face* OCTA image at ~ 250 µm below the tissue surface. Yellow lines delineate the proximal lateral margin of the residual dysplastic lesion. **C, D,** shows cross-sectional OCT images of the areas in black lines in **A.** Solid red arrow in **C** points to a debris-filled dilated gland. Dotted red arrows in **D** point to LP, MM and submucosa layers underneath the homogeneous squamous epithelium layer typical of normal esophagus. **E, F, G, H**, show 2x zoom over the boxed areas in **A** and **B**. Inset in **A** shows corresponding WLE/NBI image prior to EMR. Solid red arrows point to the nodular lesion at the squamocolumnar junction. Inset in **B** shows H&E histology of the resected specimen. Scale bars are 1 mm.

In summary, probe-based OCT/OCTA provides cross-sectional and *en face* microstructural images as well as *en face* microvascular images which may improve diagnostic capabilities and enhance clinical utility by identifying dysplastic areas, assessing lesion margins, and evaluating regions immediately post-treatment and on follow-up. Probe-based OCT/OCTA may have advantages over balloon- and capsule-based OCT and confocal endomicroscopy in certain settings.

Chapter IV

Non-endoscopic OCT Assessment of Chronic Radiation Proctopathy

4.1. Motivation

Chronic radiation proctopathy (CRP) occurs as a result of pelvic radiation therapy and is associated with formation of abnormal vascular lesions that may lead to persistent rectal bleeding. Up to 20% of patients receiving radiation therapy for prostate and cervical cancer may develop CRP [12]. While the incidence is declining [23, 168] due to the refinement of radiation delivery techniques [169-171], CRP remains one of the major complications of pelvic radiation therapy and significantly affects patient quality of life.

For symptomatic patients who had received pelvic radiation therapy, the current clinical standard for diagnosis and assessment of disease severity for CRP is colonoscopy [172] to examine the rectal mucosa for its hallmarks, such as hemorrhage, ulcerations and telangiectasias [16]. The rectal telangiectasia density (RTD) scoring system was developed for endoscopic assessment of CRP and was shown to have a good correlation with clinical symptomatic assessment [173]. In this scoring system, endoscopic appearance is evaluated based on telangiectasia density and vascular coalescence, and a score from 0 to 3 is assigned. Biopsies can be taken during the endoscopy to rule out other diseases associated with abnormal vascular lesions (such as inflammatory bowel disease), but are recommended only for select cases due to the potential of further bleeding, ulcerations and fistulae formation [17].

Management options for CRP range from non-endoscopic treatment with topical or oral medications, to endoscopic interventions such as dilation [174], bipolar electrocoagulation [175], argon plasma coagulation (APC) [176], cryotherapy [177], laser ablation [178] and radiofrequency

ablation (RFA) [19]. More severe and refractory cases of CRP may necessitate surgical interventions such as colostomy and proctectomy [179, 180]. Due to varying degrees of invasiveness and associated morbidity and mortality, it is essential to choose an effective treatment strategy, which may begin by employing the least invasive non-endoscopic approaches such as observation or medical therapy, and escalate in accord with patient's response to the interventions [18].

Optical Coherence Tomography (OCT) enables three-dimensional visualization of tissue microstructure and is recently commercialized as Volumetric Laser Endomicroscopy (VLE, NinePoint Medical, Bedford, MA) [111, 181]. Previous OCT studies have primarily focused on upper gastrointestinal pathologies, specifically Barrett's esophagus (BE) and have shown utility in endoscopic surveillance for detecting dysplastic lesions that are indiscernible under white light endoscopy (WLE) [43, 151]. We have recently developed an ultrahigh-speed OCT system which is more than 10 times faster than commercial instruments and can acquire volumetric images with higher transverse resolution and voxel density. This enabled visualization of depth-resolved *en face* mucosal and microvascular features (known as OCT Angiography, OCTA), in addition to standard cross-sectional OCT imaging [31].

This pilot study investigated OCTA for assessing subsurface tissue microvasculature around the dentate line and rectum of patients with normal rectum as well as CRP patients who were RFA-naïve or had previous RFA treatments. OCTA features of normal and abnormal rectal microvasculature were established. We have performed blinded reading of the OCTA features to demonstrate associations of abnormal rectal microvasculature with RFA-naïve patients in comparison with normal and RFA follow-up patients, as well as associations of abnormal rectal microvasculature with the endoscopic RTD scores. OCT imaging was performed by directly placing the micromotor catheter into the rectum of the patients without endoscopic guidance. Results showed that OCTA can play an important role in the clinical management of CRP and improve understanding of CRP pathophysiology.

The prototype ultrahigh-speed endoscopic OCT system and data acquisition system used in this work was developed by the team described in **Chapter II.** All human imaging experiments

were conducted at the VA hospital by the endoscopy team including Hsiang-Chieh Lee, Kaicheng Liang and Zhao Wang with the help of our clinical collaborators and the VA staff. The OCT and OCTA analysis methods were developed by the thesis author and Kaicheng Liang with insight and inputs from James Fujimoto and Hiroshi Mashimo. Kaicheng Liang performed blinded assessments of the OCTA images. Hsiang-Chieh Lee and Kaicheng Liang were involved in the majority of the discussions related to the studies described in this chapter.

4.2. Clinical overview of CRP

4.2.1. Pathophysiology

Overall structure and vasculature of mucosal and submucosal layers of the normal rectum are given **Figure 4.1**. Mucosal layer of the rectum consists of intestinal crypt structures with columnar-lined epithelium and interspersed lamina propria between the mucosal crypts. The superficial mucosal vasculature consists of a "honeycomb-like" capillary network, which on the *en face* plane looks like circular or hexagonal loops with vessel diameters < 15 µm. This capillary network is fed by ascending capillaries that reside within the mucosal layer that connect to the submucosal arterioles. Similarly, collecting venules exist within the mucosal layer that connect the superficial capillary network to the submucosal venules.

The exact pathophysiology of CRP is not well elucidated [22], while it is generally agreed that CRP is preceded by an acute phase that is associated with an acute inflammatory response to irradiation. However, some patients still develop CRP in the absence of a history of acute proctitis [182, 183]. The acute and chronic phases of RP have different clinical, symptomatic as well as histological manifestations [23, 184]. The primary site of injury in the rectum subsequent to irradiation is hypothesized to be the rectal epithelial cells and the endothelial cells. Damage to the rectal epithelial cells causes apoptosis and breakage of the crypt epithelial lining. This exposes underlying lamina propria to luminal bacteria causing an acute inflammatory response involving T-cells, macrophages, and neutrophils [23]. Inflammation causes further degradation of extracellular matrix and injury to mucosal and submucosal tissue. After radiation is ceased, intestinal crypt cells regenerate and the mucosal surface is repopulated, which subsides the acute inflammatory response.

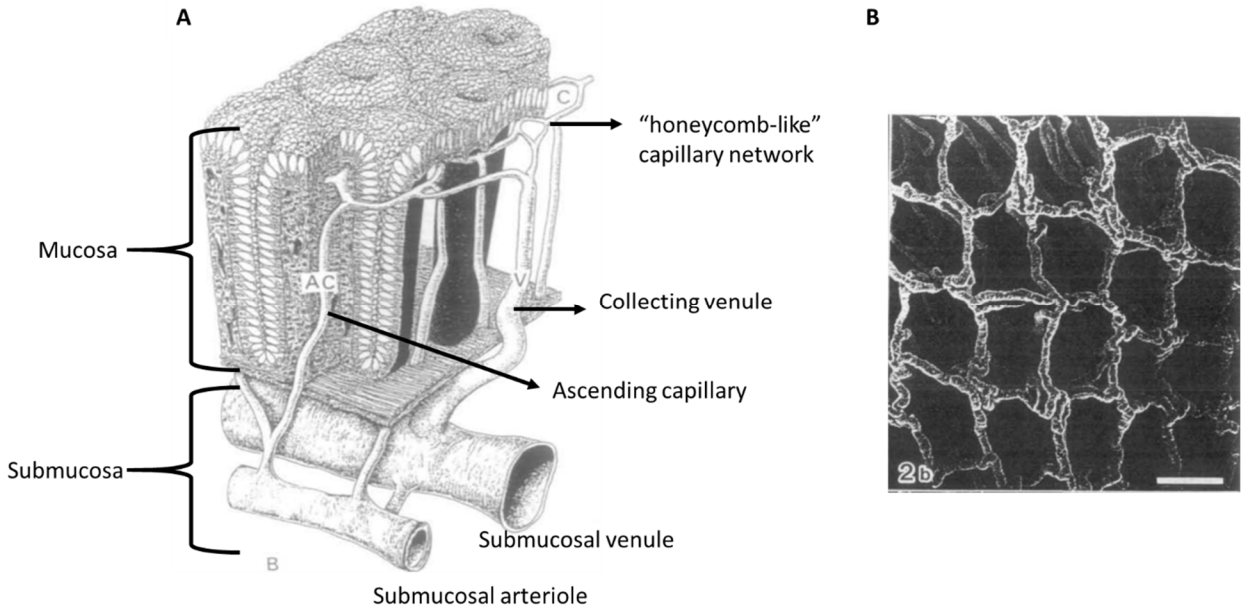

Figure 4.1. Overall structure and vasculature of the normal human rectum. **A,** graphical depiction of the mucosal and submucosal layers of the rectum. **B,** scanning electron microscopy image of honeycomb-like subsurface capillary networks as viewed from the *en face* plane. Scale bar is 100 µm. Images are modified from [185].

Chronic RP, on the other hand, is associated with angiogenic changes and a corresponding tissue remodeling. Different models have been hypothesized regarding the onset and progression of CRP. In the widely recognized model it is believed that CRP originates within the mucosal layer. The damage to the endothelial cells due to irradiation causes hypoxemia which degrades the extracellular matrix and basement membrane to provide space for angiogenesis. [186, 187]. Transcription factors such as hypoxia-inducible factor (HIF) are subsequently induced which promote angiogenic factors such as VEGF, angiogenin and FGF1, which then leads to angiogenesis in the mucosal layer. Neovascularization and dilatation of small vessels lead to telangiectasia formation in the mucosal layer and mucosal atrophy. Progressive ischemia and fibrosis develop in severely affected portions of the rectum which can cause stricture and fistulae formation, and in rare cases perforation. According to this model, inhibition of angiogenic factors such as angiogenin and FGF1 may be a valid approach to treat CRP [187].

In an alternative model it has been suggested that the angiogenic changes during CRP progression are initiated within the submucosal layer and the vascular changes in the mucosal

layer occur as secondary compensatory changes [188]. In this study, the researchers collected fresh surgical rectal specimens from 30 patients with CRP and 29 patients without CRP. The inclusion of surgical specimens allowed assessment of the entire rectal wall for immunohistochemistry arrays of angiogenesis-related factors. This was in contrast to most prior studies which evaluated rectal biopsy samples that only sampled the mucosal layer. This study found that rectal vessels have angiostatin deposits inside, where a damage to vascular endothelial cells cause the angiostatins to perfuse throughout the mucosal-submucosal layer. Angiogstatins suppress microvessel formation, causing vessel stenosis and fibrotic vascular sclerosis and decreasing microvessel density in the submucosal layer. It is then claimed that vascular changes and formation of telangiectasias in the mucosal layer are compensatory changes in response to the alteration of the vasculature in the submucosal layer. This study then went on to suggest that restoration of vascular functionality by promoting angiogenesis in the submucosal layer may help in reversing the effects of CRP.

It is worth noting that the two different models of CRP onset and progression discussed in this section lead to opposing recommendations in terms of inhibiting vs. promoting angiogenesis for preventing or treating CRP. In order to have a more optimal management, it might be also possible to use these two approaches synergistically, at different time points during the course of treatment. Nevertheless, it is critical to have a better understanding on the pathophysiology of the disease in order to develop improved treatment options. There are several factors that make it challenging to study the pathophysiology of CRP. First of all, due to progressive nature of this disease longitudinal studies are required, which is challenging to perform in humans. Currently, the only way to visually assess CRP is to perform sigmoidoscopy or colonoscopy, which is not practical to perform in a frequent fashion due to cost and time constraints. When colonoscopy is performed, it is not recommended to take biopsies due to the potential formation of ulcers and fistulas. Furthermore, as discussed previously biopsies only sample the mucosal layer and changes that occur in the submucosal layer cannot be studied. Animal CRP models, such as rat, have been developed but they have found to not reproduce the same pathophysiologic changes that occur in humans [187]. Consequently, currently there is no

method suitable to comprehensively study the pathophysiology and progression of CRP in human patients which motivates the need for a non-invasive approach to study this disease.

4.2.2. Prevalence and Diagnosis

It has been estimated that in 2016 more than 400,000 patients will be diagnosed with pelvic cancer (prostate, urinary bladder, uterus, rectum, cervix or anal cancer) in the US [9]. Furthermore, in 30-60% of these cases, radiation therapy will be used as part of the treatment modality, making this patients prone to develop RP [10, 11]. It is estimated that up to 75% of patients who receive pelvic radiation therapy have acute RP symptoms [13]. During this phase, patients exhibit symptoms such as diarrhea, cramping, increased bowel frequency and rectal discomfort, while rectal bleeding is not typically reported. In the majority of the cases, the acute symptoms cease within 6 months after cessation of the radiation therapy [14, 15].

Hematochezia (rectal bleeding) is the hallmark of the chronic stage of RP and is the most commonly occurring symptom [183]. Acute RP symptoms such as diarrhea, incontinence, rectal discomfort may be present as well [23]. The true incidence of CRP is not well known due to potential underdiagnoses of the disease [18, 189], but a prevalence on the order of 5-30% for patients who have received radiation therapy for pelvic cancer has been estimated [190-192]. A median time of 8 – 12 months have been reported as the onset of the clinical symptoms [182].

Patients who have received pelvic radiation therapy and exhibiting rectal bleeding are candidates for a CRP diagnosis. In a number of patients, rectal bleeding causes iron-deficiency anemia necessitating patients to have blood transfusions. The gold standard diagnostic test is direct rectal examination via sigmoidoscopy and colonoscopy, which assess the rectal mucosa for the presence of ulceration, friability and telangiectasias [16]. Rectal examination is essential to render a CRP diagnosis as rectal bleeding can also be caused by reasons unrelated to radiation [193]. Biopsy can be taken to rule out other conditions that may present similar symptoms such as inflammatory bowel disease, but as mentioned previously, it is generally not recommended due to the potential of fistulae formation [17]. Biopsies are also linked to initiation of chronic, poorly healing wounds [194]. After a CRP diagnosis is given, the severity of the disease can be

rated using a grading system, such as the previously discussed RTD scoring system, in order to assess progression and efficacy of subsequent interventions.

4.2.3. Clinical Management and Treatment

The overall treatment strategy for clinical management of CRP involves three tiers, with gradually escalating treatment invasiveness: 1) observation or medical therapy, 2) endoscopic therapy, 3) surgical therapy [18]. Initially, patients are observed or given medical treatments which can be administrated topically (via enema or colonoscopy), orally or intravenously. Medical agents used to treat CRP include sucralfate, formalin, hyperbaric oxygen, salicylic acid, short chain fatty acid, probiotics and antioxidants. Endoscopic therapies include cauterization and heater probe, argon plasma coagulation (APC), Nd:YAG and KTP laser ablation, radiofrequency ablation (RFA) and cryoablation. Purpose of endoscopic therapies is to control acute rectal bleeding and achieve hemostasis by coagulating bleeding vessels. Surgical treatment options include local excision, proctectomy and diverting ostomy. A schematic summarizing the currently recommended clinical management strategy for CRP is given in **Figure 4.2**.

In the following sections mechanism of some of the most commonly used medical and endoscopic treatment approaches of CRP will be outlined and a general overview about their use and effectiveness will be given. An in-depth review and discussion of these treatment options can be found in other references [18, 21-24]. Surgical treatment has severe complications and thus is reserved for refractory cases where medical and endoscopic treatment options fail, and is outside of the scope of this thesis.

Medical therapy: sucralfate

Sucralfate is an aluminum salt that adheres to mucosal cells and forms a protective coating on the inner surface of the rectum to mechanically protect it from the GUT microbiome. It is also thought to promote mucosal healing by increasing angiogenesis [195]. Studies that administrated sucralfate via topical application reported symptom improvement in 73% to 100% of the patients within a four to six weeks follow-up period, while a recurrence of symptoms also reported in 10% to 20% of patients during longer-term surveillance [196-198]. A study with oral administration,

on the other hand, did not show similar improvement of symptoms, when it was used in conjunction with APC treatment [199]. Given the relatively high number of studies indicating its effectiveness as well as high patient tolerance and good safety profile, sucralfate, by topical administration, has been suggested as one of the best available medical treatment options [22].

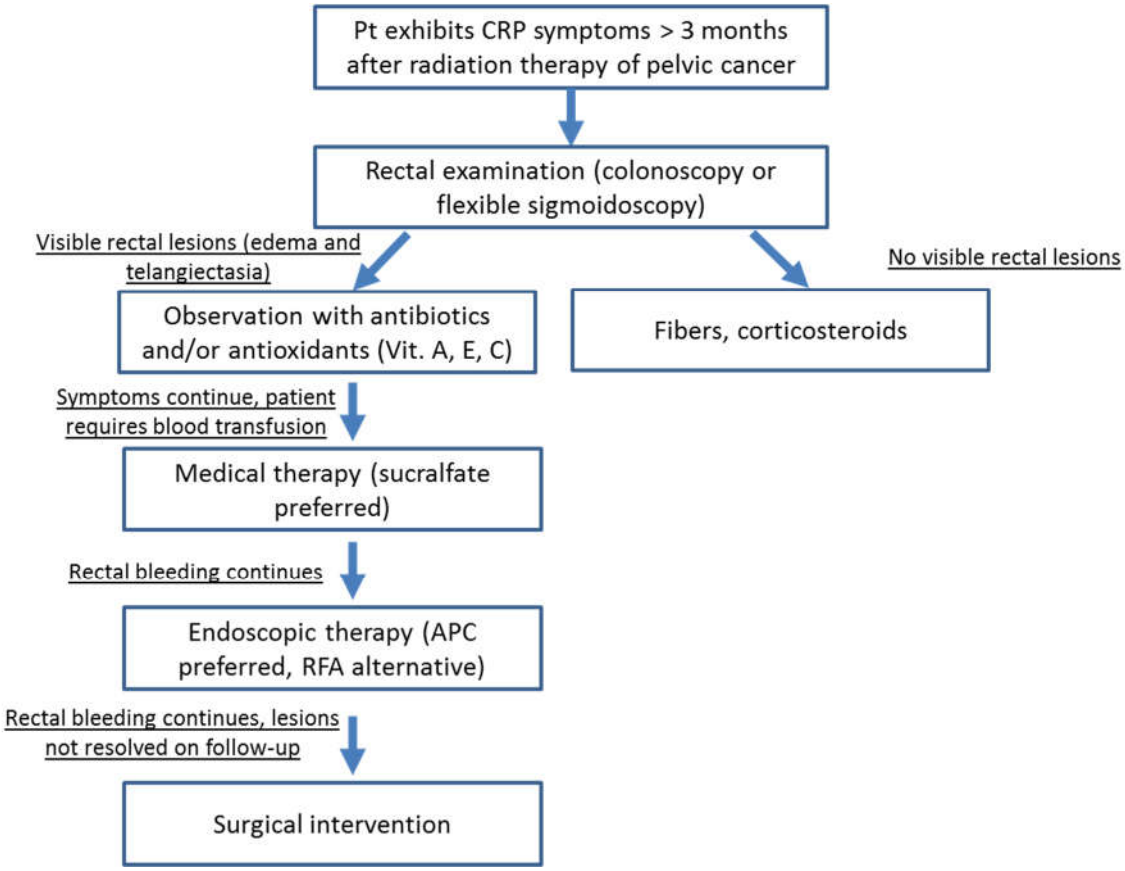

Figure 4.2. Optimal clinical management of CRP based on current clinical evidence and recommendations.

Medical therapy: formalin

Formalin has a direct effect on achieving hemostasis as it induces a chemical-mediated coagulation necrosis, immediately shutting the bleeding vessels [18, 200]. One study assessed the use of topical formalin is 24 patients refractory to sucralfate therapy [201]. Authors reported cessation of rectal bleeding in 19 out of 24 patients, one month after the treatment. 5 out of 16 and 1 out of 9 patients complained of rectal bleeding at 1 and 2 years, respectively. 19 out of 24 patients received only one course of treatment while the remaining 5 patients required a second

course. Although it has been shown to have benefit in treating CRP in other studies [18, 202], formalin causes severe pain/discomfort to patient has treatment-related morbidity as it causes the formation of strictures in as high as 18% of the patients [202]. Given its high complication rate formalin treatment is only recommended for patients refractory to endoscopic therapy options [18]. However, it is still worth noting that some recent studies suggested a better safety profile upon a more refined and controlled application of formalin [201].

Medical therapy: antibiotics

Antibiotics such as Metronidazole terminates the anaerobic and microaerophilic bacteria, which contribute to hypoxia, as well as have an immunomodulatory effects. Studies who compared the topical application of Metronidazole to observation (no treatment) or formalin treatment reported higher rates of symptomatic improvement [203, 204]. Other advantages of antibiotics are their wide availability and inexpensiveness. However, they also have frequent side effects which include rash, nausea and vomiting, as well as rare, but life threating reactions known as Stevens Johnson syndrome [18, 205].

Medical therapy: short chain fatty acids

Short chain fatty acids such as butyrate are preferred nutrient for mammalian colonocytes [206]. In the human rectum, these compounds are mainly produced by the probiotic bacterial colonies. Since the acute phase of RP is associated with epithelial cell depletion, enhancement of the short chain fatty acids may bolster healing and regeneration of the epithelial cells [18]. A prospective, randomized, controlled study with 20 patients, as well as another non-randomized study with 31 patients showed strong evidence for the use of butyrate to treat acute RP [207, 208]. It is worth noting that butyrate is currently the only medical treatment that has shown to have benefit in treating acute RP. However, other studies have shown no benefit in preventing the development of acute or chronic RP, as well as no benefit in treating CRP [209, 210].

Medical therapy: hyperbaric oxygen

Hyperbaric oxygen therapy involves inhalation of 100% oxygen inside a full body chamber with increased atmospheric pressure. Its mechanism in CRP is thought to be in promoting regrowth of

damaged endothelial cells and improving the activity of antioxidant enzymes [198, 211]. Although initial studies showed promising results in its use to treat CRP [212], a recent trial with 88 patients failed to show a reduction of rectal bleeding in CRP patients [213]. Furthermore, it has limited availability, it is expensive and requires a significant investment of patients' time (reduction of symptoms requires > 30 sessions) [21]. These factors limit the practicality of this treatment option.

Medical therapy: probiotics and antioxidants

Probiotics and antioxidants are proposed for treating CRP as they have antimicrobial properties and alleviate oxidative injury due to free radicals [214]. Moreover, they have the most favorable side effect profile amongst medical therapies used for CRP [18]. However, very few controlled trials exist regarding the effectiveness of these agents and show mixed results [215, 216].

Medical therapy: salicylic acid

Salicylic acid is the active metabolite of aspirin and acts as an antioxidant to reduce metabolic byproducts such as free radicals. They also have an anti-inflammatory role. However, it has been tested only relatively small studies so far which showed mixed results regarding its effectiveness, and currently is not used as a standalone medical therapy to treat CRP [217, 218].

Endoscopic therapy: cauterization

There are several types of cauterization probes, such as heater probe and bipolar electrocautery probes, which produce hemostasis by applying direct current or by contacting a heated tip to coagulate the target tissue. These probes have been found effective in controlling rectal bleeding in smaller-scale controlled studies [219, 220]. A 30 patient study assessed the effectiveness of bipolar electrocautery probe in comparison to APC and found them to be equally effective with only one treatment failure in each of the randomized arms [175]. However, significantly more complications rates were observed in the bipolar electrocautery arm in comparison to APC arm.

The advantage of the cauterization probes is they are inexpensive and readily available in an endoscopy setting. On the other hand, direct tissue contact is necessary for these probes and

control of treatment area and depth is not possible. This makes the use of these probes very susceptible to serious complications such as perforation. Furthermore, the probe tips need to be cleaned frequently which makes it to impractical to use them to treat a large area [221]. Therefore, they are typically used in settings to control active rectal bleeding where alternative endoscopic treatment modalities are not available.

Endoscopic therapy: argon plasma coagulation (APC)

APC is a non-contact coagulation method which uses a jet of sprayed argon gas that is ionized into plasma by high voltage sparks. The ionized plasma then seeks ground in the nearest tissue depositing thermal energy [18]. APC is currently the most commonly used endoscopic treatment modality in CRP, and around 80% of studies with endoscopic treatment are conducted using APC [21]. Furthermore, extensive animal studies have been conducted in determining optimal energy and dosing setting to achieve complete ablation of the superficial telangiectasias without affecting the deeper submucosal layers [222]. Relatively larger scale studies have been conducted to prove the effectiveness of APC in controlling rectal bleeding in CRP. In a 65 patient study, APC was successful in 98.5% of the patients after a median of two sessions [222]. A meta-analysis evaluated studies where APC used as the standalone treatment modality with a total of 416 patients [21]. They reported improvement or complete resolution of symptoms in 406 (98%) of the patients over a 2 – 60 months follow-up period.

APC is proposed as an alternative to contact based cauterization methods such as electrocautery to have a better control of the ablation depth. However, it still suffers from the relatively high rate of complications such as the formation of strictures, rectal ulcers, and perforations. Reports suggested complications rates between 5 to 20% [223], while some studies reported ulcer formation in more than >50% of patients [224]. However, these ulcers were asymptomatic and the majority were resolved without 141 days without any intervention. Therefore, given its strong track record APC is currently the preferred endoscopic intervention for CRP, however, the need for comparative studies to further assess its effectiveness has been acknowledged [21]. Moreover, it suffers from the limitation of being a very focal treatment

modality, in which potential for overtreatment especially in areas with densely populated telangiectasias is high.

Endoscopic therapy: Nd:YAG and KTP laser ablation

Nd:YAG and KTP lasers produces coagulation by performing ablation with 1060 nm and 532 nm wavelengths, respectively. A single center study assessed Nd:YAG laser therapy with 47 patients who had failed medical therapy to control rectal bleeding [225]. Within 6 months of treatment number of patients exhibiting rectal bleeding reduced to 11%. KTP laser therapy was assessed in a 23 patient study and a statistically significant reduction of rectal bleeding was observed after a median of 2 treatment sessions [178].

The advantage of laser ablation is that it does not necessitate contact with the target tissue, as opposed to most of the alternative endoscopic therapies. However, control of treatment area and depth is challenging similar to the cauterization probes and high rates of complications are observed including transmural necrosis, fibrosis, stricture, and rectovaginal fistula [23]. The wavelength of the KTP laser (532 nm) has a more favorable depth control profile as the hemoglobin within the blood has peak absorption at this wavelength, which limits the ablation to superficial highly vascularized layers. Moreover, laser ablation systems tend to be expensive and are not widely available, limiting their widespread use in the CRP setting.

Endoscopic therapy: radiofrequency ablation (RFA)

RFA uses tightly spaced bipolar electrodes that make direct contact with the tissue to produce a controlled and superficial ablation depth. RFA has been extensively used to treat dysplastic Barrett's esophagus and became the gold standard treatment modality due to its superiority over APC and other alternative endoscopic treatment modalities in terms of its effectiveness and low rate of complications such as stricture formation [128, 226-229].

The use of RFA in CRP was initially proposed by our group and OCT was used to monitor the treatment and follow-up in a case series of 3 patients [20]. This study has shown that RFA produced hemostasis in all patients that is conserved over a 19 months follow-up. Furthermore, using the depth-resolved OCT images a 1-2 cm squamous epithelium growth at the dentate line

over the previous telangiectatic area was observed. The largest RFA study to date included 39 patients, where all patients had complete resolution of rectal bleeding over a mean follow-up period of 28 months (with a mean number of 1.49 RFA sessions per patient) [19]. Another study with 17 patients reported an increase in blood hemoglobin levels in all patients treated with RFA after 6 months of treatment and symptomatic improvement in 16 of the patients [95]. 9 out of 13 patients who were blood transfusion dependent weaned off transfusions after treatment. The only observed complication was the formation of ulcers in 2 patients.

Although small in numbers, RFA studies so far showed high efficacy for RFA in controlling rectal bleeding with favorable safety profile. Formation of strictures and ulcers were rare. Therefore, RFA may be a promising alternative to APC as an endoscopic therapy for CRP. However, controlled comparative studies are required to assess the relative effectiveness of both treatment modalities.

Endoscopic therapy: cryoablation

Cryoablation uses liquid nitrogen to freeze the tissues below -40°C to cause irreversible cellular damage to the endothelium by producing ischemic necrosis. It is increasingly used in eradication malignant lesions in upper GI diseases such as dysplastic Barrett's esophagus [230] and OCT studies have found that it produces almost twice treatment depth in comparison to RFA [231]. Only few studies exist yet regarding its use in CRP, but they show promising results in terms of controlling rectal bleeding with relatively few complications [232].

4.3. Non-endoscopic OCT assessment of CRP

4.3.1. Materials and methods

Study setting and patient requirement

This study was conducted at the Veteran Affairs Boston Healthcare System (VABHS). A total of 8 patients referred for or undergoing endoscopic treatment with RFA for CRP were enrolled in the study between October 2013 and November 2016. OCT imaging was performed during scheduled colonoscopy visits immediately before the colonoscopy procedure. Patients were also imaged at follow-up visits within the study period, yielding a total of 13 OCT/colonoscopy visits. Standard

rectal examination with the colonoscope was conducted subsequent to OCT imaging. RFA was performed in patients with active rectal bleeding and/or based on endoscopic indication. A focal ablation catheter (Barrx 90, Medtronic, MN) attached to the colonoscope (CF-HQ190L or CF-2T160, Olympus, Japan) was typically used in the six o'clock and retroflexed position, as previously described [19]. In some cases requiring RFA, OCT imaging was also performed immediately after treatment. Endoscopic RTD scores were assigned by the study physician (H.M.), who was blinded to the OCT images and OCTA CRP scores. Patient charts were reviewed to obtain information about the rectal bleeding status and hemoglobin concentrations before and after the colonoscopy visits.

Ultrahigh-speed OCT system

OCT imaging was performed with a prototype ultrahigh-speed OCT system operating at an axial scan repetition rate of 600 kHz and a micromotor catheter imaging at 400 frames per second [31] (More technical details of the clinical ultrahigh-speed OCT system and micromotor catheter were provided in **Chapter II**). OCT and OCTA images from the distal and proximal anterior side of the dentate line were acquired by directly placing the micromotor catheter into the rectum and anal canal of the patients without endoscopic guidance, but with real-time OCT imaging guidance. Each OCT/OCTA dataset covered an area of 10 mm x 16 mm (circumferential x longitudinal) and was acquired in 8 seconds, as previously described. Multiple acquisitions were performed by varying micromotor catheter placement around the dentate line, guided by real-time OCT imaging, to ensure that the squamocolumnar junction (SCJ) and a longitudinal margin of ±2 cm were captured in the images.

Endoscopic grading of CRP severity and validation of OCTA assessment

Endoscopic RTD scores were assigned by the study physician (H.M.) during or shortly after the colonoscopy procedure, who was blinded to the OCTA assessment. All OCT and OCTA images were reviewed by a researcher experienced in OCT and OCTA interpretation (O.O.A.), who was not blinded to the clinical status of the patients. Rectal mucosal and submucosal microvasculature was assessed in normal and CRP patients in conjunction with standard histology references on rectal vasculature to determine normal and abnormal microvascular features. All

OCTA images were then read by another researcher experienced in OCT and OCTA interpretation (K.C.L.) to assess the occurrence of abnormal OCTA features in the mucosal and submucosal layers. Reader assessed depth-resolved *en face* OCTA images in conjunction with the cross-sectional and *en face* OCT images in order to visualize the structure of and delineate between the mucosal and submucosal layers. The reader was blinded to the clinical status and RTD scores of the patients.

Normal and abnormal rectal OCTA features

Examples of OCT and OCTA images of rectal microstructural and microvascular architecture of normal and CRP patients are given in **Figure 4.3 – Figure 4.5**. Based on a review of the images the following OCTA features were defined as normal and abnormal rectal microvasculature in the mucosal and submucosal layers (**Figure 4.6**): Normal rectal mucosal microvasculature consisted of a honeycomb-like microvascular pattern corresponding to subsurface capillary network described in the literature [185]. Abnormal rectal mucosal microvasculature had distortions to the honeycomb-like microvascular pattern, and had ectatic and tortuous microvasculature. Normal rectal submucosal microvasculature consisted of arterioles and venules with diameters < 200 μm, in addition to the projection of the mucosal microvasculature. Abnormal rectal submucosal microvasculature had unusually high-caliber arterioles and venules (diameters > 200 μm).

Statistical analysis

MATLAB (Mathworks, Inc, MA) was used to perform all statistical calculations. Quantitative metrics were represented as mean ± standard deviation. A two-tailed t-test was used to compare the quantitative metrics between the RFA-naïve and RFA follow-up patients. A p-value of < 0.05 was considered statistically significant.

4.3.2. Results

Patient demographics and baseline clinical status

Patient demographics were summarized in **Table 4.1**. The baseline RFA follow-up patients had a mean of 2 RFA sessions at the time of initial OCT imaging (range: 1 – 3). Baseline RTD scores were

significantly different between the RFA-naïve and the baseline RFA follow-up patients (mean score: 2 ± 0.7 vs. 0.3 ± 0.6, respectively, p = 0.007). While the mean hemoglobin concentrations were higher for the baseline RFA follow-up patients compared to RFA-naïve patients, the difference did not reach statistical significance (mean: 13.7 ± 1.8 g/dL vs. 12 ± 0.8 g/dL, respectively, p = 0.23). 4 out of 5 (80%) RFA-naïve patients presented with rectal bleeding at the baseline visit, while none of the baseline RFA follow-up patients exhibited rectal bleeding.

Patient demographics (N = 10)			
Age, mean (range)		73 (67 – 85)	
Sex, male, no. (%)		10 (100)	
Race, white, no. (%)		10 (100)	
CRP Patients (N = 8)			
Prior treatment	RFA-naïve, N = 5	RFA follow-up, N = 3	p - value
Prior RFA sessions, mean (range)	0 (0)	2 (1-3)	
Baseline RTD score, mean (range)	2 (1-3)	0.3 (0-1)	0.007
Baseline Hgb, g/dL, mean ± std	13.7 ± 1.8	12 ± 0.8	0.23

Hgb: Hemoglobin concentration, std: standard deviation.

Table 4.1 Patient Demographics

RFA treatment and response

5 out of 5 (100%) RFA-naïve patients and 1 out of 3 (33%) RFA follow-up patients received RFA based on active rectal bleeding and/or endoscopic indication at the baseline visit. At the end of the study period, rectal bleeding had resolved in 4 out of 4 RFA-naïve patients who initially had rectal bleeding. For the patients treated with RFA at baseline visit (N = 6), a paired comparison showed a significant increase in the hemoglobin concentrations at the baseline visit and at the end of the study period (mean: 13.3 ± 1.9 g/dL vs. 14.3 ± 1.4 g/dL, respectively, p = 0.03).

Rectal OCT and OCTA features of normal and CRP patients

On average, for each patient, OCT imaging was completed in less than 10 minutes (mean: 8 ± 4 minutes, range: 4 – 18 minutes). OCT and OCTA images enabled depth-resolved visualization of rectal microstructural and microvascular architecture of patients with normal rectum (**Figure 4.3**). *En face* OCT images showed regular circular mucosal patterns characteristics of the normal

rectum (**Figure 4.3A** and **Figure 4.3B**). Images at superficial depths showed the outline of the mucosal crypt architecture **(Figure 4.3A)** whereas images at deeper depths delineated the mucosal architecture and patterns in greater detail and contrast **(Figure 4.3B)**. *En face* OCTA images at superficial depths showed regular honeycomb-like microvascular pattern corresponding to the subsurface capillary network in the mucosal layer **(Figure 4.3C)** [185]. *En face* OCTA images at deeper depths showed rectal microvasculature corresponding to arterioles and venules in the submucosal layer, in addition to the projection of the mucosal microvasculature **(Figure 4.3D)**. The submucosal arterioles and venules had a diameter typically less than < 200 µm. Cross-sectional OCT image showed the regular columnar architecture of normal rectum and allowed determination of mucosal and submucosal layer depths **(Figure 4.3E)** [233].

OCT and OCTA images enabled depth-resolved visualization of rectal microstructural and microvascular architecture of patients with CRP (**Figure 4.4** and **Figure 4.5**). OCT, OCTA and endoscopy images over the dentate line of an RFA-naïve CRP patient were shown in **Figure 4.4**. *En face* OCT images showed regular circular mucosal patterns on the rectal side with no apparent abnormalities (**Figure 4.4A**). *En face* OCTA images at superficial depths showed distortions on the honeycomb-like microvascular pattern with ectatic and tortuous microvasculature in the mucosal layer **(Figure 4.4C)**. *En face* OCTA images at deeper depths showed unusually high-caliber vessels (diameters > 200 µm) suggesting the presence of abnormal arterioles and venules in the submucosal layer **(Figure 4.4D)**. Rectal examination confirmed the OCTA findings and the corresponding endoscopy image showed ulcerations, and edematous and non-confluent telangiectasias **(Figure 4.4B)**.

OCT, OCTA and endoscopy images over the dentate line of an RFA follow-up patient were shown in **Figure 4.5**.*En face* OCT images showed regular circular mucosal patterns on the rectal side with no apparent abnormalities (**Figure 4.5A**). *En face* OCTA images at superficial depths showed a regular honeycomb-like microvascular pattern in the mucosal layer suggesting normalization of rectal mucosal microvasculature following RFA treatment **(Figure 4.5C)**. *En face* OCTA images at deeper depths showed unusually high-caliber vessels suggesting presence of

persistent abnormal arterioles and venules in the submucosal layer **(Figure 4.5D)**. Corresponding endoscopy image showed healing of the rectal mucosa with some residual telangiectatic areas **(Figure 4.5B)**.

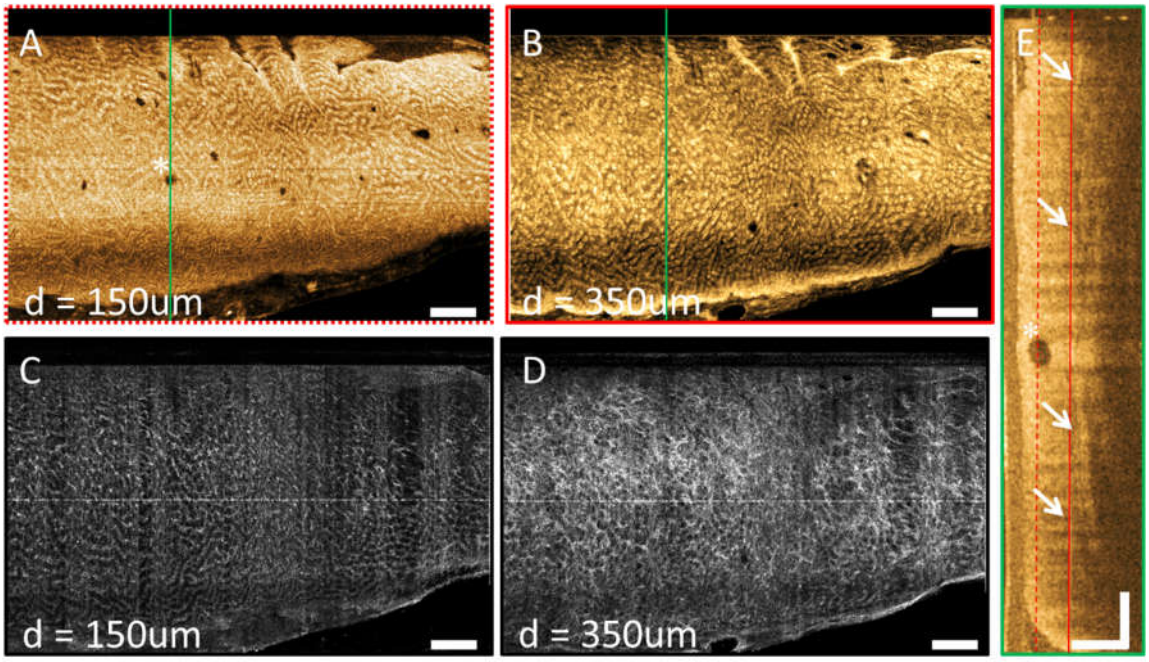

Figure 4.3. Depth-resolved *en face* OCT and OCTA images and cross-sectional OCT image over the rectum of a patient with the normal rectum. **A**, *En face* OCT at 150 µm depth and **B**, *en face* OCT at 350 µm showing regular circular mucosal patterns characteristics of the normal rectum. **C**, *En face* OCTA image at 150 µm showing regular honeycomb-like microvascular pattern corresponding to the subsurface capillary network in the mucosal layer. **D**, *En face* OCTA image at 350 µm showing microvasculature corresponding to arterioles and venules in the submucosal layer, in addition to the projection of the mucosal microvasculature. **E**, cross-sectional OCT image from the solid green lines in **A** and **B**, showing the regular columnar architecture of normal rectum. Submucosal layer can be identified by the vertical layers traversing across the image (arrows). A dilated mucosal gland can be observed in both *en face* and cross-sectional image (asterisks). Dashed and solid lines indicate 150 µm and 350 µm depth levels, respectively. Scale bars are 1 mm in A – D, 500 µm in E.

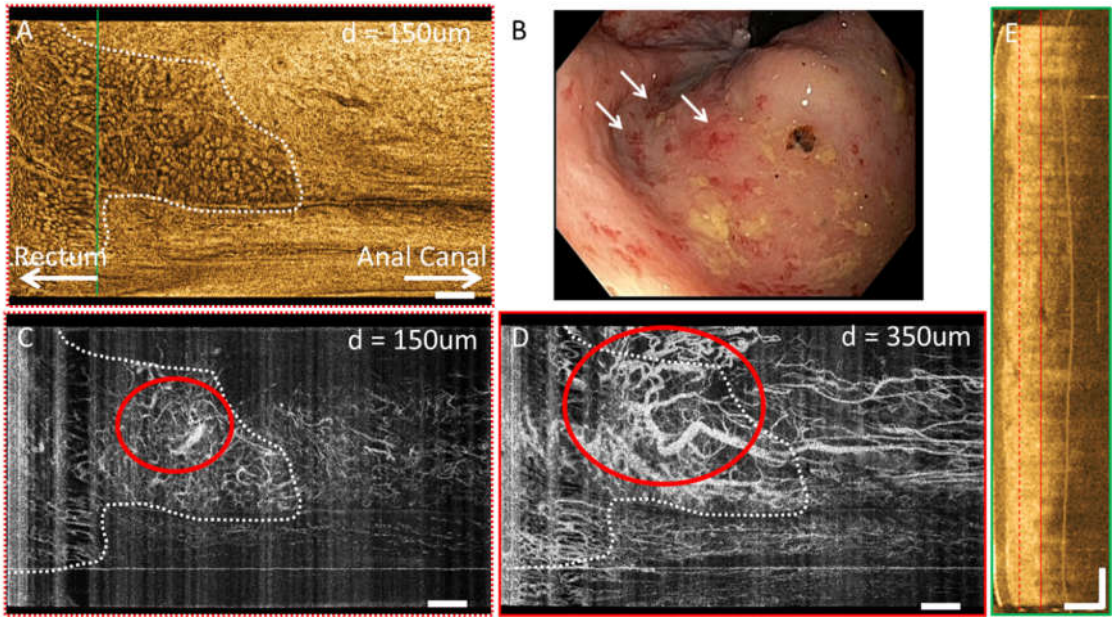

Figure 4.4. Depth-resolved *en face* OCT and OCTA images, cross-sectional OCT image, and corresponding endoscopy image over the dentate line of an RFA-naïve CRP patient. **A,** *En face* OCT at 150 µm depth showing regular circular mucosal patterns on the rectal side and squamous epithelium with a smooth appearance on the anal canal side. **B,** shows the corresponding endoscopy image of the dentate line showing ulcerations, and edematous and non-confluent telangiectasias (RTD = 2). White arrows highlight areas of telangiectasias on the rectal side. **C,** *En face* OCTA image at 150 µm showing distortions to the honeycomb-like microvascular pattern, and ectatic and tortuous vasculature (red oval) in the mucosal layer. **D,** *En face* OCTA image at 350 µm showing unusually high-caliber abnormal vessels (red oval) suggesting the presence of abnormal arterioles and venules in the submucosal layer. **E,** cross-sectional OCT image from the solid green line in **A** showing mucosal and submucosal layers. Dashed and solid lines indicate 150 µm and 350 µm depth levels, respectively. Scale bars are 1 mm in **A – D**, 500 µm in **E**.

OCTA reading results

Blinded OCTA reading results were given in **Table 4.2**. The occurrence of abnormal rectal OCTA features was higher in RFA-naïve patients compared with normal or RFA follow-up patients. 0 out of 2 (0%) normal, 3 out of 5 (60%) RFA-naïve and 0 out of 8 (0%) RFA follow-up patients had abnormal rectal mucosal microvasculature. 1 out of 2 (50%) normal, 5 out of 5 (100%) RFA-naïve and 2 out of 8 (13%) RFA follow-up patients had abnormal rectal submucosal microvasculature.

OCTA reading results for the CRP patients were also stratified according to endoscopic RTD scores (**Table 4.3**). Occurrence of abnormal rectal OCTA features increased with increasing RTD scores, suggesting a correlation of abnormal rectal microvasculature, as observed with OCTA,

with the RTD scores. 0 out of 5 (0%) patients with RTD = 0, 0 out of 3 (0%) patients with RTD = 1, 2 out of 4 (50%) patients with RTD = 2 and 1 out of 1 (100%) patient with RTD = 3 had abnormal mucosal microvasculature. 1 out of 5 (20%) patients with RTD = 0, 2 out of 3 (66%) patients with RTD = 1, 3 out of 4 (75%) patients with RTD = 2 and 1 out of 1 (100%) patient with RTD = 3 had abnormal submucosal microvasculature.

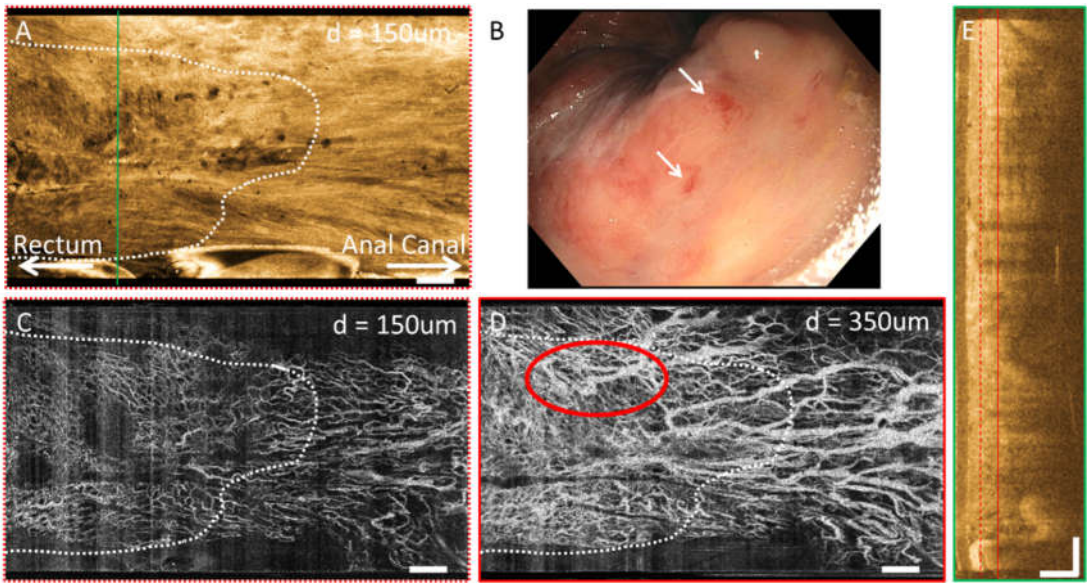

Figure 4.5. Depth-resolved *en face* OCT and OCTA images, cross-sectional OCT image, and corresponding endoscopy image over the dentate line of an RFA follow-up patient. **A,** *En face* OCT at 150 µm depth showing regular circular mucosal patterns on the rectal side and squamous epithelium with a smooth appearance on the anal canal side. **B,** shows the corresponding endoscopy image of the dentate line showing some residual telangiectatic areas (arrows, RTD = 1). **C,** *En face* OCTA image at 150 µm showing a regular honeycomb-like microvascular pattern. **D,** *En face* OCTA image at 350 µm showing unusually high-caliber abnormal vessels (red oval) suggesting the presence of abnormal arterioles and venules in the submucosal layer. **E,** cross-sectional OCT image from the solid green line in **A** showing mucosal and submucosal layers. Dashed and solid lines indicate 150 µm and 350 µm depth levels, respectively. Scale bars are 1 mm in **A – D**, 500 µm in **E**.

Category	Total Imaging Sessions	Endoscopy	*En face* OCTA	
		RTD ± std	Abnormal mucosal microvasculature, no (%)	Abnormal submucosal microvasculature, no (%)
Normal	2	Not assessed	0 (0%)	1 (50%)
RFA-naïve	5	2.0 ± 0.7	3 (60%)	5 (100%)
RFA follow-up	8	0.5 ± 0.8	0 (0%)	2 (13%)

Table 4.2 Endoscopic RTD scores and occurrence of abnormal rectal mucosal and submucosal microvasculature based on *en face* OCTA images

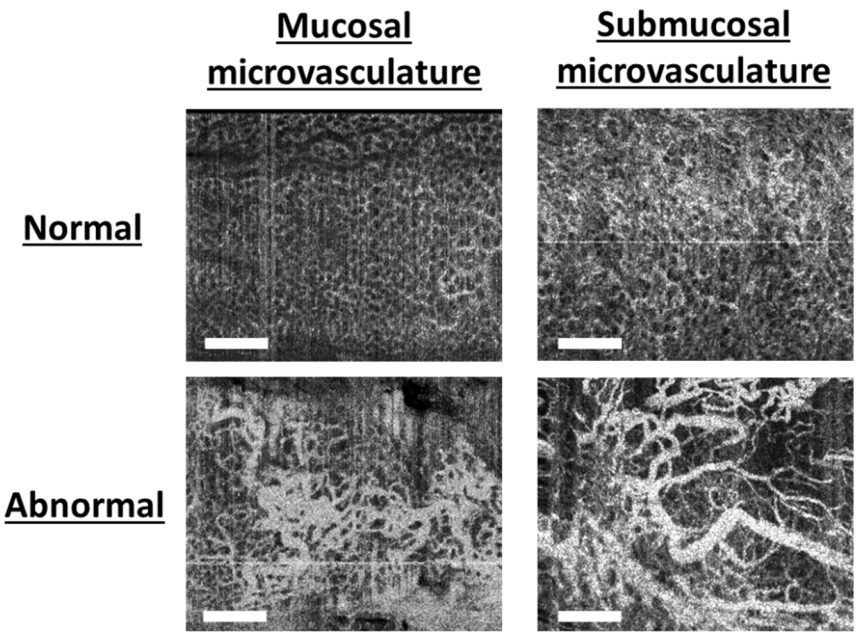

Figure 4.6. Summary of normal and abnormal microvasculature in the mucosal and submucosal layers of the rectum. Normal rectal microvasculature of the mucosal layer of consists of a honeycomb-like microvascular pattern corresponding to the subsurface capillary network. Abnormal rectal microvasculature of the mucosal layer has distortions to the honeycomb-like microvascular pattern, and ectatic and tortuous vasculature. Normal rectal microvasculature of the submucosal layer consists of arterioles and venules with a caliber < 200 μm, in addition to the projection of the mucosal microvasculature. Abnormal rectal microvasculature of the submucosal layer has unusually high-caliber arterioles and venules (> 200 μm). Scale bars are 1 mm.

RTD	Total Imaging Sessions	*En face* OCTA: Abnormal mucosal microvasculature, no (%)	*En face* OCTA: Abnormal submucosal microvasculature, no (%)
0	5	0 (0%)	1 (20%)
1	3	0 (0%)	2 (66%)
2	4	2 (50%)	3 (75%)
3	1	1 (100%)	1 (100%)

Table 4.3 Occurrence of abnormal rectal mucosal and submucosal microvasculature in the CRP patients based on *en face* OCTA images, stratified according to endoscopic RTD scores

4.3.3. Discussion

Given the abundance of treatment options for CRP, with differing reports regarding treatment success and complication rates, there is a need for comparative studies to evaluate different treatments and define the optimal treatment strategy [18]. However, in current practice, it is inherently hard to conduct such studies due to variations in assessing clinical symptoms and disease severity, and challenges associated with endoscopic procedures and pathological evaluation over the long-term patient follow-up [24]. Presently, electrocoagulation and APC are the most widely used endoscopic treatment modalities for CRP [21]. Although these treatments control rectal bleeding in the majority of patients [220, 234], the depth of ablation is poorly controlled. Therefore, complications such as strictures, ulcers, fistulas and perforations can occur in as high as 50% percent of treated patients [175, 223]. RFA has become the clinical standard for eradicating BE related dysplasia in upper GI [235] and is an emerging alternative treatment modality for CRP [19, 20, 95]. The tightly spaced bipolar electrode geometry of the commercial RFA system restricts the ablation to shallower depths, which can be an advantage for CRP over treatment modalities such as electrocoagulation and APC [24]. In the largest RFA study to date, 39 patients were treated with RFA and rectal bleeding was stopped completely in all patients during the mean follow-up of 28 months (with a mean number of 1.49 RFA sessions per patient) [19]. Furthermore, strictures, ulcers, fistulas and perforations were not observed in any of the patients, suggesting high safety profile for this treatment modality. This current study also

showed resolution of rectal bleeding and increase in hemoglobin concentrations for patients who received RFA during the study period, adding to the body of knowledge on the effectiveness of RFA. However, larger, prospective, multi-center studies are still needed to confirm RFA as an effective and safe endoscopic treatment approach for CRP.

So far, OCT studies have been primarily focused on esophageal diseases, specifically on BE and its related dysplasia. Traditionally, OCT imaging speeds were limited and it was only possible to generate cross-sectional images compared to endoscopic forward-viewing (i.e. *en face*) images. With advances in OCT technology, our group achieved imaging speeds more than 10 times faster than the present commercially-available technology [31, 166]. This enabled depth-resolved *en face* images of tissue microstructure as well as microvasculature (with OCTA) to complement the traditional cross-sectional images. To our knowledge, this is the first study demonstrating the clinical utility of this next-generation OCT technology in a lower gastrointestinal tract pathology.

The depth-resolved imaging capability of OCT can make this imaging modality an attractive tool for assessment of disease severity as well as the efficacy of endoscopic treatment modalities such as RFA, where it is crucial to assess the treatment area both laterally as well as in depth. A previous study on BE patients showed that the presence of residual BE glands and the thickness of BE epithelium in the post-RFA OCT images predicts RFA treatment response [236]. The study showed that epithelial thickness greater than 333 µm, as measured by OCT prior to RFA, predicts the presence of residual BE on follow-up visit with a sensitivity and specificity of 92.3% and 85%, respectively. A recent study on *ex vivo* swine tissue showed that OCT can monitor RFA in real time (imaging through the ablation catheter) and quantitatively assess the treatment depth based on scattering changes of the epithelial layer during ablation[237]. Another study showed that OCT can allow assessment of anal canal in CRP patients undergoing RFA [20]. Study showed re-epithelialization by neosquamous mucosa over areas of prior hemorrhage, potentially forming a protective layer to preventing rebleed [20]. This current study demonstrated depth-resolved *en face* OCT and OCTA images of the rectum from normal and CRP patients. The study further showed that rectal microvasculature in the mucosal and submucosal layers can be independently

assessed and established OCTA features of normal and abnormal rectal microvasculature. Blinded reading of the OCTA features demonstrated association of abnormal rectal microvasculature, as observed with OCTA, with RFA-naïve patients in comparison with normal and RFA follow-up patients (**Table 4.2**), as well as a correlation of abnormal rectal microvasculature, as observed with OCTA, with the endoscopic RTD scores (**Table 4.3**). Altogether, these studies demonstrate the uniquely suited utility of depth-resolved OCT and OCTA imaging in assessing disease severity of CRP as well as the efficacy of endoscopic treatment modalities such as RFA.

The OCTA depth information can also be used to choose optimal endoscopic treatment modality. For instance, the depth of abnormal microvasculature can be extracted from the OCTA datasets, and in lesions where the abnormal microvasculature is deeper than a pre-determined threshold then a treatment modality that results in deeper treatment depth, such as APC, could be chosen over a treatment modality that results in more superficial treatment depth, such as RFA. Moreover, the energy/dose of the APC/RFA treatment can be tailored based on OCTA depth information.

While it is generally acknowledged that CRP is associated with angiogenic changes and a corresponding tissue remodeling, the pathophysiology of CRP with regards to its onset and progression is not well elucidated [22]. In a widely recognized model, it is believed that CRP originates within the mucosal layer, where hypoxemia caused by irradiation damages endothelial cells inducing transcription factors such as hypoxia-inducible factor (HIF) that promote angiogenic factors such as VEGF, angiogenin and FGF1 [186, 187]. This leads to neovascularization and dilatation of small vessels, and telangiectasia formation in the mucosal layer. According to this model, inhibition of angiogenic factors such as angiogenin and FGF1 may be a valid approach to treat CRP [187].

A recent study, on the other hand, suggested a strong role of submucosal microvascular changes leading to onset and progression of CRP [188]. Researchers collected fresh surgical rectal specimens from 30 patients with CRP and 29 patients without CRP that allowed assessment of the entire rectal wall for immunohistochemistry arrays of angiogenic factors. This was in contrast

to most prior studies which evaluated rectal biopsy samples that only sampled the mucosal layer. This study found that angiostatin deposits that reside within rectal vessels are perfused throughout the mucosal-submucosal layer upon radiation damage of the endothelial cells. Angiostatins subsequently suppress microvessel formation, causing vessel stenosis and fibrotic vascular sclerosis, decreasing microvessel density in the submucosal layer[188]. The vascular changes and formation of telangiectasias in the mucosal layer are hypothesized to be compensatory changes in response to the alteration of microvasculature in the submucosal layer. This study then suggested that restoration of vascular functionality by promoting angiogenesis in the submucosal layer may help in reversing the effects of CRP.

The ability of OCTA to assess rectal microvasculature in the mucosal and submucosal layers independently may have implications in studying the pathophysiology of CRP as well as developing effective prevention and treatment approaches. OCTA allows longitudinal studies of rectal microvasculature *in situ* without injected dyes or disrupting tissue integrity as opposed to taking excisional biopsies or performing surgical resection. The results of this study demonstrated that only 3 out of 5 (60%) RFA-naïve patients had abnormal rectal mucosal microvasculature while 5 out of 5 (100%) RFA-naïve patients had abnormal rectal submucosal microvasculature. This may support the aforementioned recent hypothesis that CRP may originate in the submucosal layer and subsequently progress to the mucosal layer[188]. Furthermore, 0 out of 8 (0%) RFA follow-up patient had abnormal rectal mucosal microvasculature while 2 out of 8 (13%) RFA follow-up patients still had abnormal rectal submucosal microvasculature. This may indicate that RFA may not be effective for some of the patients to coagulate the abnormal vessels in the submucosal layer. Treatment approaches such as CSA or APC may be more appropriate in such patients to target deeper treatment.

Typically, an endoscope is required for introducing the micromotor catheter within the GI tract through its accessory channels. This limitation made it hard to argue for the utility of OCT as a replacement for endoscopic assessment. Recently, a capsule-based micromotor catheter was demonstrated for upper GI imaging, which enabled organ-level OCT imaging without the need of an endoscope [238]. In this current study, we have also performed OCT imaging

independent of the endoscope by directly placing the micromotor catheter into the dentate line and rectum of the patients. As OCTA imaging has high sensitivity and does not require administration of injected dyes, it can be used to assess areas with abnormal vascular lesions and active bleeding. OCT imaging was fast and it took an average of 8 minutes to image each patient. These advantages can make OCT a viable tool for rapid, non-endoscopic assessment of CRP, treatment follow-up, choice of endoscopic treatment modality and optimizing treatment dose/frequency.

The small diameter of the micromotor catheter used in this study restricted the field of view of a single acquisition to a 10 mm x 16 mm area. Although multiple acquisitions were performed to increase the imaging coverage in the longitudinal direction, only anterior side of the rectal wall was captured in the circumferential direction. Since CRP usually presents itself over the circumference, this was not an important issue in terms of assessing the correlation between the OCTA images and endoscopic appearance. However, it is essential to image the whole circumference of the rectum if OCT is to be used as a standalone imaging modality to assess CRP. We have recently demonstrated an OCT capsule that is compatible with the ultrahigh-speed OCT system used in this study, that enabled circumferential imaging over 40 mm x 240 mm area in 20 seconds [37]. Although only cross-sectional and structural *en face* imaging have been demonstrated so far, with further engineering it may be possible to perform OCTA with this capsule device. Furthermore, we have recently reported high-speed OCT and OCTA imaging in living swine with a balloon-based OCT catheter that performed circumferential imaging over 50 mm x 26 mm area in 18 seconds [35]. It is conceivable to translate these technologies to lower GI or develop a more optimal OCT imaging catheter to increase the coverage of the OCT imaging [239]. However, this requires further validation as anatomical constraints, such as dilation immediately adjacent to the anal sphincter, may make it challenging to achieve circumferential contact with OCT catheters. As an example, if might be challenging to image areas near the dentate line with a balloon-based OCT catheter due to difficulties in placing the distal balloon portion of the catheter onto the tissue near that region.

It should be noted that OCTA images are generated by detecting the OCT signal intensity changes caused by the moving erythrocytes within the microvascular network. Excessive pressure exerted by the OCT catheter on the bowel wall may impair vascular flow and affect the visualization of these microvessel [164, 240]. Precise control of pressure exerted by the catheter remains difficult, and repeat acquisitions were performed over the same regions while applying minimal pressure but maintaining contact with the tissue. During analysis, we discarded the datasets that showed lack of microvasculature over all imaging depths and the datasets that showed effacement of mucosal patterns (on the rectal side) as a surrogate marker of this excessive pressure. Future studies would benefit from a better control of the applied catheter pressure such as using a balloon-based catheter with controlled inflation pressures to standardize the pressure.

The OCTA reading and endoscopic RTD scoring were performed by independent researchers who were blinded to the clinical status of the patients as well as each other's respective readings. However, inter-observer and intra-observer agreement of these two readings were not assessed. Previous studies have shown that RTD scoring system has a good inter-observer agreement, but this has not been widely validated yet [173]. Moreover, this was a retrospective study and was limited in small patient enrollment, and a fraction of patients (3 out of 8) was not imaged when they were RFA-naïve. Furthermore, RFA follow-up patients were at different stages of their treatment, and there was not a fixed interval between RFA and follow-up. Overall, this caused a fairly heterogeneous and small sample from which it was hard to draw strong statistical conclusions. Therefore, prospective studies with larger sample sizes and multiple readers are needed to further validate the results of this study.

In summary, this study demonstrated that OCTA can visualize depth-resolved tissue microvasculature and features around the dentate line and rectum, relevant to assessment and treatment of CRP. We have established OCTA features of normal and abnormal rectal microvasculature. Blinded reading of these OCTA features demonstrated the association of abnormal rectal microvasculature with RFA-naïve patients in comparison with normal and RFA follow-up patients, as well as a correlation of abnormal rectal microvasculature with the

endoscopic RTD scores. OCTA does not require injected dyes and can rapidly image large regions of the rectum to identify regions of telangiectasias that may necessitate endoscopic treatment. Rectal microvasculature in the mucosal and submucosal layers can be independently assessed without the need for an endoscope which may allow comprehensive, longitudinal studies of CRP pathophysiology, as well as developing more effective prevention and treatment approaches. (More detailed information on possible future studies were given in the next chapter). All in all, OCTA may play an important role in clinical management of CRP and improve understanding of CRP pathophysiology.

Chapter V

Integrated OCT Imaging and Electrical Muscle Stimulation (EMS)

5.1. Motivation

One of the challenges with catheter-based imaging in the esophagus is achieving circumferential coverage of the esophageal tissue around the imaging catheter. One approach is to use balloon-based imaging catheters that expand to a fixed diameter to achieve circumferential contact and image the esophagus. This method is used in commercial RFA (Barrx Halo360^{TM}) or clinical endoscopic OCT imaging devices (i.e. NinePoint Medical^{TM}). However, due to elastic nature of the esophagus as well as variations in diameter, it is challenging to achieve contact with the full circumference of the esophagus. This is exacerbated when using smaller diameter balloons or capsule imaging devices. Lack of contact can cause sampling errors during diagnostic imaging or missed areas during treatment.

One method to improve contact with an imaging or therapeutic catheter is to stimulate the esophageal muscles such that they contract around the catheter. Electrical muscle stimulation of the lower esophageal sphincter (LES) muscle of the esophagus has been demonstrated in canine models [241, 242]. Furthermore, this technique is used in patients to normalize the contraction of the LES in treating acid reflux through applying chronic stimulation to the LES thereby increasing its tone [243, 244]. Electrical stimulation has also been used to propel capsule devices within the esophagus and small intestine in swine models, independent of the natural peristaltic movement [245].

In this study, we have developed integrated electrical muscle stimulation/OCT catheters to test the hypothesis that stimulation is feasible and improves tissue contact of the catheter.

Electrical stimulation was applied to the distal portion of the esophagus, near the LES. OCT imaging pre-, during and post-stimulation was performed to assess the increase in tissue coverage upon the application of the stimulation waveform. We used balloon-based micromotor catheters that have stimulation electrodes on the outer surface of the catheter sheath to make direct contact with the esophageal tissue. Stimulation was achieved by a programmed electrical waveform with a frequency of 4 – 100 Hz. In the following sections, we provide details of the construction of the integrated EMS/OCT catheters and demonstrate the results of *in vivo* swine experiments.

The prototype ultrahigh-speed endoscopic OCT system used in this work was based on a clinical system developed by the team described in **Chapter II.** This endoscopic OCT system was replicated and adapted by Hsiang-Chieh Lee and Kaicheng Liang to develop a lab porotype that was used in the swine experiments at the MIT animal facilities. All swine experiments were conducted at the MIT E25 animal facility by the endoscopy team including Hsiang-Chieh Lee and Kaicheng Liang, in collaboration with Prof. G. Traverso and with the help and oversight of veterinary personnel and staff at the animal facility including Alison Hayward. The micromotor balloon catheter was designed and constructed by Hsiang-Chieh Lee. The fabrication method of the flexible circuits described in this chapter was initially proposed by James Fujimoto and was subsequently researched and implemented the author of this thesis. The EMS circuits were constructed by the author of this thesis with the assistance of Tan Nguyen. Tan Nguyen was involved in the later stages of this project and assisted the thesis author shortly before, during and after the second swine experiment. Aaron Aguirre and Hiroshi Mashimo contributed to the discussion on mechanism of esophageal muscle stimulation, esophageal motility and safety considerations with regards to possible interference with cardiac rhythm.

5.2. Mechanism and safety considerations of EMS

EMS has been widely used on human skeletal muscles [246-248]. Using pulses with repetition rates of 2-100 Hz, the aim is to activate motor fibers in order to improve muscle strength in athletes, to decrease atrophy in disabled patients or to fasten the recovery process of patients healing from injuries. It was shown that bipolar pulses with small pulse widths produce maximal

contraction while requiring an overall low stimulation current (see **Figure 5.2A** for an example of typical EMS waveform). It was also shown that different muscle types are optimally contracted at different stimulation frequencies as they are associated with different neuromuscular control mechanisms [249]. As an example, for esophagus, the inner circular muscles of the muscularis external layer contract maximally at 5 to 20 Hz while the outer longitudinal muscles of the muscularis external layer contract at 10 to 40 Hz. In addition, duration of the electrical pulse determines the penetration of the signal and it was shown that longer pulse durations penetrate more deeply into subcutaneous tissues [246]. Finally, for complete muscle contraction, it is important for the electrodes to be placed over the correct muscle groups and ensure that sufficient stimulation intensity is used.

There are important structural, physiological and biochemical differences between the constitution and contraction mechanisms of smooth and striated (skeletal) muscles [250]. Striated muscles consist of actin and myosin filaments arranged in sarcomeres, while smooth muscles have a greater (12 to 1) actin to myosin ratio without an organized sarcomeric structure [251], allowing the generation of comparable or higher forces than striated muscles [245]. In ruminant and dogs, all the esophageal muscles are striated. However, in humans and pigs, the muscularis propria at the distal 2/3 of the esophagus consists of smooth muscles, while at the proximal 1/3 of the esophagus it consists of striated muscles [252]. Moreover, within ~ 2 cm near the GEJ, the esophageal wall consist of a tonically controlled muscle (lower esophageal sphincter), which is in a baseline contractile state that relaxes by neurogenic control. Therefore, it is important to test positions at distal as well as proximal esophagus to ensure that EMS is feasible throughout the esophagus that has different muscle constituents.

Electrical stimulation effecting muscular contraction could be aimed toward neuronal or muscular responses. While neuronal stimulation generally requires far less voltage and would be deemed safer for internal applications, the smooth muscle of the esophagus is innervated by both relaxatory (mainly nitric oxide and vasoactive intestinal peptide) and contractile mediators (acetylcholine and substance P) released for specific nerves to coordination of timing and sequence of the relaxation followed by contraction that constitutes the peristaltic wave [253,

254]. Depending on stimulation parameters and position, this could result mainly in the simultaneous release of both mediators, leading to little or no sum contraction, and in tonic regions of the esophagus such as the LES, may lead to largely relaxation. As such, parameters were chosen to effect direct smooth muscular contraction using generally higher voltage and frequencies as reported in the literature.

One of the potential risks of EMS arises from the proximity of the esophagus to the heart. This can potentially cause interference of the stimulation current with the cardiac conduction pathways and affect the contraction of the atria and ventricles of the heart. Transesophageal atrial and ventricular pacing methods were developed to exploit this anatomical proximity and are being used in diagnostic and emergency situations [255-257]. Simulations have shown that when the separation between stimulation electrodes are kept less than <10 mm in the distal esophagus, stray currents to the heart are <1 μA, which is one order of magnitude less than the maximum permissible current above which can cause fibrillation [258]. Therefore, it is desired to have the separation of the stimulation electrodes as small as possible to prevent a possible interference to the cardiac rhythm. Here the limiting factor would be the depth of muscles as the electrical current needs to reach the target muscle to achieve stimulation. At the same time, the outer longitudinal smooth muscles of the distal esophagus cause shortening/lengthening of the organ, while the inner circular smooth muscles cause constriction of it [253]. Therefore, penetration of the EMS current may also affect the contraction of the circular vs. longitudinal layers.

5.3. Electrical muscle stimulation experiments

5.3.1. Construction of the flexible, semi-transparent EMS circuits

Flexible circuits can be fabricated in-house using a solid-ink printer to draw the circuit mask onto flexible PCBs and using ferric chloride solution to etch excess copper. Flexible PCBs consist of a non-conducting base material, typically polyimide, coated with a conducting material such as copper. An adhesive is applied between the copper and polyimide to achieve bonding. The thickness of the copper coating depends on the maximum current to be carried over the circuit and is typically on the order of 10 – 100 μm. The thickness of the underlying polyimide material

depends on the robustness/flexibility required for the application where thicker polyimide decreases the flexibility of the circuit while increasing robustness. Furthermore, regarding the integration with OCT imaging, increasing the thickness of the polyimide also decreases the transparency (i.e. optical transmission) of the material.

Figure 5.1A shows an example circuit with bipolar electrodes drawn onto a flexible PCB using a solid-ink printer (Xerox^{TM} ColorQube 8580N). The solid ink printer essentially overlays a circuit mask onto the PCB to protect those regions from being etched in the subsequent step. When this circuit is immersed into a liquid ferric chloride solution for ~ 20 – 30 minutes then the copper dissolves, except the masked circuit, revealing the underlying semi-transparent polyimide (**Figure 5.1A,** right panel). As previously discussed, polyimide with different thicknesses and compositions results in a different optical transparency as shown in **Figure 5.1B.** Therefore, for the integrated EMS/OCT catheter it is important to select the polyimide thickness as small as possible in order to maximize optical transmission. For the subsequent experiments we have used a flexible PCB from Dupont (Pyralux^{TM} 9110R) that had 25 µm adhesive thickness, 25 µm polyimide thickness and 35 µm copper thickness (sample VI in **Figure 5.1B**). Optical transmission of this material, after etching of the copper, was measured to be ~ 85% at 1310 nm wavelength that is used in the OCT imaging experiments.

After etching with ferric chloride, the ink overlying the circuit layout can be easily removed by abrasion using a sponge-like material and warm water, exposing the underlying copper (**Figure 5.1C,** left panel). Without further treatment, when exposed to air and humidity the copper would be oxidized, reducing the conductivity of the conductor. To prevent this, the circuit is immersed in a liquid tin solution for ~ 10 – 20 minutes to achieve a tin coating over the copper. This step also makes it easier to solder electrical connections to the electrodes. **Figure 5.2B and C** shows drawing and photograph of a prototype flexible EMS circuit fabricated using the procedure described in this section. The electrode layout drawn there has subsequently changed to the layouts shown in **Figure 5.3** and **Figure 5.5** (by taping the vertical electrode stripes using a isolating tape)**,** as the larger spacing between those vertical electrode stripes causes current to

flow over a longer path, causing larger effective electrode spacing and likely deeper than intended penetration into the tissue.

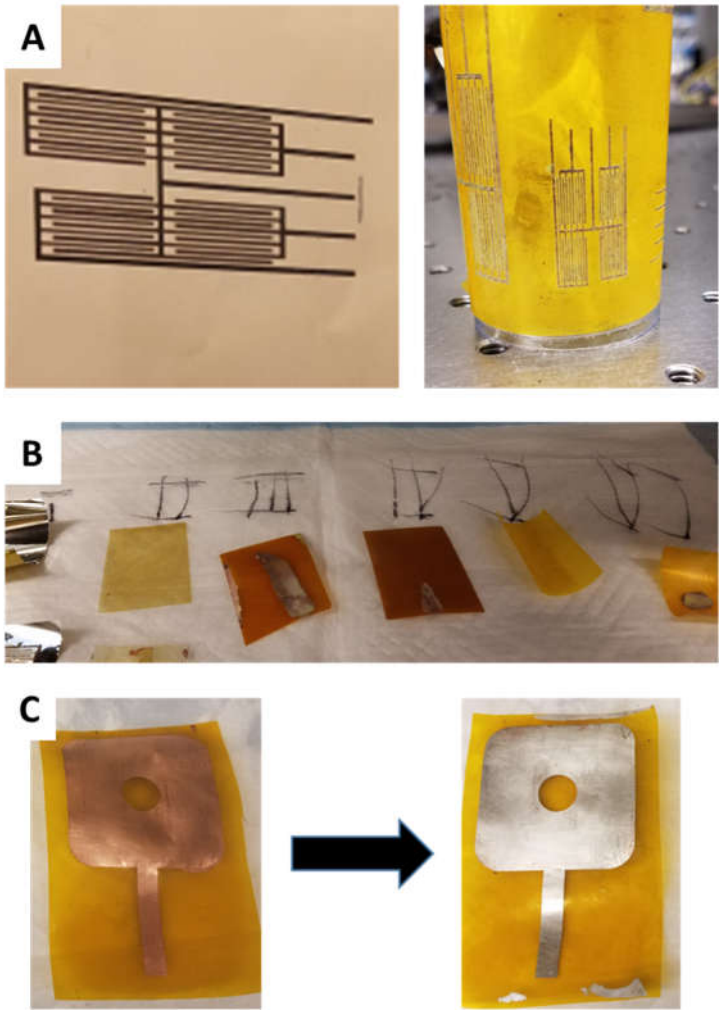

Figure 5.1. **A**, A circuit layout drawn on a flexible PCB using a solid-ink printer (left). After etching with ferric chloride solution the flexible circuit becomes flexible and semi-transparent and can be wrapped around cylindrical materials. This circuit includes four separate zones with electrodes with 1 mm width and 1 mm spacing, and can be used to construct a multi-zone radiofrequency ablation catheter. **B,** transparency of the resulting flexible circuit depends on the thickness of the underlying polyimide material. **C,** coating of the exposed copper with liquid tin prevents oxidation of the copper and makes it easier to solder electrical wires onto the electrodes.

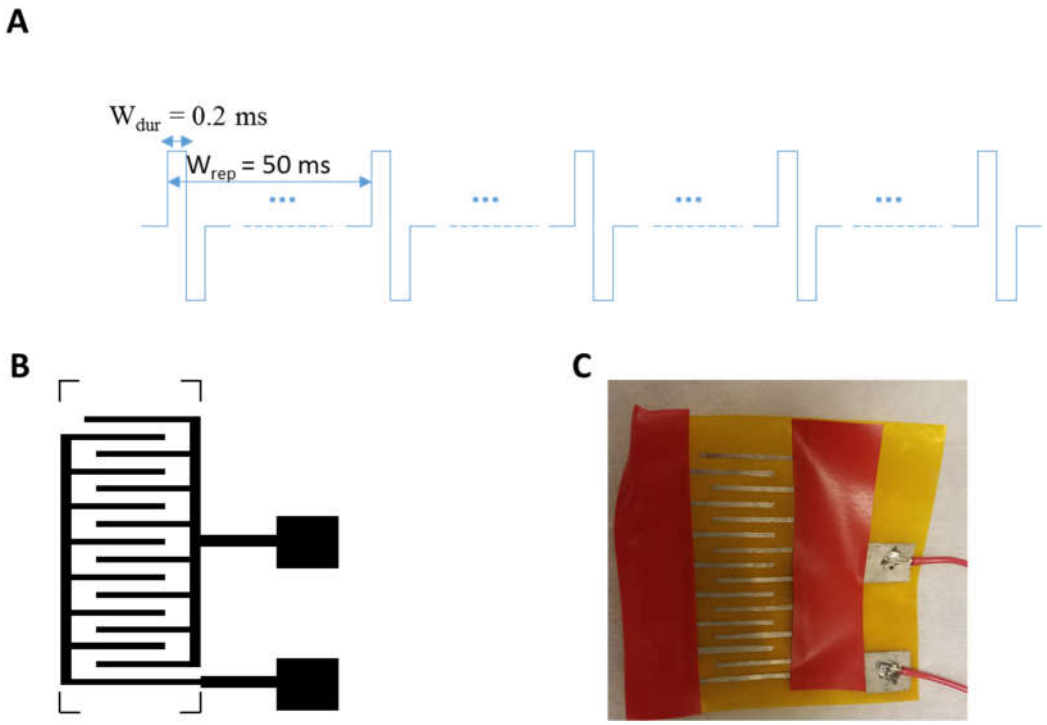

Figure 5.2. **A**, Drawing of a typical EMS waveform, with a pulse duration of 0.2 ms and repetition rate of 20 Hz. **B, C,** drawing and photograph of one the constructed prototype EMS circuits fabricated on a flexible, semi-transparent polyimide material.

5.3.2. Integrated EMS/OCT balloon catheter and *in vivo* swine experiments

The *in vivo* swine experiments were approved under an MIT Committee on Animal Care (CAC) protocol. Per this protocol, all experiments were conducted at the MIT E25 animal facility in collaboration with Prof. G. Traverso under MIT (Division of Comparative Medicine) DCM supervision. Animals under Prof. Langer's protocol 1215-116-18 were used for the experiments with the oversight of Dr. Alison Hayward from DCM. Terminal animals were used once for the electrical stimulation experiments on the day of their scheduled sacrifice. Standard endoscopy was performed as part of the protocol and used to examine the esophagus after the EMS experiments in order to confirm that there is no injury to the esophagus. Heart rate, EKG and other vitals of the animal was monitored during to procedure to confirm that the EMS stimulation does not interfere with the normal physiological processes. Veterinarians from the DCM, including Dr. Alison Hayward, were present during the experiments and were advised of the

potential of cardiac stimulation. They closely monitored any changes in the heart rate, EKG, other vitals, and any other signs of complications. In the case of any physiological changes (such as a sudden change in the cardiac rhythm), EMS current was to be immediately ceased. A defibrillator was on standby in an unlikely case of ventricular fibrillation induction. In swine and canine models, the thoracic cavity conformation increases the distance of the esophagus to the ventricles, in comparison to the human, hence the likelihood of stimulating the ventricles was expected to be minimal [259].

Pilot swine experiment

A micromotor balloon catheter previously developed by our group member Hsiang-Chieh Lee was modified to construct the integrated EMS/OCT balloon catheter [35]. A flexible EMS circuit was constructed following the procedures described in the previous sections with a schematic shown in **Figure 5.3A.** This circuit was then subsequently glued onto the micromotor balloon using a low-viscosity epoxy. The longitudinal length of the electrodes and the underlying polyimide was selected so that a portion of the balloon is not covered by the EMS circuit, as shown in **Figure 5.3B.** For this layout, the electrode spacing was 8 mm and the electrode width was 4 mm. For the connection diagram shown in **Figure 5.3C** every other electrode was used as the bipolar electrode pair, resulting in an effective electrode spacing of 16 mm. The electrode connections were switched between the two indicated states using an electrical switch.

During this experiment, the endoscopic OCT system was operated with the same parameters as the original micromotor balloon catheter publication [35]. That study had shown that it was possible to perform OCT angiography (OCTA) with the selected imaging parameters and we wanted to test the effects of esophageal muscle contraction on the vascular flow. One concern was the possibility of increased catheter pressure on the resulting in decreased blood flow and loss of visualization of the vasculature as discussed in **Chapter III**. Therefore, we have selected imaging parameters that would potentially generate OCTA. Briefly, the system was operated at 600 kHz bi-directional sweep rate resulting in a 1.2 MHz effective A-scan rate. The tuning range was set to 100 nm. The MZI clock rate was set to the maximum of ~ 1.1 GHz resulting in a ~ 1.2 mm imaging range in tissue. The power on the sample arm was ~ 40 mW (~ 20 mW

after the catheter) with a measured sensitivity of 101 dB using a flat-cleaved fiber, which corresponds to ~ 96 dB including the losses due to the catheter. The micromotor was rotated at 240 Hz and the catheter was pulled back at 1.5 mm/sec for a total pullback length of 30 mm over a 20 sec acquisition. There were a total of 4800 cross-sectional OCT images (frames) per acquisition, with 2500 A-scans per frame and 768 samples per A-scan.

During these experiments, three pulse repetition rates were tested: 4 Hz, 20 Hz and 50 Hz. The pulse duration was 0.2 msec. The EMS intensity was gradually increased. While no contraction was observed at 10 V peak pulse intensity, contraction was observed at 20 V and higher voltages. **Figure 5.4** shows *en face* and cross-sectional images prior to, during and after EMS activation at 20 Hz pulse repetition rate and 25 V pulse intensity at distal swine esophagus, approximately 10 cm proximal from the GEJ. As shown in the cross-sectional OCT image in **Figure 5.4D,** prior to EMS activation tissue was not making any contact with the micromotor catheter over the first imaging window (on the left of the image), while it was making partial contact over the other two windows.

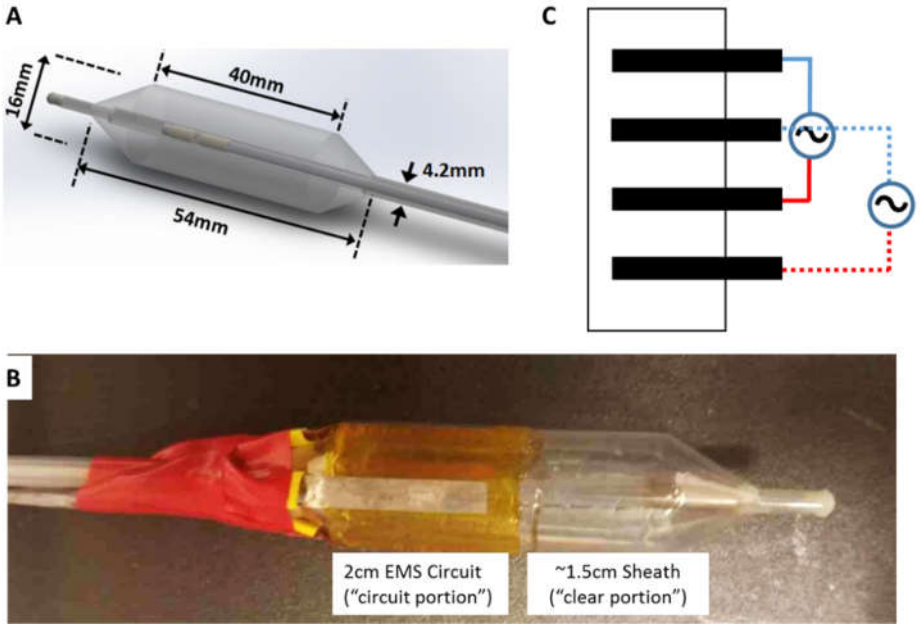

Figure 5.3 **A,** three-dimensional rending of the distal end of the micromotor balloon probe showing the size of the balloon. **B,** photograph of the integrated EMS/OCT catheter where the electrodes are glued onto the micromotor balloon catheter. **C,** schematic of the flexible EMS circuit and connection layout of the electrodes to the EMS signal generator for the first swine experiment.

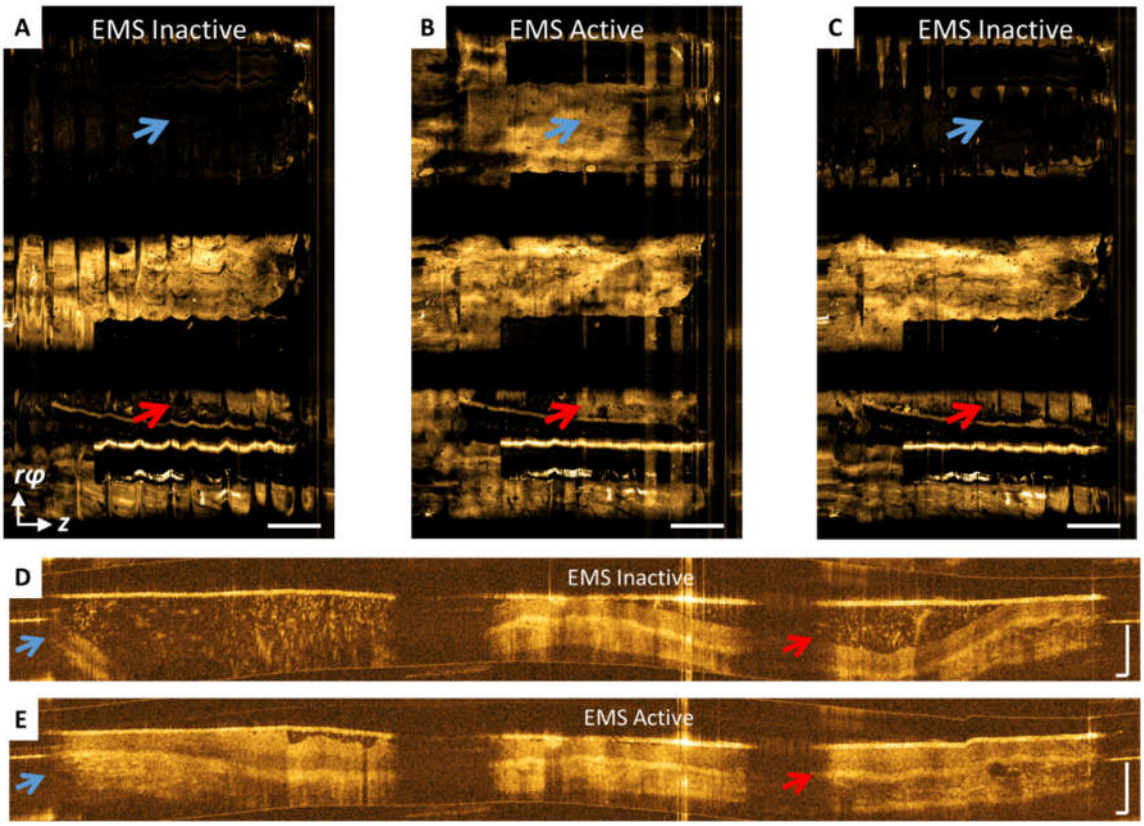

Figure 5.4 *En face* and cross-sectional image of swine esophagus. *En face* images of the swine esophagus (a) esophagus prior to EMS activation, (b) during active EMS, and (c) after cessation of the EMS signal. Blue and red arrows point to regions where tissue contact improves upon activation of EMS. Scale bars are 5 mm. *rϕ*: circumferential direction, *z*: longitudinal direction. **D**, prior to EMS activation, and **E**, during active EMS. Blue and red arrows point to regions where tissue contact improves upon activation of EMS. The catheter is placed at the distal swine esophagus, approximately 10 cm proximal from the GEJ. Scale bars are 500 µm.

After EMS was activated, complete circumferential coverage and tissue contact over all three imaging windows were achieved (**Figure 5.4E**). Similar observations can be made on the *en face* projection maps depicted in in **Figure 5.4A – 5.4C.** Furthermore, the periodic imaging artifacts due to cardiac motion observed over the portions where there was partial contact (middle and bottom imaging windows in **Figure 5.4A**) were eliminated after EMS activation (**Figure 5.4B**). This can have important implications for reducing the imaging artifacts due to cardiac and other physiological motion described in the previous chapters. We have also observed that the effect of the EMS was rapid and reversible with no hysteresis or muscle fatigue. The muscles were contracted within milliseconds upon the activation of the EMS and relaxed to

the original state immediately after the cessation of the stimulation (**Figure 5.4C**). No discernible differences in the muscle contraction were observed between 20 Hz and 50 Hz pulse repetition rates at the same pulse intensities while no contraction was observed at 4 Hz, consistent with the previous EMS literature.

EMS currents were not measured during the pilot swine experiments, hence it was not possible to deduce conductivity of the esophagus with the given electrode geometry. Furthermore, we have hypothesized that a smaller electrode spacing can achieve muscle contraction with less pulse intensity/current while having less tissue penetration. All these factors would improve the safety of the procedure by decreasing the potential interference with the cardiac rhythm. Furthermore, we decided that assessing the effects of EMS on pressure and resulting OCTA signal was less critical compared to achieving higher imaging range. Therefore, we have made several modifications to the EMS circuit, system setup and imaging parameters and designed a second swine experiment that will be described in the next section. Briefly, we have constructed two different EMS balloon sheaths with different electrode separation that could be interchanged during the experiment, in order to test dependency of EMS threshold to the electrode separation. Furthermore, we have modified the system and acquisition software so that currents during EMS activation could be recorded. We have also modified the system to record the EKG signal that was continually displayed by the ECG monitor and monitored by the veterinary staff. The EKG signal used at the MIT animal facility was a 3 lead EKG with electrodes connected to L arm, R arm and L leg. Finally, we have reduced the OCT imaging speed to increase the sensitivity of the OCT imaging as well as the imaging range. These experiments will be continued by other group members.

Second swine experiment

As previously mentioned, to test the dependency of EMS threshold to the electrode separation, we have constructed two different EMS balloon sheaths with different electrode separation. The schematic and connection layout for those EMS circuits are given in **Figure 5.5A.** The “large spacing” EMS sheath is the same as shown in **Figure 5.3** where the EMS connections are changed so that all electrodes will be simultaneously active with an 8 mm bipolar electrode spacing. The

“small spacing” EMS sheath has electrodes with 4 mm bipolar electrode spacing. A photograph of the integrated EMS/OCT catheter with this EMS sheath is given in **Figure 5.5B.** This was constructed very similar to the “large spacing” EMS sheath in which the EMS circuit covered a ~ 2 cm longitudinal portion of the balloon while the remaining ~ 1.5 cm sheath was left uncovered by the EMS circuit.

The OCT imaging parameters were optimized to increase imaging range and sensitivity of the system. Imaging speed was reduced to 100 kHz bi-directional sweep rate resulting in a 200 kHz A-scan rate. The tuning range was 110 nm. The MZI clock rate was set to the maximum of ~ 1.1 GHz resulting in a ~ 10.1 mm imaging range (in air). The VCSEL sweep was linearized to improve the symmetry of forward and backward sweeps and achieve increased imaging range. The sensitivity of the system was measured to be 108.6 dB using a flat-cleaved fiber, and ~ 104 dB including the losses due to the catheter. The power on the sample arm was ~ 41 mW (~ 20 mW after the catheter).

The micromotor will be rotated at 200 Hz and the catheter will be pulled back at 5 mm/sec for a total pullback length of 30 mm over a 6 sec acquisition. This will yield for a total of 1200 cross-sectional OCT images (frames) per acquisition, with 1000 A-scans per frame and 4608 samples per A-scan. These parameters will result in sub-nyquist sampling in the rotational as well as pullback direction, but sensitivity and imaging range were considered to be more critical than obtaining nyquist sampled images.

In this experiment, four pulse repetition rates will be tested: 5 Hz, 20 Hz, 50 Hz and 100 Hz. The pulse duration will be 0.2 msec. The main objective will be to determine EMS threshold currents with the two EMS sheaths that have different electrode spacing. Therefore, the EMS voltage will be increased by 1V increments until full muscle contraction was observed. Cross-sectional OCT images at a fixed longitudinal position will be continuously captured during the EMS voltage ramp-up. The voltage will be increased up to 2 times the observed threshold voltage. Afterwards, EMS voltage will be continuously reduced from the maximum level while continuously capturing cross-sectional OCT images at the same longitudinal position, to assess possible hysteresis effects. This measurement will be repeated 3 times for each EMS setting and

will be repeated at different longitudinal positions along the esophagus to ensure that different segments of the esophagus that has different muscle constituents are tested. Finally, stimulation current and EKG signal will be recorded before, during and after stimulations. 3 lead ECG will be used with electrodes connected to L arm, R arm and L leg.

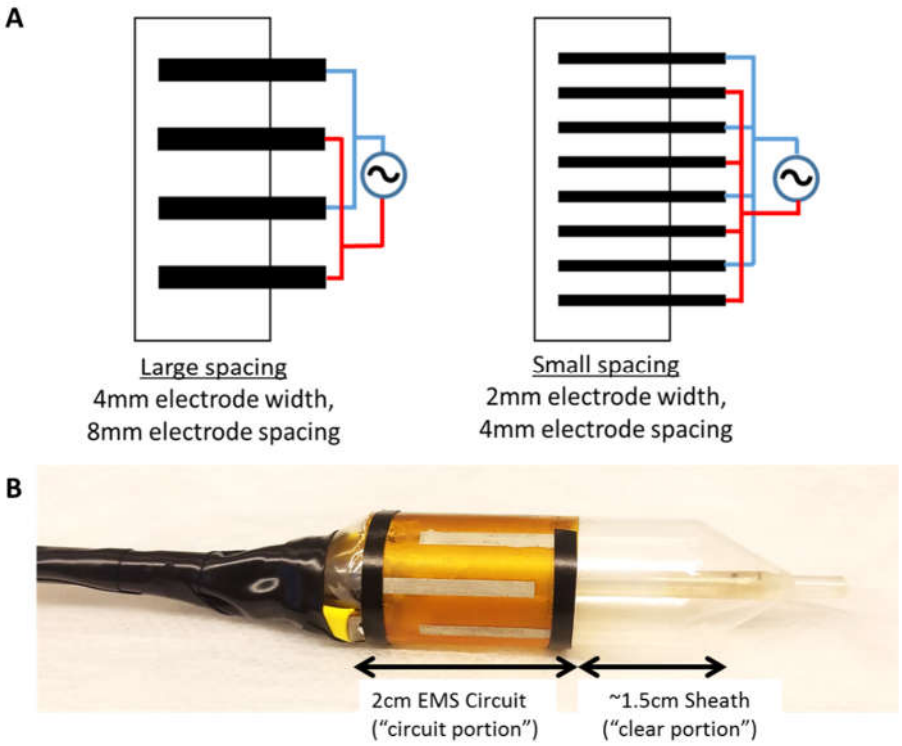

Figure 5.5 **A**, schematic of the flexible EMS circuit and connection layout of the electrodes to the EMS signal generator for the second swine experiment. **B**, photograph of the integrated EMS/OCT catheter with the small spacing electrode.

Chapter VI

Conclusion and Biography

6.1. Summary of thesis work

In summary, this thesis presented a subset of novel clinical and engineering applications that were enabled by the next generation ultrahigh-speed endoscopic OCT technology as well as hardware and software developments to improve endoscopic OCT instrument robustness and clinical imaging workflow.

Chapter II described methods to improve the scanning stability and robustness of the ultrahigh-speed endoscopic OCT system, as well as hardware and software improvements to optimize data acquisition and visualization. Pullback of the micromotor catheter was optimized by using an uncoated stainless steel torque coil pulled back within a PTFE sheath. Rotation of the micromotor catheter was optimized by developing a computationally efficient algorithm for correcting the non-uniform rotational distortion (NURD). This method improved NURD performance of the catheter by more than an order of magnitude, allowing robust visualization of *en face* mucosal patterns and OCT angiography (OCTA). Parallel and asynchronous data acquisition, processing and saving schemes have been implemented to the endoscopic OCT acquisition and control software to improve data acquisition efficiency and clinical imaging workflow. Image processing methods such as high-dynamic-range filtering, depth projection and false colormaps were applied to improve *en face* image visualization.

Chapter III demonstrated two clinical studies with the ultrahigh-speed endoscopic OCT system related to Barrett's esophagus and dysplasia. In the first study, we investigated a novel approach of interpreting OCT data by assessing a combination of depth-resolved *en face* and cross-sectional OCT features. In *en face* OCT, readers identified irregular mucosal patterns in

100% of neoplasia datasets, and in 35% of NDBE datasets (43% of short and 28% of long-segment NDBE, respectively). In cross-sectional OCT, mucosal layering was absent and surface signal > subsurface in 35% and 29% of neoplasia datasets (21% and 21% in the treatment-naïve subgroup), and in 53% and 30% of NDBE datasets, respectively. Atypical glands (>5) were present in 75% of neoplasia datasets (96% in the treatment-naïve subgroup) and in 59% of NDBE datasets. Atypical glands under irregular mucosal patterns occurred in 75% of neoplasia (96% of treatment-naïve neoplasia) versus 30% of NDBE datasets (43% of short and 18% of long-segment NDBE). Mucosal layering was absent in 35% of neoplasia and 53% of NDBE datasets, and surface signal > subsurface in 29% of neoplasia and 30% of NDBE datasets. This study demonstrated that atypical glands either under irregular mucosal patterns or independently might be a potential marker for dysplasia, especially in long-segment BE in proximal regions further from the GEJ, where interpretation is not confounded by non-neoplastic cardiac glands and where dysplasia most frequently occurs. In the second study, we have demonstrated the clinical utility of the ultrahigh-speed endoscopic OCT and OCTA for assessing a dysplastic lesion at the gastroesophageal junction (GEJ), its lateral margins before and immediately after EMR, and at 2-months follow-up. OCT/OCTA prior to EMR visualized the dysplastic lesion and its lateral margins. Immediately post EMR, when WLE/NBI visualization can be compromised by tissue distortion, electrocautery and blood, the OCT probe allowed direct lavage over the area, and OCT/OCTA showed residual dysplasia at the distal resection margin. This was confirmed at the follow-up endoscopy visit. This study suggested that probe-based OCT/OCTA may improve diagnostic capabilities and enhance clinical utility by identifying dysplastic areas, assessing lesion margins, and evaluating regions immediately post-treatment and on follow-up.

Chapter IV discussed an application of OCT in the non-endoscopic assessment of chronic radiation proctopathy (CRP). A detailed overview of CRP pathophysiology and shortcomings of current clinical management strategies were discussed. An OCT study was reported, in which the rectum and anal canal of 8 CRP patients undergoing RFA treatment and 2 normal patients were assessed non-endoscopically by directly placing the micromotor catheter into the dentate line and rectum of the patients without endoscopic guidance. OCTA features of normal and abnormal microvasculature were assessed in the mucosal and submucosal layers of the rectum. Blinded

reading of the OCTA features was performed to demonstrate the association of abnormal rectal microvasculature with CRP and RFA treatment, and endoscopic rectal telangiectasia density (RTD) scoring system. Abnormal rectal mucosal microvasculature had distortions to the honeycomb-like microvascular pattern, and had ectatic and tortuous microvasculature, which was observed in 0 out of 2 (0%) normal, 3 out of 5 (60%) RFA-naïve, and 0 out of 8 (0%) RFA follow-up patients. Abnormal rectal submucosal microvasculature had unusually high-caliber arterioles and venules with diameters > 200 μm, which was observed in 1 out of 2 (50%) normal, 5 out of 5 (100%) RFA-naïve and 2 out of 8 (13%) RFA follow-up patients. The occurrence of abnormal rectal OCTA features increased with increasing RTD scores, suggesting a correlation of abnormal rectal microvasculature with the RTD scores. This study concluded that OCTA can play an important role in the clinical management of CRP and improve understanding of CRP pathophysiology.

Chapter V discussed development of esophageal electrical muscle stimulation (EMS) techniques and their integration with a balloon-based micromotor catheter. EMS has the potential to improve circumferential coverage of the esophageal tissues around the imaging catheter as lack of contact can cause sampling errors during diagnostic imaging or missed areas during treatment. We demonstrated methods to fabricate flexible, semi-transparent EMS circuits that can be integrated with the OCT catheters. Feasibility of esophageal muscle contraction was subsequently demonstrated with *in vivo* swine experiments conducted at the MIT animal facility. Muscle contraction and full circumferential coverage were observed at 20 V and higher stimulation voltages with 20 and 50 Hz pulse repetition rates. Moreover, periodic imaging artifacts due to cardiac motion observed over the portions where there was partial contact were also eliminated after EMS activation. The muscles were contracted within milliseconds upon the activation of the EMS, and relaxed to the original state immediately after cessation of the stimulation.

Possible future research directions will be discussed in the next section.

6.2. Future work and conclusion

In conclusion, as exemplified in this thesis, ultrahigh-speed endoscopic OCT technology powered by the next generation swept-source light sources and precision scanning micromotor catheters opened new research directions. The following studies can be envisioned to extend the research presented in this thesis and to further explore the potential and establish the clinical utility of this technology.

The structural reading study discussed in **Chapter III** showed the potential of a combined *en face* and cross-sectional OCT assessment in identifying dysplasia. However, one of the technical limitations of this endoscopic OCT system was the limited diameter of the micromotor catheter (3.4 mm). The catheter covered only a fraction of the esophageal circumference, so comprehensive imaging would require repositioning the catheter to different esophageal quadrants. This approach is valid for an exploratory study as the one reported in this thesis, however, it would be cumbersome to perform standard BE surveillance with this approach. On the other hand, we have demonstrated circumferential imaging with balloon [35] and capsule [37] catheters that can improve coverage within a single data acquisition. OCTA was demonstrated with the micromotor balloon catheter in living swine, however, translation of this catheter into human use requires further engineering to improve image quality and validating methods for sterilization of the internal aspects of the balloon. Capsule catheter also requires further engineering to improve the pullback uniformity (the entire capsule is pulled pack within the esophagus, rather than within a sheath) as well as to improve the circumferential coverage (capsule has a smaller diameter than the balloon).

Furthermore, the PIVI criteria mentioned in **Chapter III** requires certain diagnostic performance metrics to be achieved under specific study designs. Specifically, it requires a “per-patient sensitivity” of at least 90% and a negative predictive value (NPV) of at least 98% for detecting HGD or EAC compared with the current standard protocol of “WLE with Seattle protocol and targeted biopsies”. However, the study reported in this chapter was not prospectively designed to assess the PIVI criteria. Particularly, the limitation on circumferential coverage made it unfeasible to image the entire BE segments circumferentially, so that a “per-

patient" sensitivity/specificity could be extracted. Rather, areas suspicious of dysplasia were imaged only for the dysplasia cases. Moreover, the fact that suspicious areas were detected by NBI/WLE, rather than with OCT guidance, prevented the assessment of incremental OCT yield for dysplasia detection compared with the current standard protocol (random and WLE/NBI targeted biopsies). Therefore, future studies should be designed by taking these factors into consideration.

A prospective, tandem study design that would assess PIVI in BE surveillance patients would be the following: In one arm of the study, OCT with either a capsule or balloon catheter could be used to image entire circumferential BE segments before endoscopy and mark areas of suspicion by a technique such as laser marking [47]. During the subsequent endoscopy, those areas marked by OCT would be biopsied, followed by performing standard endoscopy surveillance with the Seattle protocol and WLE/NBI guided biopsies. This study may also have a second arm, in which patients would undergo standard endoscopy surveillance with the Seattle protocol and WLE/NBI guided biopsies first, followed by OCT imaging and OCT-guided biopsies from additional areas of suspicion. The first arm of the study would assess "per-patient" sensitivity/specificity of OCT, without being biased by the WLE/NBI examination. The second arm of the study would assess added dysplasia yield of OCT, i.e. additional areas detected by OCT examination. This would strengthen the OCT sensitivity results compared with the standard surveillance protocol. Similar prospective, tandem studies have been extensively conducted in the NBI/WLE literature and can be studied for more information [260, 261].

Chapter IV highlighted the potential of OCT for non-endoscopic assessment of rectal and anal canal pathologies. This study had limited patient enrollment but showed promising clinical applications about elucidating CRP pathophysiology as well as developing more optimal intervention strategies. As discussed in that chapter, the clinical challenges about CRP can be approached from various angles and a number of studies can be designed.

One study can investigate the development of CRP and CRP pathophysiology longitudinally. Although as high as 120,00 – 240,000 patients will receive pelvic radiation therapy each year in the US, there is a radiation dose dependence on the subsequent CRP development [262]. Hence patients more likely to develop CRP can be pre-selected and enrolled in this study.

These patients can be imaged with OCT at regular time intervals (2 – 4 weeks for a total of 10 – 12 months) until CRP develops. OCT and OCTA changes during the progression of CRP can be assessed. Depth-resolved OCTA can provide better insights in terms of the origin of CRP (mucosal vs submucosal layer) as discussed in **Chapter IV.** Moreover, patients who develop CRP can be compared to the patients who do not develop CRP, and OCT, OCTA as well as clinical factors can be assessed to understand markers that may be predictors of CRP development. This study can establish OCT and OCTA features that can predict bleeding and worse prognosis that would warrant earlier or a more aggressive treatment. This study can also include another arm where patients receive a compound for prophylaxis (prevention) such as antibiotics and antioxidants. Efficacy of these compounds and their effect on rectal microstructure and microvasculature can be assessed by OCT and OCTA.

A second study can focus on patients who have developed CRP and can be designed as a comparative study to assess efficiency and safety of different endoscopic treatment modalities. For this purpose, RFA can be compared to APC, as APC is the current gold standard of endoscopic CRP treatment and RFA has been emerged as an alternative to APC with superior safety and efficacy profile. In this study, it would be critical to have the treatment intervals in both arms to be standardized, as this was noted to be a major limitation in comparing the previous RFA and APC literature. OCT imaging can be performed before and immediately after each treatment session. OCT information can be used to compare treatment depth and other structural changes due to RFA vs APC treatment in a quantitative way, similar to previously referenced OCT/RFA studies. Healing after endoscopic therapy and normalization of microvasculature can be assessed with OCT and OCTA. OCT and OCTA differences related to response to RFA vs APC can be assessed. Complications rates can be compared in these two arms to establish comparative safety profiles of these two interventions. Patients can be continued to followed-up with OCT imaging for another 1 – 2 years after achieving hemostasis to assess factors related to possible recurrence.

As described in the previous paragraphs, studies to assess CRP generally require repeated follow-up visits. Hence it will be important to improve the ergonomics and ease of use of the OCT

imaging system. The small diameter of the micromotor catheter is a major limitation to assess large and circumferential regions. Hence a larger diameter catheter tailored for rectal and anal canal imaging would be needed. For the majority of CRP cases the lesions are localized to the rectum, hence a rigid catheter may be sufficient for this application as maneuvering into the sigmoid colon might not be needed. Moreover, a rigid catheter can allow better placement over the areas near the dentate line in comparison to a balloon-based catheter. Similar to the reported study, OCT imaging can be performed non-endoscopically. Furthermore, except the time points where endoscopic visualization is necessary, such as time points for treatment, non-endoscopic OCT imaging can be performed in an office setting without the need for sedation or other endoscopic preparation. A rectal enema might be sufficient for patient preparation. All these factors can make it feasible to perform a longitudinal study with OCT imaging and can put OCT imaging modality in a unique position to study CRP pathophysiology and CRP treatment efficacy/response.

Chapter V demonstrated the feasibility of EMS to achieve esophageal muscle contraction and circumferential imaging coverage in *in vivo* swine experiments. This study can be continued from different aspects in an effort to translate the technology to clinical use. As discussed in that chapter, one of the major potential limitations of EMS is its unknown safety profile, especially its potential to interfere with cardiac conduction pathways and cardiac rhythm. The commercial esophageal EMS devices to treat GERD have been shown to be safe, however, the electrodes for those devices are implanted into the GEJ, which may not have the closest proximity to heart along the esophagus. An integrated EMS/OCT catheter could be activated at an arbitrary longitudinal position along the distal esophagus that can include positions that would have closer proximity to heart (as it is the case of transesophageal pacing methods). Although it is unlikely that pacing can be induced at EMS-relevant pulse repetition rates (20 – 50 Hz), it is possible to induce atrial or ventricular fibrillation if the stray currents are high enough. Therefore, proving the safety of EMS would be of paramount importance.

This chapter also discussed follow-up experiments with varying electrode separations. If EMS can be demonstrated with a small electrode separation (2 – 4 mm), then further

mathematical modeling, simulations and/or experimental work can prove that it would be unlikely to have penetration to the heart with these electrode geometries. Experiments in animal models closer to human esophageal and heart anatomy, such as macaque models could then be conducted with EKG monitoring to demonstrate the safety of esophageal EMS. During these experiments, EMS threshold currents can be determined and an increased threshold current (by a factor of 5 – 10) can be used to establish a safe margin. Currents can be potentially increased until a cardiac event or change in cardiac rhythm is observed. To further reduce the possibility of interfering with the cardiac rhythm, electrical stimulation can be gated by the EKG signal in a way to avoid cardiac hyperexcitable states such as the supernormal period within the T wave [263, 264]. Theoretical demonstration of the safety, followed by macaque experiments might make a strong case for an investigational device exemption (IDE) application to the FDA so that EMS can be tested in pilot human studies.

6.3. Publications produced during thesis

The following publications were produced during the author's thesis period.

Journal Articles

[1] O. O. Ahsen, K. Liang, H. Lee, M. Giacomelli, Z. Wang, B. Potsaid, M. Figueiredo, Q. Huang, V. Jayaraman, J. Fujimoto, and H. Mashimo, "Assessment of Barrett's Esophagus and Dysplasia with Ultrahigh-speed Volumetric En face and Cross-sectional Optical Coherence Tomography," *Endoscopy,* 2018, in review.

[2] K. Liang, Z. Wang, O. O. Ahsen, H.-C. Lee, B. M. Potsaid, V. Jayaraman, A. Cable, H. Mashimo, X. Li, and J. G. Fujimoto, "Cycloid scanning for wide field optical coherence tomography endomicroscopy and angiography in vivo," *Optica,* vol. 5, pp. 36-43, 2018/01/20 2018.

[3] K. Liang, O. O. Ahsen, Z. Wang, H.-C. Lee, W. Liang, B. M. Potsaid, T.-H. Tsai, M. G. Giacomelli, V. Jayaraman, H. Mashimo, and J. G. Fujimoto, "Endoscopic forward-viewing optical coherence tomography and angiography with MHz swept source," *Optics letters,* vol. 42, pp. 3193-3196, 2017.

[4] H.-C. Lee, O. O. Ahsen, J. J. Liu, T.-H. Tsai, Q. Huang, H. Mashimo, and J. G. Fujimoto, "Assessment of the radiofrequency ablation dynamics of esophageal tissue with optical coherence tomography," *Journal of Biomedical Optics,* vol. 22, pp. 076001-076001, 2017.

[5] H. Lee, O. O. Ahsen, K. Liang, Z. Wang, M. Figueiredo, M. Giacomelli, B. Potsaid, Q. Huang, H. Mashimo, and J. Fujimoto, "Endoscopic optical coherence tomography angiography microvascular features associated with dysplasia in Barrett's esophagus: a pilot study (with video)," *Gastrointestinal endoscopy,* vol. 86, pp. 476-484. e3, 2017.

[6] O. O. Ahsen, H.-C. Lee, K. Liang, Z. Wang, M. Figueiredo, Q. Huang, B. Potsaid, V. Jayaraman, J. G. Fujimoto, and H. Mashimo, "Ultrahigh-speed endoscopic optical coherence tomography and angiography enables delineation of lateral margins of endoscopic mucosal resection: a case report," *Therapeutic advances in gastroenterology,* vol. 10, pp. 931-936, 2017.

[7] K. Liang, O. O. Ahsen, H.-C. Lee, Z. Wang, B. M. Potsaid, M. Figueiredo, V. Jayaraman, A. E. Cable, Q. Huang, H. Mashimo, and J. G. Fujimoto, "Volumetric Mapping of Barrett's Esophagus and Dysplasia With en face Optical Coherence Tomography Tethered Capsule," *The American Journal of Gastroenterology,* vol. 111, pp. 1664-1666, 2016.

[8] H.-C. Lee, O. O. Ahsen, K. Liang, Z. Wang, C. Cleveland, L. Booth, B. Potsaid, V. Jayaraman, A. E. Cable, H. Mashimo, and J. G. Fujimoto, "Circumferential optical coherence tomography angiography imaging of the swine esophagus using a micromotor balloon catheter," *Biomedical Optics Express,* vol. 7, pp. 2927-42, Aug 1 2016.

[9] K. Liang, G. Traverso, H.-C. Lee, O. O. Ahsen, Z. Wang, B. Potsaid, M. Giacomelli, V. Jayaraman, R. Barman, and A. Cable, H. Mashimo, and J. G. Fujimoto, "Ultrahigh speed en face OCT capsule for endoscopic imaging," *Biomedical optics express,* vol. 6, pp. 1146-1163, 2015.

[10] N. Zhang, T. H. Tsai, O. O. Ahsen, K. Liang, H. C. Lee, P. Xue, X. Li, and J. G. Fujimoto, "Compact piezoelectric transducer fiber scanning probe for optical coherence tomography," *Opt Lett,* vol. 39, pp. 186-8, Jan 15 2014.

[11] Z. Wang, H. C. Lee, O. O. Ahsen, B. Lee, W. Choi, B. Potsaid, J. Liu, V. Jayaraman, A. Cable, M. F. Kraus, K. Liang, J. Hornegger, and J. G. Fujimoto, "Depth-encoded all-fiber swept source polarization sensitive OCT," *Biomed Opt Express,* vol. 5, pp. 2931-49, Sep 1 2014.

[12] T. H. Tsai, H. C. Lee, O. O. Ahsen, K. Liang, M. G. Giacomelli, B. M. Potsaid, Y. K. Tao, V. Jayaraman, M. Figueiredo, Q. Huang, A. E. Cable, J. Fujimoto, and H. Mashimo, "Ultrahigh speed endoscopic optical coherence tomography for gastroenterology," *Biomed Opt Express,* vol. 5, pp. 4387-404, Dec 1 2014.

[13] T. H. Tsai, O. O. Ahsen, H. C. Lee, K. Liang, M. Figueiredo, Y. K. Tao, M. G. Giacomelli, B. M. Potsaid, V. Jayaraman, Q. Huang, A. E. Cable, J. G. Fujimoto, and H. Mashimo, "Endoscopic optical coherence angiography enables 3-dimensional visualization of subsurface microvasculature," *Gastroenterology,* vol. 147, pp. 1219-21, Dec 2014.

[14] Y. K. Tao, D. J. Shen, Y. Sheikine, O. O. Ahsen, H. H. Wang, D. B. Schmolze, N. B. Johnson, J. S. Brooker, A. E. Cable, J. L. Connolly, and J. G. Fujimoto, "Assessment of breast pathologies using nonlinear microscopy," *Proceedings of the National Academy of Sciences of the United States of America,* vol. 111, pp. 15304-15309, Oct 28 2014.

[15] O. O. Ahsen, H. C. Lee, M. G. Giacomelli, Z. Wang, K. Liang, T. H. Tsai, B. Potsaid, H. Mashimo, and J. G. Fujimoto, "Correction of rotational distortion for catheter-based en face OCT and OCT angiography," *Opt Lett,* vol. 39, pp. 5973-6, Oct 15 2014.

[16] A. Li, O. O. Ahsen, J. J. Liu, C. Du, M. L. McKee, Y. Yang, W. Wasco, C. H. Newton-Cheh, C. J. O'Donnell, J. G. Fujimoto, C. Zhou, and R. E. Tanzi, "Silencing of the Drosophila ortholog of SOX5 in heart leads to cardiac dysfunction as detected by optical coherence tomography," *Hum Mol Genet,* vol. 22, pp. 3798-806, Sep 15 2013.

[17] O. O. Ahsen, Y. K. Tao, B. M. Potsaid, Y. Sheikine, J. Jiang, I. Grulkowski, T. H. Tsai, V. Jayaraman, M. F. Kraus, J. L. Connolly, J. Hornegger, A. Cable, and J. G. Fujimoto, "Swept source optical coherence microscopy using a 1310 nm VCSEL light source," *Opt Express,* vol. 21, pp. 18021-33, Jul 29 2013.

[18] C. Zhou, T. H. Tsai, H. C. Lee, T. Kirtane, M. Figueiredo, Y. K. Tao, O. O. Ahsen, D. C. Adler, J. M. Schmitt, Q. Huang, J. G. Fujimoto, and H. Mashimo, "Characterization of buried glands before and after radiofrequency ablation by using 3-dimensional optical coherence tomography (with videos)," *Gastrointest Endosc,* vol. 76, pp. 32-40, Jul 2012.

[19] T. H. Tsai, C. Zhou, Y. K. Tao, H. C. Lee, O. O. Ahsen, M. Figueiredo, T. Kirtane, D. C. Adler, J. M. Schmitt, Q. Huang, J. G. Fujimoto, and H. Mashimo, "Structural markers observed with endoscopic 3-dimensional optical coherence tomography correlating with Barrett's esophagus radiofrequency ablation treatment response (with videos)," *Gastrointest Endosc,* vol. 76, pp. 1104-12, Dec 2012.

[20] T. H. Tsai, C. Zhou, H. C. Lee, Y. K. Tao, O. O. Ahsen, M. Figueiredo, D. C. Adler, J. M. Schmitt, Q. Huang, J. G. Fujimoto, and H. Mashimo, "Comparison of Tissue Architectural Changes between Radiofrequency Ablation and Cryospray Ablation in Barrett's Esophagus Using Endoscopic Three-Dimensional Optical Coherence Tomography," *Gastroenterol Res Pract,* vol. 2012, p. 684832, 2012.

Journal Articles (in preparation)

[1] O. O. Ahsen, K. Liang, H. Lee, J. Fujimoto, and H. Mashimo, "Non-endoscopic assessment of chronic radiation proctopathy and radiofrequency ablation treatment follow-up with Optical Coherence Tomography angiography: a pilot study," *World Journal of Gastroenterology* 2018, in preparation.

Book Chapters and Theses

[1] A. D. Aguirre, C. Zhou, H.-C. Lee, O. O. Ahsen, and J. G. Fujimoto, "Optical Coherence Microscopy," *Optical Coherence Tomography: Technology and Applications,* pp. 865-911, 2015.

[2] O. O. Ahsen, "Swept source optical coherence microscopy for pathological assessment of cancerous tissues," *Massachusetts Institute of Technology*, 2013.

Patent Applications

[1] K. Liang, J. G. Fujimoto, H. Mashimo, O. O. Ahsen, H. C. Lee, M. G. Giacomelli, and Z. Wang, "Scanning optical probe," WO2015168594, 2016.

Conference Abstracts and Presentations

[1] H.-C. Lee, O. Fass, O. O. Ahsen, K. Liang, Z. Wang, M. Figueiredo, B. Potsaid, V. Jayaraman, Q. Huang, and J. G. Fujimoto, "Mo1993 Endoscopic Optical Coherence Tomography Microangiography Identifies the Altered Microvasculature of the Terminal Ileum in Crohn's Disease," *Gastrointestinal Endoscopy,* vol. 85, pp. AB511-AB512, 2017.

[2] M. G. Giacomelli, T. Yoshitake, L. C. Cahill, O. O. Ahsen, L. A. Husvogt, Y. Sheykin, H. Vardeh, J. Brooker, J. L. Connolly, J. Hornegger, A. E. Cable, and J. G. Fujimoto, "Design of a portable, wide field of view, GPU-accelerated multiphoton imaging system for real-time surgical pathology," *SPIE Photonics West,* 2017.

[3] O. O. Ahsen, H.-C. Lee, K. Liang, Z. Wang, B. M. Potsaid, M. Figueiredo, V. Jayaraman, A. E. Cable, Q. Huang, H. Mashimo, and J. G. Fujimoto, "Clinical utility of ultrahigh speed endoscopic optical coherence tomography and angiography in gastroenterology," *SPIE Photonics West,* 2017.

[4] O. O. Ahsen, H.-C. Lee, K. Liang, Z. Wang, M. Figueiredo, Q. Huang, B. Potsaid, V. Jayaraman, J. G. Fujimoto, and H. Mashimo, "Association Between Cross-Sectional and En Face Image Features of Barrett's Esophagus and Dysplasia with Endoscopic Optical Coherence Tomography," *Gastroenterology,* vol. 152, pp. S841-S842, 2017.

[5] Z. Wang, H.-C. Lee, O. O. Ahsen, K. Liang, M. Figueiredo, Q. Huang, J. G. Fujimoto, and H. Mashimo, "Sa2030 Novel Optical Coherence Tomography Image Analysis Reveals Subsquamous Glandular Structures as Strong Predictors of Poorer Response to Radiofrequency Ablation in Barrett's Esophagus," *Gastroenterology,* vol. 150, p. S434, 2016.

[6] K. Liang, O. O. Ahsen, H.-C. Lee, Z. Wang, B. M. Potsaid, M. Figueiredo, M. G. Giacomelli, V. Jayaraman, Q. Huang, H. Mashimo, and J. G. Fujimoto, "Ultrahigh speed en face OCT capsule imaging for endoscopic surveillance," *SPIE Photonics West,* 2016.

[7] H.-C. Lee, O. O. Ahsen, K. Liang, Z. Wang, M. Figueiredo, B. Potsaid, V. Jayaraman, Q. Huang, H. Mashimo, and J. G. Fujimoto, "Sa2034 Novel Ultrahigh Speed Endoscopic OCT Angiography Identifies Both Architectural and Microvascular Changes in Patients With Gastric Antral Vascular Ectasia (GAVE) Undergoing Radiofrequency Ablation (RFA) Treatment," *Gastroenterology,* vol. 150, pp. S435-S436, 2016.

[8] M. G. Giacomelli, T. Yoshitake, L. C. Cahill, O. O. Ahsen, Y. Sheykin, H. Vardeh, J. Brooker, L. A. Husvogt, J. Hornegger, J. L. Connolly, A. E. Cable, and J. G. Fujimoto, "Nonlinear microscopy for rapid assessment of breast surgical specimens," *SPIE Photonics West,* 2016.

[9] M. G. Giacomelli, T. Yoshitake, O. O. Ahsen, L. A. Husvogt, Y. Sheykin, H. Vardeh, J. Brooker, J. L. Connolly, J. Hornegger, A. E. Cable, and J. G. Fujimoto, "Design of a portable, wide field of view, GPU-accelerated multiphoton imaging system for real-time imaging of breast surgical specimens," *SPIE Photonics West,* 2016.

[10] O. O. Ahsen, H.-C. Lee, K. Liang, Z. Wang, M. Figueiredo, M. G. Giacomelli, Q. Huang, B. Potsaid, V. Jayaraman, and J. G. Fujimoto, "Mo1977 Endoscopic OCT Angiography Enables Visualization of Microvascular Changes to Assess RFA Treatment of Chronic Radiation Proctitis," *Gastrointestinal Endoscopy,* vol. 83, p. AB481, 2016.

[11] Z. Wang, H.-C. Lee, M. G. Giacomelli, K. Liang, O. O. Ahsen, M. Figueiredo, Q. Huang, J. G. Fujimoto, and H. Mashimo, "Su2034 Automated Optical Coherence Tomography Image Processing for Three Dimensional Detection and Visualization of Subsurface Glands in Barrett's Esophagus With Dysplasia," *Gastroenterology,* vol. 148, pp. S-580-S-581, 2015.

[12] Z. Wang, H.-C. Lee, O. O. Ahsen, B. Lee, W. Choi, B. M. Potsaid, V. Jayaraman, A. E. Cable, K. Liang, and J. G. Fujimoto, "Endoscopic and Ophthalmic Swept Source Polarization Sensitive OCT," *SPIE Photonics West,* 2015.

[13] K. Liang, Z. Wang, O. O. Ahsen, H.-C. Lee, M. Figueiredo, B. Potsaid, M. G. Giacomelli, V. Jayaraman, Q. Huang, and H. Mashimo, "Su2036 Ultrahigh Speed Optical Coherence Tomography

Imaging Capsule for En Face and Cross Sectional Mapping of Esophageal Architecture," *Gastroenterology,* vol. 148, pp. S-581, 2015.

[14] K. Liang, O. O. Ahsen, Z. Wang, H.-C. Lee, M. G. Giacomelli, B. M. Potsaid, V. Jayaraman, T.-H. Tsai, W. Liang, A. E. Cable, H. Mashimo, and J. G. Fujimoto, "Ultrahigh Speed Swept Source OCT Forward Viewing Endomicroscopy," *SPIE Photonics West,* 2015.

[15] H.-C. Lee, K. Liang, O. O. Ahsen, M. G. Giacomelli, Z. Wang, M. Figueiredo, Q. Huang, B. Potsaid, V. Jayaraman, and J. G. Fujimoto, "Su2035 Ultrahigh Speed Endoscopic Optical Coherence Tomography and Angiography for Investigating Terminal Ileum With Chronic Inflammation," *Gastroenterology,* vol. 148, pp. S-581, 2015.

[16] H.-C. Lee, O. O. Ahsen, K. Liang, Z. Wang, M. G. Giacomelli, M. Figueiredo, Q. Huang, B. Potsaid, V. Jayaraman, and H. Mashimo, "Su1715 Ultrahigh Speed Endoscopic Optical Coherence Tomography Angiography for Visualization of Subsurface Vasculature in Barrett's Esophagus and Dysplasia," *Gastrointestinal Endoscopy,* vol. 5, p. AB388, 2015.

[17] H.-C. Lee, O. O. Ahsen, K. Liang, M. G. Giacomelli, Z. Wang, B. M. Potsaid, V. Jayaraman, M. Figueiredo, Q. Huang, A. E. Cable, H. Mashimo, and J. G. Fujimoto, "Ultrahigh Speed Endoscopic Structural and Angiographic OCT Imaging," *SPIE Photonics West,* 2015.

[18] O. O. Ahsen, H.-C. Lee, K. Liang, M. G. Giacomelli, Z. Wang, B. M. Potsaid, M. Figueiredo, Q. Huang, A. E. Cable, V. Jayaraman, H. Mashimo, and J. G. Fujimoto, "Ultrahigh Speed Endoscopic Optical Coherence Tomography for Structural and Angiographic Imaging," *SPIE Photonics West,* 2015.

[19] O. O. Ahsen, H.-C. Lee, K. Liang, M. G. Giacomelli, Z. Wang, M. Figueiredo, Q. Huang, B. Potsaid, V. Jayaraman, and J. G. Fujimoto, "Su2030 En Face Optical Coherence Tomography Visualization of Mucosal Surface Patterns for Identifying Early Malignancy in the Upper GI Tract," *Gastroenterology,* vol. 148, pp. S-579, 2015.

[20] T.-H. Tsai, O. O. Ahsen, H.-C. Lee, K. Liang, M. G. Giacomelli, B. M. Potsaid, Y. K. Tao, V. Jayaraman, M. F. Kraus, J. Hornegger, M. Figueiredo, Q. Huang, H. Mashimo, A. E. Cable, and J. G.

Fujimoto, "Ultrahigh Speed Endoscopic Swept Source Optical Coherence Tomography using a VCSEL Light Source and Micromotor Catheter," *SPIE Photonics West* 2014.

[21] H.-C. Lee, O. O. Ahsen, T.-H. Tsai, M. G. Giacomelli, Z. Wang, K. Liang, M. Figueiredo, Q. Huang, B. Potsaid, and J. G. Fujimoto, "Su2007 Novel Ultrahigh Speed Optical Coherence Tomography System and Micromotor Imaging Probe for Investigating Microvasculature in the Gastrointestinal Tract," *Gastroenterology,* vol. 5, pp. S-520-S-521, 2014.

[22] M. G. Giacomelli, T.-H. Tsai, O. O. Ahsen, H.-C. Lee, K. Liang, Z. Wang, M. Figueiredo, Q. Huang, B. Potsaid, and J. G. Fujimoto, "Su2009 Ultrahigh Speed Micromotor Optical Coherence Tomography Enables Improved Access, Image Quality, and Maneuverability in Upper and Lower Endoscopy," *Gastroenterology,* vol. 5, pp. S-521, 2014.

[23] O. O. Ahsen, H.-C. Lee, K. Liang, M. G. Giacomelli, T.-H. Tsai, Z. Wang, M. Figueiredo, Q. Huang, B. Potsaid, and J. G. Fujimoto, "Su2003 Ultrahigh Speed Optical Coherence Tomography With Micromotor Imaging Probe Enables Three-Dimensional Visualization of Mucosal Surface Patterns in the Gastrointestinal Tract," *Gastroenterology,* vol. 5, pp. S-519, 2014.

[24] T.-H. Tsai, H.-C. Lee, Y. K. Tao, O. O. Ahsen, K. Liang, M. G. Giacomelli, M. Figueiredo, C. Zhou, D. C. Adler, and J. M. Schmitt, "963 Length of Proximal Extent of Subsquamous Intestinal Metaplasia Correlates With Difficult Eradication of Barrett Esophagus by Radiofrequency Ablation," *Gastroenterology,* vol. 144, pp. S-174, 2013.

[25] Y. K. Tao, O. O. Ahsen, P. Fendel, A. E. Cable, D. Shen, J. L. Connolly, and J. G. Fujimoto, "Diagnosis and Subclassification of Breast Pathologies Using Mosaicked Large-Field Two-Photon Microscopy," *SPIE Photonics West* 2013.

[26] Y. Sheykin, Y. K. Tao, O. O. Ahsen, D. Shen, D. Schmolze, N. Johnson, J. G. Fujimoto, and J. L. Connolly, "Evaluation of Breast Pathologies Using Multi-Photon Microscopy," *Laboratory Investigation,* vol. 93, pp. 69a-69a, Feb 2013.

[27] O. O. Ahsen, Y. K. Tao, J. Jiang, B. M. Potsaid, Y. Sheykin, A. D. Aguirre, V. Jayaraman, A. Cable, J. L. Connolly, and J. G. Fujimoto, "Swept Source Optical Coherence Microscopy using VCSEL Technology," *SPIE Photonics West* 2013.

[28] O. O. Ahsen, M. G. Giacomelli, T.-H. Tsai, Y. K. Tao, H.-C. Lee, K. Liang, C. Zhou, M. Figueiredo, D. C. Adler, and J. M. Schmitt, "Tu1963 Contrast Enhancement for Three-Dimensional Optical Coherence Tomography Images for Improved Delineation of Subsurface Structures," *Gastroenterology,* vol. 144, pp. S-892, 2013.

[29] C. Zhou, T. H. Tsai, H. C. Lee, T. Kirtane, M. Figueiredo, Y. K. Tao, O. O. Ahsen, D. C. Adler, J. M. Schmitt, and Q. Huang, "Sa1834 Identification and Characterization of Subsquamous Intestinal Metaplasia Pre-and Post-Radiofrequency Ablation Using Three-Dimensional Optical Coherence Tomography," *Gastroenterology,* vol. 142, pp. S-336-S-337, 2012.

[30] C. Zhou, T. H. Tsai, H. C. Lee, M. Figueiredo, T. Kirtane, Y. K. Tao, O. O. Ahsen, D. C. Adler, J. M. Schmitt, Q. Huang, J. G. Fujimoto, and H. Mashimo, "Characterization of Sub-squamous Intestinal Metaplasia (SSIM) Pre- and Post-Radiofrequency Ablation using Three-dimensional Optical Coherence Tomography," *SPIE Photonics West,* 2012.

[31] T. H. Tsai, C. Zhou, H. C. Lee, Y. K. Tao, O. O. Ahsen, T. Kirtane, M. Figueiredo, D. C. Adler, J. M. Schmitt, Q. Huang, J. G. Fujimoto, and H. Mashimo, "547 Structural Markers Observed With Three-Dimensional Optical Coherence Tomography Predict Treatment Response of Radiofrequency Ablation of Barrett's Esophagus," *Gastroenterology,* vol. 142, pp. S-109-S-110, 2012.

[32] Y. K. Tao, O. O. Ahsen, P. Fendel, A. E. Cable, D. Shen, J. L. Connolly, and J. G. Fujimoto, "Breast Pathology Assessment Using Two-Photon Microscopy," *SPIE Photonics West* 2012.

[33] Y. Tao, O. O. Ahsen, T. H. Tsai, C. Zhou, H. C. Lee, T. Kirtane, M. Figueiredo, D. C. Adler, J. M. Schmitt, Q. Huang, J. G. Fujimoto, and H. Mashimo, "549 Follow-up of Treatment Response of Radiofrequency Ablation of Barrett's Esophagus Using Optical Coherence Tomography," *Gastroenterology,* vol. 142, pp. S-110, 2012.

[34] T. H. Tsai, C. Zhou, H. C. Lee, T. Kirtane, Y. K. Tao, O. O. Ahsen, M. Figueiredo, D. C. Adler, J. M. Schmitt, and Q. Huang, "Three-Dimensional Optical Coherence Tomography Assessment During Radiofrequency Ablation in Barrett's Esophagus Reveals Depths of Tissue Destruction and Potential Areas of Residual Glands," *Gastroenterology,* vol. 140, pp. S-767-S-768, 2011.

[35] H. C. Lee, C. Zhou, T. H. Tsai, T. Kirtane, Y. K. Tao, O. O. Ahsen, D. C. Adler, J. M. Schmitt, Q. Huang, and J. G. Fujimoto, "Three-Dimensional Optical Coherence Tomography on Endoscopic Mucosal Resection Specimens Confirms Identification of Malignant From Metaplastic Lesions in Patients With Barrett's Esophagus," *Gastroenterology,* vol. 140, pp. S-762, 2011.

Appendix – training materials

Volumetric (En face and Cross-sectional) OCT Reading - Overall Study Design

- Part 1 - Training:
  - En face and cross-sectional OCT images of normal squamous esophagus, non-dysplastic BE and neoplasia will be shown.
  - En face and cross-sectional features will be taught.
  - Several volumetric datasets will be assessed by the researcher.
- Part 2 – Pre-test:
  - Reader will go over several datasets by himself/herself and then will receive feedback from the researcher.
- Part 3 – Validation:
  - Reader will read the remaining OCT datasets.

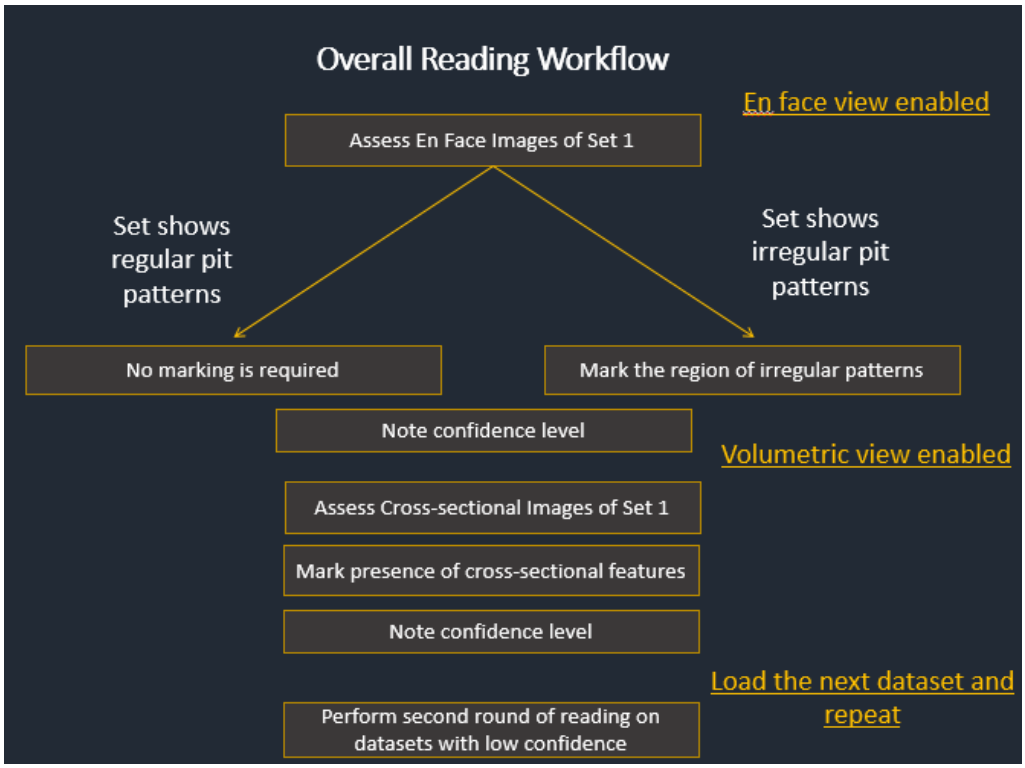

Workflow Overview on the Visualization Software

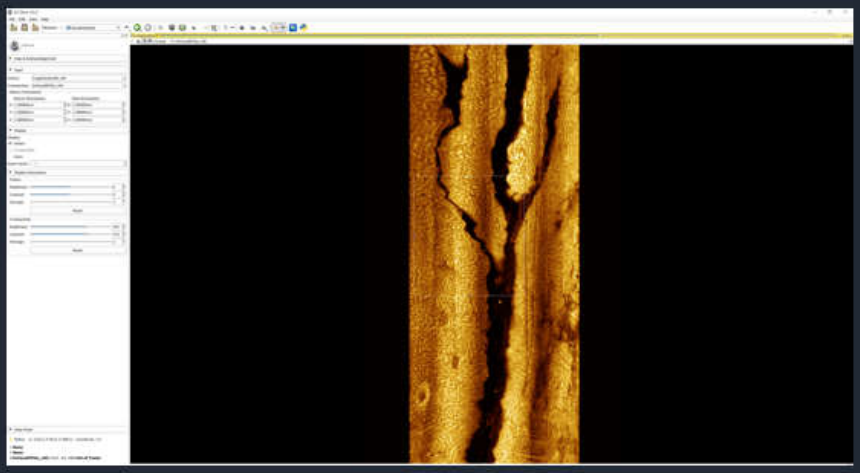

"En face only" view

Workflow Overview on the Visualization Software

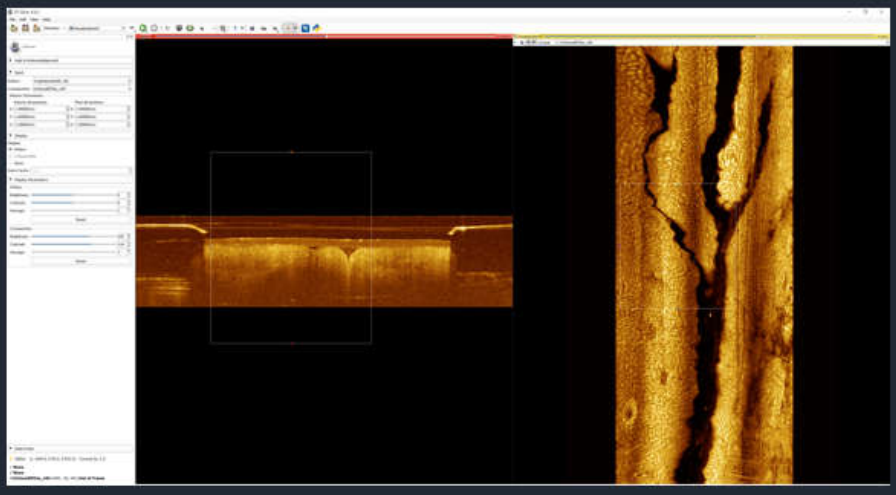

Enable volumetric view to
assess cross sections

Concept of Pit Patterns

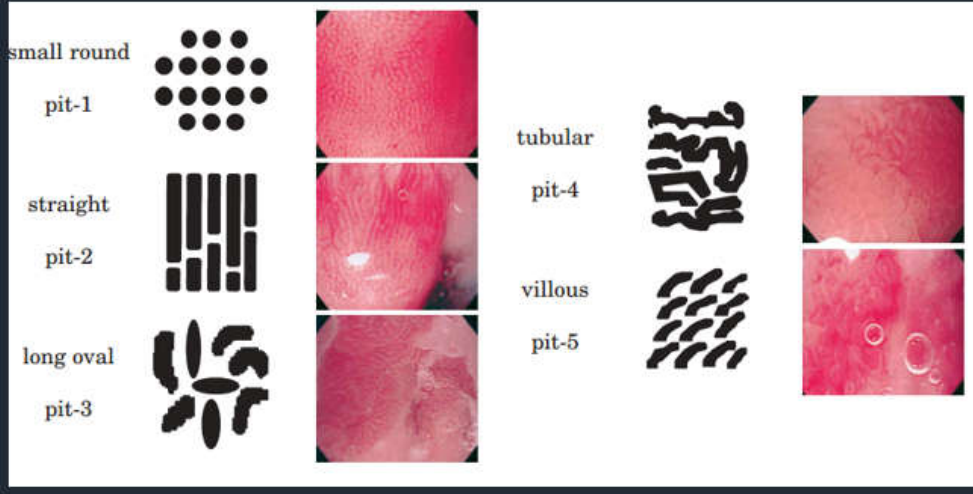

- Intestinal tissues have specific mucosal en face features (pit patterns) that are associated with disease presence and progression.

Endo, GIE02

Size and Morphological Variation of Pit Patterns, Narrow band Imaging Literature

Note, the features can be large, small, oval, curved etc. The main feature is to look at the regularity of the features.

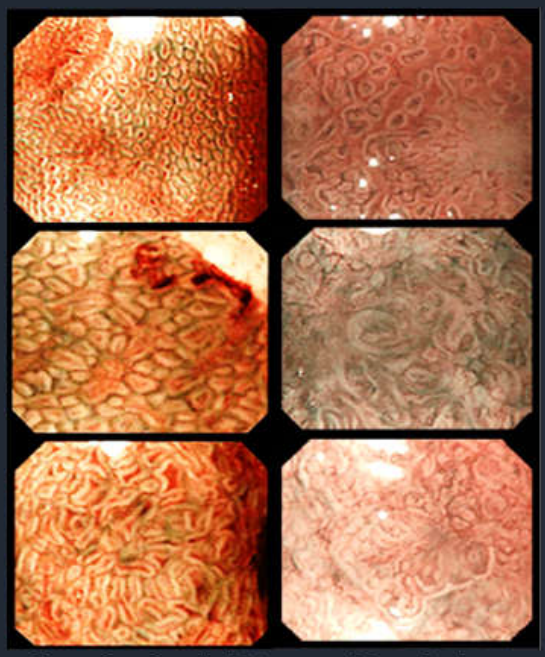

Non-dysplastic BE | Neoplasia

Kara, GIE06

Normal Squamous Esophagus

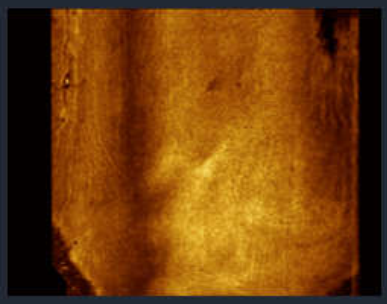

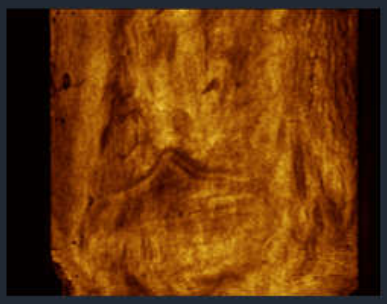

1mm

Epithelial layer

Lamina propria/Muscularis mucosa layer

- The main defining criteria for normal squamous esophagus is the presence of a featureless appearance (i.e. no pit patterns) within the superficial epithelial layer. When you go deeper to the lamina propria/muscularis mucosa layers you expect to see some complex structures.
- There can be local areas that look different in a normal squamous esophagus due to differences in contact, pressure, erosion, sheath reflection, epithelial thickness etc.

Variations of Regular Pit Patterns in Non-dysplastic BE

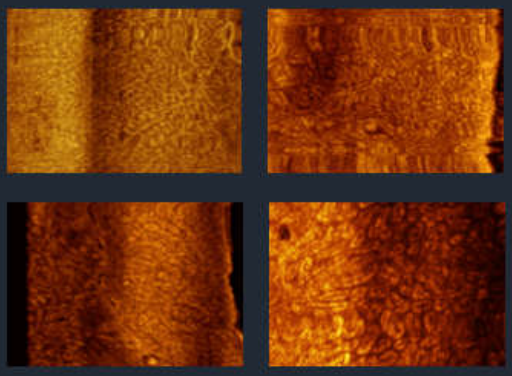

1mm

- Pit patterns in non-dysplastic BE can have different shape and sizes. Main feature to look at is presence of regular pit patterns.

Irregular Pit Patterns in Neoplasia

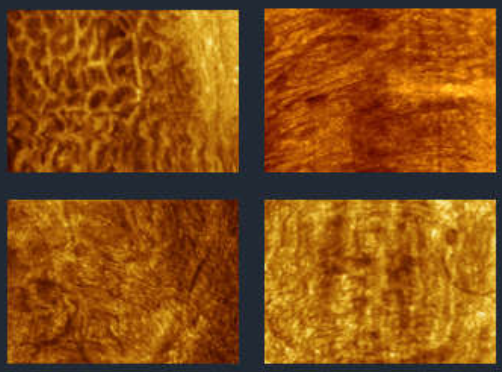

1mm

- Neoplasia is characterized by irregularity of the pit pattern architecture, which manifests itself as a combination of abnormally elongated, enlarged and branched pit pattern structures, and areas with loss of pit pattern structures.

Concept of Variations of Pit Pattern Morphology on a Large FOV Image

Narrow band Image of **Non-dysplastic BE**

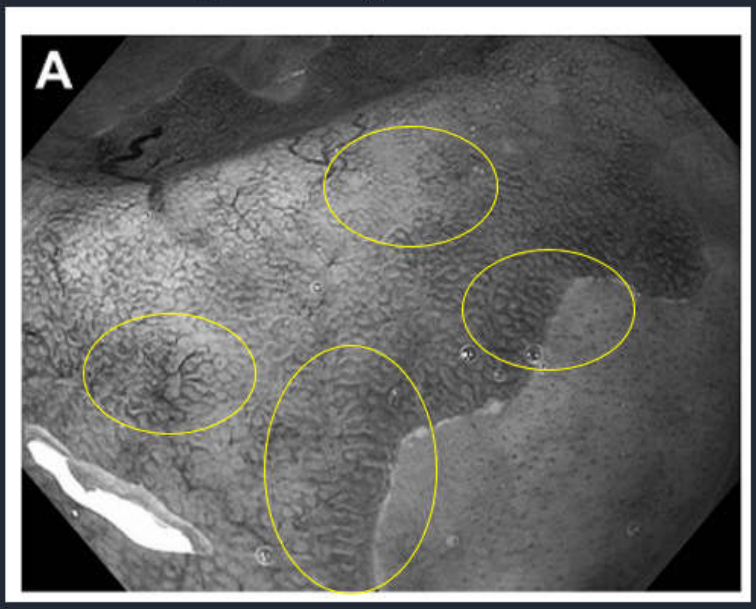

Bergman, Sharma, GUT13

Concept of Variations of Pit Pattern Morphology on a Large FOV Image

Narrow band Image of **Neoplasia**

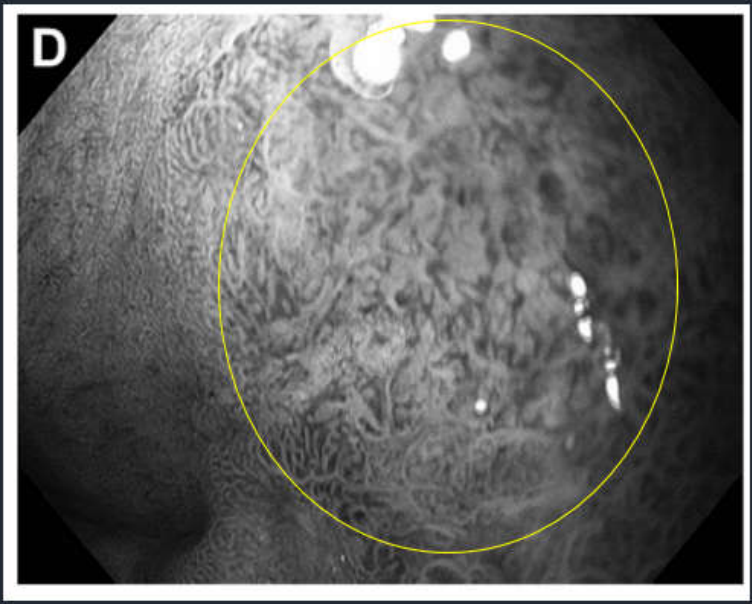

Bergman, Sharma, GUT13

Examples of Pit Patterns as seen with en face OCT

- Some commonly observed pit pattern structures.
- The exact shape and size can vary from these examples.
- Motion artifacts, loss of contact etc. can cause further changes in the appearance within a given region of a dataset as well as at different regions of the dataset.

Examples of Regular and Irregular Pit Patterns

Regular

Overall homogeneous appearance with mostly similar type of pits within the region. Patterns are densely packed.

Irregular

Sparse distribution of pits (regions with loss of pit patterns). Some pits are enlarged. Heterogeneity in the observed pit pattern types.

Examples of Regular and Irregular Pit Patterns

Regular

Motion artifacts cause disruption of structures.

Irregular

Pits are distributed sparsely. Regions with loss of pit pattern structures.

Examples of Regular and Irregular Pit Patterns

Regular

Motion artifacts cause disruption of structures. There can be a few pits that look enlarged compared to others.

Irregular

Patterns look "significantly" enlarged. Some of the pits show branching structures.

Examples of Regular and Irregular Pit Patterns

Irregular

"Significant" heterogeneity in the observed pit pattern types.

Examples of Artifacts on Regular Pit Patterns

Regular

Stretched and wavy appearance, followed by a compressed appearance.

Regular

A region where no clear patterns can be observed within normal, densely packed pit patterns.

3 Depth Levels of En Face Stack

1 – Out of Tissue

- Identify parts with high sheath reflection and struts. Ignore anything below those.

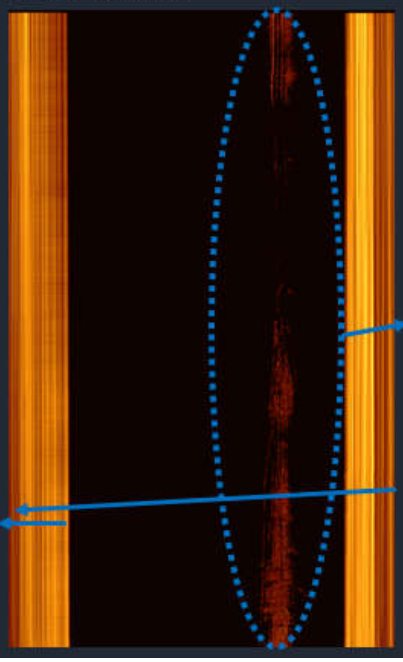

3 Depth Levels of En Face Stack

2 – Tissue Surface

- Identify regions of BE and normal squamous esophagus (if exist).

3 Depth Levels of En Face Stack

3 – Evaluation Depth

- Between <u>100 - 300 um</u> below "Tissue Surface" level. Shows best visualization of pit patterns. Reading should be focused around this level.

Reading Examples
Non-dysplastic BE 1

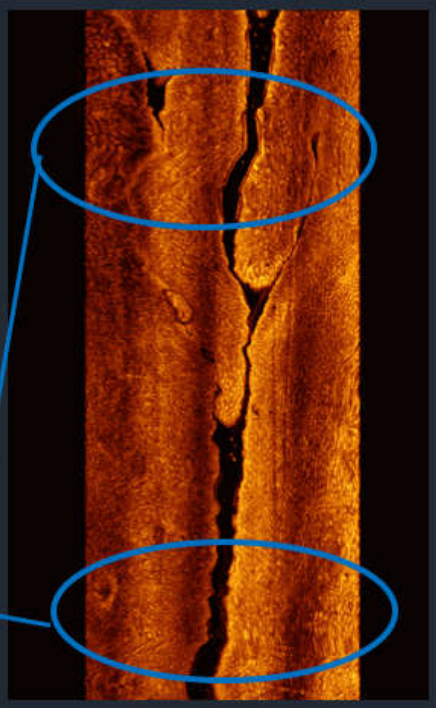

Regular

Reading Examples
Non-dysplastic BE 2

- Scroll back and forth in depth. Evaluation depth can be different in different parts of the tissue.
- Structures below high sheath reflection can look distorted.

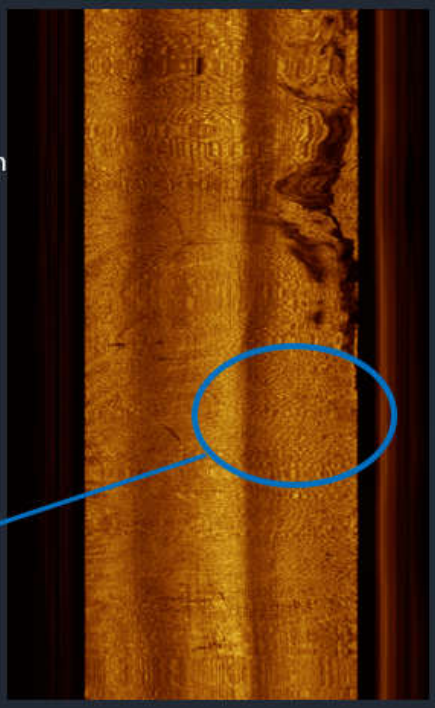

Regular

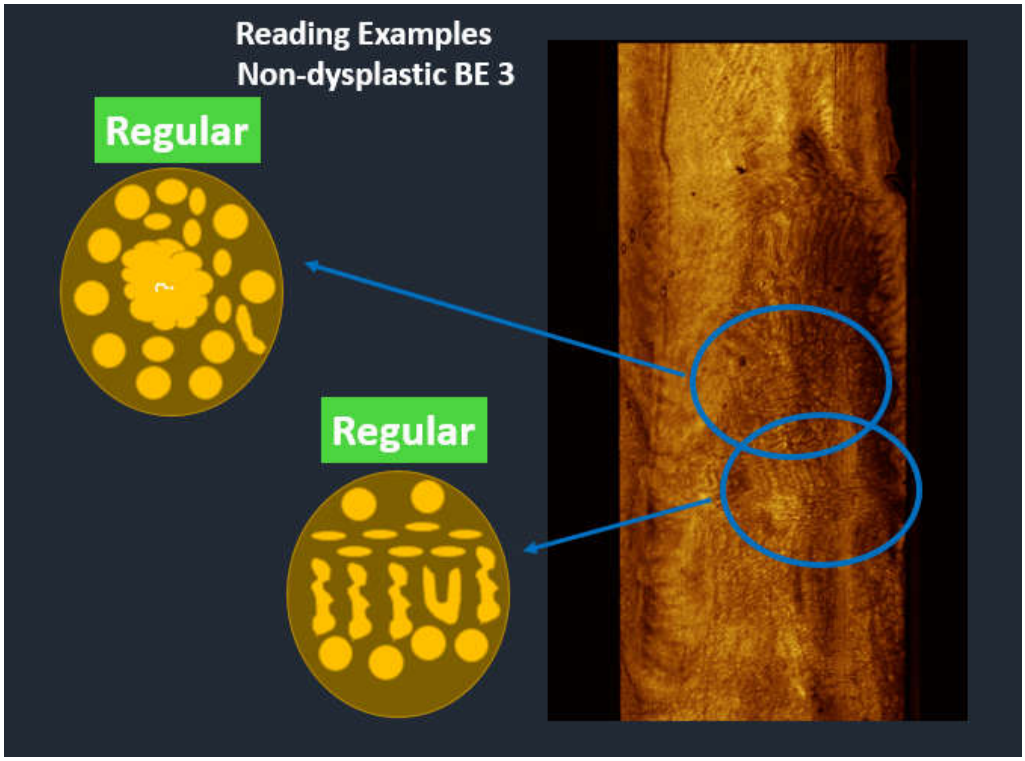
Reading Examples
Non-dysplastic BE 3
Regular
Regular

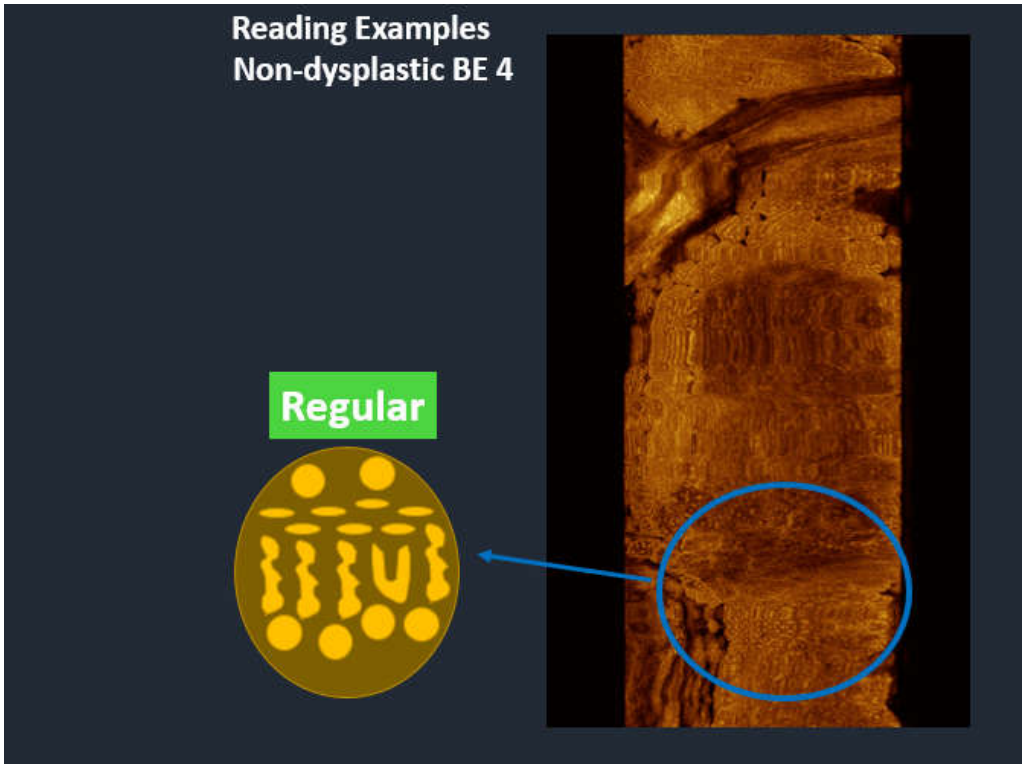
Reading Examples
Non-dysplastic BE 4
Regular

Reading Examples
Non-dysplastic BE 5

- Be careful to the contact and signal variations along the circumference.

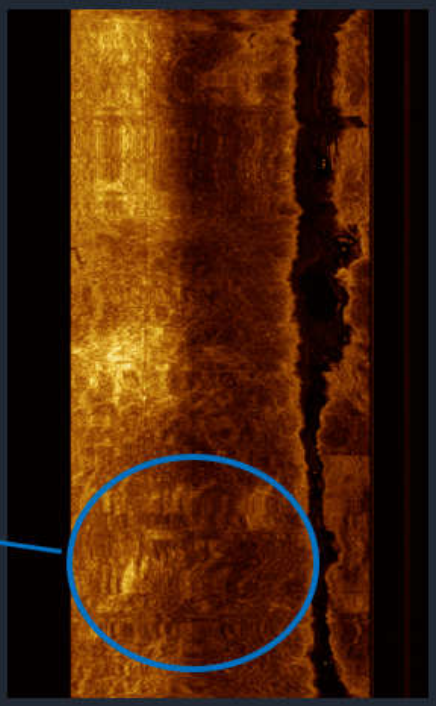

Reading Examples
Non-dysplastic BE 6

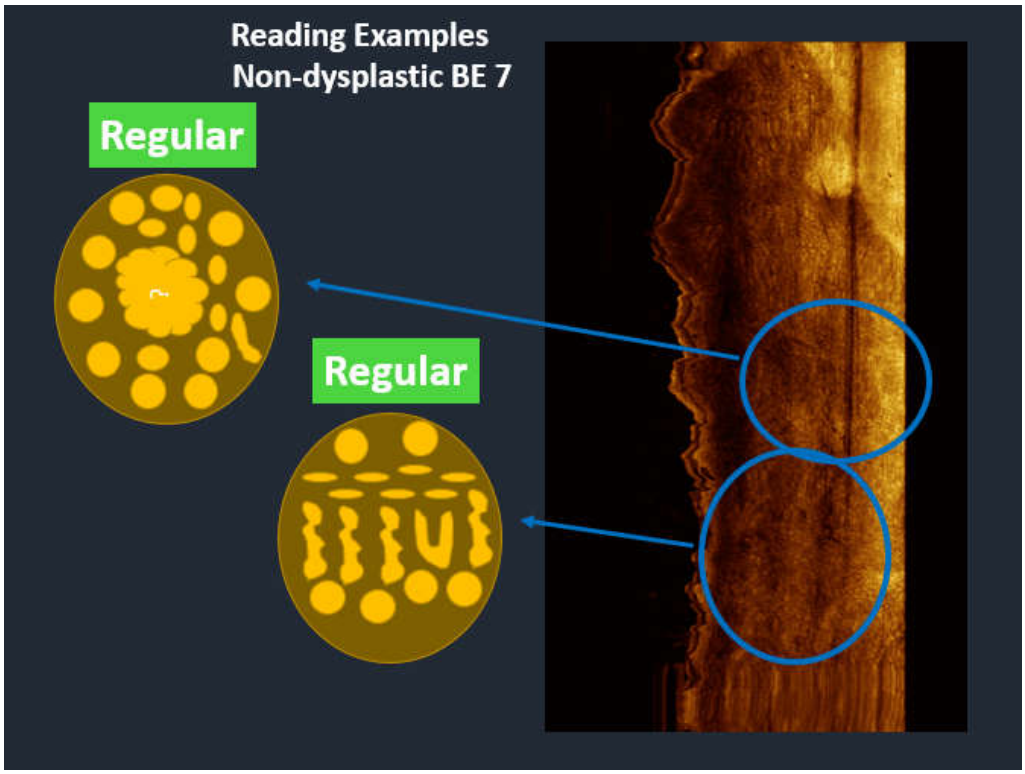
Reading Examples
Non-dysplastic BE 7
Regular
Regular

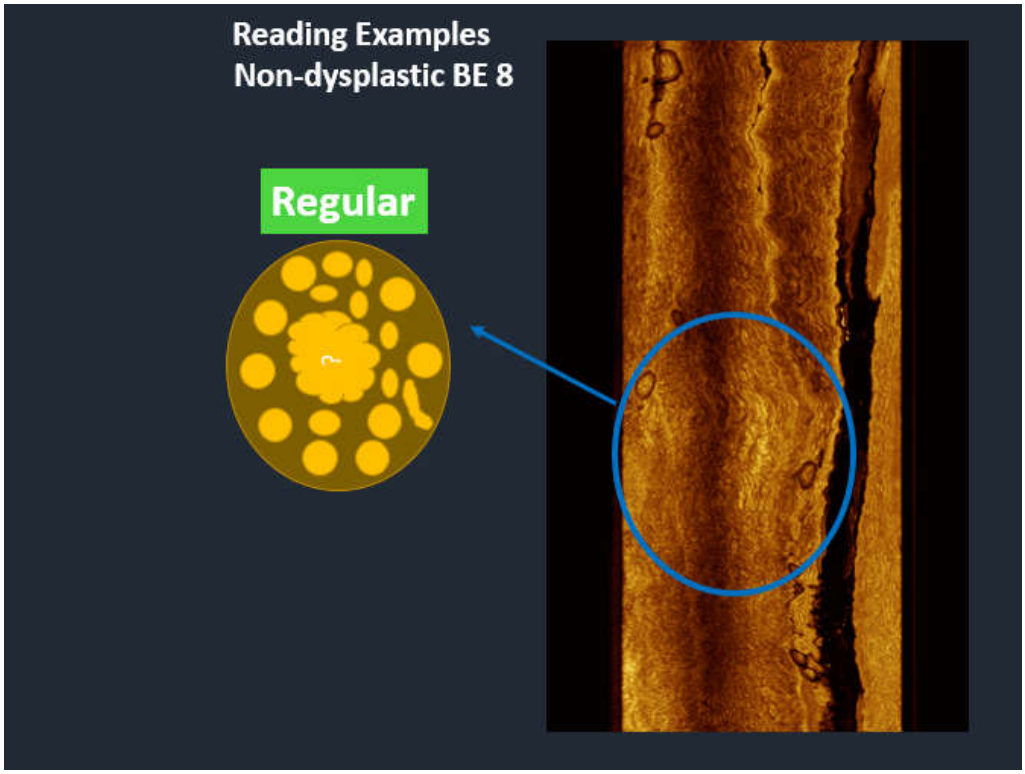
Reading Examples
Non-dysplastic BE 8
Regular

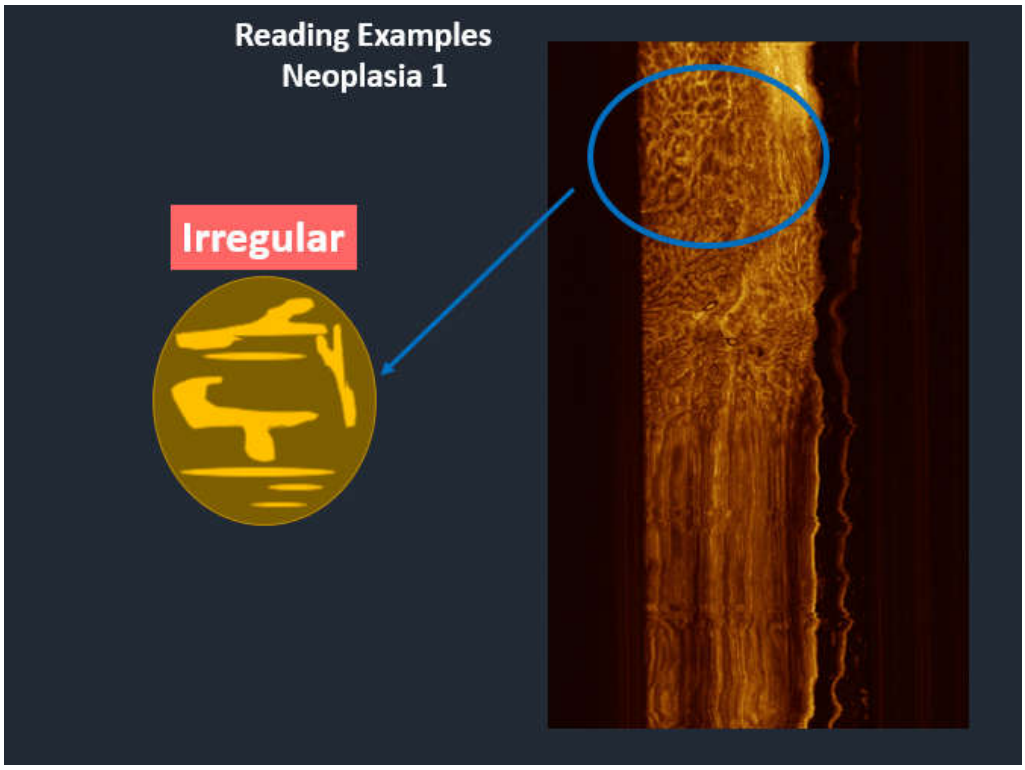
Reading Examples
Neoplasia 1
Irregular

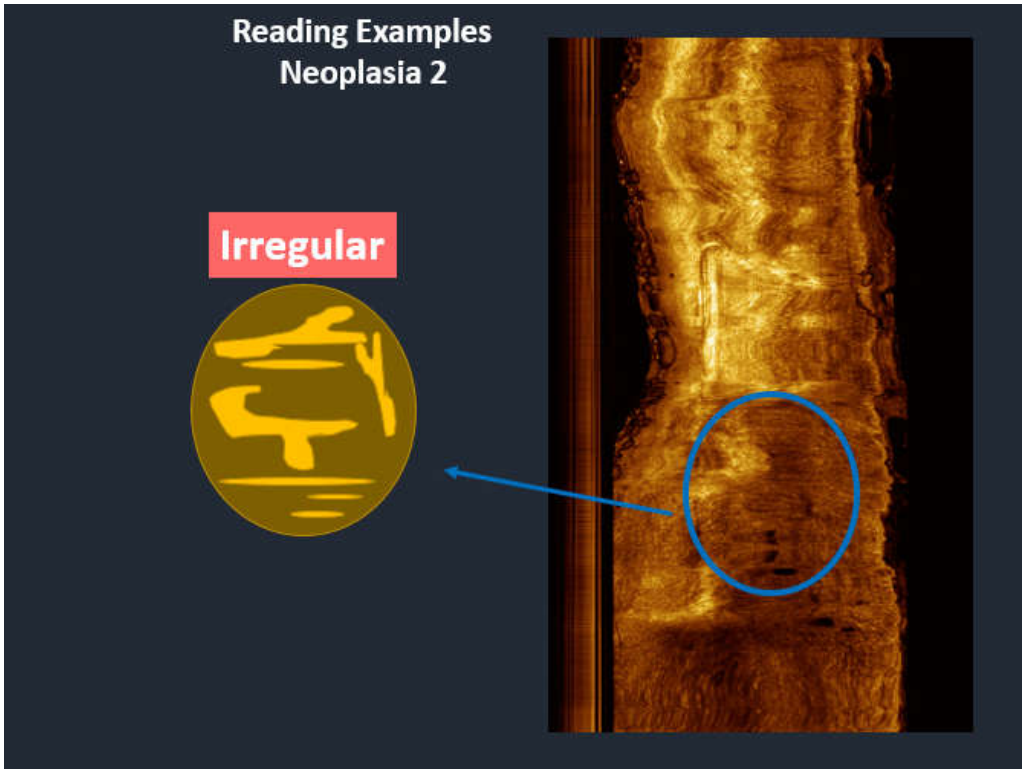
Reading Examples
Neoplasia 2
Irregular

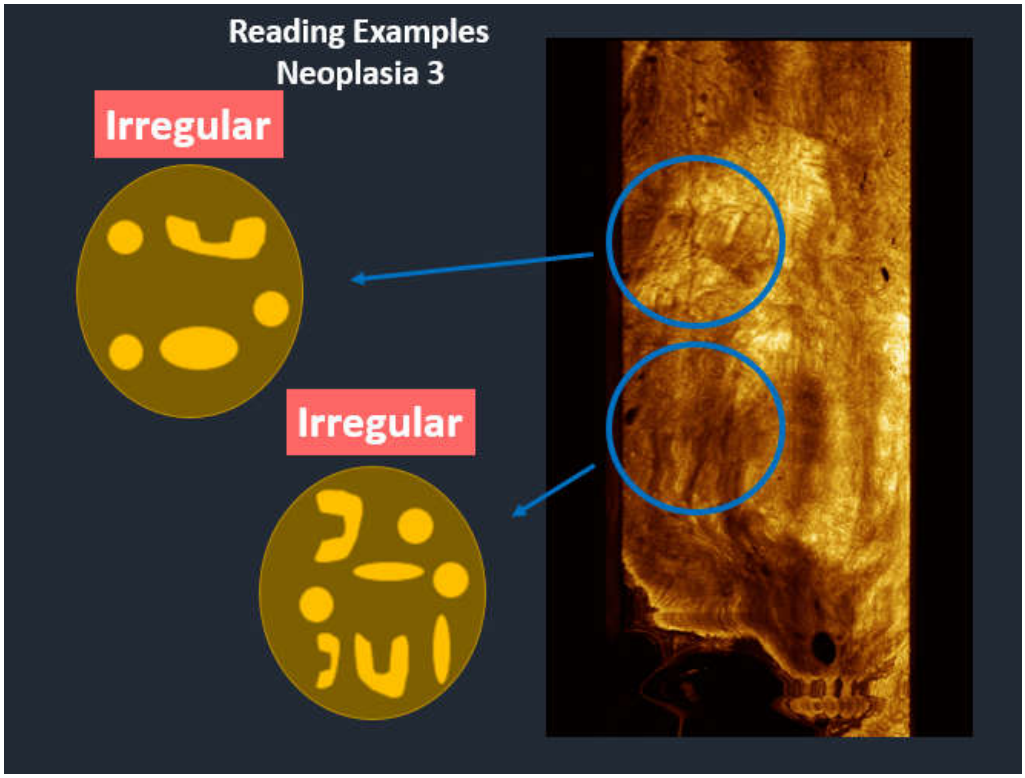
Reading Examples
Neoplasia 3
Irregular
Irregular

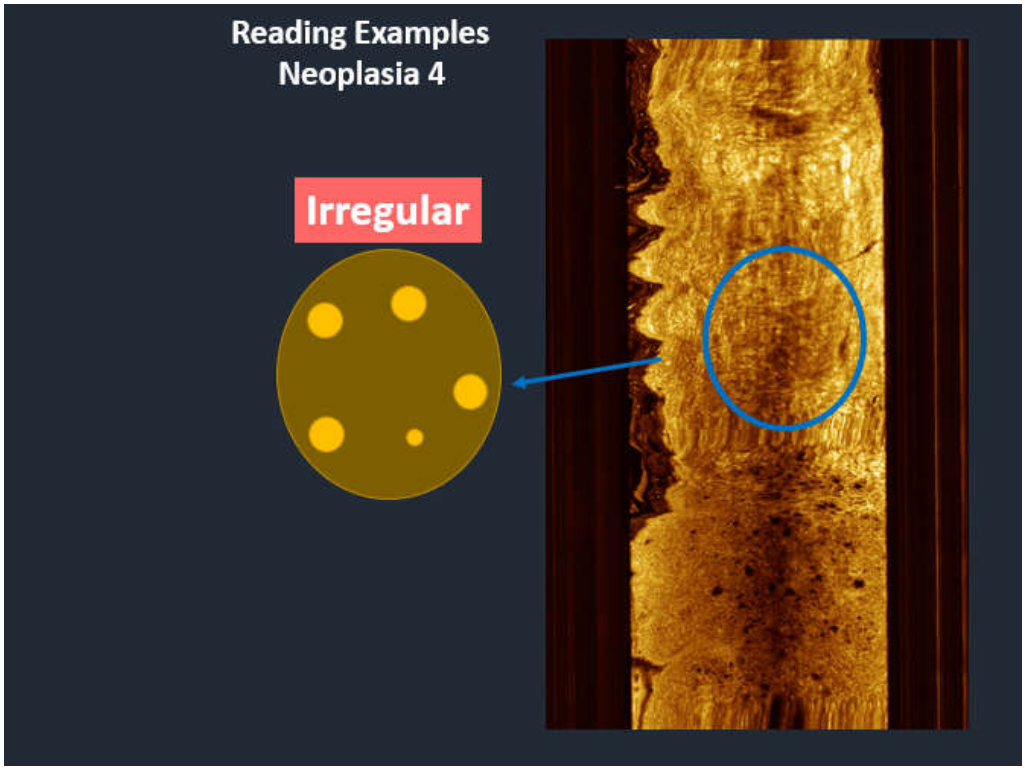
Reading Examples
Neoplasia 4
Irregular

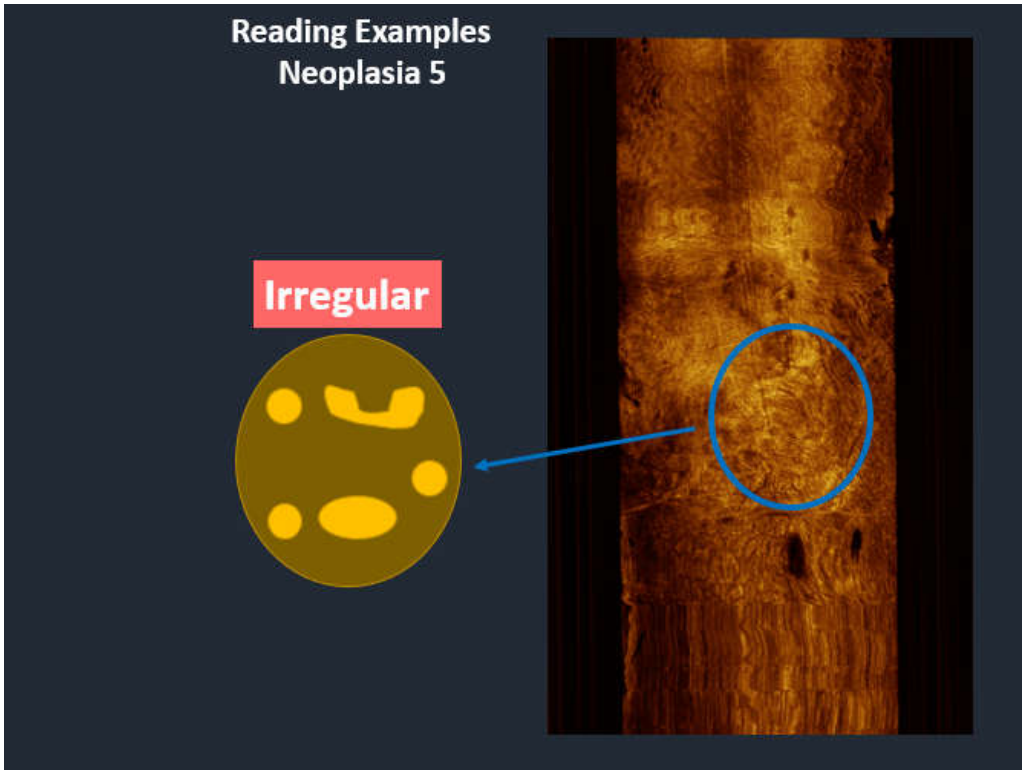
Reading Examples
Neoplasia 5
Irregular

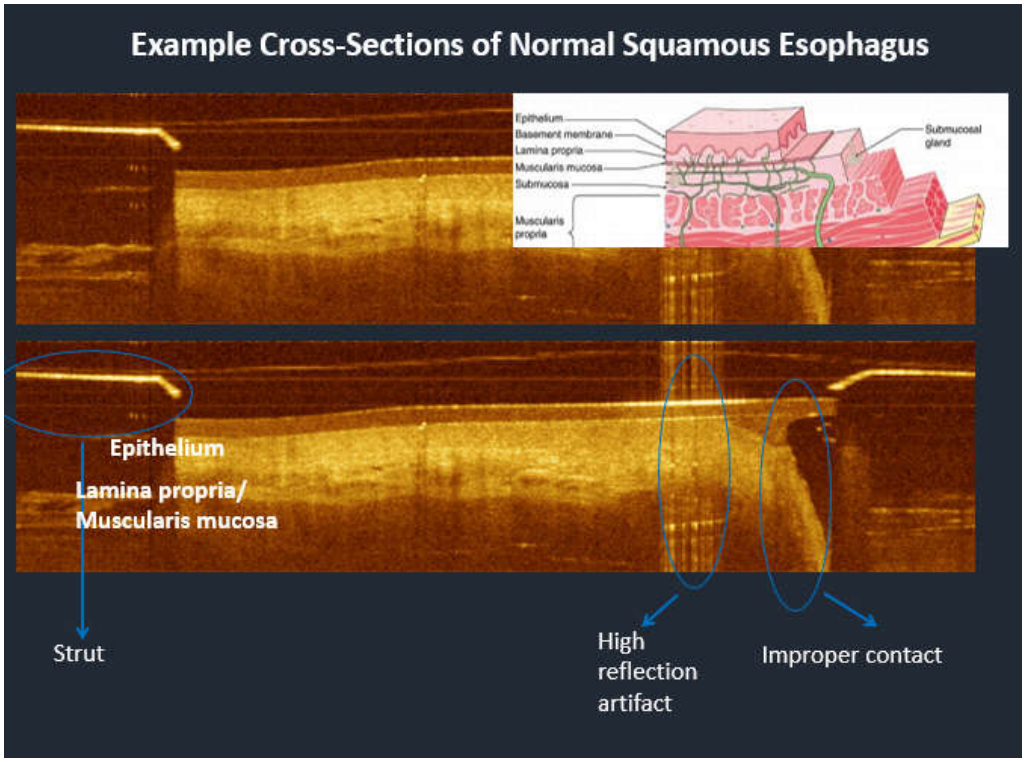
Example Cross-Sections of Normal Squamous Esophagus
Epithelium
Basement membrane
Lamina propria
Muscularis mucosa
Submucosa
Muscularis propria
Submucosal gland
Epithelium
Lamina propria/
Muscularis mucosa
Strut
High reflection artifact
Improper contact

Example Cross-Sections of Barrett's Esophagus

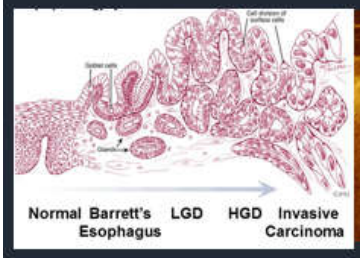

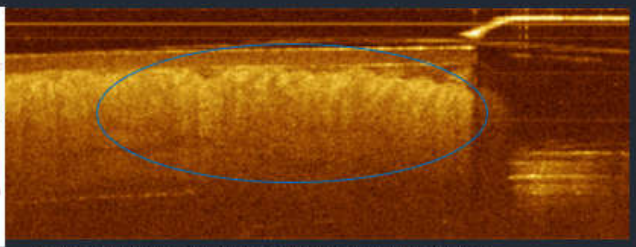

Epithelium shows crypt(columnar) features

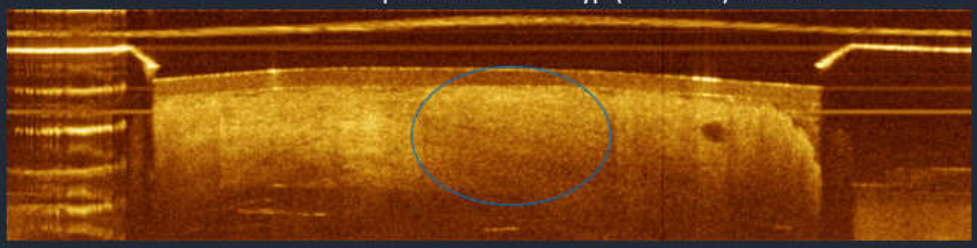

Epithelium does not show crypt(columnar) features

(A) Mucosal Layering (present vs. absent)

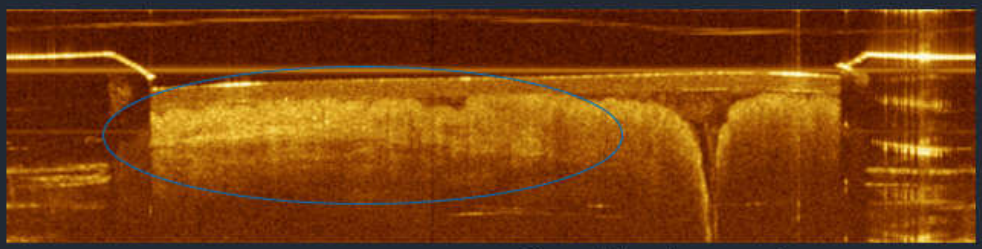

Mucosal layering **present**

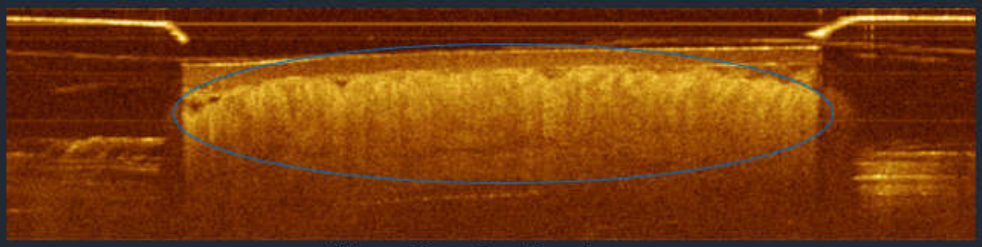

Mucosal layering **absent**

(B) Surface/subsurface Intensity (lower vs. higher)

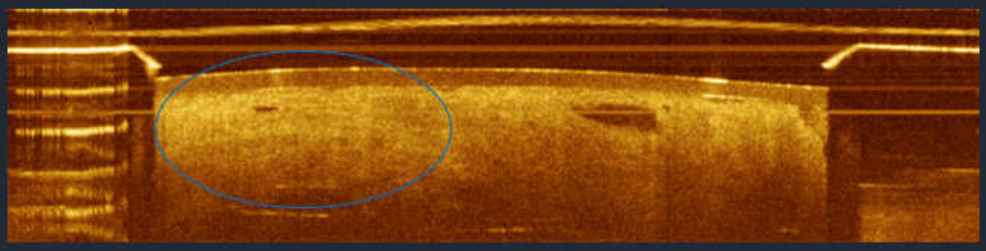

Surface signal **lower or equal** to subsurface signal

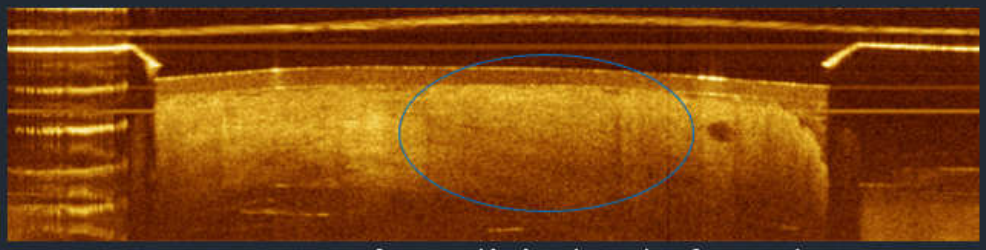

Surface signal **higher** than subsurface signal

(C) Atypical Glandular Structures (<=5 vs. >5)

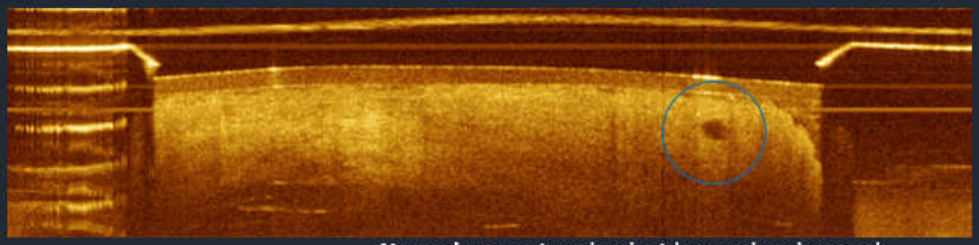

Normal appearing gland with round and smooth contour

Atypical gland with abnormal contour and debris

(C) Atypical Glandular Structures (<=5 vs. >5)

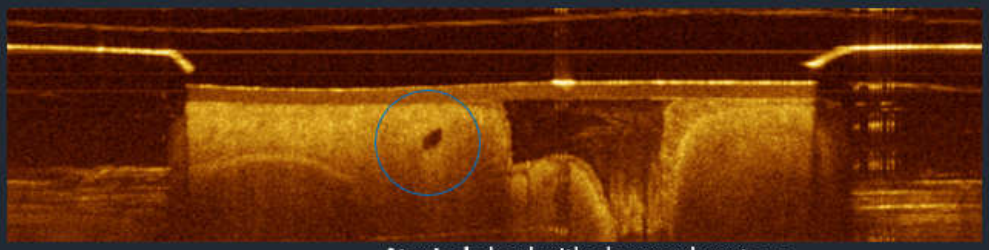

Atypical gland with abnormal contour

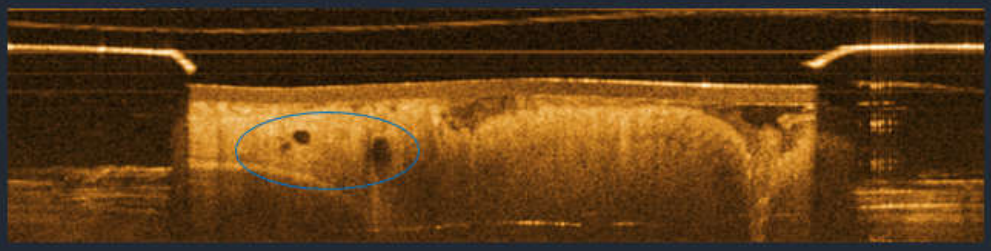

Atypical glands with heterogeneous size and clustering

(C) Atypical Glandular Structures (<=5 vs. >5)

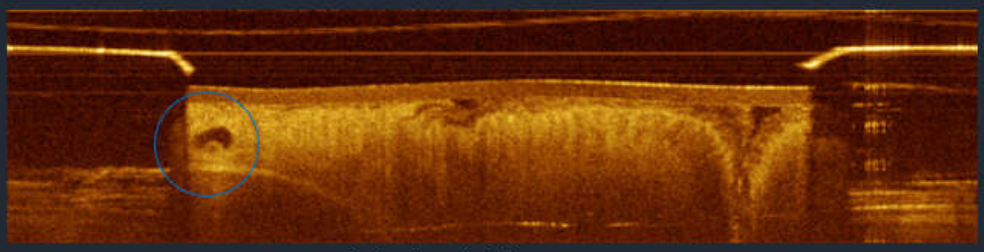

Atypical gland with debris

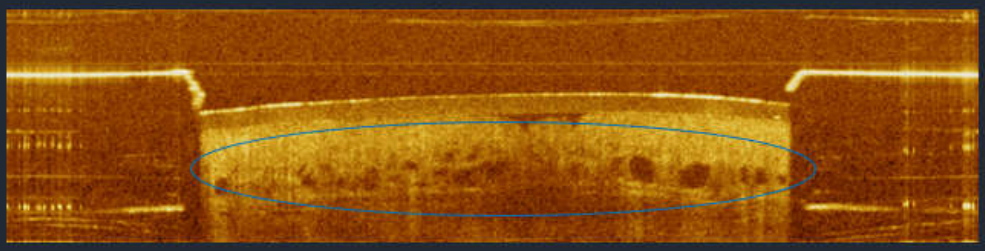

Atypical glands with heterogeneous size and clustering

Bibliography

[1] R. L. Siegel, K. D. Miller, and A. Jemal, "Cancer Statistics, 2017," *CA Cancer J Clin,* vol. 67, pp. 7-30, Jan 2017.

[2] S. J. Spechler, "Dysplasia in Barrett's esophagus: limitations of current management strategies," *American Journal of Gastroenterology,* vol. 100, pp. 927-935, Apr 2005.

[3] A. Rastogi, S. Puli, H. B. El-Serag, A. Bansal, S. Wani, and P. Sharma, "Incidence of esophageal adenocarcinoma in patients with Barrett's esophagus and high-grade dysplasia: a meta-analysis," *Gastrointestinal endoscopy,* vol. 67, pp. 394-398, 2008.

[4] A. G. Association, "American Gastroenterological Association medical position statement on the management of Barrett's esophagus," *Gastroenterology,* vol. 140, pp. 1084-1091, 2011.

[5] N. J. Shaheen, B. F. Overholt, R. E. Sampliner, H. C. Wolfsen, K. K. Wang, D. E. Fleischer, V. K. Sharma, G. M. Eisen, M. B. Fennerty, J. G. Hunter, M. P. Bronner, J. R. Goldblum, A. E. Bennett, H. Mashimo, R. I. Rothstein, S. R. Gordon, S. A. Edmundowicz, R. D. Madanick, A. F. Peery, V. R. Muthusamy, K. J. Chang, M. B. Kimmey, S. J. Spechler, A. A. Siddiqui, R. F. Souza, A. Infantolino, J. A. Dumot, G. W. Falk, J. A. Galanko, B. A. Jobe, R. H. Hawes, B. J. Hoffman, P. Sharma, A. Chak, and C. J. Lightdale, "Durability of radiofrequency ablation in Barrett's esophagus with dysplasia," *Gastroenterology,* vol. 141, pp. 460-8, Aug 2011.

[6] S. J. Spechler, P. Sharma, R. F. Souza, J. M. Inadomi, N. J. Shaheen, J. I. Allen, J. V. Brill, R. E. Pruitt, P. J. Kahrilas, J. H. Peters, K. Nix, E. A. Montgomery, B. D. Mitchell, J. Yao, and P. Aga Inst Medical Position, "American Gastroenterological Association Medical Position Statement on the Management of Barrett's Esophagus," *Gastroenterology,* vol. 140, pp. 1084-1091, Mar 2011.

[7] A. J. Cameron and H. A. Carpenter, "Barrett's esophagus, high-grade dysplasia, and early adenocarcinoma: A pathological study," *American Journal of Gastroenterology,* vol. 92, pp. 586-591, Apr 1997.

[8] P. Sharma, T. J. Savides, M. I. Canto, D. A. Corley, G. W. Falk, J. R. Goldblum, K. K. Wang, M. B. Wallace, and H. C. Wolfsen, "The American Society for Gastrointestinal Endoscopy PIVI (Preservation and Incorporation of Valuable Endoscopic Innovations) on imaging in Barrett's Esophagus," *Gastrointestinal endoscopy,* vol. 76, pp. 252-254, 2012.

[9] R. L. Siegel, K. D. Miller, and A. Jemal, "Cancer statistics, 2015," *CA: a cancer journal for clinicians,* vol. 65, pp. 5-29, 2015.

[10] G. Delaney, S. Jacob, and M. Barton, "Estimation of an optimal radiotherapy utilization rate for gynecologic carcinoma," *Cancer,* vol. 101, pp. 671-681, 2004.

[11] B. D. Smith, B. G. Haffty, L. D. Wilson, G. L. Smith, A. N. Patel, and T. A. Buchholz, "The future of radiation oncology in the United States from 2010 to 2020: will supply keep pace with demand?," *Journal of clinical oncology,* vol. 28, pp. 5160-5165, 2010.

[12] P. P. Tagkalidis and J. J. Tjandra, "Chronic radiation proctitis," *ANZ J Surg,* vol. 71, pp. 230-7, Apr 2001.

[13] D. Hayne, C. Vaizey, and P. Boulos, "Anorectal injury following pelvic radiotherapy," *British journal of surgery,* vol. 88, pp. 1037-1048, 2001.

[14] M. G. Sanda, R. L. Dunn, J. Michalski, H. M. Sandler, L. Northouse, L. Hembroff, X. Lin, T. K. Greenfield, M. S. Litwin, and C. S. Saigal, "Quality of life and satisfaction with outcome among prostate-cancer survivors," *New England Journal of Medicine,* vol. 358, pp. 1250-1261, 2008.

[15] M. J. Resnick, T. Koyama, K.-H. Fan, P. C. Albertsen, M. Goodman, A. S. Hamilton, R. M. Hoffman, A. L. Potosky, J. L. Stanford, and A. M. Stroup, "Long-term functional outcomes after treatment for localized prostate cancer," *New England Journal of Medicine,* vol. 368, pp. 436-445, 2013.

[16] P. C. O'Brien, C. S. Hamilton, J. W. Denham, R. Gourlay, and C. I. V. Franklin, "Spontaneous improvement in late rectal mucosal changes after radiotherapy for prostate cancer," *International Journal of Radiation Oncology* Biology* Physics,* vol. 58, pp. 75-80, 2004.
[17] D. Theodorescu, J. Y. Gillenwater, and P. G. Koutrouvelis, "Prostatourethral-rectal fistula after prostate brachytherapy," *Cancer,* vol. 89, pp. 2085-2091, 2000.
[18] J. P. Weiner, A. T. Wong, D. Schwartz, M. Martinez, A. Aytaman, and D. Schreiber, "Endoscopic and non-endoscopic approaches for the management of radiation-induced rectal bleeding," *World journal of gastroenterology,* vol. 22, p. 6972, 2016.
[19] T. Rustagi, F. S. Corbett, and H. Mashimo, "Treatment of chronic radiation proctopathy with radiofrequency ablation (with video)," *Gastrointestinal endoscopy,* vol. 81, pp. 428-436, 2015.
[20] C. Zhou, D. C. Adler, L. Becker, Y. Chen, T.-H. Tsai, M. Figueiredo, J. M. Schmitt, J. G. Fujimoto, and H. Mashimo, "Effective treatment of chronic radiation proctitis using radiofrequency ablation," *Therapeutic advances in gastroenterology,* vol. 2, pp. 149-156, 2009.
[21] B. Hanson, R. MacDonald, and A. Shaukat, "Endoscopic and medical therapy for chronic radiation proctopathy: a systematic review," *Diseases of the Colon & Rectum,* vol. 55, pp. 1081-1095, 2012.
[22] L. Frazzoni, M. La Marca, A. Guido, A. G. Morganti, F. Bazzoli, and L. Fuccio, "Pelvic radiation disease: Updates on treatment options," *World journal of clinical oncology,* vol. 6, p. 272, 2015.
[23] M. B. Grodsky and S. M. Sidani, "Radiation proctopathy," *Clinics in colon and rectal surgery,* vol. 28, pp. 103-11, 2015.
[24] L. Lenz, R. Rohr, F. Nakao, E. Libera, and A. Ferrari, "Chronic radiation proctopathy: A practical review of endoscopic treatment," *World journal of gastrointestinal surgery,* vol. 8, p. 151, 2016.
[25] T. Klein, W. Wieser, L. Reznicek, A. Neubauer, A. Kampik, and R. Huber, "Multi-MHz retinal OCT," *Biomedical optics express,* vol. 4, pp. 1890-1908, 2013.
[26] M. P. Minneman, J. Ensher, M. Crawford, and D. Derickson, "All-semiconductor high-speed akinetic swept-source for OCT," in *Communications and Photonics Conference and Exhibition, 2011. ACP. Asia*, 2011, pp. 1-10.
[27] S. Song, J. Xu, and R. K. Wang, "Long-range and wide field of view optical coherence tomography for in vivo 3D imaging of large volume object based on akinetic programmable swept source," *Biomedical optics express,* vol. 7, pp. 4734-4748, 2016.
[28] V. Jayaraman, J. Jiang, H. Li, P. Heim, G. Cole, B. Potsaid, J. G. Fujimoto, and A. Cable, "OCT imaging up to 760kHz axial scan rate using single-mode 1310nm MEMs-tunable VCSELs with> 100nm tuning range," in *CLEO: Science and Innovations*, 2011, p. PDPB2.
[29] V. Jayaraman, G. Cole, M. Robertson, A. Uddin, and A. Cable, "High-sweep-rate 1310 nm MEMS-VCSEL with 150 nm continuous tuning range," *Electronics letters,* vol. 48, pp. 867-869, 2012.
[30] B. Potsaid, V. Jayaraman, J. G. Fujimoto, J. Jiang, P. J. S. Heim, and A. E. Cable, "MEMS tunable VCSEL light source for ultrahigh speed 60kHz-1MHz axial scan rate and long range centimeter class OCT imaging," *Optical Coherence Tomography and Coherence Domain Optical Methods in Biomedicine Xvi,* vol. 8213, 2012.
[31] T.-H. Tsai, O. O. Ahsen, H.-C. Lee, K. Liang, M. Figueiredo, Y. K. Tao, M. G. Giacomelli, B. M. Potsaid, V. Jayaraman, and Q. Huang, "Endoscopic optical coherence angiography enables 3-dimensional visualization of subsurface microvasculature," *Gastroenterology,* vol. 147, pp. 1219-1221, 2014.
[32] P. Herz, Y. Chen, A. Aguirre, K. Schneider, P. Hsiung, J. Fujimoto, K. Madden, J. Schmitt, J. Goodnow, and C. Petersen, "Micromotor endoscope catheter for in vivo, ultrahigh-resolution optical coherence tomography," *Optics Letters,* vol. 29, pp. 2261-2263, 2004.
[33] T.-H. Tsai, B. Potsaid, Y. K. Tao, V. Jayaraman, J. Jiang, P. J. Heim, M. F. Kraus, C. Zhou, J. Hornegger, and H. Mashimo, "Ultrahigh speed endoscopic optical coherence tomography using

micromotor imaging catheter and VCSEL technology," *Biomedical optics express,* vol. 4, pp. 1119-1132, 2013.

[34] H.-C. Lee, O. O. Ahsen, K. Liang, Z. Wang, M. Figueiredo, M. G. Giacomelli, B. Potsaid, Q. Huang, H. Mashimo, and J. G. Fujimoto, "Endoscopic optical coherence tomography angiography microvascular features associated with dysplasia in Barrett's esophagus (with video)," *Gastrointestinal endoscopy,* vol. 86, pp. 476-484. e3, 2017.

[35] H. C. Lee, O. O. Ahsen, K. Liang, Z. Wang, C. Cleveland, L. Booth, B. Potsaid, V. Jayaraman, A. E. Cable, H. Mashimo, R. Langer, G. Traverso, and J. G. Fujimoto, "Circumferential optical coherence tomography angiography imaging of the swine esophagus using a micromotor balloon catheter," *Biomed Opt Express,* vol. 7, pp. 2927-42, Aug 1 2016.

[36] K. Liang, G. Traverso, H.-C. Lee, O. O. Ahsen, Z. Wang, B. Potsaid, M. Giacomelli, V. Jayaraman, R. Barman, and A. Cable, "Ultrahigh speed en face OCT capsule for endoscopic imaging," *Biomedical optics express,* vol. 6, pp. 1146-1163, 2015.

[37] K. Liang, O. O. Ahsen, H. C. Lee, Z. Wang, B. M. Potsaid, M. Figueiredo, V. Jayaraman, A. E. Cable, Q. Huang, H. Mashimo, and J. G. Fujimoto, "Volumetric Mapping of Barrett's Esophagus and Dysplasia With en face Optical Coherence Tomography Tethered Capsule," *Am J Gastroenterol,* vol. 111, pp. 1664-1666, Nov 2016.

[38] M. J. Gora, J. S. Sauk, R. W. Carruth, W. Lu, D. T. Carlton, A. Soomro, M. Rosenberg, N. S. Nishioka, and G. J. Tearney, "Imaging the upper gastrointestinal tract in unsedated patients using tethered capsule endomicroscopy," *Gastroenterology,* vol. 145, pp. 723-725, 2013.

[39] K. Liang, Z. Wang, O. O. Ahsen, H.-C. Lee, B. M. Potsaid, V. Jayaraman, A. Cable, H. Mashimo, X. Li, and J. G. Fujimoto, "Cycloid scanning for wide field optical coherence tomography endomicroscopy and angiography in vivo," *Optica,* vol. 5, pp. 36-43, 2018.

[40] C. L. Leggett, E. Gorospe, V. L. Owens, M. Anderson, L. Lutzke, and K. K. Wang, "Volumetric laser endomicroscopy detects subsquamous Barrett's adenocarcinoma," *The American journal of gastroenterology,* vol. 109, p. 298, 2014.

[41] A. J. Trindade, A. S. Vamadevan, and D. V. Sejpal, "Finding a needle in a haystack: use of volumetric laser endomicroscopy in targeting focal dysplasia in long-segment Barrett’s esophagus," *Gastrointestinal endoscopy,* vol. 82, pp. 756-757, 2015.

[42] A.-F. Swager, G. J. Tearney, C. L. Leggett, M. G. van Oijen, S. L. Meijer, B. L. Weusten, W. L. Curvers, and J. J. Bergman, "Identification of volumetric laser endomicroscopy features predictive for early neoplasia in Barrett’s esophagus using high-quality histological correlation," *Gastrointestinal endoscopy,* vol. 85, pp. 918-926. e7, 2017.

[43] C. L. Leggett, E. C. Gorospe, D. K. Chan, P. Muppa, V. Owens, T. C. Smyrk, M. Anderson, L. S. Lutzke, G. Tearney, and K. K. Wang, "Comparative diagnostic performance of volumetric laser endomicroscopy and confocal laser endomicroscopy in the detection of dysplasia associated with Barrett’s esophagus," *Gastrointestinal endoscopy,* vol. 83, pp. 880-888. e2, 2016.

[44] A.-F. Swager, F. van der Sommen, S. R. Klomp, S. Zinger, S. L. Meijer, E. J. Schoon, J. J. Bergman, H. Peter, and W. L. Curvers, "Computer-aided detection of early Barrett’s neoplasia using volumetric laser endomicroscopy," *Gastrointestinal endoscopy,* vol. 86, pp. 839-846, 2017.

[45] N. Gupta, U. Siddiqui, I. Waxman, C. Chapman, A. Koons, V. Valuckaite, S.-Y. Xiao, N. Setia, J. Hart, and V. Konda, "Use of volumetric laser endomicroscopy for dysplasia detection at the gastroesophageal junction and gastric cardia," *World journal of gastrointestinal endoscopy,* vol. 9, p. 319, 2017.

[46] M. S. Smith, B. A. Jobe, B. D. Cash, M. McKinley, V. Joshi, A. Trindade, M. Kahaleh, P. R. Tarnasky, H. C. Wolfsen, and V. J. Konda, "236 Volumetric Laser Endomicroscopy Improves Patient Management by Enhancing Detection and Sampling of Esophageal Histopathology: Results From the Interim Analysis of a Multi-Center Registry," *Gastroenterology,* vol. 150, pp. S55-S56, 2016.

[47] A.-F. Swager, A. J. de Groof, S. L. Meijer, B. L. Weusten, W. L. Curvers, and J. J. Bergman, "Feasibility of laser marking in Barrett's esophagus with volumetric laser endomicroscopy: first-in-man pilot study," *Gastrointestinal Endoscopy,* vol. 86, pp. 464-472, 2017.

[48] B. F. Kennedy, X. Liang, S. G. Adie, D. K. Gerstmann, B. C. Quirk, S. A. Boppart, and D. D. Sampson, "In vivo three-dimensional optical coherence elastography," *Optics express,* vol. 19, p. 6623, 2011.

[49] W. M. Allen, L. Chin, P. Wijesinghe, R. W. Kirk, B. Latham, D. D. Sampson, C. M. Saunders, and B. F. Kennedy, "Wide-field optical coherence micro-elastography for intraoperative assessment of human breast cancer margins," *Biomedical optics express,* vol. 7, pp. 4139-4153, 2016.

[50] K. M. Kennedy, B. F. Kennedy, R. A. McLaughlin, and D. D. Sampson, "Needle optical coherence elastography for tissue boundary detection," *Optics letters,* vol. 37, pp. 2310-2312, 2012.

[51] Y. Qiu, Y. Wang, Y. Xu, N. Chandra, J. Haorah, B. Hubbi, B. J. Pfister, and X. Liu, "Quantitative optical coherence elastography based on fiber-optic probe for in situ measurement of tissue mechanical properties," *Biomedical optics express,* vol. 7, pp. 688-700, 2016.

[52] M. R. Hee, D. Huang, E. A. Swanson, and J. G. Fujimoto, "Polarization-sensitive low-coherence reflectometer for birefringence characterization and ranging," *JOSA B,* vol. 9, pp. 903-908, 1992.

[53] J. F. De Boer, T. E. Milner, M. J. van Gemert, and J. S. Nelson, "Two-dimensional birefringence imaging in biological tissue by polarization-sensitive optical coherence tomography," *Optics letters,* vol. 22, pp. 934-936, 1997.

[54] W. Oh, S. Yun, B. Vakoc, M. Shishkov, A. Desjardins, B. Park, J. De Boer, G. Tearney, and B. Bouma, "High-speed polarization sensitive optical frequency domain imaging with frequency multiplexing," *Optics express,* vol. 16, pp. 1096-1103, 2008.

[55] M. Villiger, E. Z. Zhang, S. K. Nadkarni, W.-Y. Oh, B. J. Vakoc, and B. E. Bouma, "Spectral binning for mitigation of polarization mode dispersion artifacts in catheter-based optical frequency domain imaging," *Optics express,* vol. 21, pp. 16353-16369, 2013.

[56] Z. Wang, H.-C. Lee, O. O. Ahsen, B. Lee, W. Choi, B. Potsaid, J. Liu, V. Jayaraman, A. Cable, and M. F. Kraus, "Depth-encoded all-fiber swept source polarization sensitive OCT," *Biomedical optics express,* vol. 5, pp. 2931-2949, 2014.

[57] D. C. Adams, L. P. Hariri, A. J. Miller, Y. Wang, J. L. Cho, M. Villiger, J. A. Holz, M. V. Szabari, D. L. Hamilos, and R. S. Harris, "Birefringence microscopy platform for assessing airway smooth muscle structure and function in vivo," *Science translational medicine,* vol. 8, pp. 359ra131-359ra131, 2016.

[58] J. N. van der Sijde, A. Karanasos, M. Villiger, B. E. Bouma, and E. Regar, "First-in-man assessment of plaque rupture by polarization-sensitive optical frequency domain imaging in vivo," *European heart journal,* vol. 37, pp. 1932-1932, 2016.

[59] T.-H. Tsai, C. L. Leggett, A. J. Trindade, A. Sethi, A.-F. Swager, V. Joshi, J. J. Bergman, H. Mashimo, N. S. Nishioka, and E. Namati, "Optical coherence tomography in gastroenterology: a review and future outlook," *Journal of biomedical optics,* vol. 22, p. 121716, 2017.

[60] S. R. Puli, J. B. Reddy, M. L. Bechtold, D. Antillon, J. A. Ibdah, and M. R. Antillon, "Staging accuracy of esophageal cancer by endoscopic ultrasound: a meta-analysis and systematic review," *World journal of gastroenterology: WJG,* vol. 14, p. 1479, 2008.

[61] J. Yin, X. Li, J. Jing, J. Li, D. Mukai, S. Mahon, A. Edris, K. Hoang, K. K. Shung, and M. Brenner, "Novel combined miniature optical coherence tomography ultrasound probe for in vivo intravascular imaging," *Journal of biomedical optics,* vol. 16, pp. 060505-060505-3, 2011.

[62] Y. Li, J. Jing, Y. Qu, Y. Miao, B. Zhang, T. Ma, M. Yu, Q. Zhou, and Z. Chen, "Fully integrated optical coherence tomography, ultrasound, and indocyanine green-based fluorescence tri-modality system for intravascular imaging," *Biomedical optics express,* vol. 8, pp. 1036-1044, 2017.

[63] L. Xi, C. Duan, H. Xie, and H. Jiang, "Miniature probe combining optical-resolution photoacoustic microscopy and optical coherence tomography for in vivomicrocirculation study," *Applied optics,* vol. 52, pp. 1928-1931, 2013.
[64] X. Dai, H. Yang, T. Shan, H. Xie, S. A. Berceli, and H. Jiang, "Miniature endoscope for multimodal imaging," *ACS Photonics,* vol. 4, pp. 174-180, 2016.
[65] H. F. Zhang, K. Maslov, M. Sivaramakrishnan, G. Stoica, and L. V. Wang, "Imaging of hemoglobin oxygen saturation variations in single vessels in vivo using photoacoustic microscopy," *Applied physics letters,* vol. 90, p. 053901, 2007.
[66] H. Pahlevaninezhad, A. M. Lee, A. Ritchie, T. Shaipanich, W. Zhang, D. N. Ionescu, G. Hohert, C. MacAulay, S. Lam, and P. Lane, "Endoscopic Doppler optical coherence tomography and autofluorescence imaging of peripheral pulmonary nodules and vasculature," *Biomedical optics express,* vol. 6, pp. 4191-4199, 2015.
[67] H. Yoo, J. W. Kim, M. Shishkov, E. Namati, T. Morse, R. Shubochkin, J. R. McCarthy, V. Ntziachristos, B. E. Bouma, and F. A. Jaffer, "Intra-arterial catheter for simultaneous microstructural and molecular imaging in vivo," *Nature medicine,* vol. 17, pp. 1680-1684, 2011.
[68] G. J. Ughi, J. Verjans, A. M. Fard, H. Wang, E. Osborn, T. Hara, A. Mauskapf, F. A. Jaffer, and G. J. Tearney, "Dual modality intravascular optical coherence tomography (OCT) and near-infrared fluorescence (NIRF) imaging: a fully automated algorithm for the distance-calibration of NIRF signal intensity for quantitative molecular imaging," *The international journal of cardiovascular imaging,* vol. 31, pp. 259-268, 2015.
[69] J. Mavadia, J. Xi, Y. Chen, and X. Li, "An all-fiber-optic endoscopy platform for simultaneous OCT and fluorescence imaging," *Biomedical optics express,* vol. 3, pp. 2851-2859, 2012.
[70] T. Endo, T. Awakawa, H. Takahashi, Y. Arimura, F. Itoh, K. Yamashita, S. Sasaki, H. Yamamoto, X. Tang, and K. Imai, "Classification of Barrett's epithelium by magnifying endoscopy," *Gastrointestinal endoscopy,* vol. 55, pp. 641-647, 2002.
[71] S. Kudo, S. Tamura, T. Nakajima, H. Yamano, H. Kusaka, and H. Watanabe, "Diagnosis of colorectal tumorous lesions by magnifying endoscopy," *Gastrointest Endosc,* vol. 44, pp. 8-14, Jul 1996.
[72] M. A. Kara, M. Ennahachi, P. Fockens, F. J. ten Kate, and J. J. Bergman, "Detection and classification of the mucosal and vascular patterns (mucosal morphology) in Barrett's esophagus by using narrow band imaging," *Gastrointestinal endoscopy,* vol. 64, pp. 155-166, 2006.
[73] P. Sharma, A. Bansal, S. Mathur, S. Wani, R. Cherian, D. McGregor, A. Higbee, S. Hall, and A. Weston, "The utility of a novel narrow band imaging endoscopy system in patients with Barrett's esophagus," *Gastrointestinal Endoscopy,* vol. 64, pp. 167-175, 2006.
[74] M. Raghavendra, D. G. Hewett, and D. K. Rex, "Differentiating adenomas from hyperplastic colorectal polyps: narrow-band imaging can be learned in 20 minutes," *Gastrointestinal endoscopy,* vol. 72, pp. 572-576, 2010.
[75] D. G. Hewett, T. Kaltenbach, Y. Sano, S. Tanaka, B. P. Saunders, T. Ponchon, R. Soetikno, and D. K. Rex, "Validation of a simple classification system for endoscopic diagnosis of small colorectal polyps using narrow-band imaging," *Gastroenterology,* vol. 143, pp. 599-607. e1, 2012.
[76] P. Sharma, J. J. Bergman, K. Goda, M. Kato, H. Messmann, B. R. Alsop, N. Gupta, P. Vennalaganti, M. Hall, and V. Konda, "Development and validation of a classification system to identify high-grade dysplasia and esophageal adenocarcinoma in Barrett's esophagus using narrow-band imaging," *Gastroenterology,* vol. 150, pp. 591-598, 2016.
[77] D. Adler, C. Zhou, T.-H. Tsai, H.-C. Lee, L. Becker, J. Schmitt, Q. Huang, J. Fujimoto, and H. Mashimo, "Three-dimensional optical coherence tomography of Barrett's esophagus and buried glands beneath neosquamous epithelium following radiofrequency ablation," *Endoscopy,* vol. 41, pp. 773-776, 2009.

[78] D. C. Adler, Y. Chen, R. Huber, J. Schmitt, J. Connolly, and J. G. Fujimoto, "Three-dimensional endomicroscopy using optical coherence tomography," *Nature Photonics,* vol. 1, pp. 709-716, 2007.

[79] Y. Kawase, Y. Suzuki, F. Ikeno, R. Yoneyama, K. Hoshino, H. Q. Ly, G. T. Lau, M. Hayase, A. C. Yeung, and R. J. Hajjar, "Comparison of nonuniform rotational distortion between mechanical IVUS and OCT using a phantom model," *Ultrasound in medicine & biology,* vol. 33, pp. 67-73, 2007.

[80] W. Kang, H. Wang, Z. Wang, M. W. Jenkins, G. A. Isenberg, A. Chak, and A. M. Rollins, "Motion artifacts associated with in vivo endoscopic OCT images of the esophagus," *Optics Express,* vol. 19, pp. 20722-35, Oct 10 2011.

[81] P. R. Herz, Y. Chen, A. D. Aguirre, K. Schneider, P. Hsiung, J. G. Fujimoto, K. Madden, J. Schmitt, J. Goodnow, and C. Petersen, "Micromotor endoscope catheter for in vivo, ultrahigh-resolution optical coherence tomography," *Opt Lett,* vol. 29, pp. 2261-3, Oct 1 2004.

[82] P. H. Tran, D. S. Mukai, M. Brenner, and Z. Chen, "In vivo endoscopic optical coherence tomography by use of a rotational microelectromechanical system probe," *Opt Lett,* vol. 29, pp. 1236-8, Jun 1 2004.

[83] T. Wang, W. Wieser, G. Springeling, R. Beurskens, C. T. Lancee, T. Pfeiffer, A. F. van der Steen, R. Huber, and G. van Soest, "Intravascular optical coherence tomography imaging at 3200 frames per second," *Opt Lett,* vol. 38, pp. 1715-7, May 15 2013.

[84] J. A. Li, M. de Groot, F. Helderman, J. H. Mo, J. M. A. Daniels, K. Grunberg, T. G. Sutedja, and J. F. de Boer, "High speed miniature motorized endoscopic probe for optical frequency domain imaging," *Optics Express,* vol. 20, pp. 24132-24138, Oct 22 2012.

[85] G. van Soest, J. G. Bosch, and A. F. van der Steen, "Azimuthal registration of image sequences affected by nonuniform rotation distortion," *IEEE Trans Inf Technol Biomed,* vol. 12, pp. 348-55, May 2008.

[86] C. Gatta, O. Pujol, O. R. Leor, J. M. Ferre, and P. Radeva, "Fast Rigid Registration of Vascular Structures in IVUS Sequences," *Ieee Transactions on Information Technology in Biomedicine,* vol. 13, pp. 1006-1011, Nov 2009.

[87] J. Yin, G. Liu, J. Zhang, L. Yu, S. Mahon, D. Mukai, M. Brenner, and Z. Chen, "In vivo early detection of smoke-induced airway injury using three-dimensional swept-source optical coherence tomography," *Journal of biomedical optics,* vol. 14, pp. 060503-060503-3, 2009.

[88] G. J. Ughi, T. Adriaenssens, M. Larsson, C. Dubois, P. R. Sinnaeve, M. Coosemans, W. Desmet, and J. D'Hooge, "Automatic three-dimensional registration of intravascular optical coherence tomography images," *J Biomed Opt,* vol. 17, p. 026005, Feb 2012.

[89] C. Sun, F. Nolte, K. H. Cheng, B. Vuong, K. K. Lee, B. A. Standish, B. Courtney, T. R. Marotta, A. Mariampillai, and V. X. Yang, "In vivo feasibility of endovascular Doppler optical coherence tomography," *Biomed Opt Express,* vol. 3, pp. 2600-10, Oct 1 2012.

[90] B. Lumbroso, D. Huang, A. Romano, M. Rispoli, and G. Coscas, *Clinical En Face OCT Atlas*: JP Medical Ltd, 2013.

[91] R. K. Wang, S. L. Jacques, Z. Ma, S. Hurst, S. R. Hanson, and A. Gruber, "Three dimensional optical angiography," *Opt Express,* vol. 15, pp. 4083-97, Apr 2 2007.

[92] Y. Yasuno, Y. J. Hong, S. Makita, M. Yamanari, M. Akiba, M. Miura, and T. Yatagai, "In vivo high-contrast imaging of deep posterior eye by 1-mu m swept source optical coherence tomography and scattering optical coherence angiography," *Optics Express,* vol. 15, pp. 6121-6139, May 14 2007.

[93] I. Vogelaar, M. van Ballegooijen, D. Schrag, R. Boer, S. J. Winawer, J. D. Habbema, and A. G. Zauber, "How much can current interventions reduce colorectal cancer mortality in the U.S.?

Mortality projections for scenarios of risk-factor modification, screening, and treatment," *Cancer,* vol. 107, pp. 1624-33, Oct 01 2006.
[94] K. Liang, J. G. Fujimoto, H. Mashimo, O. O. Ahsen, H.-C. Lee, M. G. Giacomelli, and Z. Wang, "Scanning optical probe," ed: Google Patents, 2016.
[95] X. Dray, G. Battaglia, D. Wengrower, P. Gonzalez, A. Carlino, M. Camus, T. Adar, F. Pérez-Roldán, P. Marteau, and A. Repici, "Radiofrequency ablation for the treatment of radiation proctitis," *Endoscopy,* vol. 46, pp. 970-976, 2014.
[96] A. D. Aguirre, "Advances in Optical Coherence Tomography and Microscopy for endoscopic applications and functional neuroimaging," Ph D, Harvard-MIT Division of Health Sciences and Technology, 2008.
[97] O. O. Ahsen, "Swept source optical coherence microscopy for pathological assessment of cancerous tissues," Massachusetts Institute of Technology, 2013.
[98] S. M. Pizer, E. P. Amburn, J. D. Austin, R. Cromartie, A. Geselowitz, T. Greer, B. Terhaarromeny, J. B. Zimmerman, and K. Zuiderveld, "Adaptive Histogram Equalization and Its Variations," *Computer Vision Graphics and Image Processing,* vol. 39, pp. 355-368, Sep 1987.
[99] S. M. Pizer and J. B. Zimmerman, "Color Display in Ultrasonography," *Ultrasound in Medicine and Biology,* vol. 9, pp. 331-345, 1983.
[100] K. W. Beach, J. F. Primozich, and D. E. Strandness, "Pseudocolor B-Mode Arterial Images to Quantify Echogenicity of Atherosclerotic Plaque," *Ultrasound in Medicine and Biology,* vol. 20, pp. 731-742, 1994.
[101] C. Hur, M. Miller, C. Y. Kong, E. C. Dowling, K. J. Nattinger, M. Dunn, and E. J. Feuer, "Trends in esophageal adenocarcinoma incidence and mortality," *Cancer,* vol. 119, pp. 1149-1158, 2013.
[102] X. Chen and C. S. Yang, "Esophageal adenocarcinoma: a review and perspectives on the mechanism of carcinogenesis and chemoprevention," *Carcinogenesis,* vol. 22, pp. 1119-29, Aug 2001.
[103] S. J. Spechler, "Dysplasia in Barrett's esophagus: limitations of current management strategies," *The American journal of gastroenterology,* vol. 100, p. 927, 2005.
[104] F. Hvid-Jensen, L. Pedersen, A. M. Drewes, H. T. Sorensen, and P. Funch-Jensen, "Incidence of Adenocarcinoma among Patients with Barrett's Esophagus," *New England Journal of Medicine,* vol. 365, pp. 1375-1383, Oct 13 2011.
[105] N. J. Shaheen, P. Sharma, B. F. Overholt, H. C. Wolfsen, R. E. Sampliner, K. K. Wang, J. A. Galanko, M. P. Bronner, J. R. Goldblum, and A. E. Bennett, "Radiofrequency ablation in Barrett's esophagus with dysplasia," *New England Journal of Medicine,* vol. 360, pp. 2277-2288, 2009.
[106] D. LEVINE, R. HAGGITT, P. BLOUNT, P. RABINOVITCH, V. RUSCH, and B. REID, "An endoscopic biopsy protocol can differentiate high-grade dysplasia from early adenocarcinoma in Barretts esophagus," *Gastroenterology,* vol. 105, pp. 40-50, 1993.
[107] M. A. Kara, M. Ennahachi, P. Fockens, F. J. W. ten Kate, and J. J. G. H. M. Bergman, "Detection and classification of the mucosal and vascular patterns (mucosal morphology) in Barrett's esophagus by using narrow band imaging," *Gastrointestinal Endoscopy,* vol. 64, pp. 155-166, Aug 2006.
[108] R. Kiesslich, J. Burg, M. Vieth, J. Gnaendiger, M. Enders, P. Delaney, A. Polglase, W. McLaren, D. Janell, S. Thomas, B. Nafe, P. R. Galle, and M. F. Neurath, "Confocal laser endoscopy for diagnosing intraepithelial neoplasias and colorectal cancer in vivo," *Gastroenterology,* vol. 127, pp. 706-13, Sep 2004.
[109] M. Wallace, G. Y. Lauwers, Y. Chen, E. Dekker, P. Fockens, P. Sharma, and A. Meining, "Miami classification for probe-based confocal laser endomicroscopy," *Endoscopy,* vol. 43, pp. 882-91, Oct 2011.

[110] B. J. Vakoc, M. Shishko, S. H. Yun, W. Y. Oh, M. J. Suter, A. E. Desjardins, J. A. Evans, N. S. Nishioka, G. J. Tearney, and B. E. Bouma, "Comprehensive esophageal microscopy by using optical frequency-domain imaging (with video)," *Gastrointest Endosc,* vol. 65, pp. 898-905, May 2007.
[111] H. C. Wolfsen, P. Sharma, M. B. Wallace, C. Leggett, G. Tearney, and K. K. Wang, "Safety and feasibility of volumetric laser endomicroscopy in patients with Barrett's esophagus (with videos)," *Gastrointestinal endoscopy,* vol. 82, pp. 631-640, 2015.
[112] N. J. Shaheen, "Advances in Barrett's esophagus and esophageal adenocarcinoma," *Gastroenterology,* vol. 128, pp. 1554-1566, May 2005.
[113] S. Haag and G. Holtmann, "Reflux disease and Barrett's esophagus," *Endoscopy,* vol. 35, pp. 112-117, Feb 2003.
[114] P. J. Kahrilas, N. J. Shaheen, and M. Vaezi, "American Gastroenterological Association institute technical review on the management of gastroesophageal reflux disease," *Gastroenterology,* vol. 135, pp. 1392-1413, Oct 2008.
[115] P. J. Kahrilas, "Gastroesophageal reflux disease," *New England Journal of Medicine,* vol. 359, pp. 1700-1707, Oct 2008.
[116] N. J. Shaheen and J. E. Richter, "Barrett's oesophagus," *Lancet,* vol. 373, pp. 850-861, Mar 7 2009.
[117] J. T. Chang and D. A. Katzka, "Gastroesophageal reflux disease, barrett esophagus, and esophageal adenocarcinoma," *Archives of Internal Medicine,* vol. 164, pp. 1482-1488, 07/26 2004.
[118] R. H. Riddell and F. R. C. Path, "Premalignant and early malignant lesions in the gastrointestinal tract: Definitions, terminology, and problems," *American Journal of Gastroenterology,* vol. 91, pp. 864-872, May 1996.
[119] B. J. Reid, D. S. Levine, G. Longton, P. L. Blount, and P. S. Rabinovitch, "Predictors of progression to cancer in Barrett's esophagus: Baseline histology and flow cytometry identify low- and high-risk patient subsets," *American Journal of Gastroenterology,* vol. 95, pp. 1669-1676, Jul 2000.
[120] N. S. Buttar, K. K. Wang, T. J. Sebo, D. M. Riehle, K. K. Krishnadath, L. S. Lutzke, M. A. Anderson, T. M. Petterson, and L. J. Burgart, "Extent of high-grade dysplasia in Barrett's esophagus correlates with risk of adenocarcinoma," *Gastroenterology,* vol. 120, pp. 1630-1639, Jun 2001.
[121] J. M. Streitz, C. W. Andrews, F. H. Ellis, D. B. Skinner, V. F. Trastek, and J. R. Benfield, "Endoscopic Surveillance of Barrett's-Esophagus - Does It Help," *Journal of Thoracic and Cardiovascular Surgery,* vol. 105, pp. 383-388, Mar 1993.
[122] B. F. Overholt, C. J. Lightdale, K. K. Wang, M. I. Canto, S. Burdick, R. C. Haggitt, M. P. Bronner, S. L. Taylor, M. G. Grace, and M. Depot, "Photodynamic therapy with porfimer sodium for ablation of high-grade dysplasia in Barrett's esophagus: international, partially blinded, randomized phase III trial," *Gastrointest Endosc,* vol. 62, pp. 488-98, Oct 2005.
[123] G. S. Dulai, D. M. Jensen, G. Cortina, L. Fontana, and A. Ippoliti, "Randomized trial of argon plasma coagulation vs. multipolar electrocoagulation for ablation of Barrett's esophagus," *Gastrointest Endosc,* vol. 61, pp. 232-40, Feb 2005.
[124] A. P. Weston and P. Sharma, "Neodymium : yttrium-aluminum garnet contact laser ablation of Barrett's high grade dysplasia and early adenocarcinorna," *American Journal of Gastroenterology,* vol. 97, pp. 2998-3006, Dec 2002.
[125] B. Dunkin, J. Martinez, P. Bejarano, C. Smith, K. Chang, A. Livingstone, and W. Melvin, "Thin-layer ablation of human esophageal epithelium using a bipolar radiofrequency balloon device," *Surgical Endoscopy,* vol. 20, pp. 125-130, 2006.
[126] P. Sharma, S. Wani, and A. Rastogi, "Endoscopic therapy for high-grade dysplasia in Barrett's esophagus: ablate, resect, or both?," *Gastrointestinal Endoscopy,* vol. 66, pp. 469-474, Sep 2007.

[127] R. A. Ganz, B. F. Overholt, V. K. Sharma, D. E. Fleischer, N. J. Shaheen, C. J. Lightdale, S. R. Freeman, R. E. Pruitt, S. M. Urayama, F. Gress, D. A. Pavey, M. S. Branch, T. J. Savides, K. J. Chang, V. R. Muthusamy, A. G. Bohorfoush, S. C. Pace, S. R. DeMeester, V. E. Eysselein, M. Panjehpour, and G. Triadafilopoulos, "Circumferential ablation of Barrett's esophagus that contains high-grade dysplasia: a U.S. multicenter registry," *Gastrointestinal Endoscopy,* vol. 68, pp. 35-40, 2008.

[128] N. J. Shaheen, P. Sharma, B. F. Overholt, H. C. Wolfsen, R. E. Sampliner, K. K. Wang, J. A. Galanko, M. P. Bronner, J. R. Goldblum, A. E. Bennett, B. A. Jobe, G. M. Eisen, M. B. Fennerty, J. G. Hunter, D. E. Fleischer, V. K. Sharma, R. H. Hawes, B. J. Hoffman, R. I. Rothstein, S. R. Gordon, H. Mashimo, K. J. Chang, V. R. Muthusamy, S. A. Edmundowicz, S. J. Spechler, A. A. Siddiqui, R. F. Souza, A. Infantolino, G. W. Falk, M. B. Kimmey, R. D. Madanick, A. Chak, and C. J. Lightdale, "Radiofrequency Ablation in Barrett's Esophagus with Dysplasia," *New England Journal of Medicine,* vol. 360, pp. 2277-2288, 2009.

[129] D. E. Fleischer, B. F. Overholt, V. K. Sharma, A. Reymunde, M. B. Kimmey, R. Chuttani, K. J. Chang, R. Muthasamy, C. J. Lightdale, N. Santiago, D. K. Pleskow, P. J. Dean, and K. K. Wang, "Endoscopic radiofrequency ablation for Barrett's esophagus: 5-year outcomes from a prospective multicenter trial," *Endoscopy,* vol. 42, pp. 781,789, 30.09.2010 2010.

[130] N. J. Shaheen, B. F. Overholt, R. E. Sampliner, H. C. Wolfsen, K. K. Wang, D. E. Fleischer, V. K. Sharma, G. M. Eisen, M. B. Fennerty, J. G. Hunter, M. P. Bronner, J. R. Goldblum, A. E. Bennett, H. Mashimo, R. I. Rothstein, S. R. Gordon, S. A. Edmundowicz, R. D. Madanick, A. F. Peery, V. R. Muthusamy, K. J. Chang, M. B. Kimmey, S. J. Spechler, A. A. Siddiqui, R. F. Souza, A. Infantolino, J. A. Dumot, G. W. Falk, J. A. Galanko, B. A. Jobe, R. H. Hawes, B. J. Hoffman, P. Sharma, A. Chak, and C. J. Lightdale, "Durability of Radiofrequency Ablation in Barrett's Esophagus With Dysplasia," *Gastroenterology,* vol. 141, pp. 460-468, 2011.

[131] E. S. Orman, N. Li, and N. J. Shaheen, "Efficacy and durability of radiofrequency ablation for Barrett's Esophagus: systematic review and meta-analysis," *Clinical Gastroenterology and Hepatology,* vol. 11, pp. 1245-1255, 2013.

[132] O. Pech, L. Gossner, H. Manner, A. May, T. Rabenstein, A. Behrens, M. Berres, J. Huijsmans, M. Vieth, M. Stolte, and C. Ell, "Prospective evaluation of the macroscopic types and location of early Barrett's neoplasia in 380 lesions," *Endoscopy,* vol. 39, pp. 588-593, Jul 2007.

[133] O. Pech, "Declaration of Bankruptcy for Four-Quadrant Biopsies in Barrett's Esophagus?," *Clinical Gastroenterology and Hepatology,* vol. 7, pp. 610-612, Jun 2009.

[134] M. Bajbouj, M. Vieth, T. Rösch, S. Miehlke, V. Becker, M. Anders, H. Pohl, A. Madisch, T. Schuster, R. M. Schmid, and A. Meining, "Probe-based confocal laser endomicroscopy compared with standard four-quadrant biopsy for evaluation of neoplasia in Barrett's esophagus," *Endoscopy,* vol. 42, pp. 435,440, 26.05.2010 2010.

[135] O. Pech, L. Gossner, H. Manner, A. May, T. Rabenstein, A. Behrens, M. Berres, J. Huijsmans, M. Vieth, and M. Stolte, "Prospective evaluation of the macroscopic types and location of early Barrett's neoplasia in 380 lesions," *Endoscopy,* vol. 39, pp. 588-593, 2007.

[136] K. Gono, T. Obi, M. Yamaguchi, N. Ohyama, H. Machida, Y. Sano, S. Yoshida, Y. Hamamoto, and T. Endo, "Appearance of enhanced tissue features in narrow-band endoscopic imaging," *J Biomed Opt,* vol. 9, pp. 568-77, May-Jun 2004.

[137] R. Singh, G. K. Anagnostopoulos, K. Yao, H. Karageorgiou, P. J. Fortun, A. Shonde, K. Garsed, P. V. Kaye, C. J. Hawkey, and K. Ragunath, "Narrow-band imaging with magnification in Barrett's esophagus: validation of a simplified grading system of mucosal morphology patterns against histology," *Endoscopy,* vol. 40, pp. 457-63, Jun 2008.

[138] "Cancer Facts and Figures," American Cancer Society2013.

[139] M. Singh, A. Bansal, W. Curvers, M. Kara, S. Wani, L. A. Herrero, C. Lynch, M. van Kouwen, F. Peters, and J. Keighley, "Observer agreement in the assessment of narrowband imaging system surface patterns in Barrett's esophagus: a multicenter study," *Endoscopy,* vol. 43, pp. 745-751, 2011.

[140] P. Sharma, A. R. Meining, E. Coron, C. J. Lightdale, H. C. Wolfsen, A. Bansal, M. Bajbouj, J. P. Galmiche, J. A. Abrams, A. Rastogi, N. Gupta, J. E. Michalek, G. Y. Lauwers, and M. B. Wallace, "Real-time increased detection of neoplastic tissue in Barrett's esophagus with probe-based confocal laser endomicroscopy: final results of an international multicenter, prospective, randomized, controlled trial," *Gastrointest Endosc,* vol. 74, pp. 465-72, Sep 2011.

[141] M. I. Canto, S. Anandasabapathy, W. Brugge, G. W. Falk, K. B. Dunbar, Z. Zhang, K. Woods, J. A. Almario, U. Schell, J. Goldblum, A. Maitra, E. Montgomery, R. Kiesslich, and G. Confocal Endomicroscopy for Barrett's Esophagus or Confocal Endomicroscopy for Barrett's Esophagus Trial, "In vivo endomicroscopy improves detection of Barrett's esophagus-related neoplasia: a multicenter international randomized controlled trial (with video)," *Gastrointest Endosc,* vol. 79, pp. 211-21, Feb 2014.

[142] H. C. Wolfsen, P. Sharma, M. B. Wallace, C. Leggett, G. Tearney, and K. K. Wang, "Safety and feasibility of volumetric laser endomicroscopy in patients with Barrett's esophagus (with videos)," *Gastrointestinal endoscopy,* 2015.

[143] O. O. Ahsen, H.-C. Lee, M. G. Giacomelli, Z. Wang, K. Liang, T.-H. Tsai, B. Potsaid, H. Mashimo, and J. G. Fujimoto, "Correction of rotational distortion for catheter-based en face OCT and OCT angiography," *Optics Letters,* vol. 39, pp. 5973-5976, 2014/10/15 2014.

[144] P. Sharma, J. J. Bergman, K. Goda, M. Kato, H. Messmann, B. R. Alsop, N. Gupta, P. Vennalaganti, M. Hall, V. Konda, A. Koons, O. Penner, J. R. Goldblum, and I. Waxman, "Development and Validation of a Classification System to Identify High-Grade Dysplasia and Esophageal Adenocarcinoma in Barrett's Esophagus Using Narrow-Band Imaging," *Gastroenterology,* vol. 150, pp. 591-8, Mar 2016.

[145] K. Yao, *Zoom Gastroscopy: Magnifying Endoscopy in the Stomach*: Springer Japan, 2013.

[146] M. I. Canto, "Endomicroscopy of Barrett's Esophagus," *Gastroenterology Clinics of North America,* vol. 39, pp. 759-769, 2010.

[147] R. Kikinis, S. D. Pieper, and K. G. Vosburgh, "3D Slicer: a platform for subject-specific image analysis, visualization, and clinical support," in *Intraoperative imaging and image-guided therapy*, ed: Springer, 2014, pp. 277-289.

[148] J. R. Landis and G. G. Koch, "The measurement of observer agreement for categorical data," *biometrics,* pp. 159-174, 1977.

[149] J. L. Fleiss, B. Levin, and M. C. Paik, *Statistical methods for rates and proportions*: John Wiley & Sons, 2013.

[150] G. Isenberg, M. V. Sivak, Jr., A. Chak, R. C. Wong, J. E. Willis, B. Wolf, D. Y. Rowland, A. Das, and A. Rollins, "Accuracy of endoscopic optical coherence tomography in the detection of dysplasia in Barrett's esophagus: a prospective, double-blinded study," *Gastrointest Endosc,* vol. 62, pp. 825-31, Dec 2005.

[151] J. A. Evans, J. M. Poneros, B. E. Bouma, J. Bressner, E. F. Halpern, M. Shishkov, G. Y. Lauwers, M. Mino-Kenudson, N. S. Nishioka, and G. J. Tearney, "Optical coherence tomography to identify intramucosal carcinoma and high-grade dysplasia in Barrett's esophagus," *Clin Gastroenterol Hepatol,* vol. 4, pp. 38-43, Jan 2006.

[152] M. Alshelleh, S. Inamdar, M. McKinley, M. Stewart, J. S. Novak, R. E. Greenberg, K. Sultan, B. Devito, M. Cheung, and M. A. Cerulli, "Incremental yield of dysplasia detection in Barrett's esophagus using volumetric laser endomicroscopy with and without laser marking compared with a standardized random biopsy protocol," *Gastrointestinal endoscopy,* 2018.

[153] O. O. Ahsen, H.-C. Lee, K. Liang, Z. Wang, M. Figueiredo, Q. Huang, B. Potsaid, V. Jayaraman, J. G. Fujimoto, and H. Mashimo, "Ultrahigh-speed endoscopic optical coherence tomography and angiography enables delineation of lateral margins of endoscopic mucosal resection: a case report," *Therapeutic advances in gastroenterology,* vol. 10, pp. 931-936, 2017.
[154] S. A. McDonald, D. Lavery, N. A. Wright, and M. Jansen, "Barrett oesophagus: lessons on its origins from the lesion itself," *Nature Reviews Gastroenterology and Hepatology,* vol. 12, p. 50, 2015.
[155] T. W. Rice, J. E. Mendelin, and J. R. Goldblum, "Barrett's esophagus: pathologic considerations and implications for treatment," in *Seminars in thoracic and cardiovascular surgery*, 2005, pp. 292-300.
[156] R. Anaparthy and P. Sharma, "Progression of Barrett oesophagus: role of endoscopic and histological predictors," *Nature Reviews Gastroenterology and Hepatology,* vol. 11, p. 525, 2014.
[157] C. C. Cotton, L. C. Duits, W. A. Wolf, A. F. Peery, E. S. Dellon, J. J. Bergman, and N. J. Shaheen, "Spatial predisposition of dysplasia in Barrett's esophagus segments: a pooled analysis of the SURF and AIM dysplasia trials," *The American journal of gastroenterology,* vol. 110, p. 1412, 2015.
[158] K. N. Phoa, F. G. Van Vilsteren, B. L. Weusten, R. Bisschops, E. J. Schoon, K. Ragunath, G. Fullarton, M. Di Pietro, N. Ravi, and M. Visser, "Radiofrequency ablation vs endoscopic surveillance for patients with Barrett esophagus and low-grade dysplasia: a randomized clinical trial," *Jama,* vol. 311, pp. 1209-1217, 2014.
[159] T. Kuiper, F. Van Den Broek, S. Van Eeden, P. Fockens, and E. Dekker, "Feasibility and accuracy of confocal endomicroscopy in comparison with narrow-band imaging and chromoendoscopy for the differentiation of colorectal lesions," *The American journal of gastroenterology,* vol. 107, p. 543, 2012.
[160] M. V. Sivak, K. Kobayashi, J. A. Izatt, A. M. Rollins, R. Ung-Runyawee, A. Chak, R. C. Wong, G. A. Isenberg, and J. Willis, "High-resolution endoscopic imaging of the GI tract using optical coherence tomography," *Gastrointestinal endoscopy,* vol. 51, pp. 474-479, 2000.
[161] V. Westphal, A. M. Rollins, J. Willis, M. V. Sivak, and J. A. Izatt, "Correlation of endoscopic optical coherence tomography with histology in the lower-GI tract," *Gastrointestinal endoscopy,* vol. 61, pp. 537-546, 2005.
[162] Y. Nakanishi, M. Saka, T. Eguchi, S. Sekine, H. Taniguchi, and T. Shimoda, "Distribution and significance of the oesophageal and gastric cardiac mucosae: a study of 131 operation specimens," *Histopathology,* vol. 51, pp. 515-519, 2007.
[163] Q. Huang, "Controversies of cardiac glands in the proximal stomach: a critical review," *Journal of gastroenterology and hepatology,* vol. 26, pp. 450-455, 2011.
[164] W. J. Choi, H. Wang, and R. K. Wang, "Optical coherence tomography microangiography for monitoring the response of vascular perfusion to external pressure on human skin tissue," *Journal of biomedical optics,* vol. 19, pp. 056003-056003, 2014.
[165] P. Sharma, J. Dent, D. Armstrong, J. J. Bergman, L. Gossner, Y. Hoshihara, J. A. Jankowski, O. Junghard, L. Lundell, G. N. Tytgat, and M. Vieth, "The development and validation of an endoscopic grading system for Barrett's esophagus: the Prague C & M criteria," *Gastroenterology,* vol. 131, pp. 1392-9, Nov 2006.
[166] T.-H. Tsai, H.-C. Lee, O. O. Ahsen, K. Liang, M. G. Giacomelli, B. M. Potsaid, Y. K. Tao, V. Jayaraman, M. Figueiredo, and Q. Huang, "Ultrahigh speed endoscopic optical coherence tomography for gastroenterology," *Biomedical optics express,* vol. 5, pp. 4387-4404, 2014.
[167] A. Swager, D. Boerwinkel, D. de Bruin, B. Weusten, D. Faber, S. Meijer, T. van Leeuwen, W. Curvers, and J. Bergman, "Volumetric laser endomicroscopy in Barrett's esophagus: a feasibility study on histological correlation," *Diseases of the Esophagus,* vol. 29, pp. 505-512, 2016.

[168] A. K. Garg, W.-Y. Mai, J. E. McGary, W. H. Grant, 3rd, E. B. Butler, and B. S. Teh, "Radiation proctopathy in the treatment of prostate cancer," *International journal of radiation oncology, biology, physics,* vol. 66, pp. 1294-305, 2006.
[169] M. J. Zelefsky, E. J. Levin, M. Hunt, Y. Yamada, A. M. Shippy, A. Jackson, and H. I. Amols, "Incidence of late rectal and urinary toxicities after three-dimensional conformal radiotherapy and intensity-modulated radiotherapy for localized prostate cancer," *International Journal of Radiation Oncology* Biology* Physics,* vol. 70, pp. 1124-1129, 2008.
[170] J. Staffurth, "A review of the clinical evidence for intensity-modulated radiotherapy," *Clinical oncology,* vol. 22, pp. 643-657, 2010.
[171] J. G. Bazan, W. Hara, A. Hsu, P. A. Kunz, J. Ford, G. A. Fisher, M. L. Welton, A. Shelton, D. S. Kapp, A. C. Koong, K. A. Goodman, and D. T. Chang, "Intensity-modulated radiation therapy versus conventional radiation therapy for squamous cell carcinoma of the anal canal," *Cancer,* vol. 117, pp. 3342-51, Aug 01 2011.
[172] K. Leiper and A. Morris, "Treatment of radiation proctitis," *Clinical Oncology,* vol. 19, pp. 724-729, 2007.
[173] K. D. Chi, E. D. Ehrenpreis, and A. B. Jani, "Accuracy and reliability of the endoscopic classification of chronic radiation-induced proctopathy using a novel grading method," *Journal of clinical gastroenterology,* vol. 39, pp. 42-46, 2005.
[174] M. R. Yates and T. H. Baron, "Treatment of a radiation-induced sigmoid stricture with an expandable metal stent," *Gastrointestinal endoscopy,* vol. 50, pp. 422-426, 1999.
[175] L. Lenz, J. Tafarel, L. Correia, D. Bonilha, M. Santos, R. Rodrigues, G. Gomes, G. Andrade, F. Martins, and M. Monaghan, "Comparative study of bipolar eletrocoagulation versus argon plasma coagulation for rectal bleeding due to chronic radiation coloproctopathy," *Endoscopy,* vol. 43, pp. 697-701, 2011.
[176] J. Weiner, D. Schwartz, M. Martinez, J. Safdieh, A. Aytaman, and D. Schreiber, "Long-term results on the efficacy of argon plasma coagulation for patients with chronic radiation proctitis after conventionally fractionated, dose-escalated radiation therapy for prostate cancer," *Practical radiation oncology,* vol. 7, pp. e35-e42, 2017.
[177] F. J. Moawad, C. L. Maydonovitch, and J. D. Horwhat, "Efficacy of cryospray ablation for the treatment of chronic radiation proctitis in a pilot study," *Digestive Endoscopy,* vol. 25, pp. 174-179, 2013.
[178] J. G. Taylor, J. A. DiSario, and D. J. Bjorkman, "KTP laser therapy for bleeding from chronic radiation proctopathy," *Gastrointestinal endoscopy,* vol. 52, pp. 353-357, 2000.
[179] S.-W. Jao, R. W. Bear, and L. L. Gunderson, "Surgical treatment of radiation injuries of the colon and rectum," *The American journal of surgery,* vol. 151, pp. 272-277, 1986.
[180] M. Turina, A. M. Mulhall, S. S. Mahid, C. Yashar, and S. Galandiuk, "Frequency and surgical management of chronic complications related to pelvic radiation," *Archives of Surgery,* vol. 143, pp. 46-52, 2008.
[181] A. Swager, D. Boerwinkel, D. Bruin, B. Weusten, D. Faber, S. Meijer, T. Leeuwen, W. Curvers, and J. Bergman, "Volumetric laser endomicroscopy in Barrett's esophagus: a feasibility study on histological correlation," *Diseases of the Esophagus,* 2015.
[182] P. J. Eifel, C. Levenback, J. T. Wharton, and M. J. Oswald, "Time course and incidence of late complications in patients treated with radiation therapy for FIGO stage IB carcinoma of the uterine cervix," *International Journal of Radiation Oncology* Biology* Physics,* vol. 32, pp. 1289-1300, 1995.
[183] G. D. Kennedy and C. P. Heise, "Radiation colitis and proctitis," *Clinics in colon and rectal surgery,* vol. 20, pp. 064-072, 2007.

[184] N. Haboubi, P. Rowland, and P. Schofield, "The light and electron microscopic features of early and late phase radiation-induced proctitis," *American Journal of Gastroenterology,* vol. 83, 1988.
[185] K. Araki, Y. Furuya, M. Kobayashi, K. Matsuura, T. Ogata, and H. Isozaki, "Comparison of mucosal microvasculature between the proximal and distal human colon," *Microscopy,* vol. 45, pp. 202-206, 1996.
[186] Y. Liu, K. Kudo, Y. Abe, D.-L. Hu, H. Kijima, A. Nakane, and K. Ono, "Inhibition of transforming growth factor-β, hypoxia-inducible factor-1α and vascular endothelial growth factor reduced late rectal injury induced by irradiation," *Journal of radiation research,* vol. 50, pp. 233-239, 2009.
[187] H. Takeuchi, T. Kimura, K. Okamoto, E. Aoyagi, H. Miyamoto, M. Kaji, H. Takenaka, S. Okamura, Y. Sato, and J. Kato, "A mechanism for abnormal angiogenesis in human radiation proctitis: analysis of expression profile for angiogenic factors," *Journal of gastroenterology,* vol. 47, pp. 56-64, 2012.
[188] P. Wu, L. Li, H. Wang, T. Ma, H. Wu, X. Fan, Z. Yang, D. Chen, and L. Wang, "Role of Angiogenesis in Chronic Radiation Proctitis: New Evidence Favoring Inhibition of Angiogenesis Ex Vivo," *Digestive diseases and sciences,* pp. 1-13, 2017.
[189] P. P. Tagkalidis and J. J. Tjandra, "Cronic radiation proctitis," *ANZ journal of surgery,* vol. 71, pp. 230-237, 2001.
[190] R. R. Babb, "Radiation proctitis: a review," *American Journal of Gastroenterology,* vol. 91, 1996.
[191] A. Denton, A. Forbes, J. Andreyev, and E. Maher, "Non surgical interventions for late radiation proctitis in patients who have received radical radiotherapy to the pelvis," *Cochrane Database Syst Rev,* vol. 1, 2002.
[192] A. K. Garg, W.-Y. Mai, J. E. McGary, W. H. Grant, E. B. Butler, and B. S. Teh, "Radiation proctopathy in the treatment of prostate cancer," *International Journal of Radiation Oncology* Biology* Physics,* vol. 66, pp. 1294-1305, 2006.
[193] R. Trzcinski, A. Dziki, M. Brys, M. Moszynska-Zielinska, J. Chalubinska-Fendler, M. Mik, R. Kujawski, and L. Dziki, "Expression of vascular endothelial growth factor and its correlation with clinical symptoms and endoscopic findings in patients with chronic radiation proctitis," *Colorectal Disease,* vol. 20, pp. 321-330, 2018.
[194] B. G. Vanneste, L. Van De Voorde, R. J. de Ridder, E. J. Van Limbergen, P. Lambin, and E. N. van Lin, "Chronic radiation proctitis: tricks to prevent and treat," *International journal of colorectal disease,* vol. 30, pp. 1293-1303, 2015.
[195] S. Szabo, P. Vattay, E. Scarbrough, and J. Folkman, "Role of vascular factors, including angiogenesis, in the mechanisms of action of sucralfate," *The American journal of medicine,* vol. 91, pp. S158-S160, 1991.
[196] R. Kochhar, P. Sriram, S. Sharma, R. Goel, and F. Patel, "Natural history of late radiation proctosigmoiditis treated with topical sucralfate suspension," *Digestive diseases and sciences,* vol. 44, pp. 973-978, 1999.
[197] Y. A. Gul, S. Prasannan, F. M. Jabar, A. R. Shaker, and K. Moissinac, "Pharmacotherapy for chronic hemorrhagic radiation proctitis," *World journal of surgery,* vol. 26, pp. 1499-1502, 2002.
[198] K. McElvanna, A. Wilson, and T. Irwin, "Sucralfate paste enema: a new method of topical treatment for haemorrhagic radiation proctitis," *Colorectal Disease,* vol. 16, pp. 281-284, 2014.
[199] M. Chruscielewska-Kiliszek, J. Regula, M. Polkowski, M. Rupinski, E. Kraszewska, J. Pachlewski, E. Czaczkowska-Kurek, and E. Butruk, "Sucralfate or placebo following argon plasma coagulation for chronic radiation proctitis: a randomized double blind trial," *Colorectal Disease,* vol. 15, 2013.
[200] L. Laterza, P. Cecinato, A. Guido, A. Mussetto, and L. Fuccio, "Management of radiation-induced rectal bleeding," *Current gastroenterology reports,* vol. 15, p. 355, 2013.

[201] T.-H. Ma, Z.-X. Yuan, Q.-H. Zhong, H.-M. Wang, Q.-Y. Qin, X.-X. Chen, J.-P. Wang, and L. Wang, "Formalin irrigation for hemorrhagic chronic radiation proctitis," *World Journal of Gastroenterology: WJG,* vol. 21, p. 3593, 2015.
[202] V. de Parades, I. Etienney, P. Bauer, J. Bourguignon, N. Meary, B. Mory, S. Sultan, M. Taouk, C. Thomas, and P. Atienza, "Formalin application in the treatment of chronic radiation-induced hemorrhagic proctitis—an effective but not risk-free procedure: a prospective study of 33 patients," *Diseases of the colon & rectum,* vol. 48, pp. 1535-1541, 2005.
[203] J. Cavciæ, J. Turciæ, P. Martinac, Z. Jelinciæ, B. Zupanciæ, and R. Panijan-Pezeroviæ, "Metronidazole in the treatment of chronic radiation proctitis: clinical trial," *Croat Med J,* vol. 4, pp. 314-8, 2000.
[204] C. Sahakitrungruang, A. Patiwongpaisarn, P. Kanjanasilp, S. Malakorn, and P. Atittharnsakul, "A randomized controlled trial comparing colonic irrigation and oral antibiotics administration versus 4% formalin application for treatment of hemorrhagic radiation proctitis," *Diseases of the Colon & Rectum,* vol. 55, pp. 1053-1058, 2012.
[205] K.-T. Chen, S.-J. Twu, H.-J. Chang, and R.-S. Lin, "Outbreak of Stevens-Johnson syndrome/toxic epidermal necrolysis associated with mebendazole and metronidazole use among Filipino laborers in Taiwan," *American journal of public health,* vol. 93, pp. 489-492, 2003.
[206] D. R. Donohoe, N. Garge, X. Zhang, W. Sun, T. M. O'Connell, M. K. Bunger, and S. J. Bultman, "The microbiome and butyrate regulate energy metabolism and autophagy in the mammalian colon," *Cell metabolism,* vol. 13, pp. 517-526, 2011.
[207] P. Vernia, P. Fracasso, V. Casale, G. Villotti, A. Marcheggiano, V. Stigliano, P. Pinnaro, V. Bagnardi, and R. Caprilli, "Topical butyrate for acute radiation proctitis: randomised, crossover trial," *The lancet,* vol. 356, pp. 1232-1235, 2000.
[208] A. Hille, M. K. Herrmann, T. Kertesz, H. Christiansen, R. M. Hermann, O. Pradier, H. Schmidberger, and C.-F. Hess, "Sodium butyrate enemas in the treatment of acute radiation-induced proctitis in patients with prostate cancer and the impact on late proctitis," *Strahlentherapie und Onkologie,* vol. 184, pp. 686-692, 2008.
[209] N. A. Talley, F. Chen, D. King, M. Jones, and N. J. Talley, "Short-chain fatty acids in the treatment of radiation proctitis," *Diseases of the colon & rectum,* vol. 40, pp. 1046-1050, 1997.
[210] A. Maggio, A. Magli, T. Rancati, C. Fiorino, F. Valvo, G. Fellin, U. Ricardi, F. Munoz, D. Cosentino, and L. F. Cazzaniga, "Daily sodium butyrate enema for the prevention of radiation proctitis in prostate cancer patients undergoing radical radiation therapy: results of a multicenter randomized placebo-controlled dose-finding phase 2 study," *International Journal of Radiation Oncology* Biology* Physics,* vol. 89, pp. 518-524, 2014.
[211] J. J. Feldmeier, I. Jelen, D. A. Davolt, P. T. Valante, M. L. Meltz, and R. Alecu, "Hyperbaric oxygen as a prophylaxis for radiation-induced delayed enteropathy," *Radiotherapy and Oncology,* vol. 35, pp. 138-144, 1995.
[212] J. J. Feldmeier and N. Hampson, "A systematic review of the literature reporting the application of hyperbaric oxygen prevention and treatment of delayed radiation injuries: an evidence based approach," *Undersea & hyperbaric medicine,* vol. 29, p. 4, 2002.
[213] M. Glover, G. R. Smerdon, H. J. Andreyev, B. E. Benton, P. Bothma, O. Firth, L. Gothard, J. Harrison, M. Ignatescu, and G. Laden, "Hyperbaric oxygen for patients with chronic bowel dysfunction after pelvic radiotherapy (HOT2): a randomised, double-blind, sham-controlled phase 3 trial," *The Lancet Oncology,* vol. 17, pp. 224-233, 2016.
[214] A. Lomax and P. Calder, "Probiotics, immune function, infection and inflammation: a review of the evidence from studies conducted in humans," *Current pharmaceutical design,* vol. 15, pp. 1428-1518, 2009.

[215] E. S. Woodle, M. R. First, J. Pirsch, F. Shihab, A. O. Gaber, P. Van Veldhuisen, and A. C. W. S. Group, "A prospective, randomized, double-blind, placebo-controlled multicenter trial comparing early (7 day) corticosteroid cessation versus long-term, low-dose corticosteroid therapy," *Annals of surgery,* vol. 248, pp. 564-577, 2008.

[216] H.-A. Mansouri-Tehrani, M. Rabbani-Khorasgani, S. M. Hosseini, F. Mokarian, H. Mahdavi, and M. Roayaei, "Effect of supplements: Probiotics and probiotic plus honey on blood cell counts and serum IgA in patients receiving pelvic radiotherapy," *Journal of research in medical sciences: the official journal of Isfahan University of Medical Sciences,* vol. 20, p. 679, 2015.

[217] F. Goldstein, J. Khoury, and J. J. Thornton, "Treatment of Chronic Radiation Enteritis and Colitis with Salicylazosulfapyridine and Systemic Corticosteroids," *American Journal of Gastroenterology,* vol. 65, 1976.

[218] C. A. Baum, W. L. Biddle, and P. B. Miner, "Failure of 5-aminosalicylic acid enemas to improve chronic radiation proctitis," *Digestive diseases and sciences,* vol. 34, pp. 758-760, 1989.

[219] V. Maunoury, J. Brunetaud, and A. Cortot, "Bipolar electrocoagulation treatment for hemorrhagic radiation injury of the lower digestive tract," *Gastrointestinal endoscopy,* vol. 37, pp. 492-493, 1991.

[220] D. M. Jensen, G. A. Machicado, S. Cheng, M. E. Jensen, and R. Jutabha, "A randomized prospective study of endoscopic bipolar electrocoagulation and heater probe treatment of chronic rectal bleeding from radiation telangiectasia," *Gastrointestinal endoscopy,* vol. 45, pp. 20-25, 1997.

[221] A. Sarin and B. Safar, "Management of radiation proctitis," *Gastroenterology Clinics,* vol. 42, pp. 913-925, 2013.

[222] Y. Sato, T. Takayama, T. Sagawa, M. Hirakawa, H. Ohnuma, K. Miyanishi, T. Sato, R. Takimoto, M. Kobune, and K. Okamoto, "Argon plasma coagulation treatment of hemorrhagic radiation proctopathy: the optimal settings for application and long-term outcome," *Gastrointestinal endoscopy,* vol. 73, pp. 543-549, 2011.

[223] R. T. Villavicencio, D. K. Rex, and E. Rahmani, "Efficacy and complications of argon plasma coagulation for hematochezia related to radiation proctopathy," *Gastrointestinal endoscopy,* vol. 55, pp. 70-74, 2002.

[224] D. Ravizza, G. Fiori, C. Trovato, and C. Crosta, "Frequency and outcomes of rectal ulcers during argon plasma coagulation for chronic radiation-induced proctopathy," *Gastrointestinal endoscopy,* vol. 57, pp. 519-525, 2003.

[225] T. R. Viggiano, J. Zighelboim, D. A. Ahlquist, C. J. Gostout, K. K. Wang, and M. V. Larson, "Endoscopic Nd: YAG laser coagulation of bleeding from radiation proctopathy," *Gastrointestinal endoscopy,* vol. 39, pp. 513-517, 1993.

[226] R. D. Odze and G. Y. Lauwers, "Histopathology of Barrett's esophagus after ablation and endoscopic mucosal resection therapy," *Endoscopy,* vol. 40, pp. 1008,1015, 08.12.2008 2008.

[227] J. J. G. H. M. Bergman, "Radiofrequency Ablation - Great for Some or Justified for Many?," *New England Journal of Medicine,* vol. 360, pp. 2353-2355, May 28 2009.

[228] C. Ell, O. Pech, and A. May, "Radiofrequency Ablation in Barrett's Esophagus," *New England Journal of Medicine,* vol. 361, pp. 1021-1021, Sep 3 2009.

[229] R. Pouw, J. Gondrie, C. Sondermeijer, F. ten Kate, T. van Gulik, K. Krishnadath, P. Fockens, B. Weusten, and J. Bergman, "Eradication of Barrett Esophagus with Early Neoplasia by Radiofrequency Ablation, with or without Endoscopic Resection," *Journal of Gastrointestinal Surgery,* vol. 12, pp. 1627-1637, 2008.

[230] A. Overwater and B. L. Weusten, "Cryoablation in the management of Barrett's esophagus," *Current Opinion in Gastroenterology,* vol. 33, pp. 261-269, 2017.

[231] T. H. Tsai, C. Zhou, H. C. Lee, Y. K. Tao, O. O. Ahsen, M. Figueiredo, D. C. Adler, J. M. Schmitt, Q. Huang, J. G. Fujimoto, and H. Mashimo, "Comparison of Tissue Architectural Changes between Radiofrequency Ablation and Cryospray Ablation in Barrett's Esophagus Using Endoscopic Three-Dimensional Optical Coherence Tomography," *Gastroenterol Res Pract,* vol. 2012, p. 684832, 2012.

[232] J. K. Hou, S. Abudayyeh, and Y. Shaib, "Treatment of chronic radiation proctitis with cryoablation," *Gastrointestinal endoscopy,* vol. 73, pp. 383-389, 2011.

[233] D. C. Adler, C. Zhou, T.-H. Tsai, J. Schmitt, Q. Huang, H. Mashimo, and J. G. Fujimoto, "Three-dimensional endomicroscopy of the human colon using optical coherence tomography," *Optics express,* vol. 17, pp. 784-796, 2009.

[234] M. P. Swan, G. T. Moore, W. Sievert, and D. A. Devonshire, "Efficacy and safety of single-session argon plasma coagulation in the management of chronic radiation proctitis," *Gastrointestinal endoscopy,* vol. 72, pp. 150-154, 2010.

[235] N. J. Shaheen, P. Sharma, B. F. Overholt, H. C. Wolfsen, R. E. Sampliner, K. K. Wang, J. A. Galanko, M. P. Bronner, J. R. Goldblum, A. E. Bennett, B. A. Jobe, G. M. Eisen, M. B. Fennerty, J. G. Hunter, D. E. Fleischer, V. K. Sharma, R. H. Hawes, B. J. Hoffman, R. I. Rothstein, S. R. Gordon, H. Mashimo, K. J. Chang, V. R. Muthusamy, S. A. Edmundowicz, S. J. Spechler, A. A. Siddiqui, R. F. Souza, A. Infantolino, G. W. Falk, M. B. Kimmey, R. D. Madanick, A. Chak, and C. J. Lightdale, "Radiofrequency ablation in Barrett's esophagus with dysplasia," *N Engl J Med,* vol. 360, pp. 2277-88, May 28 2009.

[236] T. H. Tsai, C. Zhou, Y. K. Tao, H. C. Lee, O. O. Ahsen, M. Figueiredo, T. Kirtane, D. C. Adler, J. M. Schmitt, Q. Huang, J. G. Fujimoto, and H. Mashimo, "Structural markers observed with endoscopic 3-dimensional optical coherence tomography correlating with Barrett's esophagus radiofrequency ablation treatment response (with videos)," *Gastrointest Endosc,* vol. 76, pp. 1104-12, Dec 2012.

[237] H.-C. Lee, O. O. Ahsen, J. J. Liu, T.-H. Tsai, Q. Huang, H. Mashimo, and J. G. Fujimoto, "Assessment of the radiofrequency ablation dynamics of esophageal tissue with optical coherence tomography," *Journal of Biomedical Optics,* vol. 22, pp. 076001-076001, 2017.

[238] M. J. Gora, J. S. Sauk, R. W. Carruth, K. A. Gallagher, M. J. Suter, N. S. Nishioka, L. E. Kava, M. Rosenberg, B. E. Bouma, and G. J. Tearney, "Tethered capsule endomicroscopy enables less invasive imaging of gastrointestinal tract microstructure," *Nature medicine,* vol. 19, pp. 238-240, 2013.

[239] A. J. Trindade, K. Sultan, A. S. Vamadevan, C. Fan, and D. V. Sejpal, "Successful use of volumetric laser endomicroscopy in imaging a rectal polyp," *Therapeutic advances in gastroenterology,* vol. 9, pp. 128-131, 2016.

[240] G. A. Holloway, C. H. Daly, D. Kennedy, and J. Chimoskey, "Effects of external pressure loading on human skin blood flow measured by 133Xe clearance," *Journal of Applied Physiology,* vol. 40, pp. 597-600, 1976.

[241] J. Clarke, S. Jagannath, A. Kalloo, V. Long, D. Beitler, and S. Kantsevoy, "An endoscopically implantable device stimulates the lower esophageal sphincter on demand by remote control: a study using a canine model," *Endoscopy,* vol. 39, pp. 72-76, 2007.

[242] C. P. Sanmiguel, M. Hagiike, M. P. Mintchev, R. D. Cruz, E. H. Phillips, S. A. Cunneen, J. L. Conklin, and E. E. Soffer, "Effect of electrical stimulation of the LES on LES pressure in a canine model," *American Journal of Physiology-Gastrointestinal and Liver Physiology,* vol. 295, pp. G389-G394, 2008.

[243] L. Rodríguez, P. Rodriguez, B. Gómez, J. C. Ayala, J. Saba, A. Perez-Castilla, M. G. Neto, and M. D. Crowell, "Electrical stimulation therapy of the lower esophageal sphincter is successful in

treating GERD: final results of open-label prospective trial," *Surgical endoscopy,* vol. 27, pp. 1083-1092, 2013.
[244] R. Banerjee, N. Pratap, R. Kalpala, and D. N. Reddy, "Effect of electrical stimulation of the lower esophageal sphincter using endoscopically implanted temporary stimulation leads in patients with reflux disease," *Surgical endoscopy,* vol. 28, pp. 1003-1009, 2014.
[245] C. A. Mosse, T. N. Mills, M. N. Appleyard, S. S. Kadirkamanathan, and C. P. Swain, "Electrical stimulation for propelling endoscopes," *Gastrointestinal endoscopy,* vol. 54, pp. 79-83, 2001.
[246] B. M. Doucet, A. Lam, and L. Griffin, "Neuromuscular electrical stimulation for skeletal muscle function," *Yale J Biol Med,* vol. 85, pp. 201-15, Jun 2012.
[247] N. A. Maffiuletti, M. A. Minetto, D. Farina, and R. Bottinelli, "Electrical stimulation for neuromuscular testing and training: state-of-the art and unresolved issues," *Eur J Appl Physiol,* vol. 111, pp. 2391-7, Oct 2011.
[248] O. Schuhfried, R. Crevenna, V. Fialka-Moser, and T. Paternostro-Sluga, "Non-invasive neuromuscular electrical stimulation in patients with central nervous system lesions: an educational review," *J Rehabil Med,* vol. 44, pp. 99-105, Feb 2012.
[249] C. P. Sanmiguel, M. Hagiike, M. P. Mintchev, R. D. Cruz, E. H. Phillips, S. A. Cunneen, J. L. Conklin, and E. E. Soffer, "Effect of electrical stimulation of the LES on LES pressure in a canine model," *Am J Physiol Gastrointest Liver Physiol,* vol. 295, pp. G389-94, Aug 2008.
[250] H. L. Sweeney and D. W. Hammers, "Muscle contraction," *Cold Spring Harbor perspectives in biology,* vol. 10, p. a023200, 2018.
[251] G. Gabella, "Structural apparatus for force transmission in smooth muscles," *Physiological Reviews,* vol. 64, pp. 455-477, 1984.
[252] W. J. Dodds, "The physiology of swallowing," *Dysphagia,* vol. 3, pp. 171-178, 1989.
[253] R. K. Mittal, S. J. Hong, and V. Bhargava, "Longitudinal muscle dysfunction in achalasia esophagus and its relevance," *Journal of neurogastroenterology and motility,* vol. 19, p. 126, 2013.
[254] H. Mashimo and R. K. Goyal, "Physiology of esophageal motility," *GI Motility online,* 2006.
[255] B. Burack and S. Furman, "Transesophageal cardiac pacing," *The American journal of cardiology,* vol. 23, pp. 469-472, 1969.
[256] J. J. Gallagher, W. M. Smith, C. R. Kerr, J. Kasell, L. Cook, M. Reiter, R. Sterba, and M. Harte, "Esophageal pacing: a diagnostic and therapeutic tool," *Circulation,* vol. 65, pp. 336-341, 1982.
[257] J. L. Atlee, C. Z. Pattison, E. L. Mathews, and A. G. Hedma, "Transesophageal atrial pacing for intraoperative sinus bradycardia or AV junctional rhythm: Feasibility as prophylaxis in 200 anesthetized adults and hemodynamic effects of treatment," *Journal of cardiothoracic and vascular anesthesia,* vol. 7, pp. 436-441, 1993.
[258] M. Burke, "Bidirectional propulsion of devices along the gastrointestinal tract using electrostimulation," UCL (University College London), 2013.
[259] M. Schmidt, A. Estrada, J. VanGilder, H. Maisenbacher, and R. Prosek, "Safety and feasibility of transesophageal pacing in a dog," *Journal of the American Animal Hospital Association,* vol. 44, pp. 19-24, 2008.
[260] H. C. Wolfsen, J. E. Crook, M. Krishna, S. R. Achem, K. R. Devault, E. P. Bouras, D. S. Loeb, M. E. Stark, T. A. Woodward, and L. L. Hemminger, "Prospective, controlled tandem endoscopy study of narrow band imaging for dysplasia detection in Barrett's Esophagus," *Gastroenterology,* vol. 135, pp. 24-31, 2008.
[261] M. Giacchino, A. Bansal, R. E. Kim, V. Singh, S. B. Hall, M. Singh, A. Rastogi, B. Moloney, S. B. Wani, and S. Gaddam, "Clinical utility and interobserver agreement of autofluorescence imaging and magnification narrow-band imaging for the evaluation of Barrett's esophagus: a prospective tandem study," *Gastrointestinal endoscopy,* vol. 77, pp. 711-718, 2013.

[262] L. R. Coia, R. J. Myerson, and J. E. Tepper, "Late effects of radiation therapy on the gastrointestinal tract," *International Journal of Radiation Oncology* Biology* Physics,* vol. 31, pp. 1213-1236, 1995.
[263] M. W. Sweesy, J. L. Holland, and K. W. Smith, "Electromagnetic interference in cardiac rhythm management devices," *AACN Advanced Critical Care,* vol. 15, pp. 391-403, 2004.
[264] H. E. Hoff and L. H. Nahum, "The supernormal period in the mammalian ventricle," *American Journal of Physiology-Legacy Content,* vol. 124, pp. 591-595, 1938.